

A Thesis Submitted for the Degree of PhD at the University of Warwick

Permanent WRAP URL:

<http://wrap.warwick.ac.uk/150545>

Copyright and reuse:

This thesis is made available online and is protected by original copyright.

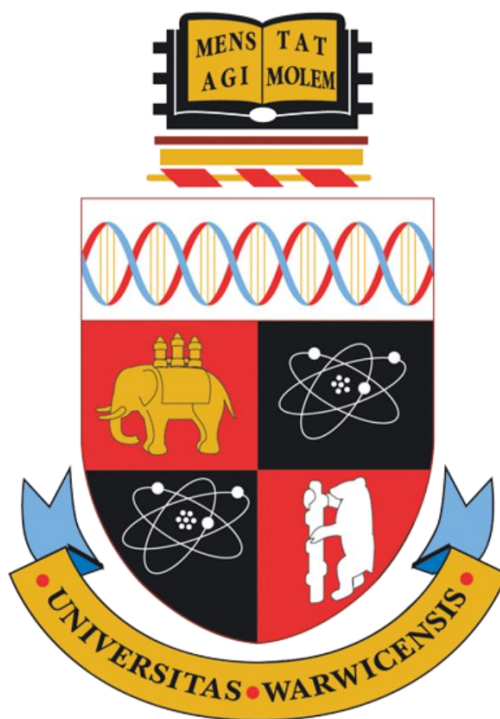
Please scroll down to view the document itself.

Please refer to the repository record for this item for information to help you to cite it.

Our policy information is available from the repository home page.

For more information, please contact the WRAP Team at: wrap@warwick.ac.uk

Half-sandwich Organo-osmium Anticancer Complexes



A Thesis Submitted for the Degree of Doctor of Philosophy

Xin Zhang

Supervisor: Prof. Peter J. Sadler, FRS

University of Warwick, Department of Chemistry

July 2019

Table of Contents

Acknowledgements	I
Declaration	III
Conferences and Courses Attended	IV
Abstract	V
Abbreviations	VII
Chapter 1 Introduction	1
1.1. Cancer and Cancer Therapies	2
1.1.1. Hallmarks of Cancer	2
1.1.2. Cancer Therapies	4
1.2. Anticancer Metallodrugs	7
1.2.1 Targets of Metallodrugs	8
1.2.1.1. DNA	8
1.2.1.2. Proteins	10
1.2.1.3. Cell Redox System	11
1.2.2. Design of Metallodrugs	14
1.2.3. Typical Examples of Metallodrugs	16
1.2.3.1. Cisplatin and Derivative Complexes	16
1.2.3.2. Metallocenes	20
1.2.3.3. Ruthenium Anticancer Complexes	22
1.3. Osmium	29

1.3.1. Background of Osmium Chemistry	29
1.3.2. Osmium Anticancer Applications	31
1.3.3. FY26 and Its Derivative Complexes	38
1.4. Azo Group	41
1.4.1. Azo Compounds	41
1.4.2. Reduction of Azo Bonds	43
1.5. Glutathione	46
1.5.1. Introduction to Glutathione	46
1.5.2. Reactions of Glutathione with Metal Complexes	48
1.6. Project Aims	53
1.7. References	54
Chapter 2 Experimental Section	73
2.1. Materials	74
2.1.1. Chemical Reagents	74
2.1.2. Buffer Solutions	75
2.1.3 Osmium Dimer Complexes	77
2.1.4. Cell culture	78
2.2. Instrumentation	79
2.2.1. UV-visible Spectroscopy	79
2.2.2. Inductively Coupled Plasma Optical Emission Spectroscopy (ICP-OES)	79

2.2.3. Inductively Coupled Plasma-Mass Spectrometry (ICP-MS)	80
2.2.4. High Performance Liquid Chromatography (HPLC)	80
2.2.5. Liquid Chromatography-Mass Spectrometry (LC-MS)	81
2.2.6. Nuclear Magnetic Resonance (NMR) Analysis	81
2.2.7. Elemental Analysis	82
2.2.8. Electrospray ionization-Mass Spectrometry (ESI-MS)	82
2.2.9. High Resolution Mass Spectrometry (HRMS)	83
2.2.10. Electron Paramagnetic Resonance (EPR)	83
2.2.11. Microwave Reactor	84
2.2.12. pH Meters	84
2.3. Methods	85
2.3.1. Products Purified by Flash Chromatography	85
2.3.2. Products Purified by HPLC	85
2.3.3. Samples Analysed by HPLC	86
2.3.4. N ₂ Protection Reactions	87
2.3.5. pK _a Measurements	89
2.3.6. X-ray Absorption Spectroscopy	90

2.3.7. Density Functional Calculations	91
2.3.8. Cell Seed and Passage	93
2.3.9. In vitro growth inhibition assay	93
2.4. References	95
Chapter 3 Synthesis and Characterisation of Os^{II} Arene Complexes	98
3.1. Introduction	99
3.2. Experimental Section	103
3.2.1. Materials	103
3.2.2. Instrumentation	103
3.2.3. Synthesis of Complexes	104
3.2.4. pK _a of [2-OH] ⁺	115
3.2.5. Anti-proliferative Activity	115
3.2.6. TD-DFT Calculations	116
3.2.7. Extinction Coefficient	116
3.2.8. HPLC and LC-MS	117
3.2.9. HRMS	118
3.2.10. The Proportionality between HPLC Peak and Concentration	118
3.3. Results	119
3.3.1. pK _a of [2-OH] ⁺	119

3.3.2. Anti-proliferative Activity	121
3.3.3. Electronic Spectra from TD-DFT Calculations	121
3.3.4. Extinction Coefficients	125
3.3.5. HPLC Retention Times and Mass Spectrometric Analysis for Osmium Species	127
3.3.6. The Proportionality between HPLC Peak Areas and Concentrations	134
3.4. Discussion	137
3.5. Conclusions	142
3.6. References	143
Chapter 4 Hydrolysis Studies on Azopyridine Osmium Arene Complexes	148
4.1. Introduction	149
4.2. Experimental Section	153
4.2.1. Materials	153
4.2.2. General Samples Preparation for HPLC	154
4.2.3. pH-Dependent Reaction Studies by HPLC	154
4.2.4. HPLC Analysis Methods	155
4.2.5. Quantitative Analysis from HPLC Traces	155
4.2.6. Reactions under N ₂ Atmosphere Studied by NMR	156

4.2.7. DFT Calculations	157
4.3. Results	160
4.3.1. Reactions of [2-I]⁺ with GSH	160
4.3.2. Reactions of [2-I]⁺ with Various Thiols	171
4.3.3. Reactions of Chlorido Complex [2-Cl]⁺ with GSH	173
4.3.4. Reactions of Imino Complex [2-imp_y-I]⁺ with GSH	178
4.3.5. Reactions of Hydroxido Complex [2-OH]⁺ with GSH	180
4.3.6. Reactions of Glutathione Adduct 2-SG with GSH	182
4.3.7. Hydrolysis Mechanism and DFT Calculations	183
4.4. Discussion	186
4.5. Conclusions	194
4.6. References	195
Chapter 5 Free Radical Detection	200
5.1. Introduction	201
5.2. Experimental Section	206
5.2.1. Materials	206
5.2.2. Radical Trapping	208
5.2.3. Sample Preparation	208

5.2.4. Spectrum Acquisition and Simulation	210
5.2.5. Effect of Superoxide Dismutase	211
5.2.6. H ₂ O ₂ Measurements	212
5.2.6.1. H ₂ O ₂ Test Strips	212
5.2.6.2. Ammonium Molybdate Method	213
5.3. Results	215
5.3.1. Reactions of 2-I•PF₆ with GSH	215
5.3.2. Reactions of 2-I•Cl with GSH	217
5.3.3. Reactions of 2-Cl•PF₆ with GSH	224
5.3.4. Reactions of 2-impy-Cl•PF₆ with GSH	229
5.3.5. Reactions of [2-OH]⁺ with GSH	230
5.3.6. Reactions of Azpy-NMe₂ with GSH	234
5.3.8. Reactions of 2-SG with GSH	236
5.3.9. Simulation of EPR Spectra	237
5.3.10. H ₂ O ₂ Detection	242
5.3.12. GSSG Detection	245
5.4. Discussion	246
5.5. Conclusions	255
5.6. References	256
Chapter 6 X-ray Absorption Spectroscopy (XAS) Studies	262
6.1. Introduction	263

6.2. Experimental Section	271
6.2.1. Materials	271
6.2.2. Methods	272
6.3. Results	277
6.3.1. XAS Spectra of Reference Complexes	277
6.3.2. FT-EXAFS Spectra of Reference Complexes	279
6.3.3. Validation of DFT Geometries against EXFAS Spectra	281
6.3.4. Validation of Models of [2-I] ⁺ in Aqueous Environments	285
6.3.5. 2-GS/NN Tracking in Reactions of [2-I] ⁺ with GSH	288
6.4. Discussion	298
6.5. Conclusions	302
6.6. References	303
Chapter 7 Conclusions and Future Work	307
7.1. Introduction	308
7.2. Conclusions from Chapters 3 – 6	308
7.3. Future Work	313
7.3.1. Interactions Between [2-I] ⁺ and Glycolysis Enzymes	313

7.3.2. Chiral Isomer Separation and Evaluation	316
7.3.3. Quantification of Intracellular Reduced Cytochrome <i>c</i>	317
7.3.4. Vibrational Spectroscopy of Reactions of [2-I] ⁺ with GSH	318
7.4. References	319
Appendix	323

Acknowledgements

The first time I met Prof. Peter J. Sadler when he gave a talk in Nanjing University (China), I was completely attracted by what he said about organometallic anticancer drugs and wished to join his group. I am really grateful for the opportunity, financial support and research guidance that Prof. Sadler has provided to me. My supervisor is very patient to me, an international student. He even corrected my English pronunciation for some simple words like “apoptosis”, “membrane”. I definitely will miss these four years in the University of Warwick.

I would like to greatly thank Dr. Carlos Sanchez Cano for countless research discussions. Every time I got problems of instruments, software and reports writing, I would drop him an email. There is also a big thank to all the guys in Sadler group and it is my fortune to meet all of you. Abraha offered his professional assistance with the synthesis aspects of my project. Cinzia and Russell helped a lot for revising my thesis. I and Lizzie went to Grenoble and finished the EXAFS experiments together. She is very lovely and helpful. Ollie is a football expert who supports Arsenal and it is very happy to discuss football matches with him. Samya and Venkat are very warm-heart India guys and we used to drink together. To the Chinese guys Feng, Wenying, Pingyu, Huaiyi, Yaqiong and Zijin,

I sincerely want to say thank you so much for all your supports and “motherland warm” during my most stressful time.

I cannot complete my projects research without Warwick Chemistry technicians and staff. Dr. Lijiang Song and Phil Aston do me great favours for the mass spectrometry studies. Ivan gives me a professional assistance for the NMR spectroscopy.

Taking this chance, I also thank all my collaborators. Prof. Emilia Sicilia (Università della Calabria, Italy) carries out high-level DFT calculations for my projects. Dr. Elisa Borfecchia (Università degli Studi di Torino, Italy) preformed incredible analysis work for my XAS data. Dr. Ben Breeze (Department of Physics, Warwick Univeristy) helped me a lot to build up EPR instrument and simulate spectra.

Greatly thanks to Warwick Rock-up & Play Football Activities and legendary football players Fuga, Liam, Tum, Simone, Adam, Wai, Yuki, Carl, and Feng. I do enjoy the happiest time when paly with you in the football pitch.

I also want to thank my family and friends, especially my parents for their support and encouragement all the time. Finally, there is a special word to Miss Wang Yinfang, the most pulchritudinous and elegant girl in my heart, that you will one thousand percent be my wife in future.

Declaration

I hereby declare that except where specific reference is made to other sources, the work contained in this thesis is the original work of the author. It has been composed by myself and has not been submitted, in whole or in part, for any other degree, diploma or other qualification.

Xin Zhang

July 2019

Conferences and Courses Attended

1. Transferable skills in science (University of Warwick, UK). June 2018.
2. Royal Society of Chemistry Dalton 2016 Conference (Coventry, UK). March 2016.
3. Postgraduate Chemistry Symposium (University of Warwick, UK). June 2017. Poster presentation.
4. Postgraduate Chemistry Symposium (University of Warwick, UK). June 2018. Oral presentation.
5. European Biological Inorganic Chemistry Conference (Birmingham, UK). June 2018. Poster presentation. Travel Prize.

Abstract

Cancer has become a public health problem worldwide. The side-effects and drug-resistance of current anticancer drugs such as cisplatin make it desirable to develop next-generation cancer therapy. Recently, half-sandwich ruthenium, iridium and osmium complexes have exhibited promising anticancer potency, of which $[\text{Os}(\eta^6\text{-}p\text{-cymene})(4\text{-(2-pyridylazo)-}N,N\text{-dimethylaniline})\text{I}]^+$ (**[2-I]**⁺, also known as FY26) showed 49× higher cytotoxicity than cisplatin towards 809 cancer cell lines. The potency of **[2-I]**⁺ was influenced by the concentration of intracellular tripeptide glutathione ($\gamma\text{-L-Glu-L-Cys-Gly}$, **GSH**). This thesis explores the chemical related mechanism of action of **[2-I]**⁺ and mainly studies the reactions of **[2-I]**⁺ with GSH.

Complexes related to the reaction of **[2-I]**⁺ with GSH under physiological conditions were synthesized and characterized, including the chlorido **[2-Cl]**⁺, hydroxido **[2-OH]**⁺ and thiolato adduct **2-SG**. For these osmium complexes, their extinction coefficients, retention times and mass spectra were determined and the proportionality between HPLC peak and concentrations is established. These studies provides the basis for the following exploration of the chemical behaviour of **[2-I]**⁺.

[2-I]⁺ is inert under physiological conditions, but the presence of GSH dramatically increases (> 100×) the extent of hydrolysis of **[2-I]**⁺. A

similar behaviour was also observed for chlorido analogue **[2-Cl]⁺**, but not for the imino analogue **[2-imp_y-I]⁺**, which indicates the importance of the azo ligand. Meanwhile, acidic conditions inhibited the promotion of hydrolysis of **[2-I]⁺** by GSH, which might be due to the deprotonation of GSH. Combined with DFT calculations, a novel mechanism of action based on deprotonated GS⁻ attack on the -N=N- azo bond to activate inert organo-osmium azopyridine complexes is proposed.

More surprisingly, free radicals O₂⁻, •OH and •H are detected in reactions of osmium azopyridine complexes (**[2-I]⁺**, **[2-Cl]⁺** and **[2-OH]⁺**) with GSH by EPR in presence of a spin trap, but no radicals were observed for the imino analogue or free azopyridine ligand. These results highlight the importance of azo bond and the osmium centre. Meanwhile, an N₂ atmosphere and acidic conditions hampered the free radical generation. A mechanism in which osmium azopyridine complexes induce electron transfer from GSH to O₂ and produce GSSG and O₂⁻ is proposed.

The sulfenylhydrazide intermediate in the reaction of **[2-I]⁺** with GSH was captured by Os L_{III}-edge X-ray absorption spectroscopy. This result supports a mechanism involving attack of deprotonated GS⁻ on the azo bond of **[2-I]⁺** to activate hydrolysis and produce free radicals. The studies in this thesis provide insights to a novel mechanism of action of this class of half-sandwich organo-osmium anticancer complexes.

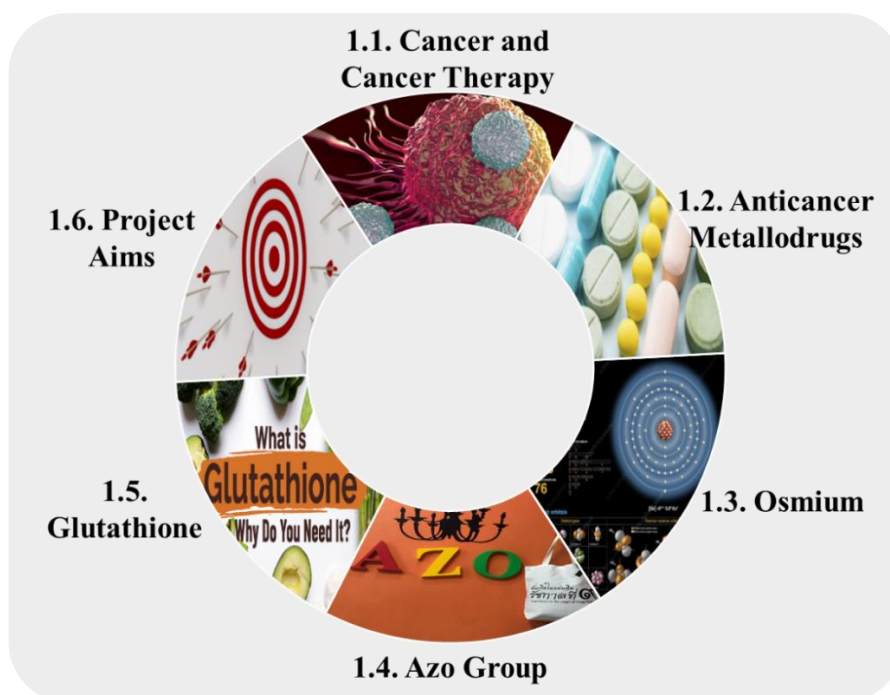
Abbreviations

AZPY	2-(phenylazo)pyridine
AZPY-NMe ₂	4-(2-pyridylazo)- <i>N,N</i> -dimethylaniline
IMPY-NMe ₂	4-(2-pyridylimino)- <i>N,N</i> -dimethylaniline
DCM	Dichloromethane
DEPMPO	5-Diethoxyphosphoryl-5-methyl-1-pyrroline N-oxide
d	doublet
dd	doublet of doublets
DFT	Density functional theory
DTT	1,4-dithiothreitol
EPR	Electron paramagnetic resonance
ESI-MS	Electrospray ionization mass spectrometry
EXAFS	Extended X-ray absorption fine structure
GAPDH	Glyceraldehyde 3-phosphate dehydrogenase
GSH	Glutathione (γ -L-Glu-L-Cys-Gly)
GSSG	Glutathione disulphide
HPLC	High pressure liquid chromatography
HRMS	High resolution mass spectrometry
ICP-MS	Inductively coupled plasma-mass spectrometry
ICP-OES	Inductively coupled plasma optical emission
IC ₅₀	50% growth inhibition concentration

Impy	Iminopyridine
K	Kelvin
K _a	Acid dissociation constant
L-BSO	L-Buthionine-Sulfoximine
LCMS	Liquid chromatography mass spectrometry
m	multiplet
mol equiv	Molar equivalent
m/z	mass/charge
NAC	N-acetyl-cysteine
NMR	Nuclear magnetic resonance
<i>p</i> -cym	<i>para</i> -cymene
ROS	Reactive Oxygen Species
s	singlet
SRB	Sulfurrhodamine B
t	triplet
TD-DFT	Time dependent-density functional theory
TFA	Trifluoroacetic acid
UV-vis	Ultraviolet-visible
XAS	X-ray absorption spectroscopy
XANES	X-ray absorption near-edge spectroscopy

Chapter 1

Introduction



1.1. Cancer and Cancer Therapies

The project in this thesis involves explorations of the mechanism of action of organo-osmium anticancer complexes. Cancer is the leading or second cause of death in over 80 countries including Europe, America and China, and has become a major public health problem worldwide. In 2018, there are an estimated 18.1 million new cancer cases and 9.6 million cancer deaths.¹ In 2019, 1,762,450 new cancer cases and 606,880 cancer deaths are projected to occur in the United States.² What cancer is (**Section 1.1.1**) and what currently cancer therapies there are (**Section 1.1.2**) will be introduced briefly.

1.1.1. Hallmarks of Cancer

Cancer is group of diseases with abnormal cell growth and unregulated cells spreading, as defined by World Health Organisation. Over 200 different types of cancers have been found in human body.³ In order for a normal cell to transform into a cancer cell, the genes that regulate cell growth and differentiation must be altered.^{4,5} More than 90% genetic mutations of cancer induction are contributed from environmental factors like chemicals, diet and obesity, infection, radiation, hormones and physical agents.⁶⁻¹⁰ The remaining 10% is due to inherited genetics.⁶ During the multistep development of human tumours,

biological capabilities are acquired, and corresponding hallmarks are observed and summarized (**Figure 1.1**).

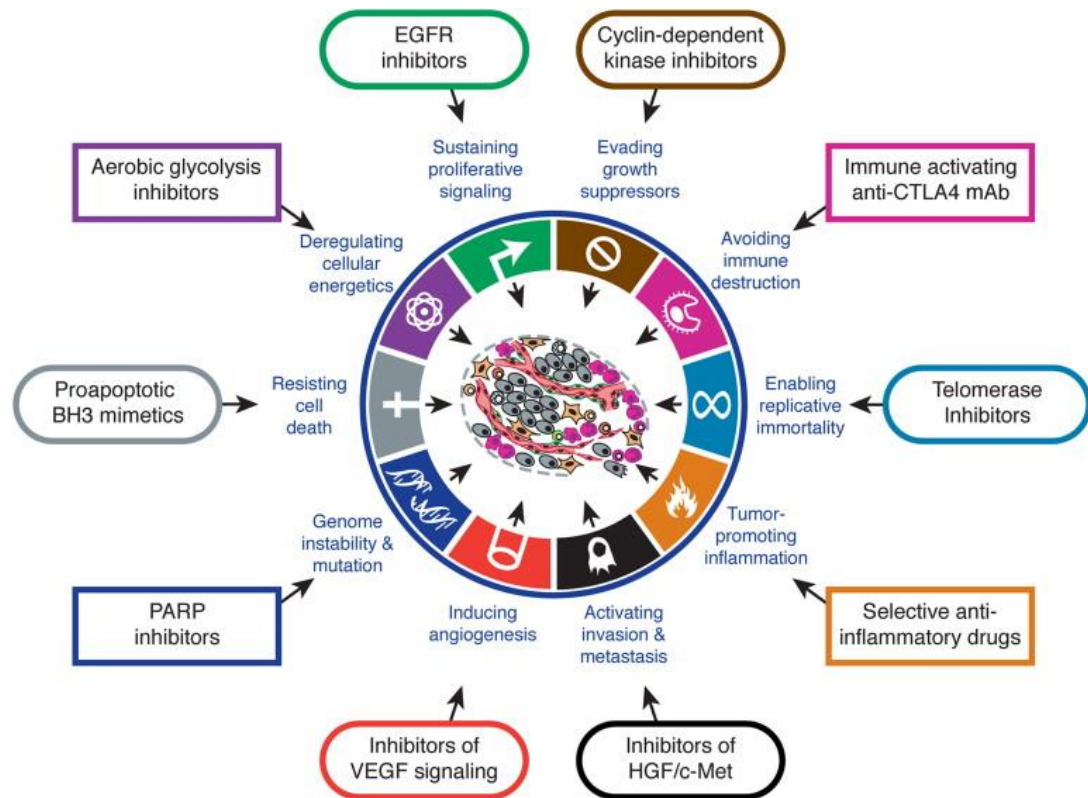


Figure 1.1. Hallmarks of cancer and corresponding cancer therapies.¹¹

These hallmarks of cancer cells include proliferative signalling, the evasion of growth suppressors, resisting cell death, enabling replicative immortality, inducing angiogenesis, and activating invasion and metastasis.¹¹ With the conceptual progress, in recent years two emerging hallmarks of potential generality have been added. These are reprogramming of energy metabolism, and the evasion of immune destruction.¹¹ Underlying these hallmarks are genome instability, which generates the genetic diversity that expedites their acquisition, and

inflammation.^{11,12} When cancer begins, it produces few specific symptoms so that it is common for people diagnosed with cancer to have been treated for other diseases. The hallmarks and characteristics of cancer benefit both cancer diagnosis and cancer therapies.

1.1.2. Cancer Therapies

Currently the methods applied for clinical anticancer treatment include surgery, radiotherapy, chemotherapy and immunotherapy. Surgery has long been a stable form to remove malignant tumours and relieve patients from the bulk of cancer immediately. The goal of surgery can be either the removal of only the tumour, or the entire organ. In theory, cancers can be cured if entirely removed by surgery, but this is not always possible in view of cancer metastasis. In clinical cancer treatment, surgery is generally used, together with chemotherapy and radiotherapy. Radiotherapy employs ionizing radiation to kill cancer cells by damaging the DNA of cancerous tissue.^{13,14} One successful example of internal radiation therapy is radioactive iodine, which is often used to treat certain types of thyroid cancer.^{15,16} Immunotherapy involves artificially stimulating the immune system to fight cancer based on the fact that cancer cells often have tumour antigens on their surface which can be detected by the immune system.^{17,18}

Immunotherapies can be categorized as active or passive. The passive immunotherapies use monoclonal antibodies, lymphocytes and cytokines to enhance existing anti-tumour responses. The U.S. Food and Drug Administration (FDA) has approved many anticancer monoclonal antibodies including Alemtuzumab, Atezolizumab, Avelumab, Ipilimumab, Ofatumumab, Nivolumab, Pembrolizumab, Rituximab and Durvalumab.^{19,20} Active immunotherapy directs the immune system to attack tumour cells by targeting tumour antigens. The drugs approved for active immunotherapy consist of Tisagenlecleucel (Kymriah), Axicabtagene ciloleucel (Yescarta) and Sipuleucel-T (Provenge).²¹⁻²³ In 2018, the Nobel Prize in Physiology or Medicine was awarded jointly to James P. Allison and Tasuku Honjo for their great contributions to cancer immunotherapy.

Chemotherapy is currently the most widely used and powerful cancer treatment, especially when patients face the problems of tumour metastasis and recurrence after surgery and radiotherapy. Chemotherapy literally means drug treatment, but now the term chemotherapy has come to mean a treatment of cancer by using anti-cancer medicines known as cytotoxic medicines. Cisplatin-based chemotherapy is the first-line treatment for many cancer types, of which cytotoxicity is achieved through DNA attack.²⁴ Due to non-selectivity

regarding normal cells, millions of patients suffer from unwanted the side-effects induced by chemotherapy including tiredness, nephrotoxicity, neurotoxicity, ototoxicity, hair loss and vomiting.²⁵ The desire for high selectivity has stimulated the emergence of targeted cancer therapy. The hallmarks of cancer cells provide a theoretical foundation and practical feasibility to develop cancer-targeted chemotherapy. For example, cancer cells share a hallmark of proliferative signalling substance caused by the overpression of EGFR (epidermal growth factor receptor).²⁶ Erlotinib (Tarceva) has been developed as EGFR inhibitor and used to prevent cancer cell proliferation selectively.²⁷ Based on the cancer hallmark of genome instability and mutation, PARP (poly ADP-ribose polymerase) inhibitor Olaparib (Lynparza) has been approved for ovarian cancer treatment.²⁸ The development of targeted drugs moves the chemotherapy from observation-driven to target-driven, and provides a promising way to kill cancer cells selectively.

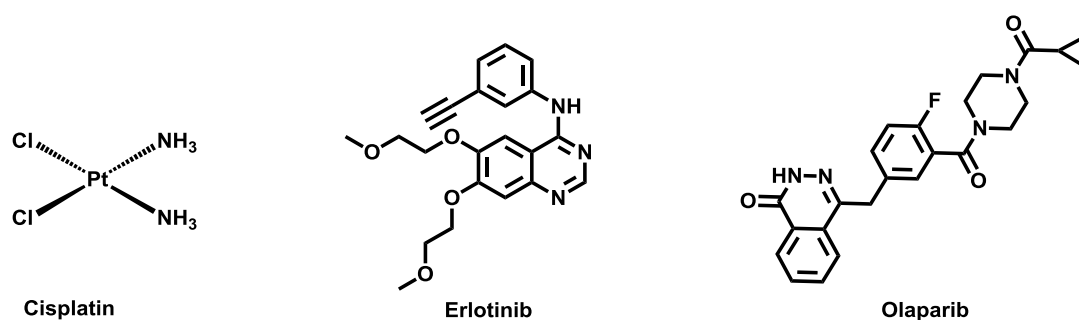


Figure 1.2. The structures of some anticancer drugs

1.2. Anticancer Metallodrugs

Metal ions play important roles in biological processes, and the use of metals in pharmaceutical potions can even be traced back to ancient civilizations of Mesopotamia, Egypt, India, and China 2500 B.C.²⁹ The modern development of metallodrugs began with the discovery of salvarsan to treat infectious diseases in 1912,³⁰ and greatly stimulated by the application of cisplatin as anticancer therapy from 1965.^{31,32} Metal ions in metallodrugs, especially transition metal ions, usually have more oxidation states than carbon, which provides potential for a higher level of versatility. Such an advantage renders metallodrugs of particular interest, and these have been developed rapidly in recent years. Currently platinum complexes are used as a component of nearly 50% of all cancer treatments,³³ gadolinium complexes are administered over 20 million doses per year as MRI (Magnetic Resonance Imaging) contrast agents and ^{99m}-technetium radiopharmaceuticals are used in about 20 million radiodiagnostic procedures each year for γ -ray imaging.³³ Hundreds of metallodrugs have achieved great success in many fields. In this part of the thesis, only anticancer metallodrugs will be described. Intracellular targets (**Section 1.2.1**), design principles (**Section 1.2.2**) and typical examples (**Section 1.2.3**) of anticancer metallodrugs will be introduced.

1.2.1 Targets of Metallodrugs

1.2.1.1. DNA

Deoxyribonucleic acid (DNA) is a macromolecule with two DNA strands that coil around each other to form a double helix, in which the two strands, also called polynucleotides, are composed of monomer nucleotides. Each nucleotide contains one of four nitrogen-containing nucleobases (cytosine [C], guanine [G], adenine [A] or thymine [T]), a sugar called deoxyribose, and a phosphate group. The adjacent nucleotides in a chain are joined to each other by covalent bond between the sugar moiety of one nucleotide and the phosphate group of the next. The opposite nucleotides in two separate chains are bound to each other by hydrogen bonds, according to base pairing rules (A with T and C with G). Due to the non-symmetrically double helix structure, two grooves are observed in DNA. The major groove is 22 Å wide, and the minor groove is 12 Å wide.³⁴

DNA stores the biological information used for cell growth, development, functioning and reproduction, and it is replicated during the cell division. Since cancer cells keep devising and spreading, DNA have been used as one of targets for anticancer drugs. The view that nuclear DNA is the important functional and pharmacological target of platinum anticancer drugs has been proved and generally accepted.

Cisplatin typically binds to primary sequences containing 2 to 3 nucleotides such as GG, AG and GNG sequences (More details are shown in **Section 1.2.3.1**). Basically, there are two ways that metallodrugs bind with DNA, one of which involves covalent binding to the nitrogen donor groups and the other is *via* π - π stacking interactions with DNA nucleobases to distort DNA's geometry and structure. Both types of binding can inhibit DNA replication, which leads to S-phase cell-cycle arrest and causes DNA damage, which induces cell apoptosis.³⁵

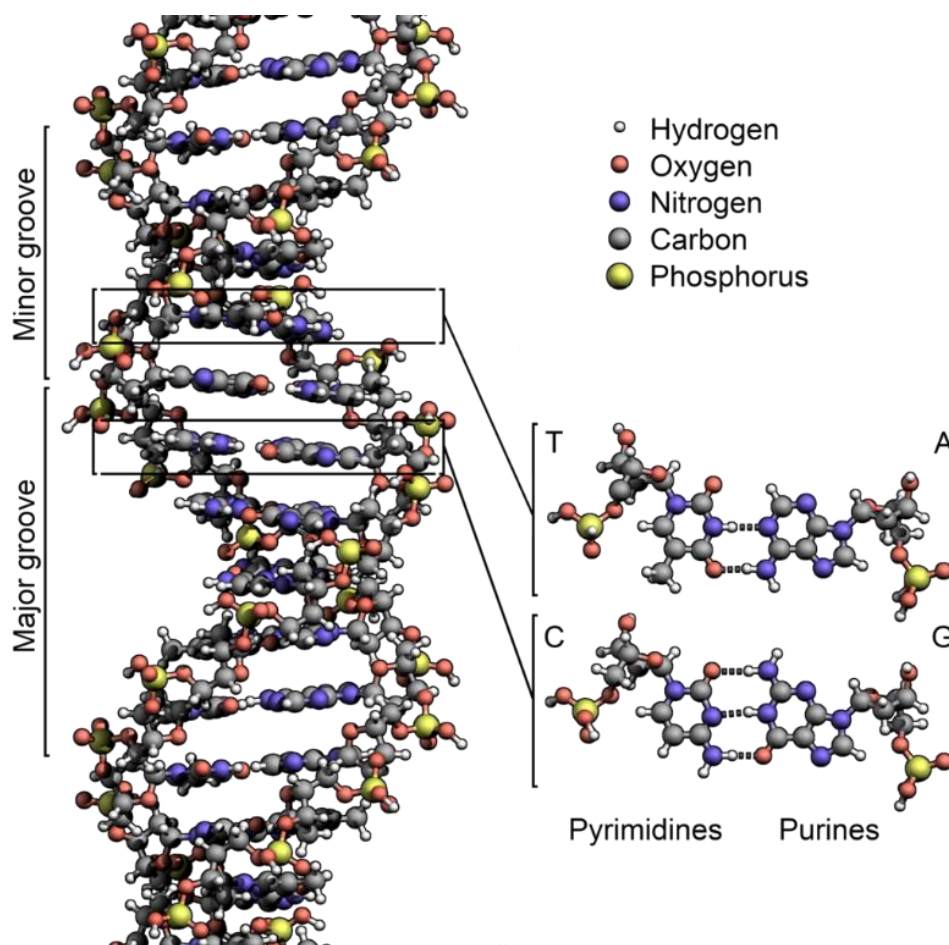


Figure 1.3. The non-symmetrically double helix structure of DNA (Wikipedia).

1.2.1.2. Proteins

Proteins are large biomolecules consisting of one or more long chains of amino acid residues. In human cells, proteins are composed of 21 kinds of amino acids. The sequence of amino acids determined by the corresponding gene is the primary structure of the protein. The secondary structure of the protein is determined by protein chain folding processes including α -helix and β -sheets. The tertiary structure is referred to compact globular structure folded from α -helix and β -sheets and quaternary structure consists of the aggregation of two or more individual polypeptide chains (sub-units) that operate as a single functional unit. Each different protein has a unique structure to perform different functions, and even the structure basis same kinds of protein also varies in different type cells.

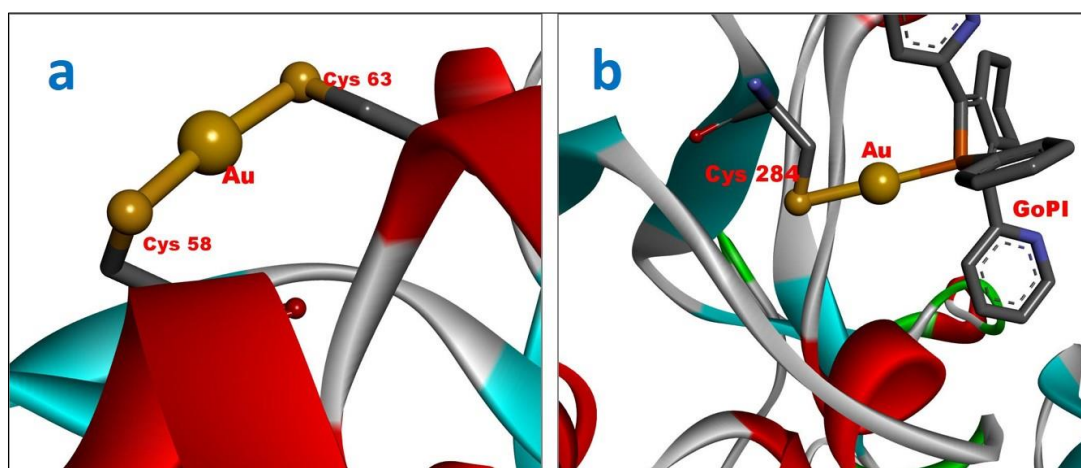


Figure 1.4. The crystal structure of human glutathione reductase (PDB code: 2AAQ) with a gold complex (GoPI) bound at (a) site 1 with Cys 58, Cys 63 and (b) site 2 with Cys 284.

Some proteins are overexpressed in cancer cells to meet their special nutrition and energy requirements, which provides good selective targets for anticancer drugs. Enzymes reducing disulfide bonds in cells, like thioredoxin reductase and glutathione reductase, are essential for cell growth and survival. They are usually upregulated in several types of cancer cells, and hence become targets of gold(I)-based anticancer complexes. The mechanism of action involves gold binding to cysteine residues at the enzymes active sites (**Figure 1.4**).³⁶

1.2.1.3. Cell Redox Systems

Besides DNA and proteins, the intracellular redox system has emerged as a novel target and provides broader opportunities to overcome cancer problems. The redox system consists of biomolecules with their reduced/oxidized form, for example GSH/GSSG and NADH/NAD⁺. One major function of such redox systems is to control the balance of reactive oxygen species (ROS) which are chemically reactive species containing oxygen such as peroxides, superoxide, hydroxyl radicals, singlet oxygen. ROS play important roles in signal transduction and intracellular metabolism.³⁷ However, too high levels of ROS are likely to induce cellular damage such as: 1) damage to DNA or RNA, 2) oxidation of polyunsaturated fatty acids in lipids to disturb intracellular

membrane, and 3) oxidation of amino acids in proteins to change their structure and functions³⁸

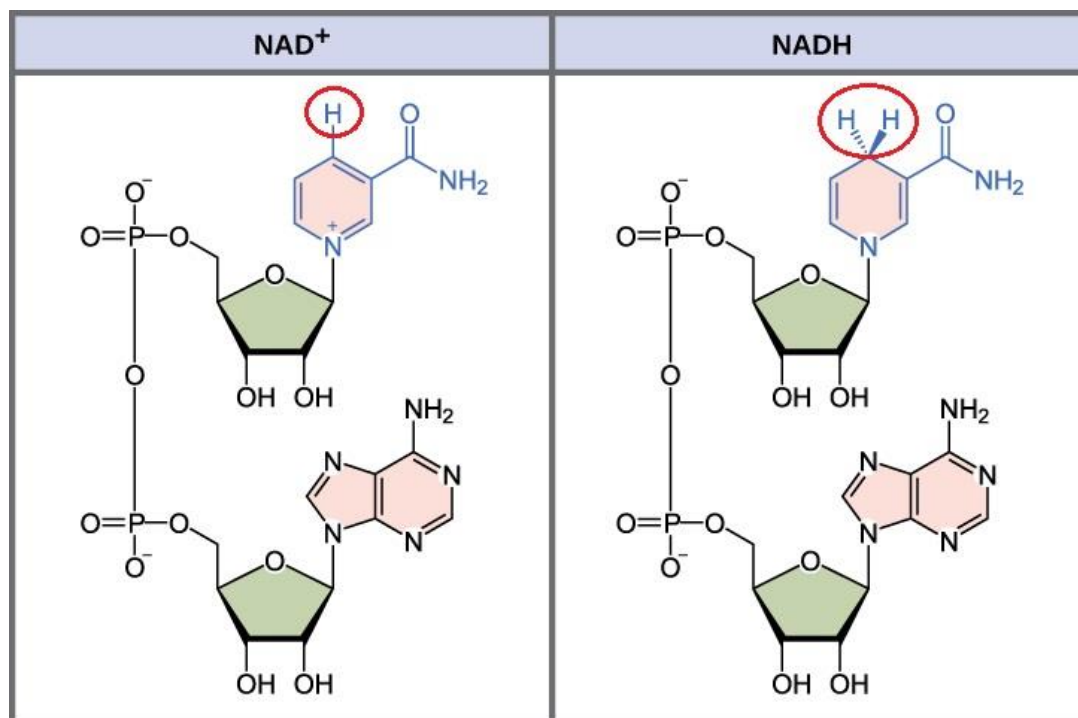


Figure 1.5. Structures of NAD⁺ and NADH

Many signalling pathways linked to tumourigenesis can regulate the metabolism of ROS, which results in the imbalances between ROS generation and elimination.³⁹ Cancer cells maintain high levels of ROS and depend heavily on antioxidant defence systems. Thus, a new anticancer therapy of elevating the ROS levels in the cells to perturb redox processes has emerged, which is known as “oxidative therapy”.⁴⁰ Significant increases in endogenous ROS can push cancer cells above a cellular tolerability threshold and induce cell death. On the other hand,

normal cells with lower ROS levels appear to have a higher capacity to cope with additional ROS-generating insults than cancer cells do.⁴⁰ The organo-iridium complex $[(\eta^5\text{-Cp}^{\text{xbiph}})\text{Ir}(\text{phpy})(\text{Cl})]$ (Cp^{xbiph} = biphenyltetramethylcyclopentadienyl, with phpy = C^N-chelated phenylpyridine) have been reported to catalyse hydride-transfer reactions using NADH as a cellular hydride source to promote peroxide generation and eventually induce cancer cell death.⁴¹

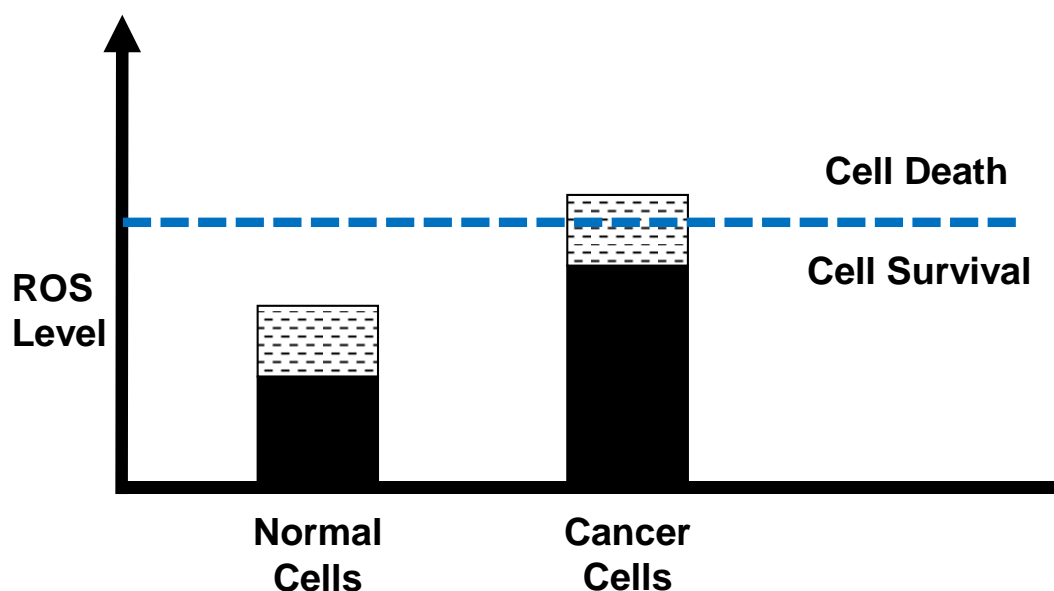


Figure 1.6. Selective killing of cancer cells by ROS. There is evidence that cancer cells have higher levels of ROS than normal cells (represented in black) and there is a threshold of ROS in which cells cannot survive. Increasing the levels of ROS (represented in striped area) can selectively give rise to cell death for cancer cells.

1.2.2. Design of Metallodrugs

Many successful metallodrugs have been discovered by chance, and the discovery stories for some of them, like cisplatin, are purely accidental. On the basis of first generation serendipitous hits, further generations of drug developments have been achieved through exploring the mechanism for potency, as well as reasons for unwanted side-effects. Currently, many efforts have been made to move the metallodrug development process from the initial serendipitous discoveries to more rational drug design process. The process of incorporating metal ions into metallodrugs generally involves the following steps:²⁹

- Finding a druggable target
- Designing metal complexes for the perfect fit
- Exploring the druggability of the target
- Studying thermodynamic stability and kinetic lability
- Constructing preclinical testing
- Constructing clinical testing

In the design part, the first two steps mainly involve finding a druggable target and designing metal complexes for the perfect fit. The targets of metallodrugs could be DNA, proteins and biomolecules related to the redox system (**Section 1.2.1**),⁴² and in the reaction of metallodrugs with targets, there are four fundamental mechanisms of action involved: 1)

binding to biological thiol groups, 2) chelating with target molecules, 3) generating reactive oxygen species, and 4) producing lipophilic ions.²⁹ Recently, a new fundamental mechanism has emerged that a metal centre may not be involved in any direct interactions with the target but provides a platform for organizing the organic ligands in the 3D space as mimics of natural protein inhibitors.⁴³

For the perfect fitting with targets, the design of a metallodrug is based on the choice of the metal, its oxidation state, the types and numbers of coordinated ligands, and the coordination geometry. The metal ions can widely range from 13 essential ones, e.g. Cu and Fe, to precious metals like Pt and Os. The types of the ligands can include wide a range of donors, with coordinating atoms such as carbon, nitrogen, oxygen, phosphorus, sulfur and halogens. Compared to organic molecules, the geometry of metal complexes is more diverse in 3D space. The basis of this diversity is from the coordination number of the metal which can be up to 8 or 9, while the “coordination number” of carbon is 4 or less. Besides linear, trigonal-planar and tetrahedral geometries which are generated in organic compounds, purely relying on carbon and dictated by the principles of hybridization, other configurations are created in metal complexes including square pyramidal, trigonal bipyramidal, octahedral, pentagonal bipyramidal, square antiprismatic and tricapped

trigonal prismatic. With more substituents, and modification of these substituents, the variety in stereoisomers and stereochemical flexibility in general increases to open up a diversity in 3D structures.

Designed metallodrugs need to fit their targets, but firstly are required to reach their targets. Once the drugs are injected and pass through the bloodstream, they eventually enter into cells, but biological substances like human serum protein can modify the metal drugs through substitution reactions. Outer sphere ligand interactions of the metallodrugs are also important to be considered in the design process.^{29,44}

1.2.3. Typical Examples of Metallodrugs

1.2.3.1. Cisplatin and Derivative Complexes

Cisplatin is on the World Health Organization's List of Essential Medicines, i.e. the most effective and safe medicines needed in a health system, and has become the best-selling anticancer drug at present. The history of cisplatin can be briefly outlined as it was first synthesized in 1835 by Michele Peyrone;⁴⁵ then its structure with a square planar geometry was deduced in 1893 by Alfred Werner;⁴⁶ its anti-tumour potency was discovered in 1969 by Barnett Rosenberg;³² clinical trials

were designed and performed in 1971 and permission for medical use was approved by the FDA in 1978.⁴⁶ Cisplatin-based chemotherapy is used to treat various types of cancers, including sarcomas, some carcinomas (e.g., small cell lung cancer, squamous cell carcinoma of the head and neck and ovarian cancer), lymphomas, bladder cancer, cervical cancer and germ cell cancer.⁴⁷ Against testicular cancer, cisplatin is particularly effective and improves the cure rate from 10 to 85%.⁴⁸

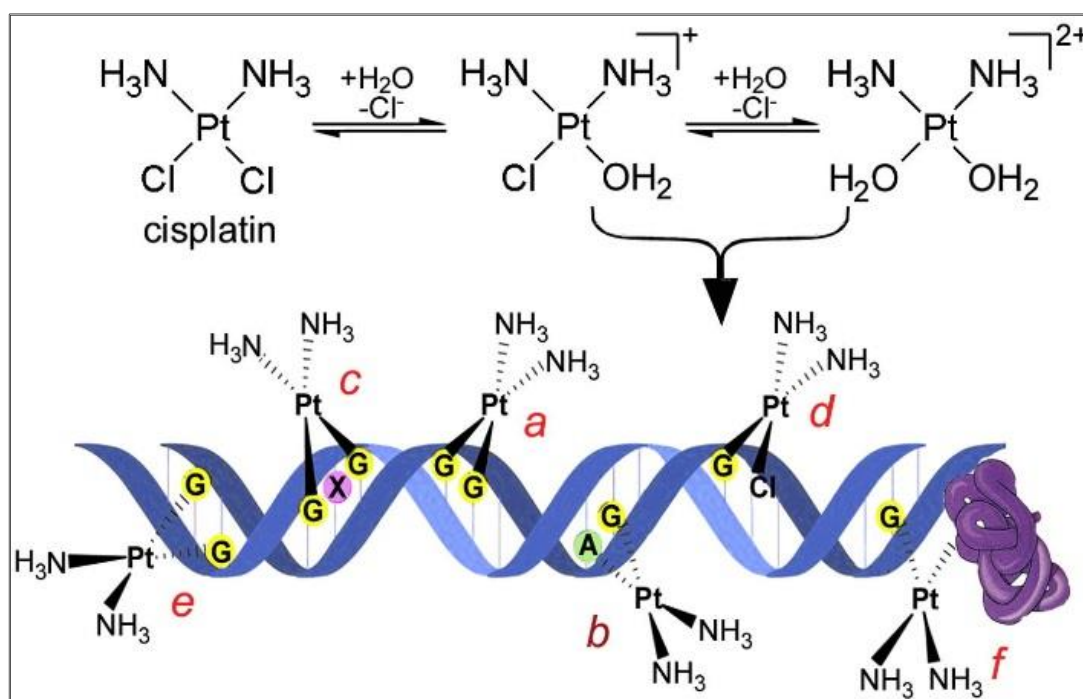


Figure 1.7. Schematic representation of cisplatin hydrolysis and adducts induced in DNA. a) intrastrand crosslinking of two adjacent guanines; b) intrastrand crosslinking of adjacent adenine and guanine; c) 1,3 intrastrand crosslinking of two guanines separated by another intervening base; d) monofunctional adduct; e) interstrand cross-link; f) DNA-platinum-protein cross-link.⁴⁹

The mechanism of action of cisplatin features attack of the Pt-Cl bond by H₂O first, and then the aquated product, which is a potent electrophile, can react with nucleophiles such as nitrogen donor atoms on DNA base residues. The most prevalent cisplatin-induced DNA adduct is an intrastrand cross-link (CL), in which the platinum(II) ion is coordinated to the *N*7 positions of the imidazole ring of two adjacent guanines (60-65% of all adducts), or to a lesser extent of one adenine and one guanine (20% of all adducts). Other less frequently produced same-strand adducts are the GpXpG 1, 3 intrastrand CL (where there is another intervening base in between the two platinated guanines; 2%) and monofunctional adducts on guanines (approximately 2%). In addition, around 2-6% of adducts involve guanines on opposite DNA strands, so-called interstrand CLs preferentially formed in the 5'-GC/5'-GC sequences.⁴⁹ Besides these DNA-platinum(II) adducts, ternary DNA-platinum-protein cross links can also be formed.⁴⁹ The binding of cisplatin to DNA makes structural distortions of DNA to arrest the cell cycle at the S-phase, and causes unrepaired DNA damage to activate the apoptosis of cells.⁵⁰ This mechanism of action is considered as the major contribution to the cisplatin cytotoxicity. However, the non-selectivity of this mechanism affects both cancer and normal cells and is associated with toxic side effects such as vomiting, neuropathy, and myelosuppression. In particular, irreversible kidney damage is a major

concern which limits the dosage that can be used.²⁵ Cisplatin resistance is another concern limiting its application. Initial cisplatin responsiveness is high but the majority of cancer patients will eventually relapse with cisplatin-resistant disease. Many mechanisms of cisplatin resistance have been proposed including changes in cellular uptake and efflux of the drug, increased detoxification of the drug, inhibition of apoptosis and increased DNA repair.⁵¹⁻⁵³ In order to overcome the side effects and drug-resistance of cisplatin, cisplatin derivatives have been developed and have achieved success in clinical application with less side effects than cisplatin. The second-generation platinum(II) complexes carboplatin and oxaliplatin have been approved and third generation platinum complexes such as nedaplatin, lobaplatin, heptaplatin and dicycloplatin are still undergoing clinical trials.^{33,54}

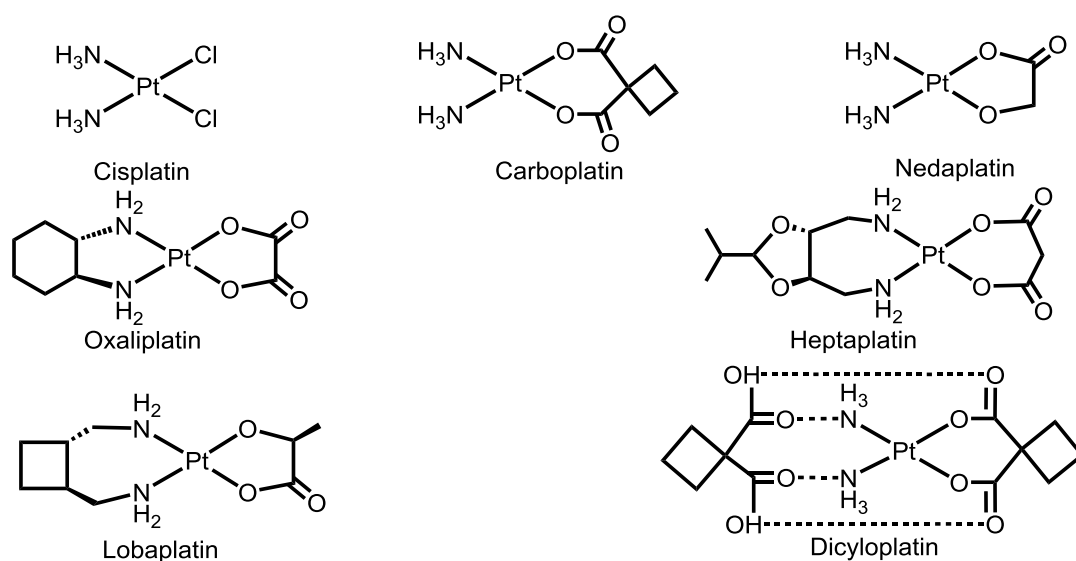


Figure 1.8. Molecular structures of platinum(II) anticancer drugs that are approved or undergoing clinical trials.

1.2.3.2. Metallocenes

Metallocenes are series of metal complexes with two π -bonded cyclopentadienyl ligands on a metal atom. Their symmetrical structures makes metallocenes resemble a “sandwich” thus such complexes are frequently referred as “sandwich complexes”.⁵⁵ The first documented metallocene complex is ferrocene that was discovered in 1951.^{56,57} Structurally, the metallocene complexes can be classified into two classes. One class is “classical metallocenes”, in which the metal bonds to parallel Cp rings such as ferrocene, ruthenocene and cobaltocenium. The other class is the “bent metallocenes” which have other ligands bonded to the metal in addition to the Cp rings including titanocene, zirconocene, vanadocene, niobocene and molybdocene.^{58,59}

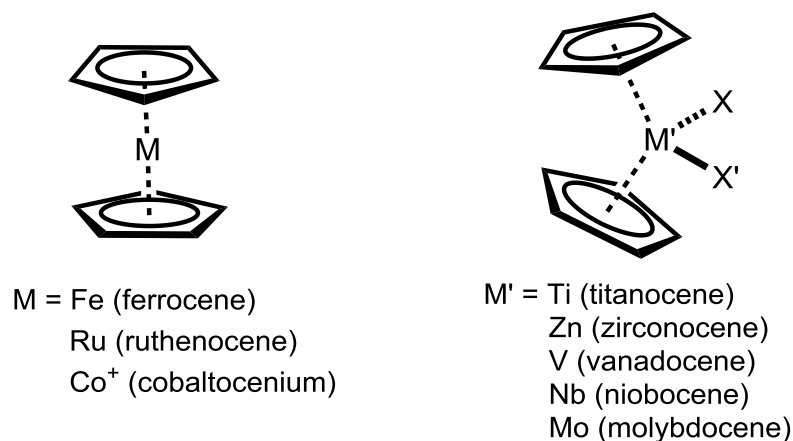


Figure 1.9. Molecular structures of classical metallocenes (left) and bent metallocenes (right).⁵⁸

From the 1970s, the anticancer activity of metallocenes has been studied, and titanocene dichloride entered into phase II clinical trials for the treatment of renal and breast cancers.⁶⁰ Unfortunately, the clinical response to titanocene dichloride was not significantly sufficient to justify continuation of the trials. The two main problems encountered with titanocene dichloride are poor aqueous solubility and hydrolytic instability.⁶¹ In order to address these problems, structural optimization to titanocene dichloride has been developed including bridging of the Cp rings to prevent Ti-Cp bond cleavage,⁶² replacing the chloride ligands with a more suitable oxalate ligand⁶³ and synthesizing ionic titanocene complexes.⁶⁴ The mechanisms of these titanocenes in the killing of cancer cells are versatile and still under exploration. They have been shown to be related to inhibition of DNA replication and transcription, induction of metallothioneins and downregulation of H4 histone genes.^{65,66}

The discovery of metallocene activity is marked as a milestone in the history of anticancer metallodrugs because they mark the time of first use of organometallic anticancer complexes. Following ferrocene and titanocene dichloride, many other organometallic anticancer complexes have been developed, e.g. ferrociphens⁶⁷ and the organo-osmium complexes studied in this thesis (**Section 1.3.3**).⁶⁸

1.2.3.3. Ruthenium Anticancer Complexes

From the 1950s, the anticancer activity of ruthenium (Ru) complexes has been recognised^{43,69}, and accelerating interest in the development of Ru-based anticancer drugs is reflected by the growth of related publications over the past 20 years.⁷⁰ So far, three Ru-based anticancer complexes (NAMI-A, KP1019 and KP1339, **Figure 1.10**) have reached clinical trials, and more candidates are still under preclinical studies. These Ru complexes provide alternatives to platinum-based drugs for anticancer therapy, and more promisingly they exhibit novel mechanisms of action to overcome the drug-resistance, and side effects observed with platinum drugs.

NAMI-A, KP1019 and KP1339 are Ru(III) complexes and such complexes can be readily reduced to their more active Ru(II) counterparts for target binding. This reduction generally occurs in the tumour microenvironment of low oxygen concentration, acidic pH and high levels of glutathione.⁷¹⁻⁷³ NAMI-A has low potency of cytotoxicity to cancer cells *in vitro*, but shows outstanding inhibition of cancer metastasis *in vivo*.⁷⁴⁻⁷⁶ KP1019 and KP1339 are analogous complexes based on the same complex anion, differing only by the counterion (sodium instead of indazolium), in view of the higher solubility of the latter. Several studies concerning the impact of KP1019/KP1339 on

cancer cells indicate a combined antiproliferative and cell-death-inducing activity^{77,78} contributed by multi-mechanisms, including the ruthenium complexes reacting with DNA, disturbing intracellular redox balance, and the targeting cellular stress and survival signaling pathways.⁷⁹⁻⁸¹

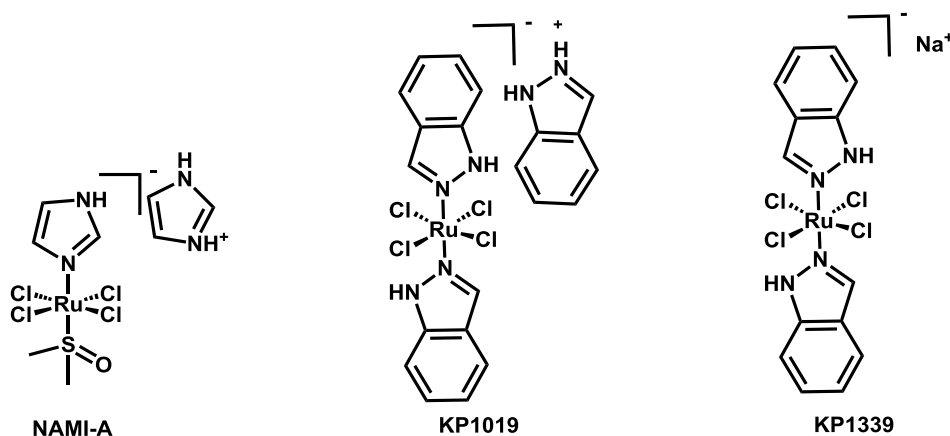
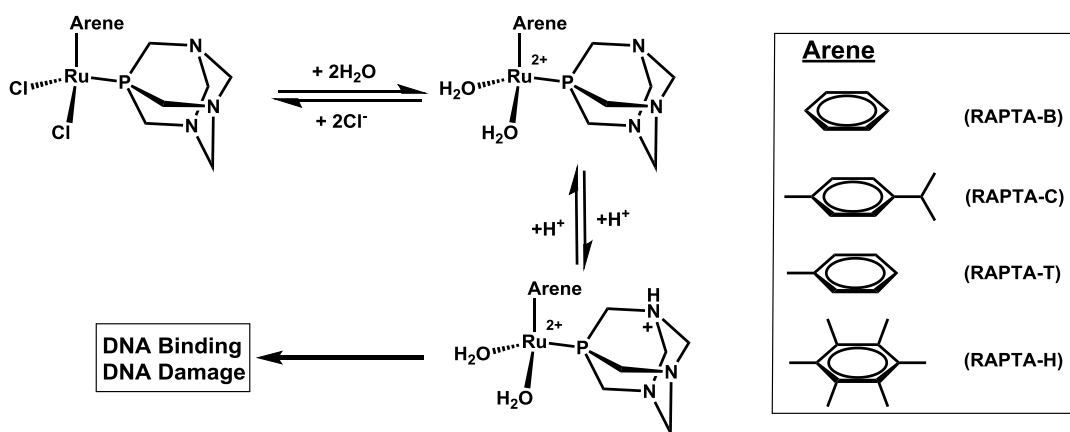


Figure 1.10. The molecular structures of NAMI-A, KP1019 and KP1339.



Scheme 1.1. RAPTA complexes and their mode of pH-dependent DNA binding.

Moreover, many research groups have also paid attention to the development of Ru(II) complexes, especially Ru(II)-arene complexes. These organo-ruthenium(II) complexes exhibit promising behaviour for medical applications but currently are still at the preclinical development.

Dyson *et al* have synthesized a series of Ru(II) η^6 -arene complexes characterized by coordinated 1,3,5-triaza-7-phosphatricyclo-[3.3.1.1]decane (PTA), and two labile chloride ligands, known as RAPTA complexes.^{82,83} These complexes inhibit cell growth effectively by triggering G2/M phase arrest and apoptosis in Ehrlich ascites carcinoma cells lines,⁸⁴ but are free of toxicity to healthy cells, even with prolonged exposure at millimolar concentrations.^{83,85} In terms of molecular mechanism, RAPTAs undergo hydrolysis in which the labile halide ligands are substituted by H₂O. The hydroxido complex can then bind to DNA pH-dependently, and hence cause DNA damage.⁸³

Meggers *et al* have developed Ru(II) complexes which mimic natural organic product staurosporine that is highly potent a ATP-competitive inhibitor for various kinases such as GSK-3 (glycogen synthase kinase 3) and Pim-1 (proto-oncogene serine/threonine-protein kinase).⁸⁶ One leading complex of these organo-ruthenium mimics, DW1/2, shows potent activity in inhibiting kinases and high cytotoxicity to cancer

cells.⁸⁷ The co-crystal structures of both the *R* and the *S* enantiomers of the ruthenium complex DW1/2 with the human protein kinase Pim-1 clearly show that these ruthenium complexes bind to their target in a fashion typical of organic enzyme inhibitors.⁸⁸ Such Ru(II) complexes inspire a new concept of designing metal complexes in which the metal center is not involved in any direct interactions with the active site but provides a platform for organizing the organic ligands in 3D space.^{43,86,89}

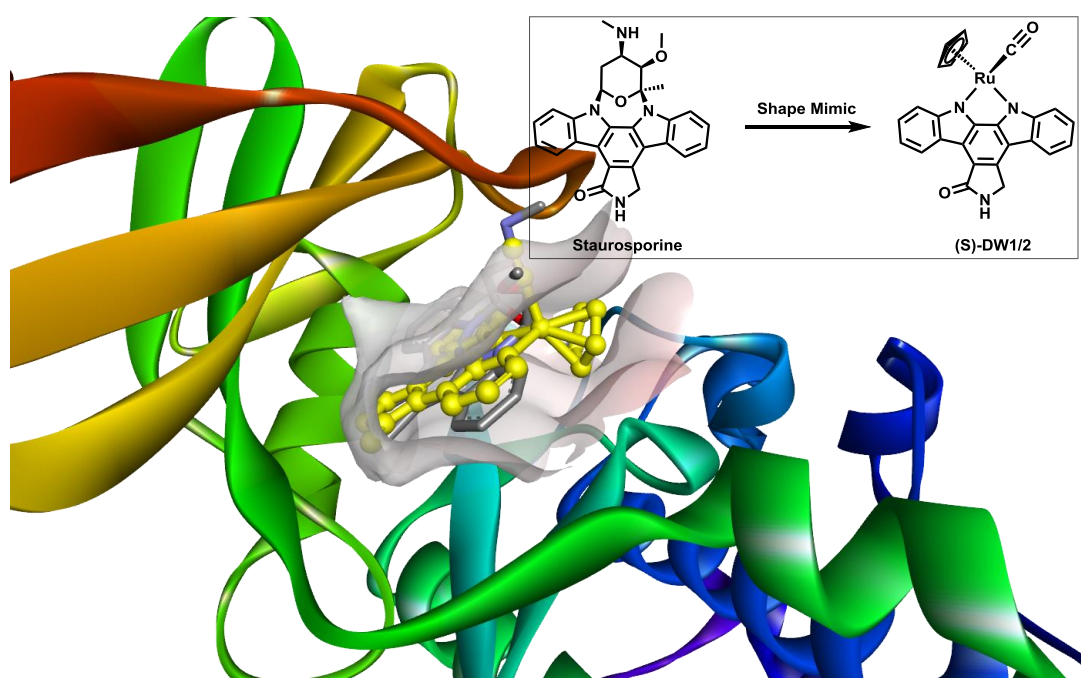


Figure 1.11. Structure (PDB Code: 2BZI) of Pim-1 with bound organo-ruthenium complex (S)-DW1/2 (yellow colour), mimicking template compound Staurosporine (grey colour).

Sadler *et al* has developed Ru(II) η^6 -arene complexes as anticancer agents. Half-sandwich complexes $[(\eta^6\text{-arene})\text{Ru}(\text{en})(\text{Cl})]^+$ (en = ethylenediamine, arene = biphenyl or *p*-cymene) were synthesized and reported to undergo a cisplatin-like mechanism of action in which a labile chloride ligand in the complex is substituted by H₂O to produce a Ru(II) aqua complex which can then bind to DNA and induce cytotoxicity.^{90,91} The high concentration of chloride outside cells (~103 mM) suppresses the hydrolysis of Ru-Cl and enables the prodrug to reach its target. However, the lower concentration of chloride in the cell (~23 mM for cytoplasm and ~4 mM for nucleus) renders such hydrolysis processes feasible.⁶³ It is interesting to mention that the binding of these Ru(II) arene complex with guanine can be enhanced by glutathione (More details in **Section 1.5.2**).⁹² On the basis of these $[(\eta^6\text{-arene})\text{Ru}(\text{en})(\text{Cl})]^+$ complexes, sulfonamido substitutes are introduced and Ru(II) sulfonamido ethyleneamine complexes have been developed. These Ru(II) sulfonamido ethyleneamine complexes display a completely different mechanism of action that use formate as the hydride source to catalyse NAD⁺ reduction to NADH, and perturbing the intracellular redox balance. The cytotoxicity of Ru(II) sulfonamido ethyleneamine complexes can be enhanced by up to 50× in presence of low non-toxic doses of formate.⁹³ Besides, a series of Ru(II) arene complexes bearing azopridine ligands have also been developed, and

these Ru(II) arene azo complexes have also been found to catalyse the oxidation of glutathione by dioxygen, and display good activity to inhibit cancer cell growth (More details in **Section 1.4.2**).⁹⁴

Overall, the application of metallodrugs in anticancer chemotherapy has been greatly stimulated by the success of cisplatin. Apart from the typical examples described above, arsenic-based anticancer complexes have also been approved.^{95,96} Gold and gadolinium complexes targeting thioredoxin reductase⁹⁷ have reached clinical trials. Currently more and more metal elements have been considered to be developed as anticancer metallodrugs, and involve various kinds of intracellular targets to enrich chemotherapy progress.

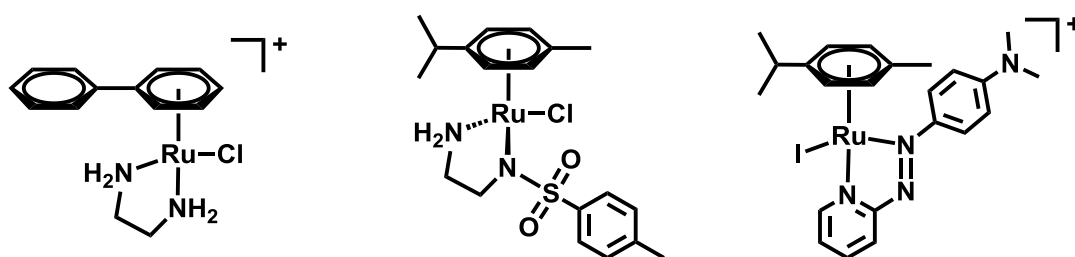


Figure 1.12. The molecular structure of organo-ruthenium complexes developed by the Sadler group.⁹²⁻⁹⁴

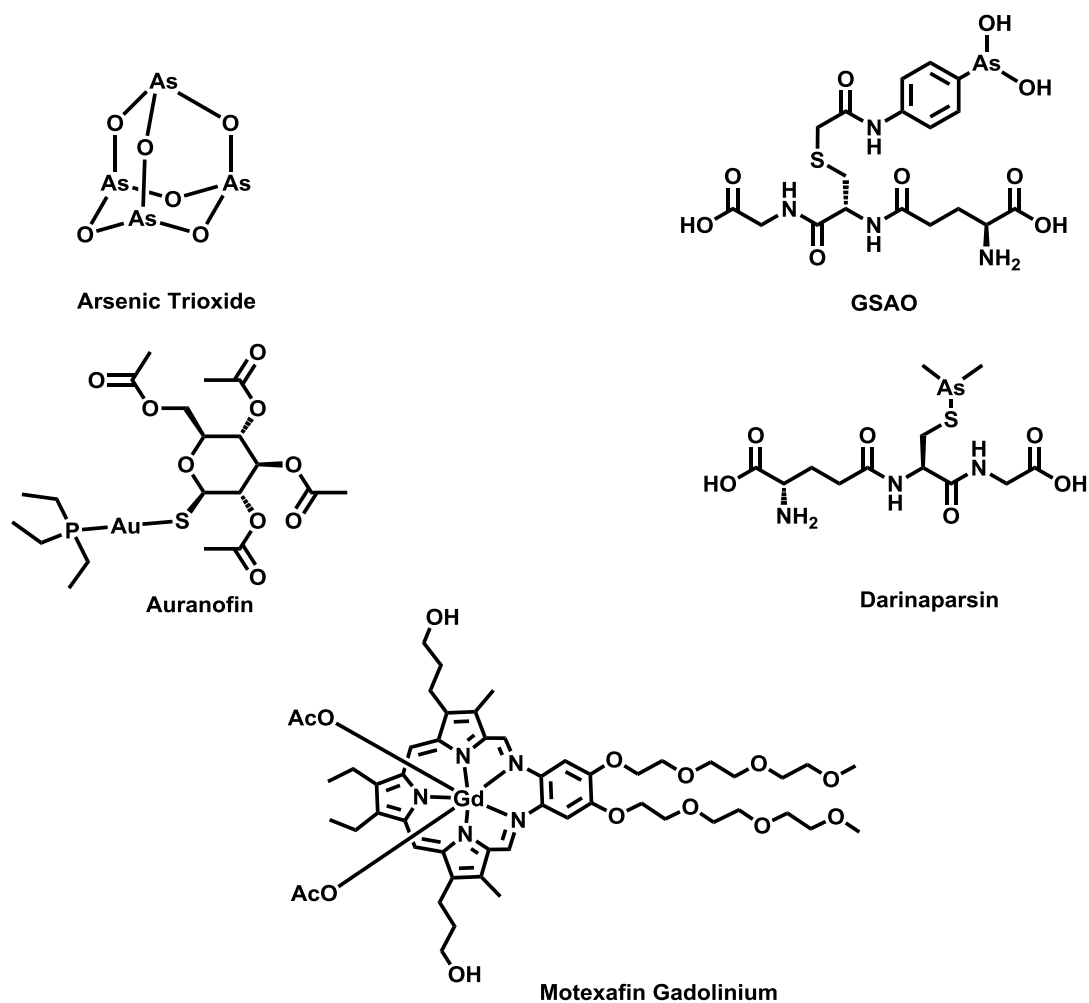


Figure 1.13. The molecular structures of arsenic(III), gold(I) and gadolinium(III) complexes that have been approved or reached clinical trials.

1.3. Osmium

This projects in this thesis are largely concerned with **FY26**, an osmium-based anticancer complex. Hence, osmium chemistry background (**Section 1.3.1**), other osmium-based anticancer complexes (**Section 1.3.2**) and previous studies of **FY26** and its derivatives (**Section 1.3.3**) will be described.

1.3.1. Background of Osmium Chemistry

Osmium is a hard, brittle, bluish-white transition metal, atomic number is 76. In the osmium atom, there are 76 electrons configured as $1s^2 2s^2 2p^6 3s^2 3p^6 3d^{10} 4s^2 4p^6 4d^{10} 5s^2 5p^6 4f^{14} 5d^6 6s^2$. Because of having similar physical and chemical properties and tending to occur together in the same mineral deposits, osmium, ruthenium, rhodium, palladium, osmium, iridium and platinum are classified as “platinum group” elements. Osmium is the densest naturally occurring element, slightly denser than iridium ($22.562 \pm 0.009 \text{ g/cm}^3$ for iridium versus $22.587 \pm 0.009 \text{ g/cm}^3$ for osmium).⁹⁸ Osmium's abundance in the Earth's crust is among the rarest, with an incidence of around 1 g per 200 tonnes.⁹⁹ Osmium was discovered in 1803 by Smithson Tennant and William Hyde Wollaston in London, England¹⁰⁰, and named after Greek *osme* meaning “smell” because of the strong odour of osmium tetroxide

which can be easily formed from the pure metal on exposure to air. There are seven naturally occurring isotopes of osmium (**Table 1.1**), of which ^{192}Os is the most abundant (40.78%) and ^{186}Os the most stable with a long half-life $(2.0 \pm 1.1) \times 10^{15}$ years, approximately 140000 times the age of the universe. The nuclei spins of ^{187}Os and ^{189}Os are 1/2 and 3/2, respectively. Osmium forms compounds with a variety of oxidation states ranging from -2 to +8 (**Table 1.2**). The volatility and extreme toxicity of osmium has limited its applications. Osmium alloys such as osmiridium are very hard and be used in the tips of fountain pens, instrument pivots, and electrical contacts, since they can resist wear from frequent operation. Osmium tetroxide has been used in fingerprint detection¹⁰¹ and staining fatty tissue for optical and electron microscopy. For medicinal application, osmium tetroxide has been used in the treatment of arthritic joints as a mimic of superoxide dismutase.¹⁰²

Table 1.1. Isotopes of osmium

Isotopes	Natural Abundance (%)	Nuclear Spin
^{184}Os	0.02%	0
^{186}Os	1.59%	0
^{187}Os	1.96%	1/2
^{188}Os	13.24%	0
^{189}Os	16.15%	3/2
^{190}Os	26.26%	0
^{192}Os	40.78%	0

Table 1.2. Oxidation states of osmium and examples of compounds

Oxidation State	Example	Oxidation State	Example
-2	$\text{Na}_2[\text{Os}(\text{CO})_4]$	+4	K_2OsCl_6
-1	$\text{Na}_2[\text{Os}_4(\text{CO})_{13}]$	+5	OsF_5
0	$\text{Os}_3(\text{CO})_{12}$	+6	$\text{K}_2[\text{OsO}_2(\text{OH})_4]$
+1	OsI	+7	OsOF_5
+2	OsI_2	+8	OsO_4
+3	OsCl_3		

1.3.2. Osmium Anticancer Drug Applications

As a third-row metal, osmium has long been considered substitution-inert and few studies concerning the anticancer activity of osmium complexes had been reported before 2005.¹⁰³⁻¹⁰⁵ However, in recent years many osmium complexes with promising anticancer potency have been developed. With extensions from ruthenium, which is a lighter congener of osmium, structurally-similar osmium analogues have been prepared from Ru(III) drug candidates NAMI-A and KP1019 (**Figure 1.14**). The Os(III) analogue of NAMI-A **Os-NA1** shows outstanding antiproliferative activity, while the Os(II) complexes **Os-NA2** and **Os-NA3** with more than one DMSO (dimethyl sulfoxide) ligands are inactive.¹⁰⁶ In physiological conditions, NAMI-A is quickly hydrolysed into different ruthenium species, and these contribute to the pharmacological effects of NAMI-A. However, the fact that the inert

osmium analogy has higher cytotoxicity suggests that hydrolysis is not an essential prerequisite for performance of this class of complexes.¹⁰⁷

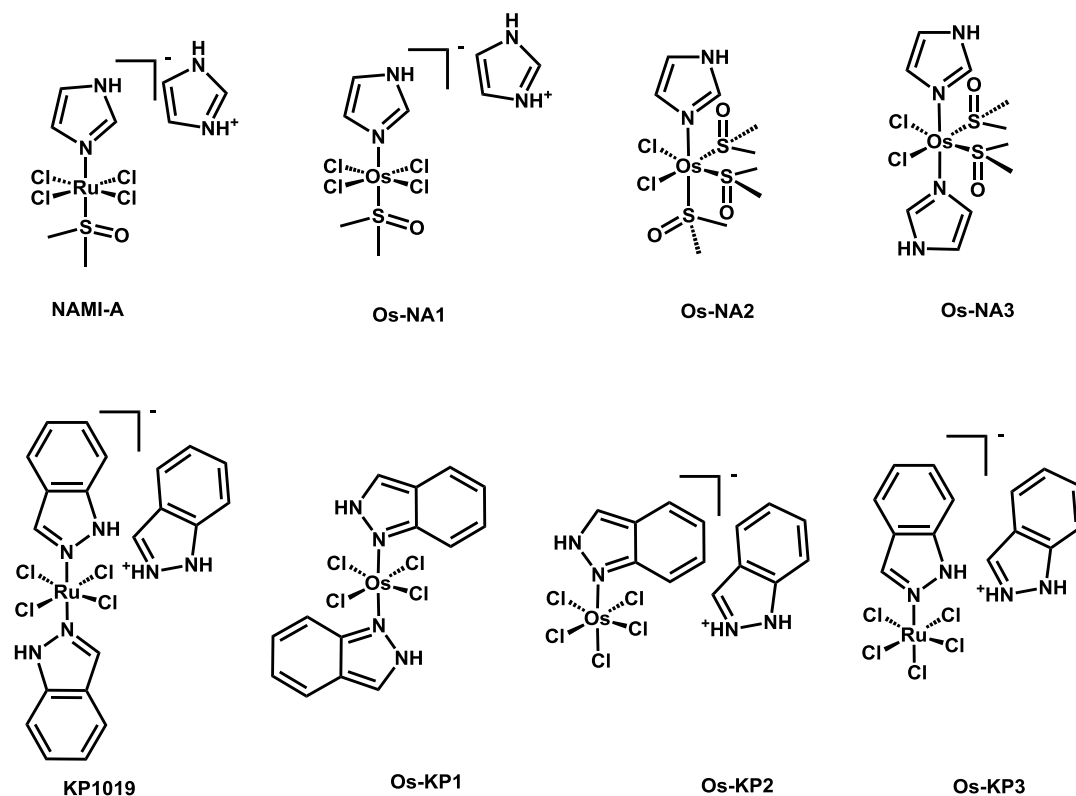


Figure 1.14. Molecular structures of osmium(III) anticancer complexes based on ruthenium complexes NAMI-A and KP1019.

For KP1019 analogues, Os(III) and also Os(IV)-azole-chlorido complexes have been studied. Surprisingly, in KP1019, indazole is coordinated to Ru(III) only through the *N2* nitrogen atom, whereas in Os(IV) complexes, indazole is bound either via *N1* atom in complexes **Os-KP1** and **Os-KP2**, or an *N2* atom in the complex **Os-KP3**. These complexes are stable in aqueous solution and show KP1019 comparable cytotoxicity towards human cancer cells.¹⁰⁸ In a Hep3B SCID mouse

xenotransplantation model, these complexes do not display any symptoms of toxicity. Complex **Os-KP3** was found to inhibit tumour growth and **Os-KP2** was found to reduce tumour necrosis and increases the survival time.¹⁰⁹

High-valent Os(VI) complexes based on the $\text{Os}^{\text{VI}}\equiv\text{N}$ fragment have been evaluated *in vitro* and *in vivo* in cancer models.¹¹⁰⁻¹¹² Notably, these complexes show lower IC_{50} values than cisplatin. Their cytotoxicity has a good correlation with their cellular accumulation. The induction of cell cycle arrest in S phase and premitotic G2 phase is considered to result from DNA damage or degradation.¹¹²

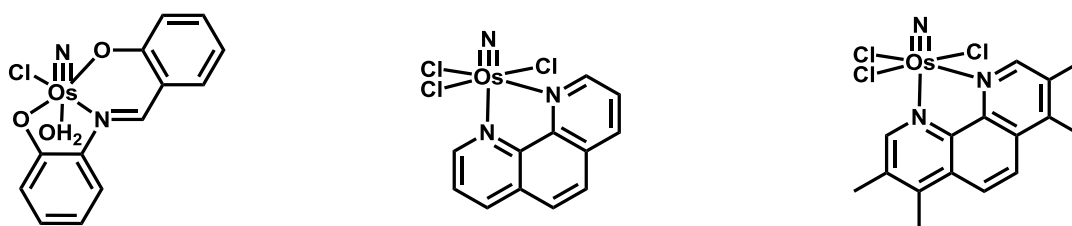


Figure 1.15. Molecular structures of $\text{Os}^{\text{VI}}\equiv\text{N}$ complexes.

Apart from targeting DNA, proteins can also represent the targets of osmium anticancer complexes. Coordination of biologically active molecules such as small molecule protein inhibitors to metal centres is an attractive approach to achieve synergistic effects of both components, and to endow multitargeting properties to the drug molecules.

Coordination of bioactive ligands, such as paullones or indolocarbazole derivatives, to the metal centres is also useful to modulate their physical and biological properties, such as solubility, bioavailability and biological activity. Based on this principle, several kinds of osmium complexes have been developed as inhibitors of GSK-3 β (glycogen synthase 3)¹¹³ and CDKs (cyclin-dependent kinases),¹¹⁴ binding histone proteins,¹¹⁵ disrupting protein-protein interaction of HIF-1 α (hypoxia inducible factor-1 α) with p300¹¹⁶ and antagonizing STAT5B (signal transducer and activator of transcription 5B) dimerization.¹¹⁷

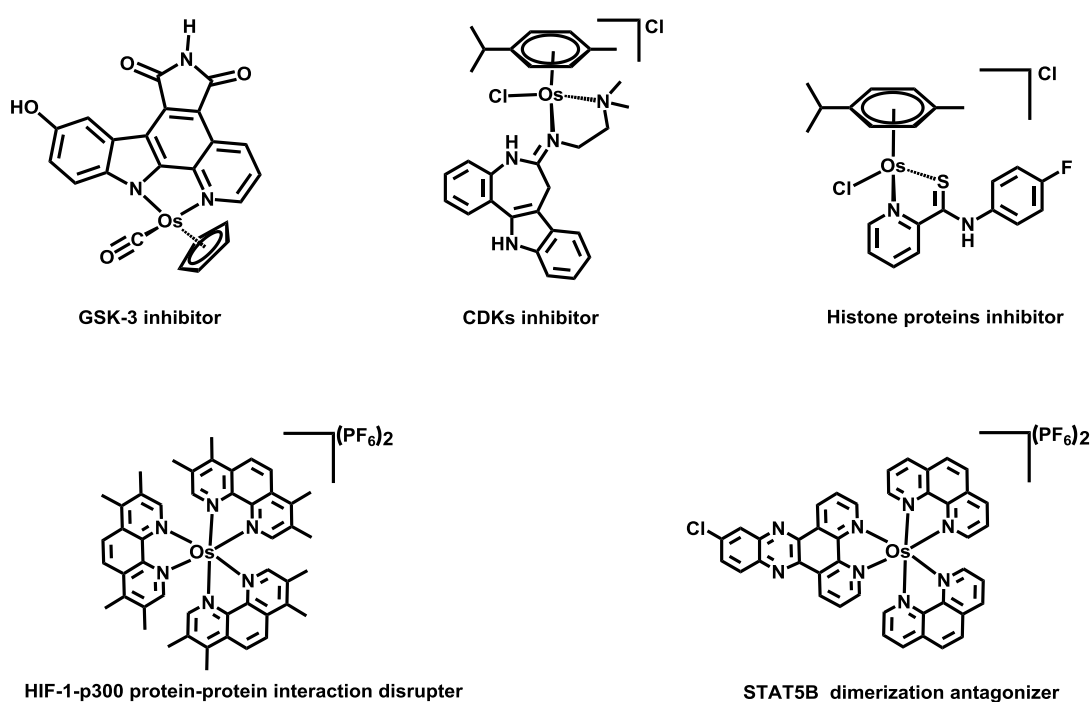


Figure 1.16. Molecular structures of osmium complexes inhibiting proteins activity, disrupting protein-protein interactions, or antagonizing protein dimerization.

The Sadler group is one of the first to turn attention to osmium anticancer therapy, especially half-sandwich “piano-stool” osmium(II) arene complexes with a typical structure $[(\eta^6\text{-arene})\text{Os}(\text{X})(\text{Y})(\text{Z})]^{n+}$. From 2006, N,N-chelating ligands (such as ethylenediamine and bipyridine) have been introduced, but these N,N-chelator-containing organo-osmium complexes are often inactive to cancer cells in view of their inertness towards hydrolysis.^{118,119} For example, one of the leading complexes, $[\text{Os}(\eta^6\text{-biphenyl})(\text{ethylenediamine})\text{Cl}]^+$ has a cytotoxicity of $\text{IC}_{50} = 9 \mu\text{M}$ towards ovarian cancer cells, with a rate of hydrolysis 100× slower than its Ru(II) counterpart.¹¹⁹ In order to improve the aqueous reactivity, O,O-chelating ligands (e.g. acetylacetonate and maltolato) have been introduced to replace N,N-chelating ligands. However, these O,O-chelated organo-osmium complexes still lack a potent level of cytotoxicity against cancer cells because they are readily hydrolysed and form an un-reactive hydroxido-bridged dimer in aqueous solution.^{119,120} Finally, N, O-chelating ligands (e.g. picolinate and oxinate) provide a balanced compromise for ready hydrolysis overcoming both over-active and too-inert problems. For example $[\text{Os}(\eta^6\text{-biphenyl})(\text{picolinate})\text{Cl}]^+$ has activity towards cancer cells comparable to cisplatin.¹²¹⁻¹²⁴ In order to further improve the performance of these organo-osmium anticancer complexes, cell-penetrating peptides (CPPs) have been used as drug delivery vectors,

and conjugated adducts of Arg₈ with [Os(η^6 -biphenyl)(picolinate)Cl]⁺ exhibit 10× increase of Os cell uptake, and a 15× increase of Os binding to DNA.¹²⁵

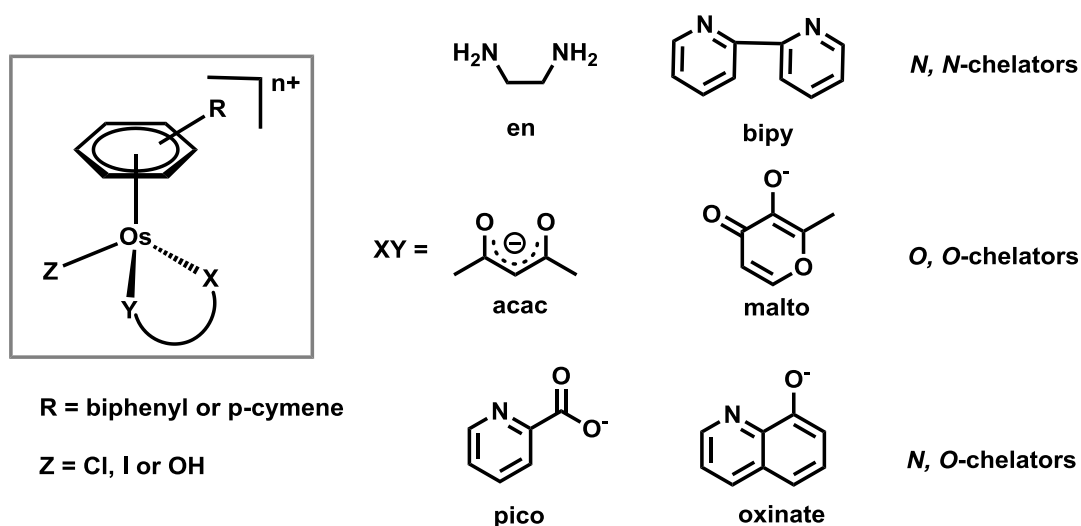
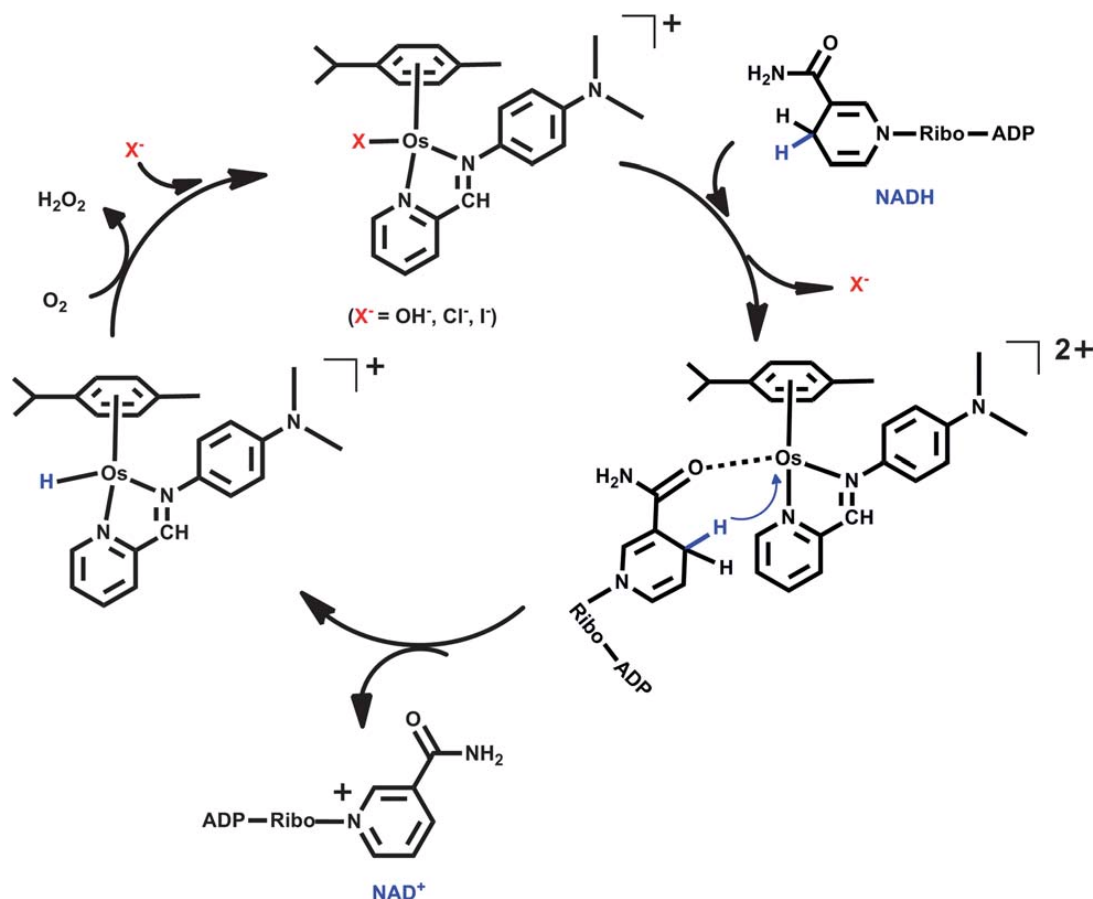


Figure 1.17. Typical structures of osmium(II) half-sandwich complexes $[(\eta^6\text{-arene})\text{Os}(\text{X})(\text{Y})(\text{Z})]^{n+}$ and selected examples of chelated ligands.

From 2010, Os(II) arene phenyliminopyridine (IMPY) complexes have been reported to exhibit potent cytotoxicity, especially the lead complex $[\text{Os}(\eta^6\text{-bip})(\text{IMPY-NMe}_2)\text{I}]\text{PF}_6$, which has a IC_{50} value of 0.14 μM towards A2780 cancer cells. The mechanism of action of these osmium-imino complexes involve the transfer of hydride from NADH to O_2 , and generation of NAD^+ and H_2O_2 to perturb the intracellular redox balance, in which case an osmium hydride complex is observed as an intermediate.^{126,127}



Scheme 1.2. A proposed mechanism for the oxidation of NADH to NAD⁺ catalysed by an Os(II) arene iminopyridine complex.¹²⁶

Considering the chirality of the osmium centre, enantiomers of these osmium imino complexes have been isolated and the mirror-image complexes show similar potent anticancer activity.¹²⁸ However, high enantioselectivity is observed for chiral organo-osmium anticancer complexes $[\text{Os}(\text{arene})(\text{TsDPEN})]$ (TsDPEN = N-(*p*-toluenesulfonyl)-1,2-diphenyl ethylenediamine, arene = biphenyl, *p*-cymene or *m*-terphenyl) in the reduction of pyruvate, a key intermediate in metabolic pathways, to lactate.¹²⁹ Moreover, multi-nuclear osmium arene

anticancer complexes have also been developed. Dinuclear hydroxido-bridged Os(II) arene complexes are biologically inactive but the tetranuclear Os(II) arene complexes formed from linking two inert dinuclear Os(II) arene units show high antiproliferative activity by inducing DNA knotting.¹³⁰

1.3.3. FY26 and Its Derivative Complexes

Amongst all the osmium-based anticancer complexes, the series of organo-osmium complexes bearing phenylazopyridine (AZPY) ligands has attracted the most medicinal interest in view of its the potent activity, high selectivity, and novel mechanism of action. With a variety of different substituents on AZPY ligands, about 40 Os(II) arene AZPY complexes have been synthesised. In the primary cytotoxicity screening test, only three complexes are inactive to A2780 ovarian cancer cells and eight complexes have IC₅₀ values in the nano-molar range.^{131,132} The lead complexes [Os (η^6 -*p*-cymene) (5-EtO-pyridylazo-4-phenyl)I] PF₆ ([**1-I**] •PF₆) and [Os (η^6 -*p*-cymene) (4-(2-pyridylazo)-NMe₂)I] PF₆ ([**2-I**] •PF₆, **FY26**) are reported as candidate drugs with IC₅₀ values of 0.92 and 0.18 μ M, respectively.^{68,132,133} Especially, **FY26** is active in human A2780, A549 lung, HCT-116 colon, MCF-7 breast, PC-3 prostate, RT-112 bladder and cisplatin-resistant A2780 ovarian cancer

FY26-exposed A2780 epithelial ovarian cancer cells undergo a metabolic shunt from glycolysis to oxidative phosphorylation.¹³⁴ Downstream events, measured by time-series reverse-phase protein microarrays, high-content imaging, and flow cytometry, show a dramatic increase in mitochondrially produced ROS (reactive oxygen species) and subsequent DNA damage with up-regulation of ATM (Ataxia Telangiectasia Mutated), p53, and p21 proteins. In contrast to platinum drugs, exposure to this organo-osmium compound does not cause significant apoptosis within a 72-h period, but superoxide production in cancer cells exposed to three other structurally related Os(II) compounds was found to be correlated with their antiproliferative activity. Experiments of **FY26** labelled with the radionuclide ¹³¹I show that once being taken up by MCF-7 cancer cells, the iodide is pumped out very rapidly, which indicates a mechanism in which **FY26** is activated in cancer cells involving I⁻ release. GSH was found to promote the hydrolysis of **FY26**, and is also involved in FY26 activation.¹³² But the mechanism by which GSH promotes the hydrolysis of **FY26** and the pathways of the reactions between osmium complexes with GSH remain unknown.

1.4. Azo Group

The work in this thesis is mainly focused on explorations of the mechanism of action of organo-osmium complexes bearing azo ligands, and involvement of the azo bond. First azo compounds (**Section 1.4.1**), and reduction of the azo bond (**Section 1.4.2**) will be briefly introduced.

1.4.1. Azo Compounds

Azo compounds are defined as: “derivatives of diazene (diimide), $\text{HN}=\text{NH}$, wherein both hydrogens are substituted by hydrocarbyl groups, e.g. $\text{PhN}=\text{NPh}$ azobenzene or diphenyldiazene” by the International Union of Pure and Applied Chemistry (IUPAC). From September 2003, consumer goods which contain listed aromatic amines originating from azo dyes have been prohibited from manufacture and sale in European Union countries since azo dyes derived from benzidine are carcinogens. Exposure to them has classically been associated with bladder cancer.¹³⁷ In addition to food, azo compounds have been widely used in many fields. One characteristic of azo compounds, especially aryl azo compounds, is π -delocalization of electrons which makes the aryl azo compounds have vivid colours, especially reds, oranges, and yellows. Azo compounds are most widely used as dyes and azo dyes are employed to treat textiles, leather articles, and some foods. In chemistry, related azo compounds are used as azo pigments which are structurally

similar to azo dyes but lack solubilizing groups. The azo group is sensitive to light and azobenzene compounds are characterized by photoactivated *trans-cis* isomerism.¹³⁸⁻¹⁴⁰ Upon irradiation with UV or visible light, the generally more stable *trans*-azobenzene complexes convert to less stable *cis* form. This transformation can be reversed by thermal isomerism. With such properties, photo-sensitive azo polymer and azo-containing protein inhibitors have been developed.¹⁴¹⁻¹⁴³

Azo compounds have wide medicinal applications. For example, phenazopyridine is used in conjunction with an antibiotic or other anti-infective medication at the beginning of treatment to help provide immediate symptomatic relief.¹⁴⁴ The nitrogen atoms in the azo bond can also provide electrons and space to coordinate with metals. Many metal complexes containing azo ligands have been reported to have many types of biological activity.¹⁴⁵⁻¹⁴⁷ The Sadler group has used azo compounds to chelate ruthenium(II) and osmium(II) ions and hence develop potent anticancer complexes (e.g. FY26 in **Section 1.3.3**).^{68,94,131} These metal azo complexes are found to modify the redox level and kill cancer cells, which indicates a novel mechanism of action compared to platinum drugs, providing a promising approach to overcome platinum-resistance in chemotherapy.

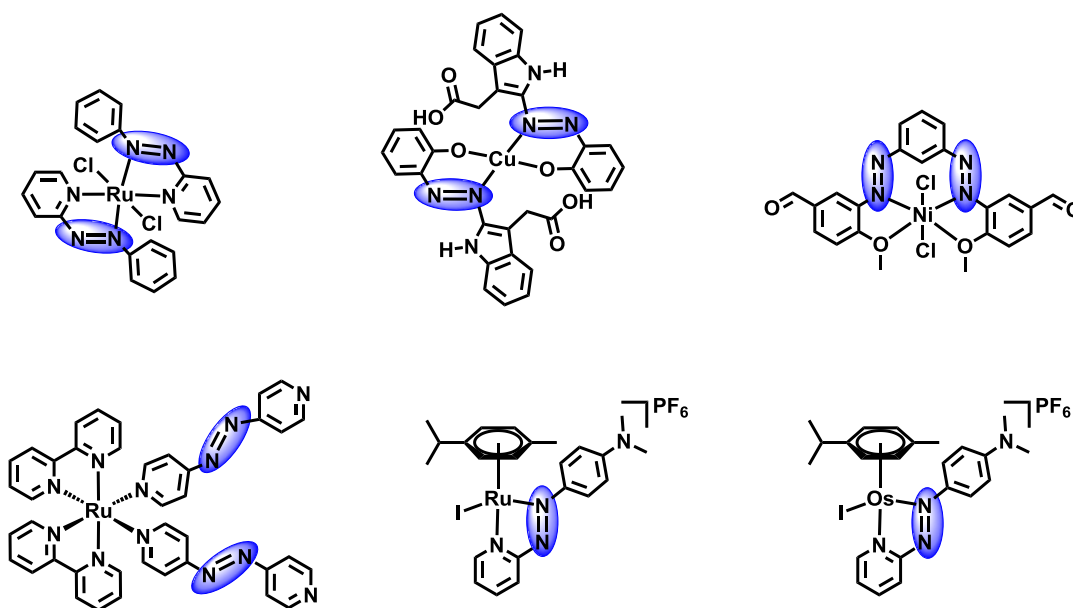


Figure 1.19. Molecular structures of anticancer metal complexes with azo ligands.

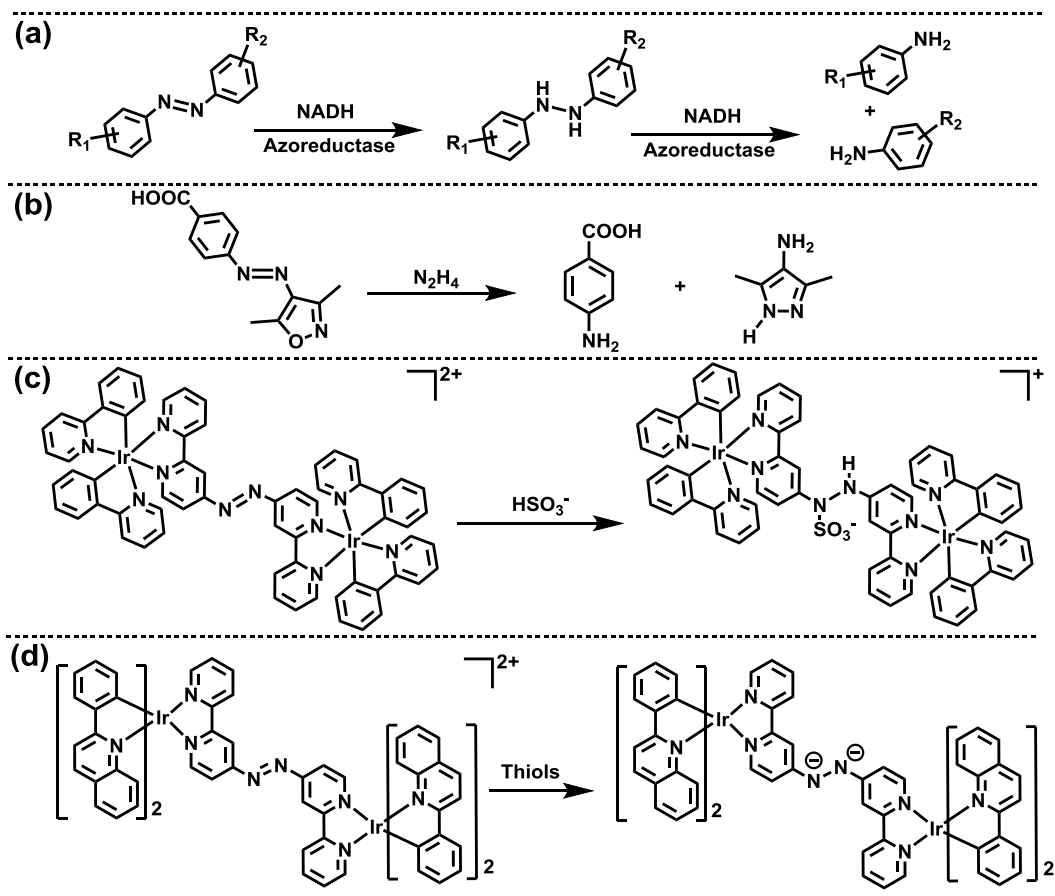
1.4.2. Reduction of Azo Bonds

The reduction of azo bonds plays important roles in many biological processes such as drug metabolism.^{148,149} Azoreductases are enzymes which reduce azo bonds and have been characterized in a range of prokaryotes and eukaryotes. Using NAD(P)H as hydride sources, azoreductases can catalytically reduce azo groups to hydrazo and amine functions at different stages.^{149,150} With more and more crystal structures of azoreductases being solved,¹⁵¹⁻¹⁵⁴ the mechanism by which this kind of enzyme reduces azo bonds has become clear. Indeed, the activity of azoreductase is dependent on the concentration of FMN (flavin mononucleotide), of which N5 accepts a hydride from NAD(P)H and donates it upon reduction of the substrate. However, azo

compounds cannot be a substrate for reduction directly. This reduction requires tautomerisation of the azo compound to a quinoneimine and then provides a unifying mechanism with the reduction of quinone substrates by azoreductases.^{149,155} In addition azoreductases, cytochrome P450 and NADPH-cytochrome P450 reductase can mediate the reduction of azo groups too. But in this reaction, the initial reduction appears to proceed via the azo anion radical and oxygen apparently reverses this process with concomitant conversion of oxygen to the superoxide anion radical.¹⁵⁶⁻¹⁵⁸ With this behaviour, azo containing hypoxia-sensitive fluorescent probes have been designed and reported.¹⁵⁹

Many chemicals have also been reported to reduce azo bonds in the absence of enzymes. In organic synthesis, reductants such as hydrazine hydrate, zinc/ammonium salts and dihydrated nickel(II) chloride/lithium/4,4'-di-*tert*-butylbiphenyl have been used to reduce azo compounds to obtain new hydrazo or amine compounds.¹⁶⁰⁻¹⁶² Thiols, bisulfite and sulfite are found to reduce azo bonds in metal complexes, and during this process the fluorescence would be switched on/off. With such a mechanism, azo group linked dinuclear Ir(III) and Ru(II) complexes have been developed as intracellular thiol and sulphite probes.¹⁶³⁻¹⁶⁵ These probes have been evaluated *in vitro* and *in vivo* and

show high sensitivity and selectivity towards their target substrates. In cancer therapy, reduction of azo bonds by GSH is found to activate the covalent binding between DNA and Ru(II)-based photoactivated chemotherapy (PACT) agents.¹⁶⁶ Azo ligands bearing half-sandwich ruthenium arene complexes catalyse the oxidation of GSH, which increases the intracellular ROS level, and exhibits highly cytotoxic actions towards to cancer cells. In the mechanism of action, GSH reduces the azo bond in the ruthenium complexes and is a key step for the catalysis process.⁹⁴



Scheme 1.3. Reduction of azo bonds by azoreductase, hydrazine hydrate, bisulfite and thiols.

1.5. Glutathione

The project in this thesis involves exploring the mechanism of action of organo-osmium anticancer complexes, especially studying the reaction between osmium complexes and glutathione. Following the introduction of osmium complexes in **Section 1.4**, glutathione (**Section 1.5.1**), and reactions between glutathione and metal complexes (**Section 1.5.2**) will be introduced.

1.5.1. Introduction to Glutathione

Glutathione (GSH) is a tripeptide with a gamma peptide linkage between the carboxyl group of the glutamate side chain and the amine group of cysteine, with the carboxyl group of cysteine attached by a normal peptide linkage to a glycine. The pK_a values of glycine carboxyl group, cysteine thiol group, glutamate carboxyl and amine group in GSH are $pK_{a1}=3.59$, $pK_{a2}=9.65$, $pK_{a3}=2.12$ and $pK_{a4}=8.75$, respectively.¹⁶⁷ Glutathione is usually synthesized in two adenosine triphosphate-dependent steps.¹⁶⁸ Firstly, gamma-glutamylcysteine is synthesized from L-glutamate and cysteine via the enzyme gamma-glutamylcysteine synthetase (glutamate cysteine ligase, GCL). This reaction is the rate-limiting step in glutathione synthesis. Secondly, glycine is added to the C-terminal of gamma-glutamylcysteine via the

enzyme glutathione synthetase. GSH is the most abundant low molecular weight thiol in all mitochondria-bearing eukaryotes, existing at a concentration of ca. 5 mM in animal cells.¹⁶⁹ It has been detected virtually in all cellular compartments such as cytosol, chloroplast, endoplasmic reticulum, vacuole, and mitochondria. There are reduced (GSH) and oxidized (GSSG) forms of glutathione. In the reduced form, the thiol group of cysteine is able to donate a reducing equivalent ($H^+ + e^-$) to other molecules, such as reactive oxygen species to neutralize them, or protein cysteines to maintain their reduced forms. After donating electrons, two GSH molecules are oxidized to form glutathione disulfide (GSSG) which can be reduced back to GSH by glutathione reductase, using NAD(P)H as an electron donor.¹⁷⁰ The ratio of GSH *versus* GSSG in the cell is used to measure of intracellular oxidative stress.¹⁷¹ In healthy cells and tissue, more than 90% of the total glutathione pool is in the reduced form (GSH) and less than 10% exists in the disulfide form (GSSG).¹⁷²

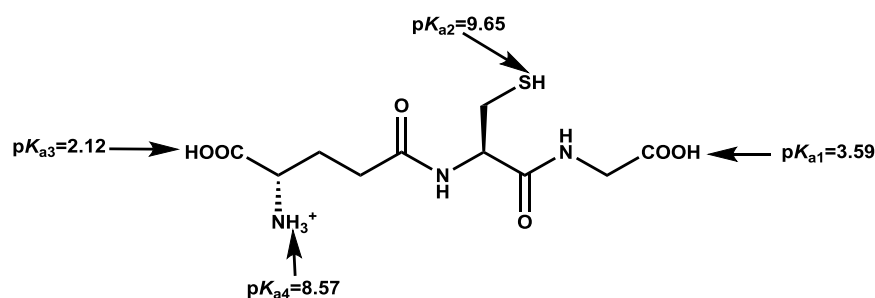


Figure 1.20. Structure of GSH and the pK_a values for each group in the molecule.¹⁶⁷

GSH/GSSG is the key part of cellular redox systems and plays critical roles in cell signalling, metabolism, defence and survival. In cells, glutathione has following functions¹⁷³:

- ✧ Glutathione maintains levels of reduced free thiols in proteins like glutaredoxin and glutathione peroxidase.
- ✧ Glutathione modulates heavy metal ion metabolism and detoxifies heavy metals in cells.
- ✧ Glutathione is one of the major endogenous antioxidants produced by the cells to neutralize reactive oxygen species (ROS) and reactive nitrogen species (RNS).
- ✧ Glutathione enhances the function of citrulline as part of the nitric oxide cycle.
- ✧ Glutathione is used in metabolic and biochemical reactions such as DNA synthesis and repair, protein synthesis, prostaglandin synthesis, amino acid transport, and enzyme activation.

1.5.2. Reactions of Glutathione with Metal Ion Complexes

The sulphur, nitrogen and oxygen atoms in the GSH molecule provide coordination sites and make it be a suitable agent to bind various kinds of metals,¹⁷⁴⁻¹⁷⁶ Thus GSH has been widely described as a “heavy metal killer” in environmental pollution abatement and human health

protection.¹⁷⁷⁻¹⁸¹ But when anticancer metallodrugs enter into cancer cells. GSH also binds these to form metal-SG adducts.¹⁸²⁻¹⁸⁴ These metal-SG adducts are usually too stable to have any biological activity and are quickly transported out of cells through the glutathione S-conjugate export pump (GS-X pump).¹⁸⁵ This GSH can be considered as the prime initiator of metallodrug degradation and drug-resistance.

However, the potency of darinaparsin (an As-SG adduct) which has entered into clinical phase II trials still reminds us that not all metal-SG adducts are inactive.¹⁸⁶ With more studies being carried out, the other aspect of GSH that benefits anticancer chemotherapy has been uncovered. GSH is the key molecule in cell redox system and likely to be used as a target for anticancer agents.¹⁸⁷ Sometimes GSH plays roles as a “protector” or “activator” of metallodrugs for killing cancer cells.

Some platinum(II) anticancer complexes such as oxaliplatin and Pt(ethylenediamine)Cl₂ react with GSH as well as GSSG to form an glutathione-bridged diplatinum(II) macrochelate.^{188,189} This unusual Pt(II)-SG adduct, contrasting with the product formed from the reaction of cisplatin with GSH,¹⁸⁴ is potentially reactive towards DNA bases. For oxaliplatin and Pt(ethylenediamine)Cl₂, GSH protects more active species from reaching the DNA targeting sites. Furthermore, GSH is

also reported to activate Pt(IV) complexes through reducing Pt(IV) prodrugs to active Pt(II) species.¹⁹⁰

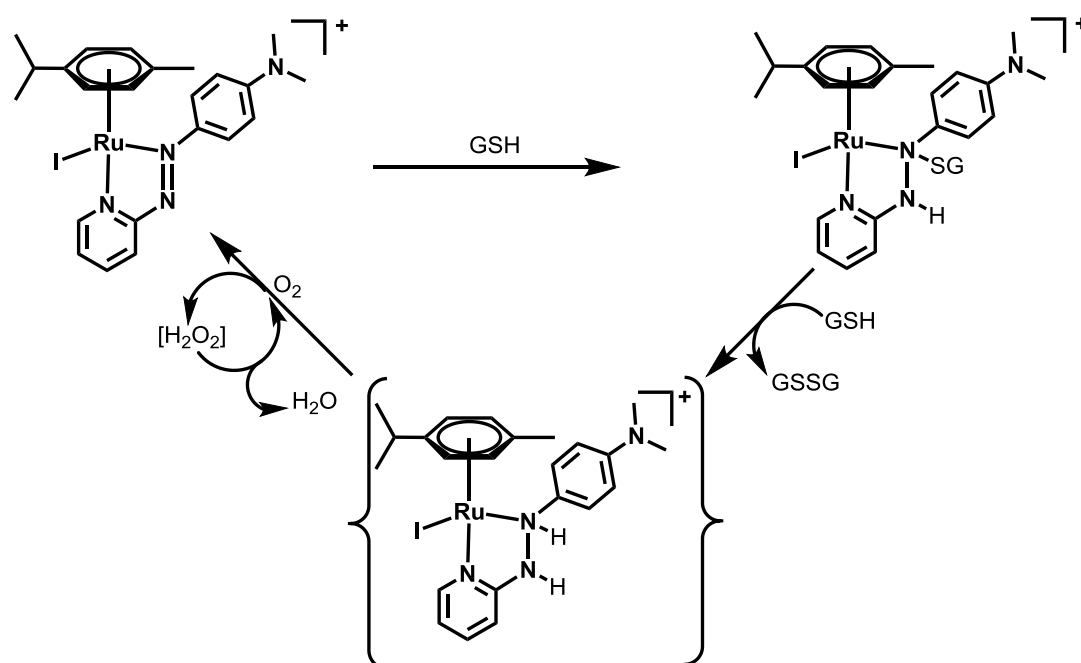
Ruthenium(III) complexes KP1019 and KP1339 are amongst the first ruthenium-based anticancer drugs to be clinically developed. During the cytotoxicity of these complexes, the reduction of Ru(III) to more active Ru(II) is key step in which GSH plays an important role.¹⁹¹ Organo-ruthenium(II) complexes $[(\eta^6\text{-arene})\text{Ru}(\text{ethylenediamine})(\text{Cl})]^+$ (arene = biphenyl or *p*-cymene) have potency comparable to carboplatin through binding to guanine bases in DNA.^{91,192} In the *in vitro* studies, the competition of GSH and guanine does not inhibit but enhances the binding of guanine to Ru(II) species. The mechanism of this interesting phenomenon is that GSH can firstly bind with Ru(II) complexes to form ruthenium thiolate (Ru-SG) adducts, and then this ruthenium thiolate adduct is subsequently oxidized to ruthenium sulfenate complex (Ru-SOG) which provides a facile route for displacement of S-bound glutathione by guanine.⁹² More interestingly, GSH also appears to induce the oxidation process from Ru-SG to Ru-SOG by oxygen.¹⁹³ The structural basis of the reactivity of ruthenium sulfenate complexes has been explored, and assigned to the differences of Ru-S bond length, charge donation and energies of the empty valence orbitals between thiolate, sulfenate and sulfonate complexes.^{194,195} In **Section 1.4.2**, GSH

activation of azo-containing ruthenium complexes through reducing the -N=N- azo bond has been introduced and this mechanism is also a good example of the importance of GSH to the anticancer potency of metallodrugs (**Scheme. 1.4**).

Besides platinum and ruthenium, GSH-induced activation of other metal anticancer complexes has been observed, For example, GSH is involved in the cell uptake of bismuth anticancer complexes¹⁹⁶ and GSH greatly enhances the zinc(II) phthalocyanine photodynamic therapy complexes which generate reactive oxygen species.¹⁹⁷

The reactions between GSH and organo-osmium azo complexes [Os(η^6 -arene)(phenylazopyridine)halide]ⁿ⁺ (arene = biphenyl or *p*-cymene, halide = Cl or I) studied in this thesis are also potentially very important. L-Buthionine-sulfoximine (L-BSO) is an inhibitor of key enzyme of GSH synthesis in the cell and normally used to decrease the intracellular concentration of GSH.¹⁹⁸ For many metallodrugs, co-incubation with L-BSO will increase their cytotoxicity, which is so called “L-BSO Potentiation”. Surprisingly, the “L-BSO Potentiation” for organo-osmium azo complexes is much lower than other metal complexes, and the cytotoxicity of some organo-osmium complexes is even decreased by co-incubation of cells with L-BSO.¹⁹⁹ Such results indicate that GSH plays crucial roles in the mechanism of action of

organo-osmium azo complexes. Radionuclide ^{131}I labelling experiments show that once taken up by cells, the iodide in organo-osmium azo complexes is released and pumped out very rapidly. In this process, GSH has been shown to promote hydrolysis of organo-osmium azo complexes.¹³² As a continuation of these studies, the work in this thesis is mainly to explore the mechanism of GSH activation of organo-osmium azo complexes.



Scheme 1.4. The proposed catalytic process for GSH oxidation by a half-sandwich ruthenium complex.⁹⁴

1.6. Project Aims

A series of half-sandwich osmium complexes, of which the lead complex is $[\text{Os}(\eta^6\text{-}p\text{-cymene})(4\text{-(2-pyridylazo)-NMe}_2)\text{I}]\text{PF}_6$ (**[2-I]•PF₆**, **FY26**), have been reported to have a high potential to represent an alternative choice to platinum drugs. The aim of the project in this thesis is to explore the mechanism of action of these “half-sandwich” osmium complexes, especially their reactions with an intracellular tripeptide GSH. Specific aims for each chapter are outlined below.

In Chapter 3, complexes related to FY26, such as the aqua and thiolato adducts, are synthesised and characterized.

In Chapter 4, the mechanism of action for the hydrolysis of osmium complexes in presence of GSH were explored via a combination of theoretical experimental approaches.

In Chapter 5, the possibility of trapping free radicals from reactions of osmium complexes with GSH is explored under various conditions.

In Chapter 6, the reactions of FY26 with GSH are studied using X-ray absorption spectroscopy and key intermediates for the reactions are probed.

In Chapter 7, the finalised conclusions and future work proposed are summarized.

1.7. References

- (1) Bray, F.; Ferlay, J.; Soerjomataram, I.; Siegel, R. L.; Torre, L. A.; Jemal, A. *CA Cancer J. Clin.* **2018**, 68, 394.
- (2) Siegel, R. L.; Miller, K. D.; Jemal, A. *CA Cancer J. Clin.* **2019**, 69, 7.
- (3) Phelps, R. M.; Smith, D. K.; Heilig, C. M.; Gardner, L. I.; Carpenter, C. C.; Klein, R. S.; Jamieson, D. J.; Vlahov, D.; Schuman, P.; Holmberg, S. D. *Int. J. Cancer* **2001**, 94, 753.
- (4) Croce, C. M. *N. Engl. J. Med.* **2008**, 358, 502.
- (5) Duesberg, P. H. *Science* **1995**, 267, 1407.
- (6) Anand, P.; Kunnumakara, A. B.; Sundaram, C.; Harikumar, K. B.; Tharakan, S. T.; Lai, O. S.; Sung, B.; Aggarwal, B. B. *Pharm. Res.* **2008**, 25, 2097.
- (7) Brenner, D. J.; Hall, E. J. *N. Engl. J. Med.* **2007**, 357, 2277.
- (8) Kushi, L. H.; Byers, T.; Doyle, C.; Bandera, E. V.; McCullough, M.; McTiernan, A.; Gansler, T.; Andrews, K. S.; Thun, M. J. *CA Cancer J. Clin.* **2006**, 56, 254.
- (9) Kuper, H.; Adami, H. O.; Boffetta, P. *J. Intern. Med.* **2002**, 251, 455.
- (10) Maltoni, C.; Minardi, F.; Holland, J. F. *Holland-Frei Cancer Medicine*; 5th ed.; BC Decker: Hamilton (ON), 2000.

- (11) Hanahan, D.; Weinberg, R. A. *Cell* **2011**, *144*, 646.
- (12) Lengauer, C.; Kinzler, K. W.; Vogelstein, B. *Nature* **1998**, *396*, 643.
- (13) Lomax, M. E.; Folkes, L. K.; O'Neill, P. *Clin. Oncol.* **2013**, *25*, 578.
- (14) Ross, G. M. *Endocr. Relat. Cancer* **1999**, *6*, 41.
- (15) Seidlin, S. M.; Marinelli, L. D.; Oshry, E. *J. Am. Med. Assoc.* **1946**, *132*, 838.
- (16) Tulchinsky, M.; Binse, I.; Campenni, A.; Dizdarevic, S.; Giovanella, L.; Jong, I.; Kairemo, K.; Kim, C. K. *J. Nucl. Med.* **2018**, *59*, 723.
- (17) Waldmann, T. A. *Nat. Med.* **2003**, *9*, 269.
- (18) Schumacher, T. N.; Schreiber, R. D. *Science* **2015**, *348*, 69.
- (19) Scott, A. M.; Wolchok, J. D.; Old, L. J. *Nat. Rev. Cancer* **2012**, *12*, 278.
- (20) Lee, A.; Sun, S.; Sandler, A.; Hoang, T. *Curr. Opin. Chem. Biol.* **2018**, *44*, 56.
- (21) Cheever, M. A.; Higano, C. S. *Clin. Cancer. Res.* **2011**, *17*, 3520.
- (22) Prasad, V. *Nat. Rev. Clin. Oncol.* **2018**, *15*, 11.
- (23) Ginn, S. L.; Amaya, A. K.; Alexander, I. E.; Edelstein, M.; Abedi, M. R. *J. Gene Med.* **2018**, *20*, e3015.
- (24) Dasari, S.; Tchounwou, P. B. *Eur. J. Pharmacol.* **2014**, *740*, 364.

- (25) Oun, R.; Moussa, Y. E.; Wheate, N. J. *Dalton Trans.* **2018**, 47, 6645.
- (26) Scaltriti, M.; Baselga, J. *Clin. Cancer. Res.* **2006**, 12, 5268.
- (27) Kobayashi, K.; Hagiwara, K. *Target. Oncol.* **2013**, 8, 27.
- (28) Ledermann, J.; Harter, P.; Gourley, C.; Friedlander, M.; Vergote, I.; Rustin, G.; Scott, C.; Meier, W.; Shapira-Frommer, R.; Safra, T. *N. Engl. J. Med.* **2012**, 366, 1382.
- (29) Mjos, K. D.; Orvig, C. *Chem. Rev.* **2014**, 114, 4540.
- (30) Ehrlich, P.; Bertheim, A. *Ber. Dtsch. Chem. Ges.* **1912**, 45, 756.
- (31) Rosenberg, B.; Vancamp, L.; Krigas, T. *Nature* **1965**, 205, 698.
- (32) Rosenberg, B.; VanCamp, L.; Trosko, J. E.; Mansour, V. H. *Nature* **1969**, 222, 385.
- (33) Barry, N. P.; Sadler, P. J. *Chem. Commun. (Camb.)* **2013**, 49, 5106.
- (34) Saenger, W. In *Principles of Nucleic Acid Structure*; Cantor, C. R., Ed.; Springer Science & Business Media: Berlin, 2013, p 253.
- (35) Hurley, L. H. *Nat. Rev. Cancer* **2002**, 2, 188.
- (36) Urig, S.; Fritz-Wolf, K.; Réau, R.; Herold-Mende, C.; Tóth, K.; Davioud-Charvet, E.; Becker, K. *Angew. Chem. Int. Ed.* **2006**, 45, 1881.
- (37) Forman, H. J.; Maiorino, M.; Ursini, F. *Biochemistry* **2010**, 49, 835.

- (38) Circu, M. L.; Aw, T. Y. *Free Radic. Biol. Med.* **2010**, 48, 749.
- (39) Sabharwal, S. S.; Schumacker, P. T. *Nat. Rev. Cancer* **2014**, 14, 709.
- (40) Trachootham, D.; Alexandre, J.; Huang, P. *Nat. Rev. Drug Discov.* **2009**, 8, 579.
- (41) Liu, Z.; Romero-Canelón, I.; Qamar, B.; Hearn, J. M.; Habtemariam, A.; Barry, N. P.; Pizarro, A. M.; Clarkson, G. J.; Sadler, P. J. *Angew. Chem. Int. Ed.* **2014**, 53, 3941.
- (42) Hocharoen, L.; Cowan, J. A. *Chem. Eur. J.* **2009**, 15, 8670.
- (43) Meggers, E. *Curr. Opin. Chem. Biol.* **2007**, 11, 287.
- (44) Soldevila-Barreda, J. J.; Sadler, P. J. *Curr. Opin. Chem. Biol.* **2015**, 25, 172.
- (45) Peyrone, M. *Justus Liebigs Ann. Chem.* **1844**, 51, 1.
- (46) Loehrer, P. J.; Einhorn, L. H. *Ann. Intern. Med.* **1984**, 100, 704.
- (47) Florea, A.-M.; Büsselberg, D. *Cancers (Basel)* **2011**, 3, 1351.
- (48) Einhorn, L. H. *J. Clin. Oncol.* **1990**, 8, 1777.
- (49) Brabec, V.; Hrabina, O.; Kasparkova, J. *Coord. Chem. Rev.* **2017**, 351, 2.
- (50) Jung, Y.; Lippard, S. J. *Chem. Rev.* **2007**, 107, 1387.
- (51) Perez, R. P. *Eur. J. Cancer* **1998**, 34, 1535.
- (52) Kuo, M. T.; Chen, H. H.; Song, I. S.; Savaraj, N.; Ishikawa, T. *Cancer Metastasis Rev.* **2007**, 26, 71.

- (53) Galluzzi, L.; Senovilla, L.; Vitale, I.; Michels, J.; Martins, I.; Kepp, O.; Castedo, M.; Kroemer, G. *Oncogene* **2012**, *31*, 1869.
- (54) Johnstone, T. C.; Suntharalingam, K.; Lippard, S. J. *Chem. Rev.* **2016**, *116*, 3436.
- (55) Wilkinson, G.; Rosenblum, M.; Whiting, M. C.; Woodward, R. B. *J. Am. Chem. Soc.* **1952**, *74*, 2125.
- (56) Kealy, T. J.; Pauson, P. L. *Nature* **1951**, *168*, 1039.
- (57) Miller, S. A.; Tebboth, J. A.; Tremaine, J. F. *J. Chem. Soc.* **1952**, *1*, 632.
- (58) Gasser, G.; Ott, I.; Metzler-Nolte, N. *J. Med. Chem.* **2011**, *54*, 3.
- (59) Green, J. C. *Chem. Soc. Rev.* **1998**, *27*, 263.
- (60) Lümme, G.; Sperling, H.; Luboldt, H.; Otto, T.; Rübber, H. *Cancer Chemother. Pharmacol.* **1998**, *42*, 415.
- (61) Kröger, N.; Kleeberg, U. R.; Mross, K.; Edler, L.; Hossfeld, D. K. *Oncol. Res. Treat.* **2000**, *23*, 60.
- (62) Strohfelddt, K.; Tacke, M. *Chem. Soc. Rev.* **2008**, *37*, 1174.
- (63) Pizarro, A. M.; Habtemariam, A.; Sadler, P. J. In *Medicinal Organometallic Chemistry. Topics in Organometallic Chemistry*; Jaouen, G., Metzler-Nolte, N., Eds.; Springer: Berlin, Heidelberg, 2010; Vol. 32, p 21.
- (64) Allen, O. R.; Croll, L.; Gott, A. L.; Knox, R. J.; McGowan, P. C. *Organometallics* **2004**, *23*, 288.

- (65) Christodoulou, C. V.; Eliopoulos, A. G.; Young, L. S.; Hodgkins, L.; Ferry, D. R.; Kerr, D. J. *Br. J. Cancer* **1998**, 77, 2088.
- (66) Olszewski, U.; Hamilton, G. *Anticancer Agents Med. Chem.* **2010**, 10, 302.
- (67) Jaouen, G.; Vessi  res, A.; Top, S. *Chem. Soc. Rev.* **2015**, 44, 8802.
- (68) Fu, Y.; Habtemariam, A.; Pizarro, A. M.; van Rijt, S. H.; Healey, D. J.; Cooper, P. A.; Shnyder, S. D.; Clarkson, G. J.; Sadler, P. J. *J. Med. Chem.* **2010**, 53, 8192.
- (69) Dwyer, F. P.; Gyarfas, E. C.; Rogers, W. P.; Koch, J. H. *Nature* **1952**, 170, 190.
- (70) Levina, A.; Mitra, A.; Lay, P. A. *Metallomics* **2009**, 1, 458.
- (71) Zeng, L.; Gupta, P.; Chen, Y.; Wang, E.; Ji, L.; Chao, H.; Chen, Z. S. *Chem. Soc. Rev.* **2017**, 46, 5771.
- (72) Hartinger, C. G.; Groessl, M.; Meier, S. M.; Casini, A.; Dyson, P. *J. Chem. Soc. Rev.* **2013**, 42, 6186.
- (73) Minchinton, A. I.; Tannock, I. F. *Nat. Rev. Cancer* **2006**, 6, 583.
- (74) Sava, G.; Capozzi, I.; Clerici, K.; Gagliardi, G.; Alessio, E.; Mestroni, G. *Clin. Exp. Metastasis* **1998**, 16, 371.
- (75) Bergamo, A.; Gagliardi, R.; Scarcia, V.; Furlani, A.; Alessio, E.; Mestroni, G.; Sava, G. *J. Pharmacol. Exp. Ther.* **1999**, 289, 559.

- (76) Gava, B.; Zorzet, S.; Spessotto, P.; Cocchietto, M.; Sava, G. *J. Pharmacol. Exp. Ther.* **2006**, *317*, 284.
- (77) Kapitza, S.; Pongratz, M.; Jakupec, M. A.; Heffeter, P.; Berger, W.; Lackinger, L.; Keppler, B. K.; Marian, B. *J. Cancer Res. Clin. Oncol.* **2005**, *131*, 101.
- (78) Heffeter, P.; Pongratz, M.; Steiner, E.; Chiba, P.; Jakupec, M. A.; Elbling, L.; Marian, B.; Korner, W.; Sevela, F.; Micksche, M.; Keppler, B. K.; Berger, W. *J. Pharmacol. Exp. Ther.* **2005**, *312*, 281.
- (79) Sadafi, F. Z.; Massai, L.; Bartolommei, G.; Moncelli, M. R.; Messori, L.; Tadini-Buoninsegni, F. *ChemMedChem* **2014**, *9*, 1660.
- (80) Kapitza, S.; Jakupec, M. A.; Uhl, M.; Keppler, B. K.; Marian, B. *Cancer Lett.* **2005**, *226*, 115.
- (81) Singh, V.; Azad, G. K.; Baranwal, S.; Tomar, R. S. *Eur. J. Pharmacol.* **2014**, *736*, 77.
- (82) Allardyce, C. S.; Dyson, P. J.; Ellis, D. J.; Salter, P. A.; Scopelliti, R. *J. Organomet. Chem.* **2003**, *668*, 35.
- (83) Scolaro, C.; Bergamo, A.; Brescacin, L.; Delfino, R.; Cocchietto, M.; Laurenczy, G.; Geldbach, T. J.; Sava, G.; Dyson, P. J. *J. Med. Chem.* **2005**, *48*, 4161.

- (84) Chatterjee, S.; Kundu, S.; Bhattacharyya, A.; Hartinger, C. G.; Dyson, P. J. *J. Biol. Inorg. Chem.* **2008**, *13*, 1149.
- (85) Scolaro, C.; Geldbach, T. J.; Rochat, S.; Dorcier, A.; Gossens, C.; Bergamo, A.; Cocchietto, M.; Tavernelli, I.; Sava, G.; Rothlisberger, U. *Organometallics* **2006**, *25*, 756.
- (86) Meggers, E.; Atilla-Gokcumen, G. E.; Bregman, H.; Maksimoska, J.; Mulcahy, S. P.; Pagano, N.; Williams, D. S. *Synlett* **2007**, *2007*, 1177.
- (87) Smalley, K. S. M.; Contractor, R.; Haass, N. K.; Kulp, A. N.; Atilla-Gokcumen, G. E.; Williams, D. S.; Bregman, H.; Flaherty, K. T.; Soengas, M. S.; Meggers, E. *Cancer Res.* **2007**, *67*, 209.
- (88) Debreczeni, J. É.; Bullock, A. N.; Atilla, G. E.; Williams, D. S.; Bregman, H.; Knapp, S.; Meggers, E. *Angew. Chem. Int. Ed.* **2006**, *45*, 1580.
- (89) Antonarakis, E. S.; Emadi, A. *Cancer Chemother. Pharmacol.* **2010**, *66*, 1.
- (90) Wang, F.; Chen, H.; Parsons, S.; Oswald, I. D. H.; Davidson, J. E.; Sadler, P. J. *Chem. Eur. J.* **2003**, *9*, 5810.
- (91) Novakova, O.; Chen, H.; Vrana, O.; Rodger, A.; Sadler, P. J.; Brabec, V. *Biochemistry* **2003**, *42*, 11544.
- (92) Wang, F.; Xu, J.; Habtemariam, A.; Bella, J.; Sadler, P. J. *J. Am. Chem. Soc.* **2005**, *127*, 17734.

- (93) Soldevila-Barreda, J. J.; Romero-Canelón, I.; Habtemariam, A.; Sadler, P. J. *Nat. Commun.* **2015**, 6, 6582.
- (94) Dougan, S. J.; Habtemariam, A.; McHale, S. E.; Parsons, S.; Sadler, P. J. *Proc. Natl. Acad. Sci. U.S.A.* **2008**, 105, 11628.
- (95) Mason, T. A.; Kolobova, E.; Liu, J.; Roland, J. T.; Chiang, C.; Goldenring, J. R. *PLoS One* **2011**, 6, e27699.
- (96) List, A.; Beran, M.; DiPersio, J.; Slack, J.; Vey, N.; Rosenfeld, C. S.; Greenberg, P. *Leukemia* **2003**, 17, 1499.
- (97) Bindoli, A.; Rigobello, M. P.; Scutari, G.; Gabbiani, C.; Casini, A.; Messori, L. *Coord. Chem. Rev.* **2009**, 253, 1692.
- (98) Arblaster, J. W. *Platinum Met. Rev.* **1995**, 39, 164.
- (99) Girolami, G. *Nat. Chem.* **2012**, 4, 954.
- (100) Venetskii, S. I. *Metallurgist* **1974**, 18, 155.
- (101) MacDonell, H. L. *J. Crim. Law Criminol. Police Sci.* **1960**, 51, 465.
- (102) Goldstein, S.; Czapski, G.; Heller, A. *Free Radic. Biol. Med.* **2005**, 38, 839.
- (103) Craciunescu, D. G.; Molina, C.; Parrondo-Iglesias, E.; Alonso, M. *P. An. Real Acad. Farm.* **1991**, 58, 207.
- (104) Craciunescu, D. G.; Molina, C.; Parrondo-Iglesias, E. *An. Real Acad. Farm.* **1991**, 57, 221.

- (105) Boussina, I.; Gerster, J.; Epiney, J.; Fallet, G. H. *Scand. J. Rheumatol.* **1976**, *5*, 33.
- (106) Cebrián-Losantos, B.; Krokhin, A. A.; Stepanenko, I. N.; Eichinger, R.; Jakupec, M. A.; Arion, V. B.; Keppler, B. K. *Inorg. Chem.* **2007**, *46*, 5023.
- (107) Egger, A.; Cebrián-Losantos, B.; Stepanenko, I. N.; Krokhin, A. A.; Eichinger, R.; Jakupec, M. A.; Arion, V. B.; Keppler, B. K. *Chem. Biodivers.* **2008**, *5*, 1588.
- (108) Büchel, G. E.; Stepanenko, I. N.; Hejl, M.; Jakupec, M. A.; Keppler, B. K.; Arion, V. B. *Inorg. Chem.* **2011**, *50*, 7690.
- (109) Büchel, G. E.; Stepanenko, I. N.; Hejl, M.; Jakupec, M. A.; Keppler, B. K.; Heffeter, P.; Berger, W.; Arion, V. B. *J. Inorg. Biochem.* **2012**, *113*, 47.
- (110) Ni, W.-X.; Man, W.-L.; Yiu, S.-M.; Ho, M.; Cheung, M. T.-W.; Ko, C.-C.; Che, C.-M.; Lam, Y.-W.; Lau, T.-C. *Chem. Sci.* **2012**, *3*, 1582.
- (111) Tang, Q.; Ni, W.-X.; Leung, C.-F.; Man, W.-L.; Lau, K. K.-K.; Liang, Y.; Lam, Y.-W.; Wong, W.-Y.; Peng, S.-M.; Liu, G.-J. *Chem. Commun.* **2013**, *49*, 9980.
- (112) Suntharalingam, K.; Johnstone, T. C.; Bruno, P. M.; Lin, W.; Hemann, M. T.; Lippard, S. J. *J. Am. Chem. Soc.* **2013**, *135*, 14060.

- (113) Maksimoska, J.; Williams, D. S.; Atilla-Gokcumen, G. E.; Smalley, K. S. M.; Carroll, P. J.; Webster, R. D.; Filippakopoulos, P.; Knapp, S.; Herlyn, M.; Meggers, E. *Chem. Eur. J.* **2008**, *14*, 4816.
- (114) Filak, L. K.; Mühlgassner, G.; Bacher, F.; Roller, A.; Galanski, M.; Jakupec, M. A.; Keppler, B. K.; Arion, V. B. *Organometallics* **2010**, *30*, 273.
- (115) Meier, S. M.; Hanif, M.; Adhireksan, Z.; Pichler, V.; Novak, M.; Jirkovsky, E.; Jakupec, M. A.; Arion, V. B.; Davey, C. A.; Keppler, B. K.; Hartinger, C. G. *Chem. Sci.* **2013**, *4*, 1837.
- (116) Yang, C.; Wang, W.; Li, G.-D.; Zhong, H.-J.; Dong, Z.-Z.; Wong, C.-Y.; Kwong, D. W. J.; Ma, D.-L.; Leung, C.-H. *Sci. Rep.* **2017**, *7*, 42860.
- (117) Liu, L.-J.; Wang, W.; Kang, T.-S.; Liang, J.-X.; Liu, C.; Kwong, D. W. J.; Wong, V. K. W.; Ma, D.-L.; Leung, C.-H. *Sci. Rep.* **2016**, *6*, 36044.
- (118) Peacock, A. F. A.; Habtemariam, A.; Moggach, S. A.; Prescimone, A.; Parsons, S.; Sadler, P. J. *Inorg. Chem.* **2007**, *46*, 4049.
- (119) Peacock, A. F. A.; Habtemariam, A.; Fernández, R.; Walland, V.; Fabbiani, F. P. A.; Parsons, S.; Aird, R. E.; Jodrell, D. I.; Sadler, P. J. *J. Am. Chem. Soc.* **2006**, *128*, 1739.

- (120) Peacock, A. F.; Melchart, M.; Deeth, R. J.; Habtemariam, A.; Parsons, S.; Sadler, P. J. *Chem. Eur. J.* **2007**, *13*, 2601.
- (121) Kostrhunova, H.; Florian, J.; Novakova, O.; Peacock, A. F.; Sadler, P. J.; Brabec, V. *J. Med. Chem.* **2008**, *51*, 3635.
- (122) Peacock, A. F.; Parsons, S.; Sadler, P. J. *J. Am. Chem. Soc.* **2007**, *129*, 3348.
- (123) van Rijt, S. H.; Peacock, A. F.; Johnstone, R. D.; Parsons, S.; Sadler, P. J. *Inorg. Chem.* **2009**, *48*, 1753.
- (124) van Rijt, S. H.; Mukherjee, A.; Pizarro, A. M.; Sadler, P. J. *J. Med. Chem.* **2010**, *53*, 840.
- (125) Rijt, S. H.; Kostrhunova, H.; Brabec, V.; Sadler, P. J. *Bioconjug. Chem.* **2011**, *22*, 218.
- (126) Fu, Y.; Romero, M. J.; Habtemariam, A.; Snowden, M. E.; Song, L.; Clarkson, G. J.; Qamar, B.; Pizarro, A. M.; Unwin, P. R.; Sadler, P. J. *Chem. Sci.* **2012**, *3*, 2485.
- (127) Romero-Canelón, I.; Salassa, L.; Sadler, P. J. *J. Med. Chem.* **2013**, *56*, 1291.
- (128) Fu, Y.; Soni, R.; Romero, M. J.; Pizarro, A. M.; Salassa, L.; Clarkson, G. J.; Hearn, J. M.; Habtemariam, A.; Wills, M.; Sadler, P. J. *Chem. Eur. J.* **2013**, *19*, 15199.

- (129) Coverdale, J. P. C.; Romero-Canelon, I.; Sanchez-Cano, C.; Clarkson, G. J.; Habtemariam, A.; Wills, M.; Sadler, P. J. *Nat. Chem.* **2018**, *10*, 347.
- (130) Fu, Y.; Romero, M. J.; Salassa, L.; Cheng, X.; Habtemariam, A.; Clarkson, G. J.; Prokes, I.; Rodger, A.; Costantini, G.; Sadler, P. J. *Angew. Chem. Int. Ed. Engl.* **2016**, *55*, 8909.
- (131) Fu, Y.; Habtemariam, A.; Basri, A. M.; Braddick, D.; Clarkson, G. J.; Sadler, P. J. *Dalton Trans.* **2011**, *40*, 10553.
- (132) Needham, R. J.; Sanchez-Cano, C.; Zhang, X.; Romero-Canelon, I.; Habtemariam, A.; Cooper, M. S.; Meszaros, L.; Clarkson, G. J.; Blower, P. J.; Sadler, P. J. *Angew. Chem. Int. Ed. Engl.* **2017**, *56*, 1017.
- (133) Peacock, A. F.; Habtemariam, A.; Moggach, S. A.; Prescimone, A.; Parsons, S.; Sadler, P. J. *Inorg. Chem.* **2007**, *46*, 4049.
- (134) Hearn, J. M.; Romero-Canelon, I.; Munro, A. F.; Fu, Y.; Pizarro, A. M.; Garnett, M. J.; McDermott, U.; Carragher, N. O.; Sadler, P. J. *Proc. Natl. Acad. Sci. U.S.A.* **2015**, *112*, E3800.
- (135) Romero-Canelón, I.; Mos, M.; Sadler, P. J. *J. Med. Chem.* **2015**, *58*, 7874.
- (136) Shnyder, S. D.; Fu, Y.; Habtemariam, A.; van Rijt, S. H.; Cooper, P. A.; Loadman, P. M.; Sadler, P. J. *MedChemComm* **2011**, *2*, 666.

- (137) Chung, K.-T. *J. Environ. Sci. Health C* **2016**, *34*, 233.
- (138) Kumar, G. S.; Neckers, D. C. *Chem. Rev.* **1989**, *89*, 1915.
- (139) Natansohn, A.; Rochon, P. *Chem. Rev.* **2002**, *102*, 4139.
- (140) Magennis, S. W.; Mackay, F. S.; Jones, A. C.; Tait, K. M.; Sadler, P. J. *Chem. Mater.* **2005**, *17*, 2059.
- (141) Braun, L.; Linder, T.; Hessberger, T.; Zentel, R. *Polymers* **2016**, *8*, 435.
- (142) Ferreira, R.; Nilsson, J. R.; Solano, C.; Andreasson, J.; Grotli, M. *Sci. Rep.* **2015**, *5*, 9769.
- (143) Sheldon, J. E.; Dcona, M. M.; Lyons, C. E.; Hackett, J. C.; Hartman, M. C. *Org. Biomol. Chem.* **2016**, *14*, 40.
- (144) Thomas, B. H.; Whitehouse, L. W.; Solomonraj, G.; Paul, C. J. *J. Pharm. Sci.* **1990**, *79*, 321.
- (145) Hotze, A. C. G.; Velders, A. H.; Ugozzoli, F.; Biagini-Cingi, M.; Manotti-Lanfredi, A. M.; Haasnoot, J. G.; Reedijk, J. *Inorg. Chem.* **2000**, *39*, 3838.
- (146) Velders, A. H.; Kooijman, H.; Spek, A. L.; Haasnoot, J. G.; de Vos, D.; Reedijk, J. *Inorg Chem* **2000**, *39*, 2966.
- (147) Azam, M.; Al-Resayes, S.; Wabaidur, S.; Altaf, M.; Chaurasia, B.; Alam, M.; Shukla, S.; Gaur, P.; Albaqami, N.; Islam, M. *Molecules* **2018**, *23*, 813.
- (148) Misal, S. A.; Gawai, K. R. *Bioresour. Bioprocess.* **2018**, *5*, 17.

- (149) Ryan, A. *Br. J. Pharmacol.* **2017**, *174*, 2161.
- (150) Ooi, T.; Shibata, T.; Sato, R.; Ohno, H.; Kinoshita, S.; Thuoc, T. L.; Taguchi, S. *Appl. Microbiol. Biotechnol.* **2007**, *75*, 377.
- (151) Ito, K.; Nakanishi, M.; Lee, W.-C.; Sasaki, H.; Zenno, S.; Saigo, K.; Kitade, Y.; Tanokura, M. *J. Biol. Chem.* **2006**, *281*, 20567.
- (152) Ryan, A.; Laurieri, N.; Westwood, I.; Wang, C.-J.; Lowe, E.; Sim, E. *J. Mol. Biol.* **2010**, *400*, 24.
- (153) Yu, J.; Ogata, D.; Gai, Z.; Taguchi, S.; Tanaka, I.; Ooi, T.; Yao, M. *Acta Crystallogr. Sect. D. Biol. Crystallogr.* **2014**, *70*, 553.
- (154) Gonçalves, A. M. D.; Mendes, S.; de Sanctis, D.; Martins, L. O.; Bento, I. *FEBS J.* **2013**, *280*, 6643.
- (155) Ryan, A.; Wang, C.-J.; Laurieri, N.; Westwood, I.; Sim, E. *Protein Cell* **2010**, *1*, 780.
- (156) Peterson, F. J.; Holtzman, J. L.; Crankshaw, D.; Mason, R. P. *Mol. Pharmacol.* **1988**, *34*, 597.
- (157) Mason, R. P.; Peterson, F. J.; Holtzman, J. L. *Mol. Pharmacol.* **1978**, *14*, 665.
- (158) Mason, R. P.; Peterson, F. J.; Holtzman, J. L. *Biochem. Biophys. Res. Commun.* **1977**, *75*, 532.
- (159) Kiyose, K.; Hanaoka, K.; Oushiki, D.; Nakamura, T.; Kajimura, M.; Suematsu, M.; Nishimatsu, H.; Yamane, T.; Terai, T.; Hirata, Y. *J. Am. Chem. Soc.* **2010**, *132*, 15846.

- (160) Alonso, F.; Radivoy, G.; Yus, M. *Tetrahedron* **2000**, *56*, 8673.
- (161) Gowda, S.; Abiraj, K.; Gowda, D. C. *Tetrahedron Lett.* **2002**, *43*, 1329.
- (162) Pasha, M. A.; Nanjundaswamy, H. M. *Synth. Commun.* **2005**, *35*, 897.
- (163) Li, G.; Chen, Y.; Wang, J.; Lin, Q.; Zhao, J.; Ji, L.; Chao, H. *Chem. Sci.* **2013**, *4*, 4426.
- (164) Li, G.; Chen, Y.; Wu, J.; Ji, L.; Chao, H. *Chem. Commun.* **2013**, *49*, 2040.
- (165) Li, G.; Chen, Y.; Wang, J.; Wu, J.; Gasser, G.; Ji, L.; Chao, H. *Biomaterials* **2015**, *63*, 128.
- (166) Zhou, Q.-X.; Zheng, Y.; Wang, T.-J.; Chen, Y.-J.; Li, K.; Zhang, Y.-Y.; Li, C.; Hou, Y.-J.; Wang, X.-S. *Chem. Commun.* **2015**, *51*, 10684.
- (167) Corazza, A.; Harvey, I.; Sadler, P. J. *Eur. J. Biochem.* **1996**, *236*, 697.
- (168) Lu, S. C. *Biochim. Biophys. Acta Gen. Subj.* **2013**, *1830*, 3143.
- (169) Meister, A.; Anderson, M. E. *Annu. Rev. Biochem.* **1983**, *52*, 711.
- (170) Couto, N.; Malys, N.; Gaskell, S. J.; Barber, J. J. *Proteome Res.* **2013**, *12*, 2885.
- (171) Kaplowitz, N. *Yale J. Biol. Med.* **1981**, *54*, 497.
- (172) Halprin, K. M.; Ohkawara, A. J. *Invest. Dermatol.* **1967**, *48*, 149.

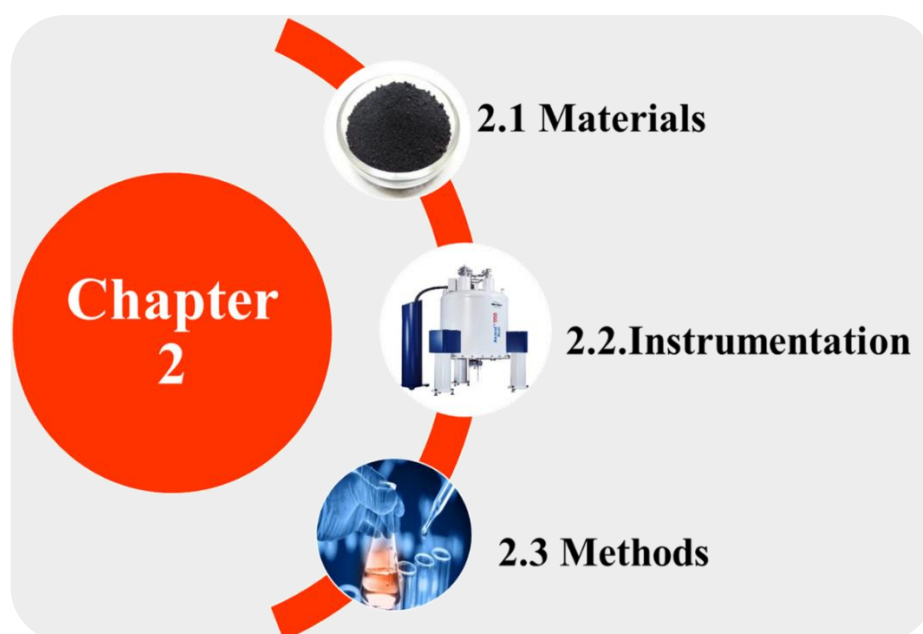
- (173) Sies, H. *Free Radic. Biol. Med.* **1999**, 27, 916.
- (174) Krężel, A.; Bal, W. *Acta Biochim. Pol.* **1999**, 46, 567.
- (175) Leverrier, P.; Montigny, C.; Garrigos, M.; Champeil, P. *Anal. Biochem.* **2007**, 371, 215.
- (176) Krezel, A.; Bal, W. *Bioinorg. Chem. Appl.* **2004**, 2, 293.
- (177) Baloun, J.; Adam, V.; Trnkova, L.; Beklova, M.; Svobodova, Z.; Zeman, L.; Kizek, R. *Environ. Toxicol. Chem.* **2010**, 29, 497.
- (178) Rubino, F. *Toxics* **2015**, 3, 20.
- (179) Hernández, L. E.; Sobrino-Plata, J.; Montero-Palmero, M. B.; Carrasco-Gil, S.; Flores-Cáceres, M. L.; Ortega-Villasante, C.; Escobar, C. *J. Exp. Bot.* **2015**, 66, 2901.
- (180) Yadav, S. K. S. *Afr. J. Bot.* **2010**, 76, 167.
- (181) Jozefczak, M.; Remans, T.; Vangronsveld, J.; Cuypers, A. *Int. J. Mol. Sci.* **2012**, 13, 3145.
- (182) Liu, Z.; Sadler, P. J. *Inorg. Chem. Front.* **2014**, 1, 668.
- (183) Kemp, S.; Wheate, N. J.; Pisani, M. J.; Aldrich-Wright, J. R. *J. Med. Chem.* **2008**, 51, 2787.
- (184) Kasherman, Y.; Sturup, S.; Gibson, D. *J. Med. Chem.* **2009**, 52, 4319.
- (185) Ishikawa, T.; Bao, J.-J.; Yamane, Y.; Akimaru, K.; Frindrich, K.; Wright, C. D.; Kuo, M. T. *J. Biol. Chem.* **1996**, 271, 14981.

- (186) Mann, K. K.; Wallner, B.; Lossos, I. S.; Miller Jr, W. H. *Expert Opin. Investig. Drugs* **2009**, *18*, 1727.
- (187) Ortega, A. L.; Mena, S.; Estrela, J. M. *Cancers (Basel)* **2011**, *3*, 1285.
- (188) Fakih, S.; Munk, V. P.; Shipman, M. A.; Murdoch, P. d. S.; Parkinson, J. A.; Sadler, P. J. *Eur. J. Inorg. Chem.* **2003**, 2003, 1206.
- (189) del Socorro Murdoch, P.; Kratochwil, N. A.; Parkinson, J. A.; Patriarca, M.; Sadler, P. J. *Angew. Chem. Int. Ed.* **1999**, *38*, 2949.
- (190) Ling, X.; Tu, J.; Wang, J.; Shajii, A.; Kong, N.; Feng, C.; Zhang, Y.; Yu, M.; Xie, T.; Bharwani, Z. *ACS nano* **2018**, *13*, 357.
- (191) Schluga, P.; Hartinger, C. G.; Egger, A.; Reisner, E.; Galanski, M.; Jakupec, M. A.; Keppler, B. K. *Dalton Trans.* **2006**, 1796.
- (192) Morris, R. E.; Aird, R. E.; del Socorro Murdoch, P.; Chen, H.; Cummings, J.; Hughes, N. D.; Parsons, S.; Parkin, A.; Boyd, G.; Jodrell, D. I. *J. Med. Chem.* **2001**, *44*, 3616.
- (193) Petzold, H.; Sadler, P. J. *Chem. Commun.* **2008**, 4413.
- (194) Sriskandakumar, T.; Petzold, H.; Bruijninx, P. C. A.; Habtemariam, A.; Sadler, P. J.; Kennepohl, P. *J. Am. Chem. Soc.* **2009**, *131*, 13355.
- (195) Petzold, H.; Xu, J.; Sadler, P. J. *Angew. Chem. Int. Ed.* **2008**, *47*, 3008.

- (196) Hong, Y.; Lai, Y.-T.; Chan, G. C.-F.; Sun, H. *Proc. Natl. Acad. Sci. U.S.A.* **2015**, *112*, 3211.
- (197) He, H.; Lo, P. C.; Ng, D. K. P. *Chem. Eur. J.* **2014**, *20*, 6241.
- (198) Bailey, H. H.; Mulcahy, R. T.; Tutsch, K. D.; Arzoomanian, R. Z.; Alberti, D.; Tombes, M. B.; Wilding, G.; Pomplun, M.; Spriggs, D. R. *J. Clin. Oncol.* **1994**, *12*, 194.
- (199) Romero-Canelon, I.; Sadler, P. J. *Inorg. Chem.* **2013**, *52*, 12276.

Chapter 2

Experimental Section



In this **Chapter**, the materials (**Section 2.1**), instrumentation (**Section 2.2**) and methods (**Section 2.3**) used in all experiments performed will be described. More details about individual experiments are available in each appropriate chapter.

2.1. Materials

2.1.1. Chemical Reagents

$\text{OsCl}_3 \cdot 3\text{H}_2\text{O}$ was purchased from Alfa Aesar. Reduced glutathione (**GSH**), N-acetyl-L-cysteine (**NAC**), silver nitrate, 1,4-dithiothreitol (**DTT**), horse heart cytochrome *c* and bovine superoxide dismutase (**SOD**) were purchased from Sigma-Aldrich (Gillingham, UK). Pyridine-2-azo-p-dimethylaniline was purchased from Alfa Aesar. Ammonium hexafluorophosphate, sodium methoxide and potassium iodate were also purchased from Sigma-Aldrich. Sodium hydroxide, sodium chloride, sodium phosphate dibasic, sodium phosphate monobasic, trifluoroacetic acid were purchased from Fisher Scientific Ltd. (Loughborough, UK). NMR tubes and deuterated solvents were purchased from Sigma Aldrich. The free radical trapping agent 5-(diethoxyphosphoryl)-5-methyl-1-pyrroline-N-oxide (DEPMPO) was purchased from Enzo Life Sciences. The osmium ICP standard solution $1000 \pm 10 \mu\text{g/mL}$ in 15% HCl (v/v) was purchased from Inorganic Ventures. Solvents used for high

performance liquid chromatography (HPLC) and liquid chromatography-mass spectrometry (LC-MS) were purchased from Fisher Scientific Ltd. Analysis grade doubly deionised water ($18\text{ M}\Omega\text{ cm}^{-1}$) was obtained from either a Millipore Simplicity UV, or an USF Elga UHQ PS purification system. All other solvents and reagents for synthesis and analysis were purchased from commercial suppliers and used as received.

2.1.2. Buffer Solutions

Phosphate Buffer. Na_2HPO_4 (3.44 g, 24.3 mmol) and $\text{H}_2\text{NaPO}_4 \cdot 2\text{H}_2\text{O}$ (0.89 g, 5.7 mmol) were dissolved into 100 mL doubly deionized water to get 300 mM phosphate buffer solution. NaCl (0.58 g, 10 mmol) was added if it was necessary to prepare physiologically relevant buffer solution. Diluted sodium hydroxide (NaOH) or nitric acid (HNO_3) solutions were used to modify the pH value of buffer solutions. In NMR experiments, the deuterated phosphate buffer solution was prepared by dissolving phosphate salts in D_2O firstly, then using freeze-drying to remove all solvent and finally adding D_2O again to obtain the completely deuterated solution. The pH values of solutions were measured with pH meters (**Section 2.2**). Considering the effect of deuterium on the glass electrode, the pH^* value (meter reading) measured in D_2O solution was corrected to pH using the equation: $\text{pH} = 0.929\text{pH}^* + 0.4$.¹

Ammonium Acetate Buffer. $\text{CH}_3\text{COONH}_4$ (1.54 g, 20 mmol) was dissolved in 100 mL doubly deionized water to give a 200 mM ammonium acetate buffer solution, $\text{pH} = 7.02$.

Citrate-Phosphate Buffer. Na_2HPO_4 (28.2 g, 200 mmol), citric acid (76.8 g, 400 mmol) were dissolved into 1 L doubly deionized water to give citrate (400 mM)-phosphate (200 mM) buffer solutions, $\text{pH} = 2.95$.

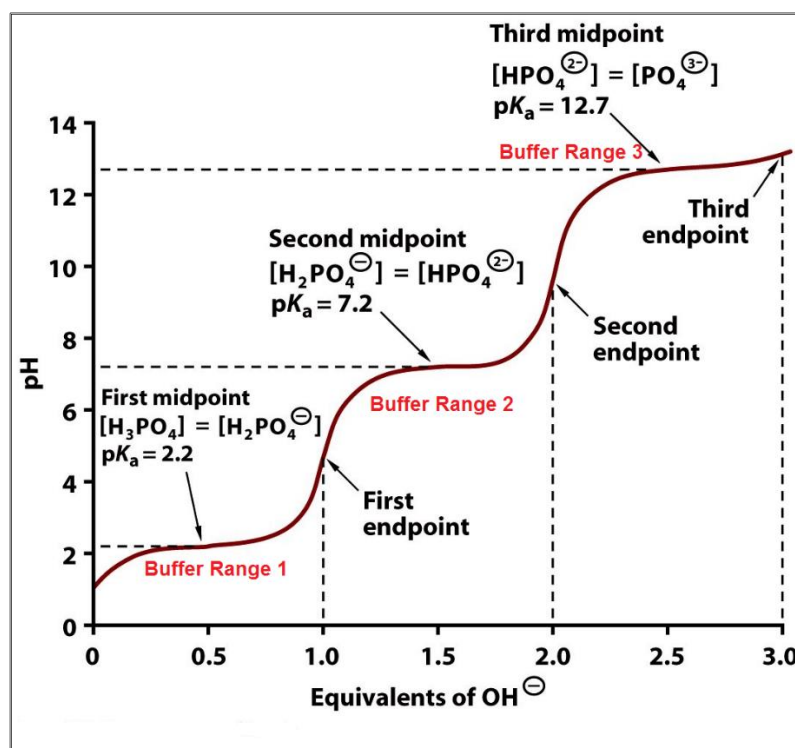


Figure 2.1. The buffer ranges for phosphate buffer.²

2.1.3 Osmium Dimer Complexes

All the organo-osmium complexes studied in this thesis were synthesized from the precursor osmium dimer complexes prepared following reported literature methods.³⁻⁵

[Os(η^6 -*p*-cym)Cl₂]₂. OsCl₃·3H₂O (500 mg, 1.43 mmol) and α -terpinene (1.6 mL, 1.43 mmol) were dissolved in methanol (6 mL). The solution was transferred into a microwave reaction vessel and then irradiated with microwave radiation for 5 min at 423 K. After reaction, the mixture was placed in a freezer (268 K) overnight, and an orange precipitate was observed. The precipitate was collected *via* vacuum filtration, then washed with ice-cold ethanol (2 \times 5 mL) and diethyl ether (2 \times 5 mL). Finally, the product was dried overnight in a vacuum desiccator. Yield: 0.56 mg (98%). ¹H NMR (DMSO-d₆): δ = 6.07 (d, 4H, *J* = 6.0 Hz), 5.99 (d, 4H, *J* = 5.9 Hz), 2.74 (m, 2H), 2.14 (s, 6H), 1.19 (d, 12H, *J* = 7.0 Hz).

[Os(η^6 -*p*-cym)I₂]₂. The dimer [Os(η^6 -*p*-cym)Cl₂]₂ (103.8 mg, 0.135 mmol) was dissolved into methanol (3 mL) which had been bubbled with N₂ for 30 min, and then a solution of KI (2.68 g, 16.18 mmol) in deionised water (10 mL) was added. The mixture was transferred to a microwave reaction vessel and irradiated with microwave radiation for 5 min at 423 K. The mixture was then placed in a fridge (273 K) overnight, and following this a red precipitate was observed. The precipitate was

collected *via* vacuum filtration and washed with H₂O (2 × 5 mL), ice-cold ethanol (2 × 5 mL) and diethyl ether (2 × 5 mL). Finally, the product was dried overnight in a vacuum desiccator. Yield: 129.8 mg (78%). ¹H NMR (DMSO-d₆): δ = 6.07 (d, 4H, *J* = 6.0 Hz), 6.04 (d, 4H, *J* = 6.0 Hz), 2.77 (m, 2H), 2.29 (s, 6H), 1.22 (d, 12H, *J* = 6.9 Hz).

2.1.4. Cell culture

All the cell work conducted in this thesis was carried out by Dr. Isolda Romero-Canelón (The University of Warwick) and related materials were purchased by her. DMEM and RPMI-1640 cell culture media, L-glutamine, foetal bovine serum, phosphate buffered saline solution (PBS), AccuMax cell dissociation solution, penicillin/streptomycin mixture, trypsin and trypsin/EDTA were all purchased from PAA Laboratories GmbH. Cell culture media were prepared with foetal bovine serum (50 mL), penicillin/streptomycin mixture (5 mL) and L-glutamine (5 mL). All cancer cell lines were purchased from the European Collection of Cell Cultures and Public Health England.

2.2. Instrumentation

2.2.1. UV-visible Spectroscopy⁶

A Cary 300 UV-Vis recording spectrophotometer was used with 1 cm path-length quartz cuvettes (0.5 mL) and a PTP1 Peltier temperature controller. Experiments were carried out at 288 K between 200-800 nm at a scan rate of 600 nm/min with 1 nm intervals unless otherwise stated. Spectra were recorded using UVWinlab software and processed using Origin 9.0.

2.2.2. Inductively Coupled Plasma Optical Emission Spectroscopy (ICP-OES)^{7,8}

A Perkin Elmer (Optical Emission Spectrometer) Optima 5300 DV instrument was used to analyse osmium solutions in this thesis. All testing and standard samples were freshly prepared on the day in doubly deionised water with distilled HNO₃ (3.2%), 5 mM thiourea and 0.28 mM ascorbic acid were used for osmium stabilization.^{9,10} The osmium standard (1000±10 µg/mL in 15% HCl (v/v) was purchased from Inorganic Ventures) and was diluted to the following concentrations for the calibration curve: 0, 25, 50, 100, 200, 400, 600, 800 and 1000 ppb. The samples were diluted by serial dilutions of typically 1 in 10 until their concentrations fitted within the calibration range and the % total dissolved solids were below 0.2%. Samples were made in triplicate and

the optical emission at 228.226 and 225.585 nm were detected and integrated.

2.2.3. Inductively Coupled Plasma-Mass Spectrometry (ICP-MS)^{7,11}

An Agilent Technologies 7500 series ICP-MS instrument was used to carry out the ICP-MS analysis of osmium in these investigations. All testing and standard samples were freshly prepared on the day in doubly deionised water with distilled HNO₃ (3.2%), 5 mM thiourea and 0.28 mM ascorbic acid solutions were used for osmium stabilization. It helps prevent the formation of volatile osmium tetroxide through thiourea binding with osmium and ascorbic acid reducing Os^{III} to Os^{II}.^{9,10} The osmium standard (1000±10 µg/mL in 15% HCl (v/v) and purchased from Inorganic Ventures) was diluted to the following concentrations for the calibration curve: 1000, 800, 400, 200, 100, 50, 10, 1, and 0.1 ppb. The samples were diluted by serial dilutions of typically 1 in 10 until their concentrations fitted within the calibration range and the % total dissolved solids were below 0.2%. The ICP-MS instrument was set to detect ¹⁸⁹Os with typical detection limits of ca. 8 ppt using no-gas mode.

2.2.4. High Performance Liquid Chromatography (HPLC)¹²

An Agilent Technologies 1200 series HPLC instrument with a VWD and 100 µL loop, plus Agilent ZORBAX Eclipse Plus C18 250×4.6 mm column with a pore size of 5 µm was used to test the purity, monitor their

reactions. Mobile phases consisted of: (A) H₂O with 0.1 % TFA, and (B) MeCN with 0.1 % TFA (HPLC grade materials were used) at a 1 mL/min flow rate. For product purification, 1 mL loop and semi-preparative ZORBAX Eclipse XDB-C18 250 × 9.4 mm column were used on HPLC instrument with same mobile phases but at 2 mL/min flow rate. The methods for mobile phase's gradient can be found **Section 2.3**.

2.2.5. Liquid Chromatography-Mass Spectrometry (LC-MS)¹³

Combined LC-MS analysis of the samples in this reactions was carried out on a Bruker Amazon X+ instrument coupled with an Agilent Technologies 1200 series HPLC instrument. The methods and conditions were consistent with the corresponding analysis on HPLC. Sample injections were 20 µL and the mass spectrometer was operated in electrospray positive mode with a scan range of 50-2000 m/z.

2.2.6. Nuclear Magnetic Resonance (NMR) Analysis¹⁴

¹H NMR spectra were acquired at 400 MHz in 5 mm NMR tubes at 298 K on a Bruker AV-400 spectrometer. Data processing was carried out using TOPSPIN version 2.1 (Bruker U.K. Ltd). ¹H NMR chemical shifts were internally referenced to TMS *via* their residual solvent peaks: methanol (δ = 3.31 ppm), water (δ = 4.79 ppm), DMSO (δ = 2.50 ppm) and 1,4-dioxane (3.71 ppm in H₂O).¹⁵ Likewise, for ¹³C NMR chemical shifts: acetonitrile (δ = 118.26 ppm), acetone (δ = 206.26 ppm) and

methanol ($\delta = 49.00$ ppm). ^{15}D ^1H NMR spectra were recorded using standard pulse sequences and acquired with 16 transients into 32 k data points over a spectral width of 14 ppm. 1D ^{13}C NMR spectra were recorded using a JMOD pulse sequence and acquired with 256 transients into 64 k data points over a spectral width of 260 ppm.

For 2D-NMR ^1H - ^1H COSY spectra, a second frequency dimension is introduced and magnetic interactions between nuclei through structural connectivity are further considered. The peaks that are mutually spin-spin coupled are shown by cross-peaks which are symmetrically placed about the spectral diagonal. The cross-peaks usually include geminally (two-bond) or vicinally (three-bond) coupled protons, but longer range couplings are not usually observed.

2.2.7. Elemental Analysis¹⁶

All samples analysed by elemental analysis were performed by Warwick Analytical Service using an Exeter Analytical elemental analyser (CE440).

2.2.8. Electrospray ionization-Mass Spectrometry (ESI-MS)¹⁷

Agilent 6130B single Quad (ESI) mass spectrometer was used to generally record the positive and negative ion electrospray mass spectra with a positive ion range of 500-1000 m/z and a negative ion range of 50-

500 m/z. The samples were typically dissolved into methanol, deionised water or acetonitrile prior to analysis.

2.2.9. High resolution Mass Spectrometry (HRMS)¹⁸

HR-MS analysis was carried with Bruker MaXis plus Q-TOF mass spectrometer equipped with electrospray ionisation source. The mass spectrometer facility was operated in electrospray positive ion mode with a scan range 50-2,400 m/z. Source conditions were: end plate offset at -500 V; capillary at -4000 V; nebulizer gas (N₂) at 0.5 bar; dry gas (N₂) at 4 L/min; dry Temperature at 453 K. Ion transfer conditions were: ion funnel RF at 200 Vpp; multiple RF at 200 Vpp; quadrupole low mass set at 50 m/z; collision energy at 5.0 eV for MS and 10-20 eV for MS/MS, MS/MS isolation window 10; collision RF at 500-2000 Vpp; transfer time set at 50-150 μ s; pre-pulse storage time set at 5 μ s. Calibration was performed with sodium formate (10 mM) prior to analysis.

2.2.10. Electron Paramagnetic Resonance (EPR) Spectroscopy⁸

EPR spectra were recorded at room temperature on a Bruker EMX (X-band) spectrometer fitted with a cylindrical Tm110 mode cavity (Bruker 4103TM). Samples were contained in quartz capillary (I.D. 1.0 mm; O.D. 1.2 mm; Wilmad Labglass) sealed with T-BluTac®, Typically, the EPR spectrometer was set as: modulation amplitude 2.0 G, microwave power 0.63 mW, 1.0×10^5 receiver gain, conversion time 81.92 ms, time

constant 81.92 ms, sweep width 200 G, and a repeated number of 10 X-scans with a resolution in Y of 5. EPR spectra were analysed and simulated using EASYSPIN software.¹⁹

2.2.11. Microwave Reactor²⁰

A CEM Discover-SP microwave reactor was used to assist the synthesis of osmium dimer complexes with the following settings: maximum power = 150 W, maximum pressure = 250 PSI. Microwave radiation of 5 mins at 150 °C was used in the osmium dimer synthesis reactions.

2.2.12. pH Meters

The pH value was generally measured using Martini instruments Mi 150 pH/Temperature bench meter with a Mettler-Toledo U402-M3-S7/200 chloride pH probe. In the pK_a measurements by NMR, the pH values of samples were specifically measured by a portable HACH H138 minilab instrument. The pH meters were calibrated using 3 buffer solutions: pH 4.01 ± 0.02 , 7.00 ± 0.02 , and 10.01 ± 0.02 . The probe was washed between measuring samples with methanol and deionised water, and stored in 1 M KCl when not in use. All pH meter readings were recorded at room temperature (*ca.* 298 K). The electrode in the pH meters is glass electrode. The pH meter readings for D₂O solutions were recorded without the correction for the effect of deuterium on the glass electrode, and are termed pH*.

2.3. Methods

2.3.1. Products Purified by Flash Chromatography

Complexes were purified using a Biotage Isolera instrument using Biotage[®] KP-Sil 10g SNAP cartridges. The mobile phase consisted of: (A) dichloromethane and (B) methanol. The crude products mixing with ISOLUTE HM-N granules were introduced onto the top of the column. The solvent gradient in **Table 2.1** was used with a 12 mL/min flow rate. The collected fractions were analysed by ESI-MS and the chosen fractions were then combined. The solvent was removed under reduced pressure.

Table 2.1. The solvent B (methanol) gradient for products purified by flash chromatography.

Start % (B)	End % (B)	Column volumes
0	0	10
0	10	20
10	50	20-50
50	50	20
50	0	10

2.3.2. Products Purified by HPLC

The HPLC instrument equipped with semi-preparative ZORBAX Eclipse XDB-C18 250 × 9.4 mm column was used to purify products. Mobile

phases consisted of: (A) H₂O with 0.1 % TFA, and (B) MeCN with 0.1 % TFA at 2 mL/min. The solvent gradient in **Table 2.2** was applied as the purification method. The samples were analysed at a detection wavelength of 254 nm with reference wavelengths set to 360 nm and 510 nm.

Table 2.2. The solvent B (acetonitrile) gradient for products purified by HPLC.

Time	% (B)
0	20
30	60
31	80
40	80
41	20
50	20

2.3.3. Samples Analysed by HPLC

HPLC instrument with Agilent ZORBAX Eclipse Plus C18 250×4.6 mm column was used to analyse the samples and reactions in this thesis. Mobile phases consisted of: (A) H₂O with 0.1 % TFA, and (B) MeCN with 0.1 % TFA at 2 mL/min. Due to the different polarity of organo-osmium bearing azo ligands and imino ligands, the solvent gradient methods are different for these two kinds of complexes. Osmium imino complexes were analysed at a detection wavelength of 254 nm with

reference wavelengths set to 360 nm and 510 nm while osmium azo complexes were analysed at 610 nm with a reference wavelength set to 360 nm.

Table 2.3. The solvent B (acetonitrile) gradient used in HPLC for analysing osmium azo and imino complexes.

Time (min)	% (B) for azo complexes	% (B) for imino complexes
0	10	20
30	80	60
40	80	60
41	10	20
55	10	20

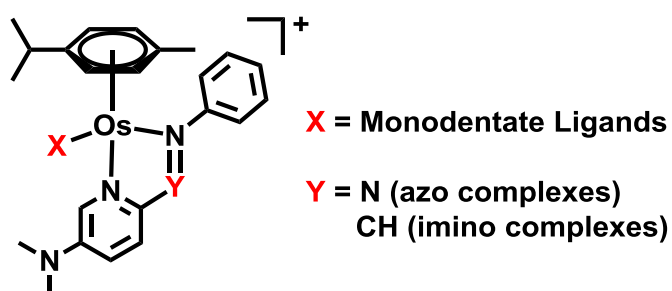


Figure 2.2. The molecular structure of osmium imino and azo complexes analysed by HPLC in this thesis.

2.3.4. N₂ Protection Reactions

There were some studies of synthesis and analysis in this thesis needed to be protected from air by N₂. A two-neck flask used for the reactions was dried, vacuumed and refilled with N₂. A balloon filled with N₂ was connected to the reaction atmosphere through a syringe needle and

protected the reaction. The solvents for the reactions were generally prepared by bubbling with N_2 for a period of 30 min.

The N_2 -protected NMR experiments were carried out using a specific NMR tube with a screw cap. The solids for experiments were transferred into this NMR tube first and then the tube was put into a long two-neck glass flask. A vacuum pump was used to remove the air from both the NMR tube and long glass flask, then N_2 was refilled back to the system. After repeating three times, the NMR solvent was added and NMR tube cap was screwed while the N_2 flow continued.

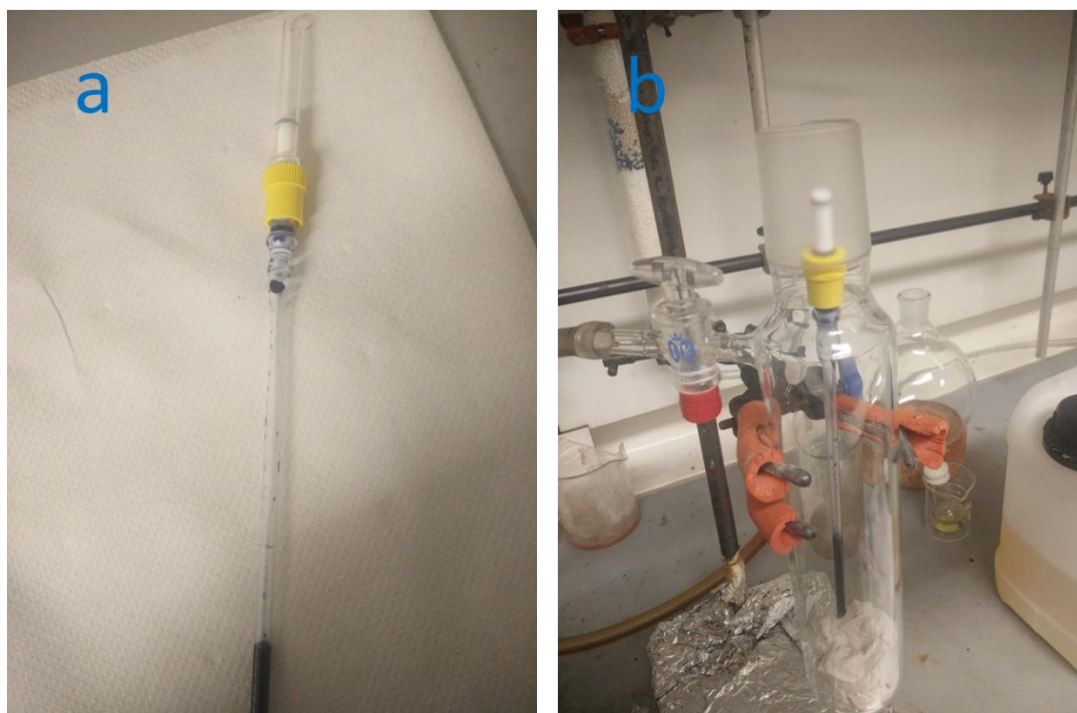


Figure 2.3. The specific NMR tube (a) and long two-neck flask for N_2 -protection NMR experiments.

2.3.5. pK_a Measurements

A 2 mM solution of complex for pK_a measurements was prepared in D₂O, and 4 mM dioxane was added as NMR standard reference (¹H chemical shift value 3.75 ppm).²¹ The solution was aliquoted into 8 samples of 600 μL and the pH* values were adjusted sequentially by adding 1-10 μL of either KOD or DNO₃ (0.01, 0.1, 1, 2, 3, 4, 6, 8 or 10 M) in D₂O. The pH value was measured over a range of 1.5 - 13.5 using a pH meter with correction for the effect of deuterium on the glass electrode. Changes in the chemical shifts of protons in the complex were followed by ¹H NMR analysis, and pH* values were corrected by equation: pH = 0.929pH* + 0.4.¹ The chemical shifts *versus* pH values were fitted to the Henderson-Hasselbalch equation (**equation 1**)^{22,23} using Origin 9.0 with the assumption that the observed chemical shifts are weighted averages of the populations of the protonated and deprotonated forms. The pK_a value is the pH value corresponding to exactly one-half of the HA is dissociated.

$$\delta_{\text{obs}} = \delta_{\text{HA}} [\text{HA}] + \delta_{[\text{A}^-]} [\text{A}^-] / ([\text{HA}] + [\text{A}^-]) \quad (\text{equation 1})$$

where δ_{obs} is the observed chemical shift, δ_{HA} is the limiting chemical shift of the fully protonated form and $\delta_{[\text{A}^-]}$ is the limiting chemical shift of the deprotonated form.

2.3.6. X-ray Absorption Spectroscopy

X-ray absorption (XAS) experiments at the Os L₃-edge (10871 eV) were performed at the BM23 beamline of the European Synchrotron Radiation Facility (ESRF, Grenoble, France).²⁴ XAS experiments were conducted in transmission mode, using a Si(111) double crystal monochromator to select the incident X-ray energy. The intensity of the incident beam I_0 and the beam transmitted through the sample (I_1) and a reference Hf metal foil (I_2) was monitored by 30 cm ionization chambers. The liquid samples were filled in a 4-mm thick EXAFS cell and solid samples were compressed to a solid pie. Such setup allowed a precise energy calibration for each collected XAS spectrum. For the analysis of data, energy calibration and alignment, normalization to the edge jump, and extraction of the $\chi(k)$ functions for all the collected spectra was also performed by Dr. Elisa Borfecchia (Università degli Studi di Torino, Italy) using the Athena program.²⁵ Spectra fitting was performed by Dr. Elisa Borfecchia (Università degli Studi di Torino, Italy) using the Artemis software.²⁶ More details related to individual experiments can be found in **Section 6.2.2 of Chapter 6**.

2.3.7. Density Functional Calculations

All the computational calculations were carried out by Prof. Emilia Sicilia (Università della Calabria, Italy). Gaussian 09 program has been employed to carry out all calculations in the framework of the density functional theory using the hybrid Becke three-parameter exchange functional²⁷ and the Lee–Yang–Parr correlation functional, B3LYP.²⁸ Dispersion corrections for non-bonding interactions have been included through the Grimme approach using atom pair-wise additive schemes,²⁹ i.e. the DFT-D3 method.

LANL2DZ effective core potential has been used for the Os atom,³⁰ along with the split valence basis set. The standard triple- ζ quality 6-311+G** basis sets of Pople and co-workers have been used for the atoms directly participating in the process, whereas in order to reduce the computational effort, the 6-31G* basis sets have been employed for peripheral atoms. Vibrational frequencies at the same level of theory have been calculated for both establishing the nature of intercepted stationary points as minima and transition states and calculating zero-point energy (ZPE) and Gibbs free energy corrections. The intercepted transition states are first order saddle points on a potential energy surface (PES) and their vibrational spectrum was characterized by one imaginary frequency, corresponding to a negative force constant, which indicates that in one direction, in the

nuclear configuration space, the energy has a maximum, while in all the other directions the energy has a minimum. Furthermore, transition states have been carefully checked to be properly connected to the correct minima by IRC (intrinsic reaction coordinate) analysis.^{31,32}

The Tomasi's implicit Polarizable Continuum Model (PCM)^{33,34} as implemented in Gaussian 09 has been used to include the effects arising from the presence of the solvent and the UFF set of radii has been used to build-up the cavity in which the solute molecules are accommodated. Solvation Gibbs free energies have been calculated performing single-point calculations for all *in vacuum* stationary points structures in implicit water ($\epsilon = 78.4$) at the same level of theory. Enthalpies and Gibbs free energies have been obtained using standard statistical procedures³⁵ at 298 K and 1 atm from total energies, including zero-point, thermal and solvent corrections. As the free energy corrections in the Gaussian's default standard state corresponds to an ideal gas at a standard pressure of 1 atm, the computed free energies have been converted³⁶ to yield Gibbs energies with a solution phase standard state of 1 mol L⁻¹ for all the species, except the water solvent. For water molecules a standard state of 55.5 M has been used. That is, to the free energy of each species, as computed in Gaussian, a free energy correction term equal to $RT \ln(V_{\text{molar gas}}/V_{\text{molar solution}})$, (R = gas constant, T = absolute temperature) has been

added, where $V_{\text{molar gas}}$ is the volume occupied by one mole of ideal gas at the considered temperature, and $V_{\text{molar solution}}$ is the volume occupied by one mole of species in a standard solution of concentration 1 mol L^{-1} .

2.3.8. Cell Seed and Passage

Cells were generally seeded by Dr. Isolda Romero-Canelón (The University of Warwick) in T-75 or T-175 culture flasks as adherent monolayers and passaged 2-3 times per week whenever confluence reached 80-90%, using 0.25% trypsin for A2780 digestion or 0.25% trypsin/EDTA for all other cell line digestions. The environment for cell growth was in an incubator pre-set at 310 K with a 5% CO_2 humidified atmosphere. The cell culture media were composed of Dulbecco's Modified Eagle Medium (DMEM), phosphate buffered saline, L-glutamine, penicillin / streptomycin, fetal bovine serum.

2.3.9. *In vitro* growth inhibition assay

The cells used in experiments were normally between 5 and 25 numbers of passages. Approximately 5000 cancer cells was seeded per well in 96-well plates, and grown at 310 K for 24 h, after which cell media containing various gradient concentrations of osmium complexes was

used to replace the drug-free media in each well, and cells were exposed to complexes for a period of 24 h at 310 K. Then the supernatant in each well was removed and the survival cell was washed by phosphate-buffered saline (PBS) and recovered for 72 h at 310 K. The cell viability was determined by SRB (Sulforhodamine B) assay,³⁷ in which absorbance measurements of the solubilised dye (BioRad iMark microplate reader, 470 nm filter) allowed the determination of viable treated cells and which were then compared to untreated controls. IC₅₀ values (the concentration of complexes required to cause 50% cell death) were determined as triplicates of duplicates for each complex. ICP-OES was used to measure the Os contents of initial stock solutions of osmium complexes.

2.4. References

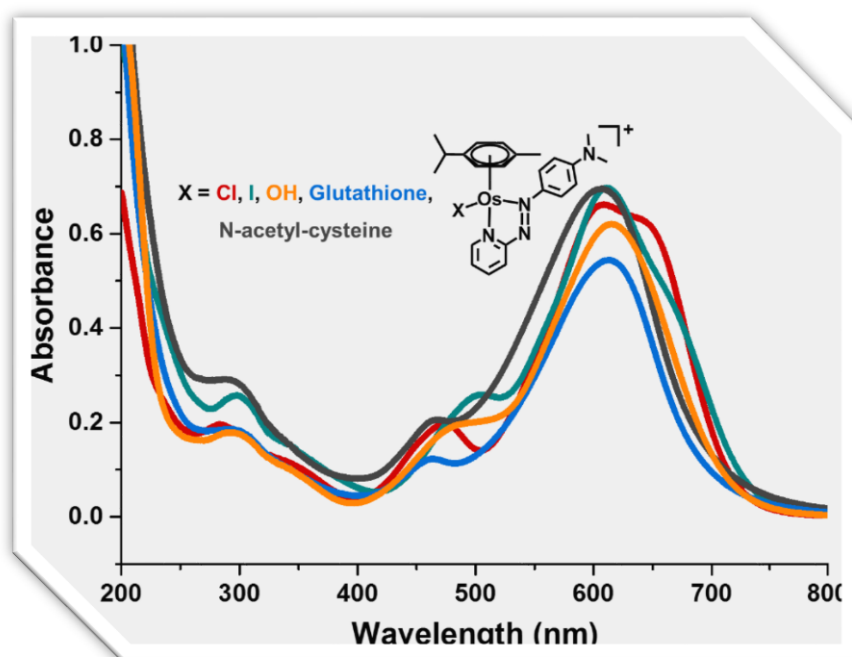
- (1) Krężel, A.; Bal, W. *J. Inorg. Biochem.* **2004**, 98, 161.
- (2) Stoll, V. S.; Blanchard, J. S. *Methods Enzymol.* **1990**, 182, 24.
- (3) Arthur, T.; Stephenson, T. A. *J. Organomet. Chem.* **1981**, 208, 369.
- (4) Peacock, A. F. A.; Habtemariam, A.; Moggach, S. A.; Prescimone, A.; Parsons, S.; Sadler, P. J. *Inorg. Chem.* **2007**, 46, 4049.
- (5) Stahl, S.; Werner, H. *Organometallics* **1990**, 9, 1876.
- (6) Misra, P.; Dubinskii, M. A. *Ultraviolet spectroscopy and UV lasers*; CRC Press: New York, NY, 2002.
- (7) Olesik, J. W. *Anal. Chem.* **1996**, 68, 469A.
- (8) Roessler, M. M.; Salvadori, E. *Chem. Soc. Rev.* **2018**, 47, 2534.
- (9) Klose, M. H. M.; Hejl, M.; Heffeter, P.; Jakupec, M. A.; Meier-Menches, S. M.; Berger, W.; Keppler, B. K. *Analyst* **2017**, 142, 2327.
- (10) Venzago, C.; Popp, M.; Kovac, J.; Kunkel, A. *J. Anal. At. Spectrom.* **2013**, 28, 1125.
- (11) Profrock, D.; Prange, A. *Appl. Spectrosc.* **2012**, 66, 843.
- (12) Snyder, L. R. *Anal. Chem.* **2000**, 72, 412 A.
- (13) Korfmacher, W. A. *Drug Discov. Today* **2005**, 10, 1357.
- (14) Bovey, F. A.; Mirau, P. A.; Gutowsky, H. S. *Nuclear magnetic resonance spectroscopy*; Academic Press: New York, NY, 1988.

- (15) Gottlieb, H. E.; Kotlyar, V.; Nudelman, A. *J. Org. Chem.* **1997**, *62*, 7512.
- (16) Cook, R. D.; Malkus, D. S.; Plesha, M. E.; Witt, R. J. *Concepts and applications of finite element analysis*; Wiley: New York, 1974.
- (17) Keith-Roach, M. J. *Anal. Chim. Acta* **2010**, *678*, 140.
- (18) Xian, F.; Hendrickson, C. L.; Marshall, A. G. *Anal. Chem.* **2012**, *84*, 708.
- (19) Stoll, S.; Schweiger, A. *J. Magn. Reson.* **2006**, *178*, 42.
- (20) Priecel, P.; Lopez-Sanchez, J. A. *ACS Sustain. Chem. Eng.* **2019**, *7*, 3.
- (21) Wishart, D. S.; Bigam, C. G.; Yao, J.; Abildgaard, F.; Dyson, H. J.; Oldfield, E.; Markley, J. L.; Sykes, B. D. *J. Biomol. NMR* **1995**, *6*, 135.
- (22) Po, H. N.; Senozan, N. M. *J. Chem. Educ.* **2001**, *78*, 1499.
- (23) Soldevila-Barreda, J. J.; Habtemariam, A.; Romero-Canelón, I.; Sadler, P. J. *J. Inorg. Biochem.* **2015**, *153*, 322.
- (24) Mathon, O.; Beteva, A.; Borrel, J.; Bugnazet, D.; Gatla, S.; Hino, R.; Kantor, I.; Mairs, T.; Munoz, M.; Pasternak, S. *J. Synchrotron Radiat.* **2015**, *22*, 1548.

- (25) Salassa, L.; Borfecchia, E.; Ruiu, T.; Garino, C.; Gianolio, D.; Gobetto, R.; Sadler, P. J.; Cammarata, M.; Wulff, M.; Lamberti, C. *Inorg. Chem.* **2010**, *49*, 11240.
- (26) Ravel, B.; Newville, M. *J. Synchrotron Radiat.* **2005**, *12*, 537.
- (27) Becke, A. D. *J. Chem. Phys.* **1993**, *98*, 5648.
- (28) Lee, C.; Yang, W.; Parr, R. G. *Phys. Rev. B* **1988**, *37*, 785.
- (29) Grimme, S.; Antony, J.; Ehrlich, S.; Krieg, H. *J. Chem. Phys.* **2010**, *132*, 154104.
- (30) Dunning, T. H.; Hay, P. J. In *Modern theoretical chemistry*; Plenum Press: New York, NY, 1977; Vol. 3, p 1.
- (31) Fukui, K. *J. Phys. Chem.* **1970**, *74*, 4161.
- (32) Gonzalez, C.; Schlegel, H. B. *J. Chem. Phys.* **1989**, *90*, 2154.
- (33) Miertuš, S.; Scrocco, E.; Tomasi, J. *Chem. Phys.* **1981**, *55*, 117.
- (34) Pascual-ahuir, J.-L.; Silla, E.; Tunon, I. *J. Comput. Chem.* **1994**, *15*, 1127.
- (35) McQuarrie, D. A.; Simon, J. D. *Molecular Thermodynamics. University Science Books, Sausalito, CA* **1999**, 581.
- (36) Ashcraft, R. W.; Raman, S.; Green, W. H. *J. Phys. Chem. B* **2007**, *111*, 11968.
- (37) Vichai, V.; Kirtikara, K. *Nat. Protoc.* **2006**, *1*, 1112.

Chapter 3

Synthesis and Characterisation of Os^{II} Arene Complexes



3.1. Introduction

The serendipitous discovery and success of cisplatin greatly stimulated the development of metal-based anticancer drugs. In recent years, many anticancer metallodrugs, such as Ru(III), Ru(II), Ir(II), Os(II) complexes, have been reported to display high potency with novel mechanism of action.¹⁻⁵ Half-sandwich osmium (II) arene complexes, following [Os(η^6 -*p*-cymene)(2-(phenylazo)pyridine)Cl/I]PF₆ (**1-Cl/I•PF₆**) as the basic template, have been developed (**Figure 3.1**),⁶ and the lead complex [Os(η^6 -*p*-cymene)(4-(2-pyridylazo)-*N,N*-dimethylaniline)I]PF₆ (**2-I•PF₆**, also known as **FY26**) exhibits a 49-fold higher cytotoxicity than cisplatin itself towards 809 cancer cell lines.⁷ More promisingly, [**2-I**]⁺ still maintains cytotoxicity to cisplatin-resistant cancer cells and significantly delays the growth of HCT116 human colon cancer xenografts in mice.⁸ In a previous study, [**2-I**]⁺ was radio-labelled with the β^-/γ emitter, ¹³¹I (*t*_{1/2} 8.02 d), and cellular accumulation of the tracer complex, [**2-¹³¹I**]⁺, in MCF-7 breast cancer cells was explored *in vitro*. The tracer complex is stable in cell culture media, but once taken up by MCF-7 cells, 99% of [**2-¹³¹I**]⁺ lost the radio-iodide ligand after 24 h, which was observed in the supernatants in the form of free iodide.⁹ Free thiols, such as GSH and cysteine, were found to play crucial roles in this process and activate the hydrolysis of [**2-I**]⁺.⁹ Based on these interesting findings, the mechanism

of action of **[2-I]⁺**, especially the reaction of **[2-I]⁺** with GSH, is explored in this thesis.

In this **Chapter 3**, several key complexes (**Figure 3.1**) related to the reaction of **[2-I]⁺** with GSH were synthesised, including the lead complex **2-I•PF₆**, the chlorido analogue **2-Cl•PF₆**, the nitrate analogue **2-NO₃•PF₆**, the hydroxido analogue **[2-OH]⁺** (solution), the glutathione adduct **2-SG** and the N-acetyl cysteine adduct **2-NAC**. Meanwhile, the non-substituted basic template complex **1-Cl•PF₆**, imino analogue **2-imp_y-I•PF₆**, **2-imp_y-Cl•PF₆** were also prepared for comparison with lead complex **2-I•PF₆**. These osmium complexes were characterized by ¹H NMR, high resolution mass spectrometry (HRMS) and CHN elemental analysis.

The pK_a value of **[2-OH₂]²⁺** was determined to understand which species (**[2-OH]⁺** or **[2-OH₂]²⁺**) predominates under physiological conditions due to Henderson–Hasselbalch equation. The cytotoxicity of **[2-OH]⁺**, **2-SG** and **2-NAC** towards cancer cells was tested for comparing with lead complex **[2-I]⁺**. The UV-vis spectra of these osmium complexes in aqueous solution were acquired and their extinction coefficients were determined using accurate concentrations of osmium obtained from inductively coupled plasma-optical emission spectrometry (ICP-OES). Time-dependent density functional theory calculations (TD-DFT) for these complexes were carried out by Prof. Emilia Sicilia (Università della

Calabria, Italy) to assist with assignment of electronic absorption bands. Moreover, the HPLC retention times on high performance liquid chromatography (HPLC), and high resolution mass spectrometry (HRMS) identification of complexes **2-I•PF₆**, **2-Cl•PF₆**, **2-imp-Cl•PF₆**, **2-imp-I•PF₆**, **[2-OH]⁺**, **2-SG**, **2-NAC** were standardised. HPLC and LC-MS are very powerful tools to explore reactions and widely used in this thesis. However, it is difficult to quantify each species observed by HPLC considering the difference of extinction coefficients for different molecules. In order to solve this problem and quantitatively analyse reactions of osmium complexes, a simple but very sensitive method was applied combining HPLC peak area integration and ICP-OES determination. The proportionality between peak area on HPLC trace and concentrations of these osmium complexes was established.

Overall, the work in this **Chapter 3** includes synthesis of key complexes, pK_a measurements, electronic spectra acquisition, extinction coefficient determination, HPLC retention times and mass spectrometry identification, HPLC peak area and concentration quantitation. These experimental results provide the basis for quantitative studies of osmium complexes in reactions with GSH in the following **Chapter 4**, and contribute to the overall aim of exploring the mechanism of action of anticancer osmium complexes in this thesis.

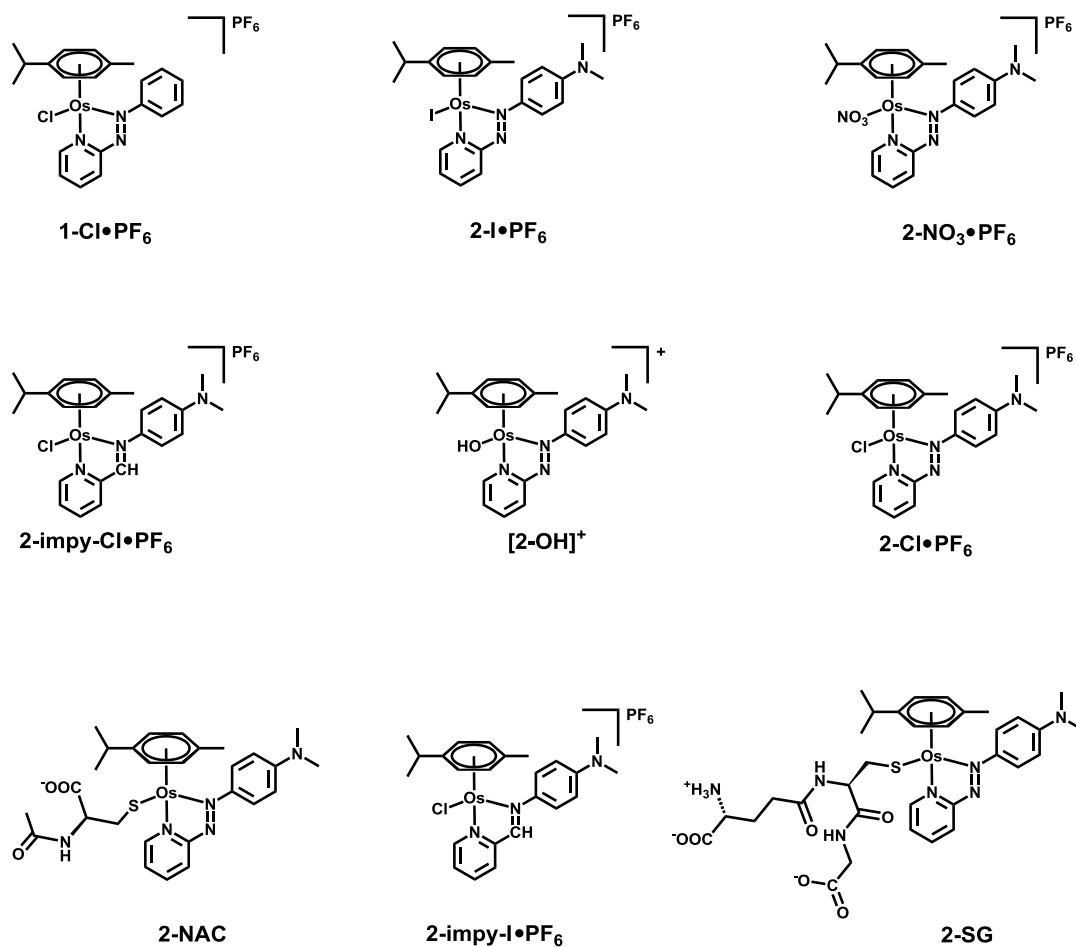


Figure 3.1. The structures of osmium(II) complexes synthesised in this chapter.

3.2. Experimental Section

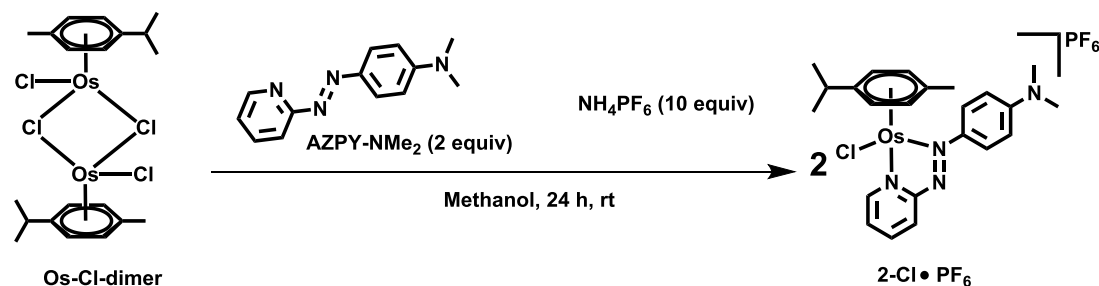
3.2.1. Materials

Osmium dimers ($[\text{Os}(\eta^6\text{-}p\text{-cym})\text{X}_2]_2$, where X = Cl or I) were prepared using reported procedures¹⁰ as described in **Chapter 2**. Reduced glutathione (**GSH**), N-acetyl-L-cysteine (**NAC**) and silver nitrate were purchased from Sigma Aldrich. Pyridine-2-azo-*p*-dimethylaniline (**AZPY-NMe₂**) was purchased from Alfa Aesar. The non-substituted ligand pyridine-2-phenyldiazenyl (**AZPY**) and imino ligand pyridine-2-imino-*p*-dimethylaniline, (**IMPY-NMe₂**) were synthesized using reported procedures.^{11,12} Sodium hydroxide, sodium chloride, sodium phosphate dibasic (Na_2HPO_4), sodium phosphate monobasic ($\text{H}_2\text{NaPO}_4 \cdot 2\text{H}_2\text{O}$) and trifluoroacetic acid were purchased from Fisher Scientific. All other solvents and reagents for synthesis and analysis were purchased from commercial suppliers and used as received.

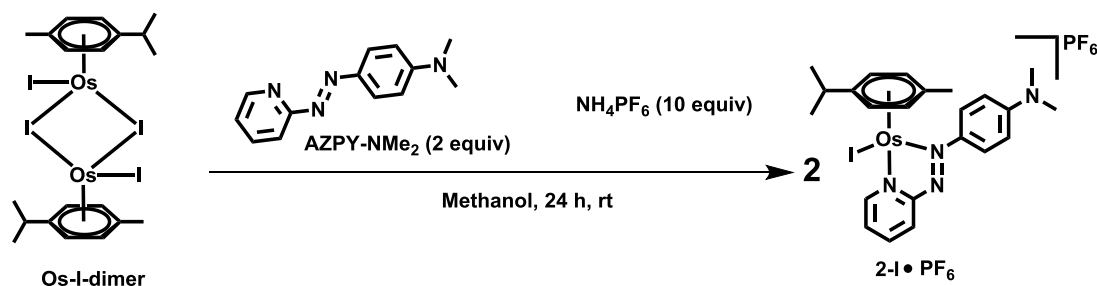
3.2.2. Instrumentation

The instrumentation used in this chapter including UV-vis, NMR, HPLC, LC-MS, CHN elemental analysis, ICP-OES, HRMS, microwave reactor, flash chromatography product purification instrument are fully described in **Chapter 2**.

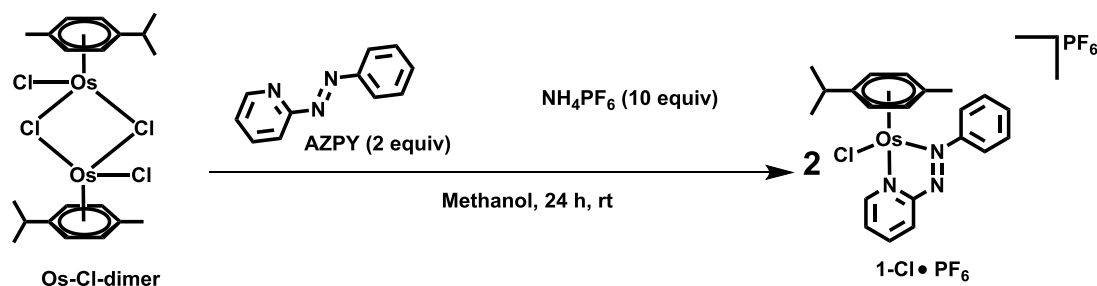
3.2.3. Synthesis of Complexes

[Os(η^6 -*p*-cymene)(AZPY-NMe₂)Cl]PF₆ (2-Cl•PF₆)

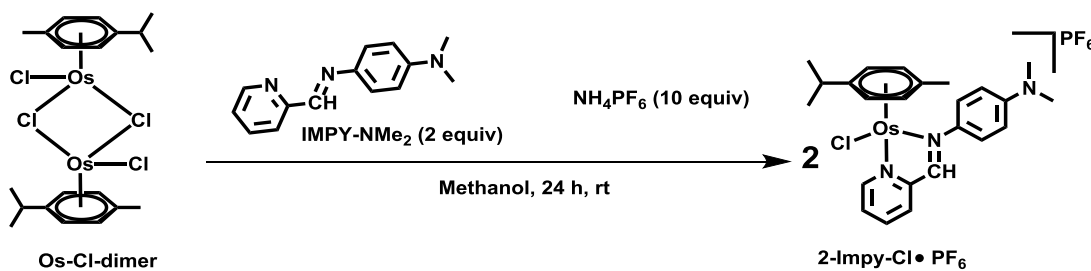
Following a previously reported protocol,⁶ to a stirred solution of [Os(η^6 -*p*-cymene) Cl₂]₂ (158.7 mg, 0.2 mmol) in methanol (10 mL), AZPY-NMe₂ (90.4 mg, 0.4 mmol) in methanol (5 mL) was added drop wise and the colour changed from orange to dark blue immediately. The solution was stirred at ambient temperature for a period of 24 h. Ammonium hexafluorophosphate (326.7 mg, 2.0 mmol) was then added. The volume was reduced to ~5 mL, then was placed in a freezer (*ca.* 268 K) overnight. A deep-blue coloured precipitate was collected *via* vacuum filtration and washed with ice-cold ethanol (2 × 1 mL), diethyl ether (2 × 5 mL), and dried overnight in a vacuum desiccator. Yield: 260.3 mg (94.3 %). HMRS calculated for [2-Cl]⁺ (C₂₃H₂₈ClN₄Os⁺) *m/z* 587.1602, found *m/z* 587.1594. ¹H NMR (CD₃OD) with 400 MHz: δ = 9.06 (d, 1H, *J* = 5.9 Hz), 8.58 (d, 1H, *J* = 8.0 Hz), 8.30-8.24 (m, 3H), 7.71 (m, 3H), 6.59 (d, 1H, *J* = 6.1 Hz), 6.32-6.26 (m, 3H), 2.80 (s, 6H), 2.48-2.46 (m, 1H), 2.45 (s, 3H), 0.98 (d, 3H, *J* = 6.9 Hz), 0.94 ppm (d, 3H, *J* = 6.9 Hz).

[Os(η^6 -*p*-cymene)(AZPY-NMe₂)I]PF₆ (2-I•PF₆)

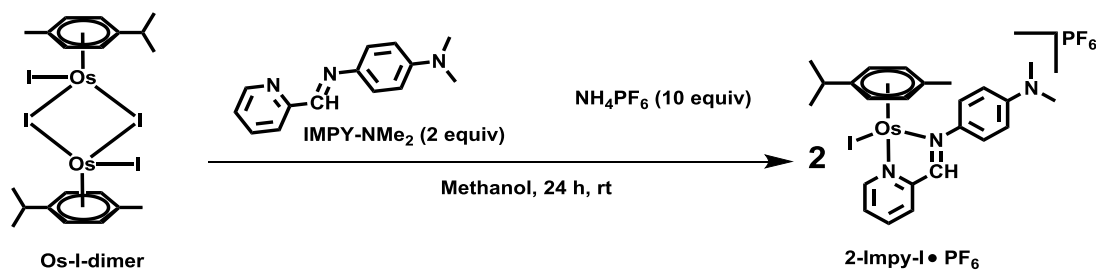
Following a previously reported protocol,⁶ to a stirred solution of [Os(η^6 -*p*-cymene) I₂]₂ (232.6 mg, 0.2 mmol) in methanol (10 mL), AZPY-NMe₂ (90.4 mg, 0.4 mmol) in methanol (5 mL) was added drop wise and the colour of the solution changed from orange to dark blue. The solution was stirred at ambient temperature for 24 h, then ammonium hexafluorophosphate (326.7 mg, 2.0 mmol) was added. The volume was then reduced to ~5 mL with rotary evaporator and then the solution was placed in a freezer (*ca.* 268 K) overnight. A deep-blue precipitate was collected *via* vacuum filtration and washed with ice-cold ethanol (2 × 1 mL), diethyl ether (2 × 5 mL), and dried overnight in a vacuum desiccator. Yield: 282.6 mg (85.8 %). HMRS calculated for [2-I]⁺ (C₂₃H₂₈IN₄Os⁺) *m/z* 679.0969, found *m/z* 679.0952. ¹H NMR (CD₃OD) with 400 MHz: δ = 9.43 (d, 1H, *J* = 6.0 Hz), 8.64 (d, 1H, *J* = 8.0 Hz), 8.30-8.22 (m, 3H), 7.65 (m, 1 H), 6.96 (d, 2H, *J* = 8.9 Hz), 6.59 (d, 1H, *J* = 6 Hz), 6.29 (m, 3H), 3.41 (s, 3H), 2.80 (s, 6H), 2.62-2.56 (m, 1H), 1.03 (d, 3H, *J* = 6.9 Hz), 0.98 (d, 3H, *J* = 6.9 Hz).

[Os(η^6 -*p*-cymene) (AZPY) Cl]PF₆ (1-Cl**•PF₆)**

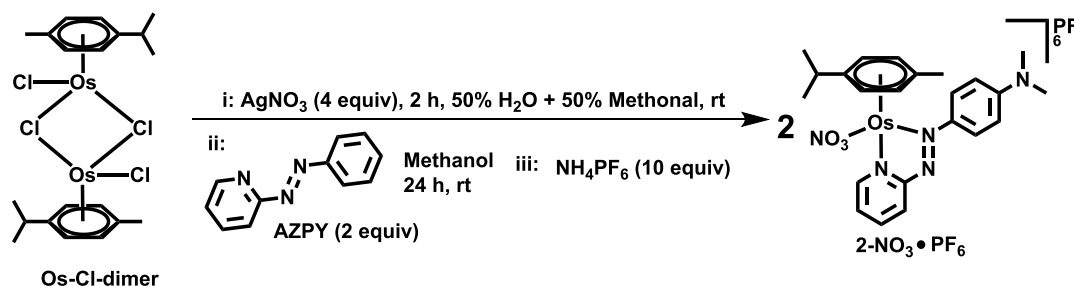
Following a previously reported protocol,⁶ to a stirred solution of [Os(η^6 -*p*-cymene) Cl₂]₂ (158.7 mg, 0.2 mmol) in 10 mL methanol, AZPY (73.3 mg, 0.4 mmol) in methanol (5 mL) was added drop wise, and the colour changed from orange to brown. The solution was stirred at ambient temperature for 24 h, then ammonium hexafluorophosphate (326.7 mg, 2.0 mmol) was added. The volume was reduced to 5 mL using rotary evaporator and then the solution was placed in a freezer (ca. 268 K) overnight. A dark-coloured precipitate was collected *via* vacuum filtration and washed with ice-cold ethanol (2 × 1 mL), diethyl ether (2 × 5 mL), and dried overnight in vacuo. Yield: 198.1 mg (81.2 %). HMRS calculated for [**1-Cl**]⁺ (C₂₁H₂₃ClN₃Os⁺) *m/z* 544.1195, found *m/z* 544.1198. ¹H NMR (CD₃OD) with 400 MHz: δ = 9.65 (d, 1H, *J* = 5.9 Hz), 9.01 (d, 1H, *J* = 8.9 Hz), 8.50-8.48 (m, 1H), 8.16 (d, 2H, *J* = 8.0 Hz), 8.01-7.99 (m, 1H), 7.77 (m, 3H), 6.79 (d, 1H, *J* = 6.1 Hz), 6.39 (d, 1H, *J* = 5.9 Hz), 6.32 (m, 2H), 2.54 (m, 1H), 2.44 (s, 3H), 1.01 (d, 3H, *J* = 6.9 Hz), 0.96 ppm (d, 3H, *J* = 6.9 Hz).

[Os(η^6 -*p*-cymene)(IMPY-NMe₂)Cl]PF₆ (2-Impy-Cl•PF₆)

Following a previously reported protocol,⁵ to a stirred solution of [Os(η^6 -*p*-cymene) Cl₂]₂ (158.7 mg, 0.2 mmol) in methanol (10 mL), IMPY-NMe₂ (90.4 mg, 0.4 mmol) in methanol (5 mL) was added drop wise. The colour changed from orange to red. The solution was stirred at ambient temperature for 24 h, then ammonium hexafluorophosphate (326.7 mg, 2.0 mmol) was added. The volume was reduced to 5 mL using rotary evaporator, the solution was left in a freezer (*ca.* 268 K) for overnight. A red precipitate was collected *via* vacuum filtration and washed with ice-cold ethanol (2 × 1 mL), diethyl ether (2 × 5 mL), and dried overnight in a vacuum desiccator. Yield 223.4 mg (80.5 %). HMRS calculated for [2-Impy-Cl]⁺ (C₂₄H₂₉ClN₃Os⁺) *m/z* 586.1649, found 586.1633. ¹H NMR(CD₃OD) with 400 MHz: δ = 9.56 (d, 1H, *J* = 4.9 Hz), 9.20 (s, 1 H), 8.46 (d, 1H, *J* = 6.9 Hz), 8.32 (t, 1H, *J* = 7.2 Hz), 7.82 (t, 1H, *J* = 6.0 Hz), 7.76 (d, 2H, *J* = 9.0 Hz), 6.91 (d, 2H, *J* = 9.1 Hz), 6.44 (d, 1H, *J* = 6.1 Hz), 6.04 (d, 1H, *J* = 5.9 Hz), 5.97 (d, 1H, *J* = 6.1 Hz), 5.85 (d, 1H, *J* = 6.2 Hz), 3.16 (s, 6H), 2.42 (s, 3H), 2.22-2.11 (m, 1H), 1.10 (d, 3H, *J* = 7.2 Hz), 1.07 ppm (d, 3H, *J* = 7.1 Hz).

[Os(η^6 -*p*-cymene)(IMPY-NMe₂)I]PF₆ (2-Impy-I•PF₆)

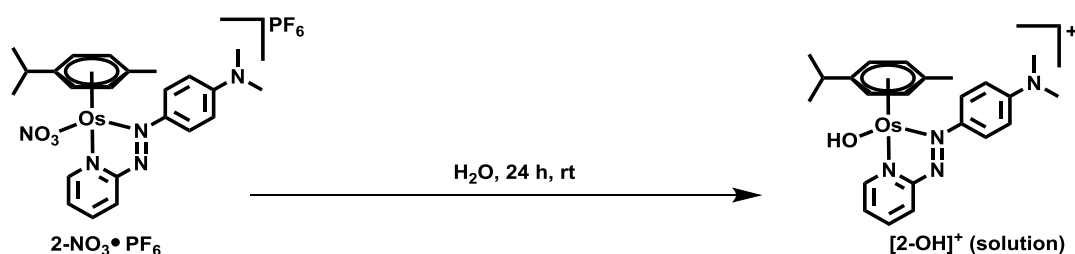
Following a previously reported protocol,⁵ to a stirred solution of [Os(η^6 -*p*-cymene) I₂]₂ (232.6 mg, 0.2 mmol) in methanol (10 mL), IMPY-NMe₂ (90.4 mg, 0.4 mmol) in methanol (5 mL) was added drop wise. The colour of the solution changed from orange to red. The solution was stirred at ambient temperature for 24 h. Ammonium hexafluorophosphate (326.7 mg, 2.0 mmol) was added. The volume was reduced to ~5 mL, then was placed in a freezer (ca. 268 K) overnight. A red precipitate was collected *via* vacuum filtration and washed with ice-cold ethanol (2 × 1 mL), diethyl ether (2 × 5 mL), and dried overnight in a vacuum desiccator. Yield 255.4 mg (77.6 %). HMRS calculated for [2-Impy-I]⁺ (C₂₄H₂₉IN₃Os⁺) *m/z* 678.1016, found 678.1028. ¹H NMR(CD₃OD) with 400 MHz: δ = 9.54 (d, 1H, *J* = 5.2 Hz), 9.13 (s, 1 H), 8.46 (d, 1H, *J* = 7.1 Hz), 8.25 (t, 1H, *J* = 7.3 Hz), 7.83 (d, 2H, *J* = 9.1 Hz), 7.74 (t, 1H, *J* = 4.9 Hz), 6.89 (d, 2H, *J* = 8.9 Hz), 6.38 (d, 1H, *J* = 6.0 Hz), 6.04 (d, 1H, *J* = 6.1 Hz), 5.92-5.87 (m, 2H), 3.15 (s, 6H), 2.65 (s, 3H), 2.21-2.13 (m, 1H), 1.09 (d, 3H, *J* = 5.9 Hz) 1.07 ppm (d, 3H, *J* = 6.1 Hz).

[Os(η^6 -*p*-cymene)(AZPY-NMe₂)NO₃]PF₆ (2-NO₃•PF₆)

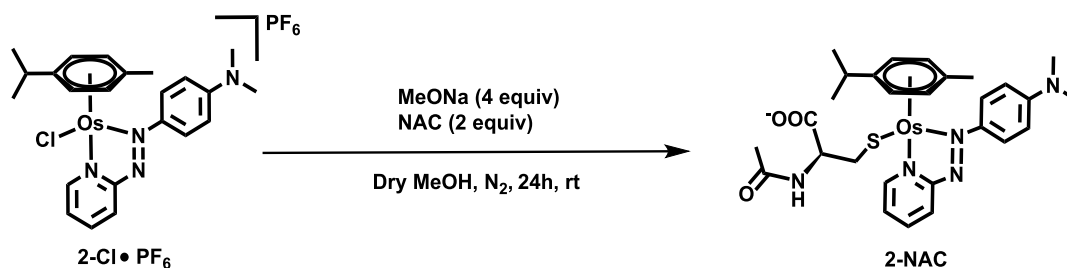
To a stirred solution of [Os(η^6 -*p*-cymene) Cl₂]₂ (158 mg, 0.2 mmol) in methanol (10 mL), AgNO₃ (136 mg, 0.8 mmol) in water (10 mL) was added. Then the solution was stirred 310 K for 2 h and generated white precipitate which was removed by filter. Then a solution of pyridine-2-azo-*p*-dimethylaniline (90.4 mg, 0.4 mmol) in methanol (5 mL) was added. The mixture was stirred for 18 h at ambient temperature. The volume of the solution was reduced to ~2 mL under reduced pressure and then ammonium hexafluorophosphate (326 mg, 2 mmol) was added, using ultrasonic to promote dissolution. The solution was left in a freezer (ca. 268 K) for overnight and a deep-blue precipitate was collected *via* vacuum filtration, washed with ice-cold ethanol (2×1 mL), diethyl ether (2 × 5 mL), and then dried overnight in a vacuum desiccator. Yield: 96 mg (40%). From HRMS, ¹H NMR and C H N analysis, the product was **2-NO₃•PF₆**. HRMS calculated for [2-NO₃]⁺ (C₂₃H₂₈N₅O₃Os⁺) m/z 614.1802, found: 614.1809. ¹H NMR (CD₃OD) with 400 MHz: δ = 9.45 (d, 1H, J = 5.2 Hz), 8.39 (d, 1H, J = 8.0 Hz), 8.30-8.24 (m, 3H), 7.60 (t,

1H, *J* = 7.1 Hz), 7.03 (d, 2H, *J* = 9.5 Hz), 6.59 (d, 1H, *J* = 5.9 Hz), 6.35 (d, 1H, *J* = 5.8 Hz), 6.20-6.00 (m, 2H), 3.43 (s, 6H), 2.39 (s, 3H), 2.30-2.20 (m, 1H), 0.95-0.82 (dd, 6H, *J* = 6.9 Hz). CHN analysis: calculated for C₂₃H₂₈F₆N₅O₃OsP (**2-NO₃•PF₆**): C, 36.46%; H, 3.72%; N, 9.24%. Found: C, 36.52%; H, 3.69%; N, 9.17%.

[Os(η⁶-*p*-cymene)(AZPY-NMe₂)OH]⁺ ([2-OH]⁺)



2-NO₃•PF₆ was dissolved into water and stirred for 24 h at ambient temperature. **[2-OH]⁺** solution with NO₃[−] was acquired. HRMS calculated for **[2-OH]⁺**(C₂₃H₂₉N₄OOs⁺): *m/z* 569.1951. Found: 569.1941. ¹H NMR(D₂O) with 400 MHz: δ = 9.23 (d, 1H, *J* = 5.7 Hz), 8.35 (d, 1H, *J* = 8.4 Hz), 8.14-8.21 (m, 3H), 7.60 (t, 1H, *J* = 6.6 Hz), 6.99 (d, 2H, *J* = 9.5 Hz), 6.38 (d, 1H, *J* = 5.7 Hz), 6.18-6.24 (m, 2H), 6.14 (d, 1H, *J* = 5.6 Hz), 3.39 (s, 6H), 2.35 (s, 3H), 2.20-2.12 (m, 1H), 0.85-0.70 (dd, 6H, *J* = 6.9 Hz).

Os (η^6 -*p*-cymene) (AZPY-NMe₂) N-acetyl-*L*-cysteine (2-NAC)

[Os (η^6 -*p*-cymene) (4-(2-pyridylazo)-*N,N*-dimethylaniline) Cl]PF₆ (**2-Cl•PF₆**) (146.2 mg, 0.2 mmol), MeONa (43.2 mg, 0.8 mmol) and N-acetyl-*L*-cysteine (65.2 mg, 0.4 mmol) was placed to 25 mL flask. The air in the flask was removed by fulfilling with dinitrogen. Dry methanol (10 mL) was injected into the flask and the solution was stirred at ambient temperature for 24 h with the protection of dinitrogen. Then the reaction mixture was filtered and the solvent was removed under reduced pressure. Flash chromatography was used to purify the product and a deep-blue solid was recovered and then dried in a vacuum desiccator. Yield 86.67 mg (50.9%). HRMS calculated for [**2-NAC** + **H**⁺]⁺ (C₂₈H₃₆N₅O₃SOs⁺): *m/z* 714.2147. Found: 714.2149. ¹H NMR (CD₃OD) with 400 MHz: δ = 9.15 (d, 1H, *J* = 5.7 Hz), 8.50 (d, 1H, *J* = 8.1 Hz), 8.12-7.94 (m, 3H), 7.5 (t, 1H, *J* = 6.6 Hz), 6.88 (d, 2H, *J* = 8.3 Hz), 6.33-6.29 (dd, 1H, *J* = 5.8 Hz), 6.10-6.04 (dd, 1H, *J* = 7.8 Hz), 5.90-5.82 (m, 2H), 4.02-3.95 (m, 1H), 3.28 (s, 6H), 2.49 (d, 3H, 5.6), 2.32-2.22 (m, 1H), 2.03-1.70 (m, 5H),

0.81-0.75 (m, 6H). CHN analysis: calculated for C₂₉H₄₀ClN₅Na₂O₅OsS

(**2-NAC** + **CH₃OH** + **NaCl** + **NaOH**): C, 42.17%; H, 4.72%; N, 8.20.

Found: C, 42.31%; H, 4.65%; N, 8.28.

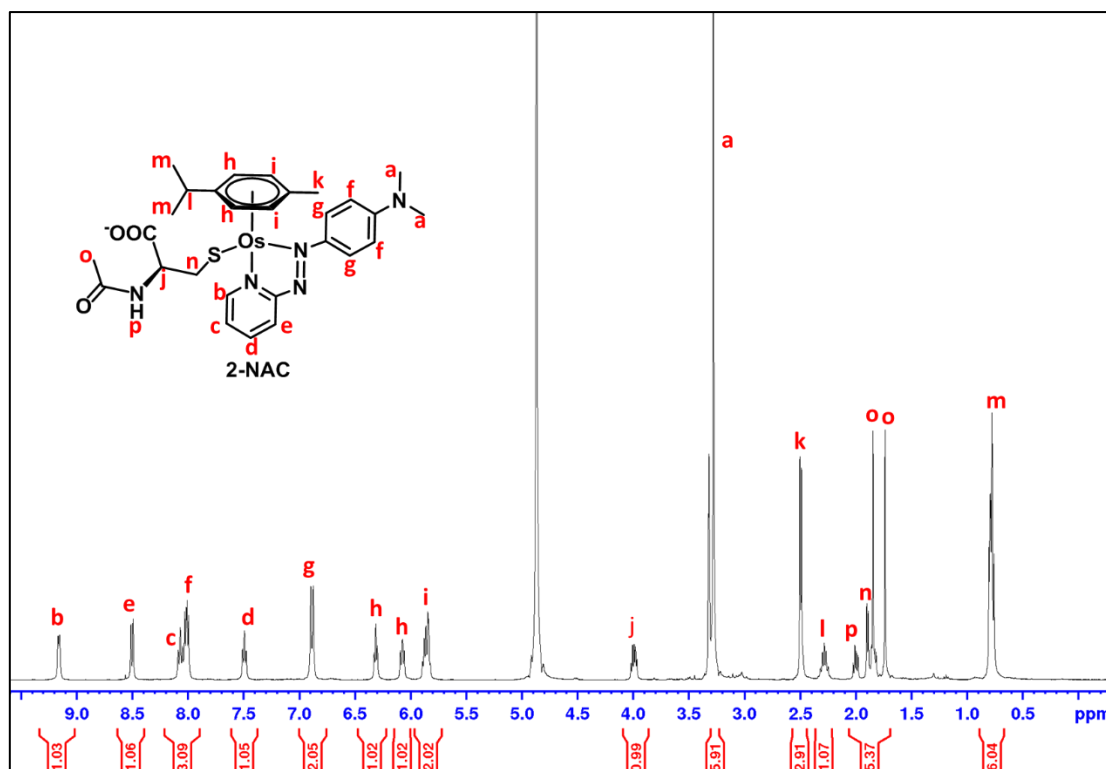
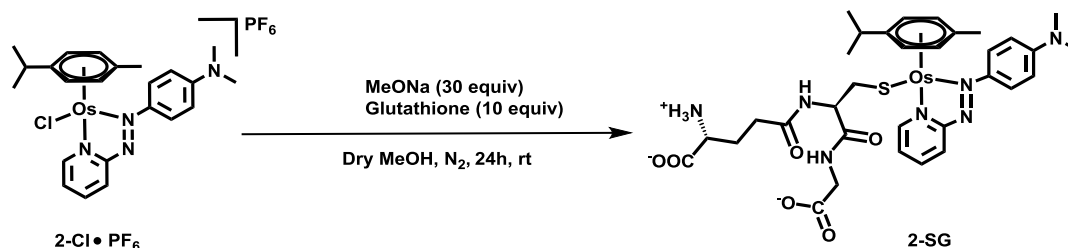


Figure 3.2. 400 MHz ¹H NMR spectrum of **2-NAC** in CD₃OD (The two sets of protons labelled with **O** may arise from different two diastereoisomers).

Os (η^6 -*p*-cymene) (AZPY-NMe₂) glutathione (2-SG)

[Os (η^6 -*p*-cymene) (4-(2-pyridylazo)-*N,N*-dimethylaniline) Cl] PF₆ (**2-Cl•PF₆**) (146.2 mg, 0.2 mmol), MeONa (324 mg, 6 mmol) and glutathione (γ -L-Glu-L-Cys-Gly) (614.4 mg, 2 mmol) were placed to a 25 mL flask. The air in the flask was removed by filling with dinitrogen. Dry methanol (10 mL) was then injected into the flask and the solution was stirred at ambient temperature for 24 h with the protection of dinitrogen. Then the reaction mixture was filtered and the solvent was removed under reduced pressure. Flash chromatography was then employed to purify the product and the deep-blue product was isolated and dried in a vacuum desiccator. Yield 106.56 mg (53.28%). HRMS calculated for [**2-SG** + **H**⁺] (C₃₃H₄₄N₇O₆OsS⁺): *m/z* 858.2682. Found: 858.2693. ¹H NMR (CD₃OD): δ = 9.20 (dd, 1H, *J* = 5.3 Hz), 8.52 (d, 1H, *J* = 8.9 Hz), 8.13-8.05 (m, 3H), 7.54 (t, 1H, 6.3 Hz), 6.94-6.88 (m, 2H), 6.29-6.26 (m, 1H), 6.05-6.03 (m, 1H), 5.90-5.86 (m, 2H), 3.85-3.50 (m, 4H), 3.36 (s, 2H), 3.31 (s, 6H), 2.46 (d, 3H, *J* = 3.6 Hz), 2.40-2.17 (m, 3H), 2.15-1.49 (m, 5H), 0.82-0.68 (m, 6H). CHN analysis: calculated for

C₃₄H₄₄Cl₂N₇NaO₆OsS (**2-SG** - H⁺ + Na⁺ + CH₂Cl₂): C, 42.41%; H, 4.61%; N, 10.18%. Found: C, 42.36%; H, 4.67%; N, 10.23%.

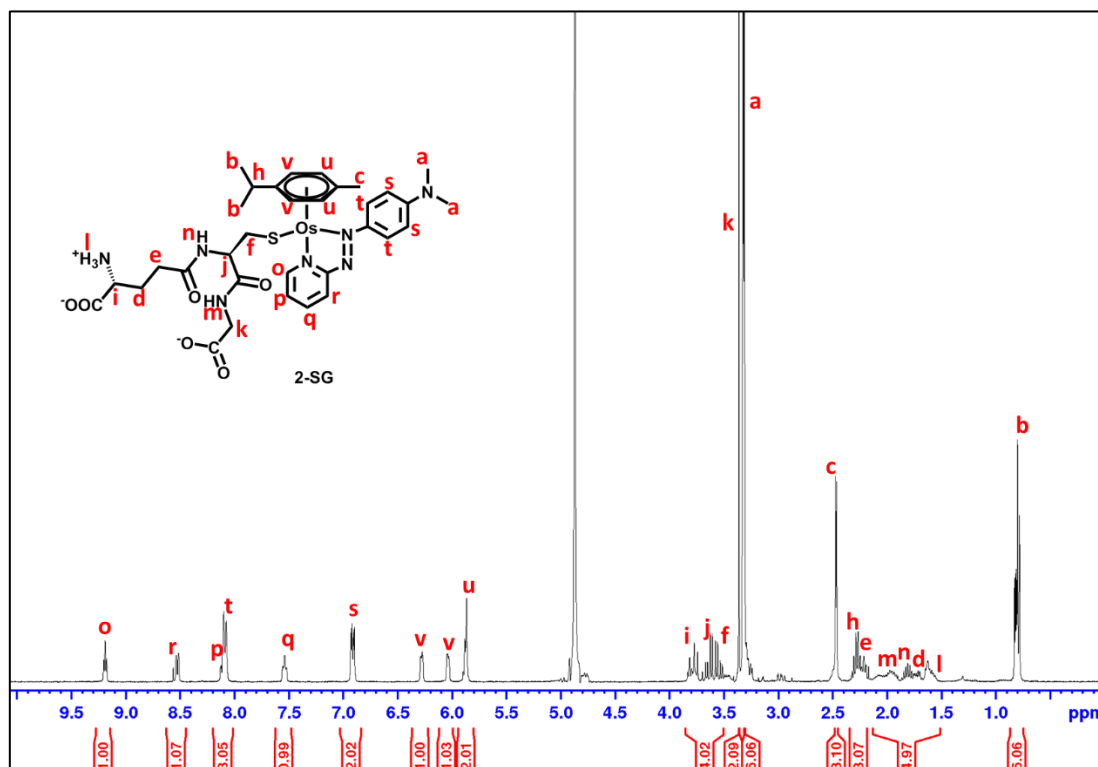


Figure 3.3. 400 MHz ¹H NMR spectrum for **2-SG** in CD₃OD.

3.2.4. pK_a of [2-OH]⁺

A solution of [2-OH]⁺ (2 mM) was prepared in D₂O, and dioxane (4 mM) was added as NMR standard reference (δ 3.75 ppm).¹³ The solution was aliquoted into 8 samples of 600 μ L and the pH* values (read from pH meter without correction for the effect of deuterium on the glass electrode) were adjusted sequentially by adding 1-10 μ L of either KOD or DNO₃ (0.01, 0.1, 1, 2, 3, 4, 6, 8 or 10 M) in D₂O. The pH* values were measured over a range of 1.5 - 13.5. Changes in the chemical shifts of protons in complex [2-OH]⁺ were followed by ¹H NMR, and pH* values were corrected *via* the equation: pH = 0.929pH* + 0.412.¹⁴ Data were fitted to the Henderson-Hasselbalch equation using Origin 8.5.

3.2.5. Anti-proliferative Activity

The IC₅₀ (half maximal inhibitory concentration) values of [2-OH]⁺, 2-NAC, 2-SG to A2780 ovarian cancer and A549 alveolar cancer cell lines were determined by Dr. Isolda Romero-Canelón (University of Warwick). More details of *in vitro* growth inhibition assay are described in **Chapter 2**.

3.2.6. TD-DFT Calculations

The time-dependent DFT calculations of **[2-I]⁺**, **[2-Cl]⁺**, **[2-OH]⁺**, **2-SG**, **2-NAC** were carried out by Prof. Emilia Sicilia (Università della Calabria, Italy). The Gaussian 09 program was employed to carry out all calculations in the framework of the density functional theory using the hybrid Becke three-parameter exchange functional¹⁵ and the Lee–Yang–Parr correlation functional, B3LYP.¹⁶ Dispersion corrections for non-bonding interactions have been included through the Grimme approach using atom pair-wise additive schemes,¹⁷ DFT-D3 method. LANL2DZ effective core potential has been used for the Os atom,¹⁸ along with the split valence basis set. The standard triple- ζ quality 6-311+G** basis sets of Pople and coworkers have been used for the atoms directly participating in the process, whereas in order to reduce the computational effort, the 6-31G* basis sets have been employed for peripheral atoms. More details of DFT calculations are described in **Chapter 2**.

3.2.7. Extinction Coefficient

Aqueous solutions of osmium complexes **2-I•PF₆**, **2-Cl•PF₆**, **[2-OH]⁺**, **2-SG**, **2-NAC** were prepared at ca. 25 μ M. The UV-vis spectra of these osmium complexes aqueous solution were acquired with a Cary 300 UV-Vis recording spectrophotometer and the accurate concentrations of these

osmium solutions were determined with ICP-OES. The extinction coefficients of these complexes were calculated using the Beer–Lambert law based on the UV-vis spectra, and concentrations of osmium from ICP-OES and the cuvette path length (1 cm).¹⁹ More details regarding UV-Vis spectroscopy and ICP-OES are available in **Chapter 2**.

3.2.8. HPLC and LC-MS

Table 3.1. The solvent B (acetonitrile) gradient used in HPLC/LC-MS for analysing osmium azo and imino complexes.

Time (min)	% (B) for azo complexes	% (B) for imino complexes
0	10	20
30	80	60
40	80	60
41	10	20
55	10	20

The solutions of **2-I•PF₆**, **2-Cl•PF₆**, **[2-OH]⁺**, **2-SG**, **2-NAC**, **2-imp-Cl•PF₆**, **2-imp-I•PF₆** in phosphate buffer (75 mM, pH = 7.4) were prepared with at ~100 μM and analysed by HPLC and LC-MS. The details of the HPLC, LC-MS instrument, the column information are described in **Chapter 2**. The mobile phases used in the experiments were solvent A (H₂O with 0.1% TFA) and solvent B (MeCN with 0.1% TFA).

Osmium imino complexes were analysed at a detection wavelength of 254 nm with reference wavelengths set to 360 nm and 510 nm, whilst osmium azo complexes were analysed at 610 nm with a reference wavelength set to 360 nm.

3.2.9. HRMS

The solutions of **1-Cl•PF₆**, **2-I•PF₆**, **2-Cl•PF₆**, **[2-OH]⁺**, **2-SG**, **2-NAC**, **2-imp-Cl•PF₆**, **2-imp-I•PF₆** in ammonium acetate buffer (5 mM, pH = 7.2) were prepared with a concentration of ca. 20 μM and these solutions were analysed with HRMS. More details regarding the HRMS instrument are provided in **Chapter 2**.

3.2.10. The Proportionality between HPLC Peak and Concentration

The solutions of **2-I•PF₆**, **2-Cl•PF₆**, **[2-OH]⁺**, **2-SG**, **2-NAC** in phosphate buffer (75 mM, pH = 7.4) were prepared with a concentration of ca. 100 μM. Then each solution was diluted 1×, 2× or 4× times and analysed by HPLC. The concentrations of the stock solutions were measured by ICP-OES. The linear proportionality between concentrations of solutions *versus* their integrated peak area on HPLC traces at 610 nm was plotted.

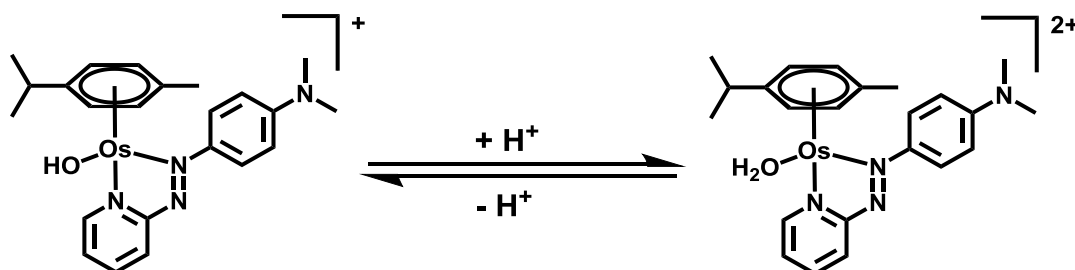
3.3. Results

In this **Chapter 3**, several osmium complexes related to FY26 (**2-I•PF₆**) were synthesised. Although **1-Cl•PF₆**, **2-I•PF₆**, **2-Cl•PF₆**, **2-imp-1•PF₆**, **2-imp-Cl•PF₆** were reported before,^{5,6} herein they are prepared with yield-improved methods. Complexes **2-NO₃•PF₆**, **[2-OH]⁺** (solution), **2-NAC**, **2-SG** are obtained and characterized here for the first time. After acquiring these osmium complexes, their properties were studied, including the pK_a value of **[2-OH₂]²⁺** (**Section 3.3.1**), anti-proliferative activity studies (**Section 3.3.2**), TD-DFT calculations for their electronic spectra (**Section 3.3.3**), extinction coefficients (**Section 3.3.4**), retention times and mass spectrometry identification (**Section 3.3.5**), and the proportionality between HPLC peak and concentration for quantification purposes (**Section 3.3.6**).

3.3.1. pK_a of **[2-OH]⁺**

The pK_a value of **[2-OH₂]²⁺** deprotonating to **[2-OH]⁺** (**Scheme 3.1.**) was determined using ¹H NMR through observing the change in chemical shift of an aromatic p-cym proton as the pH* in D₂O solution was varied (pH* corresponds to the pH reading of a D₂O solution using a H₂O calibrated pH-meter). The pH* values were corrected to pH values with $\text{pH} = 0.929\text{pH}^* + 0.412$,¹⁴ and the data was fitted to Henderson-

Hasselbalch equation. From the data, the pK_a of [2-OH]⁺ is 5.20 ± 0.02 and the error was obtained as a computer fitting error using Origin 8.5.



Scheme 3.1. Protonation of [2-OH]⁺ and deprotonation of [2-OH₂]²⁺ with dissociation of [H]⁺ under acid and basic conditions.

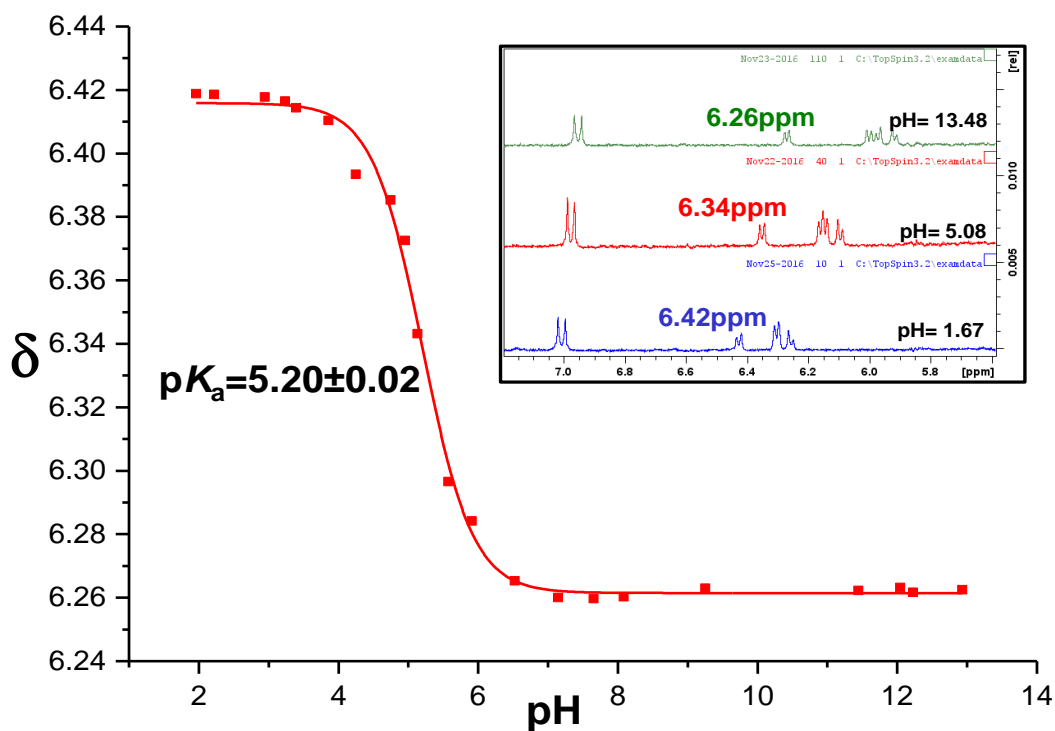


Figure 3.4. Variation of the chemical shift of an aromatic p-cym proton of [2-OH]⁺ with pH. The red line represents a computer best fit to the Henderson-Hasselbalch equation.

3.3.2. Anti-proliferative Activity

The IC₅₀ values of novel complexes **[2-OH]⁺**, **2-NAC**, **2-SG** against A2780 and A549 cancer cells were determined using the protocol described in **Chapter 2**. From these data (**Table 3.2**), all these three complexes are inactive to A549 cancer cells. For A2780 cancer cells, **[2-OH]⁺** exhibited IC₅₀ = 9.1 ± 0.7 μM, while **2-NAC** and **2-SG** were inactive (IC₅₀ > 100 μM). The cell culture media were composed of Dulbecco's Modified Eagle Medium (DMEM), phosphate buffered saline, L-glutamine, penicillin / streptomycin, fetal bovine serum.

Table 3.2. The anti-proliferative activity of **[2-OH]⁺**, **2-NAC**, **2-SG** against A2780 and A549 cancer cells.

Complexes	IC ₅₀ (A2780) (μM)	IC ₅₀ (A549) (μM)
[2-OH]⁺	9.1 ± 0.7 ^a	> 100
2-NAC	> 100	> 100
2-SG	> 100	> 100

Means ± standard deviation from three independent repeats

3.3.3. Electronic Spectra from TD-DFT Calculations

Time-dependent DFT calculations were carried out by Prof. Emilia Sicilia (Università della Calabria, Italy) for complexes **[2-I]⁺**, **[2-OH]⁺**, **[2-OH]²⁺** and **2-SG** and their electronic absorption spectra were

predicted. From the results (**Figure 3.5 – 3.8**), all these complexes had a similar maximum absorbance at 550-610 nm (553 nm for **[2-I]**⁺, 573 nm for **[2-OH]**⁺, 611 nm for **[2-OH]**²⁺, 566 nm for **2-SG**) and this predominantly arose from the excitation from highest occupied molecular orbital (HOMO) to lowest unoccupied molecular orbital (LUMO). From the model of HOMO to LUMO (**Figure 3.5-3.8**), it was clearly a charge transfer band arising from the metal centre to the ligands. Thus the maximum absorbance band at 550-610 nm can be assigned to metal-ligand charge transfer (MLCT), which was from the filled Os 5d⁶ orbitals of Os(II) to the empty π^* ligand orbitals (5d⁶ Os $\pi \rightarrow \pi^*$). Apart from MLCT, intra-ligand transitions (IL $\pi \rightarrow \pi^*$) also contribute to the absorbance from 200-400 nm. The absorbance of intraligand transitions was relatively lower than metal-ligand charge transfer, and mainly contributed by the excitation from HOMO-8 to LUMO for **[2-I]**⁺, HOMO-1 to LUMO+1 for **[2-OH]**⁺, HOMO to LUMO+2 for **[2-OH]**²⁺ and HOMO-9 to LUMO for **2-SG**, respectively.

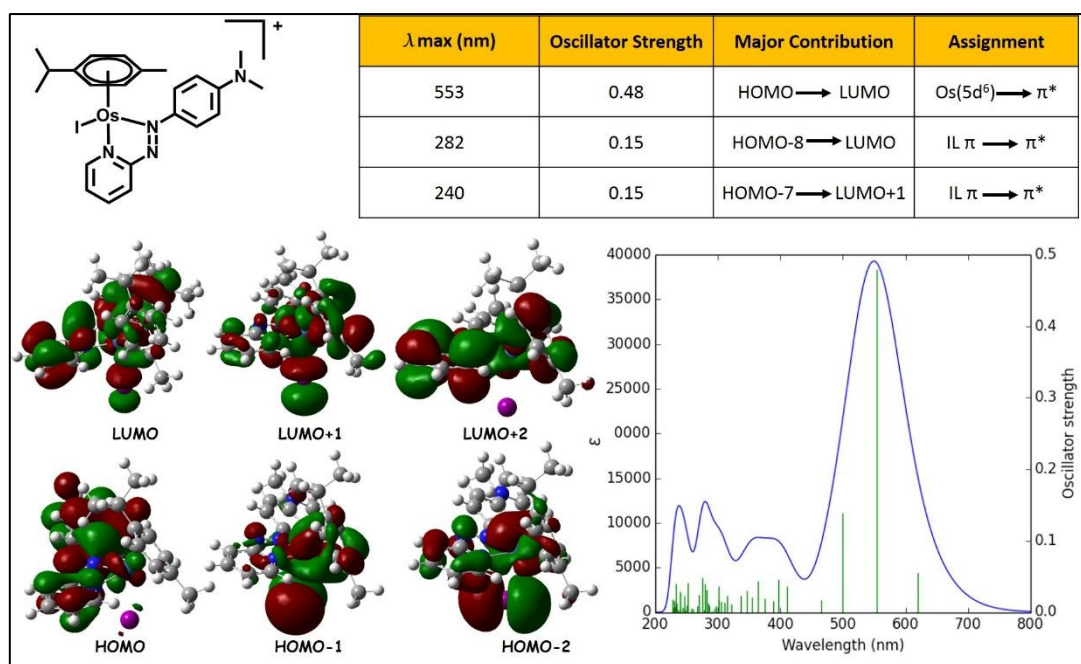


Figure 3.5. The HOMO and LUMO models, electronic spectrum (blue line) and assignments for $[\mathbf{2-I}]^+$ from the TD-DFT calculations.

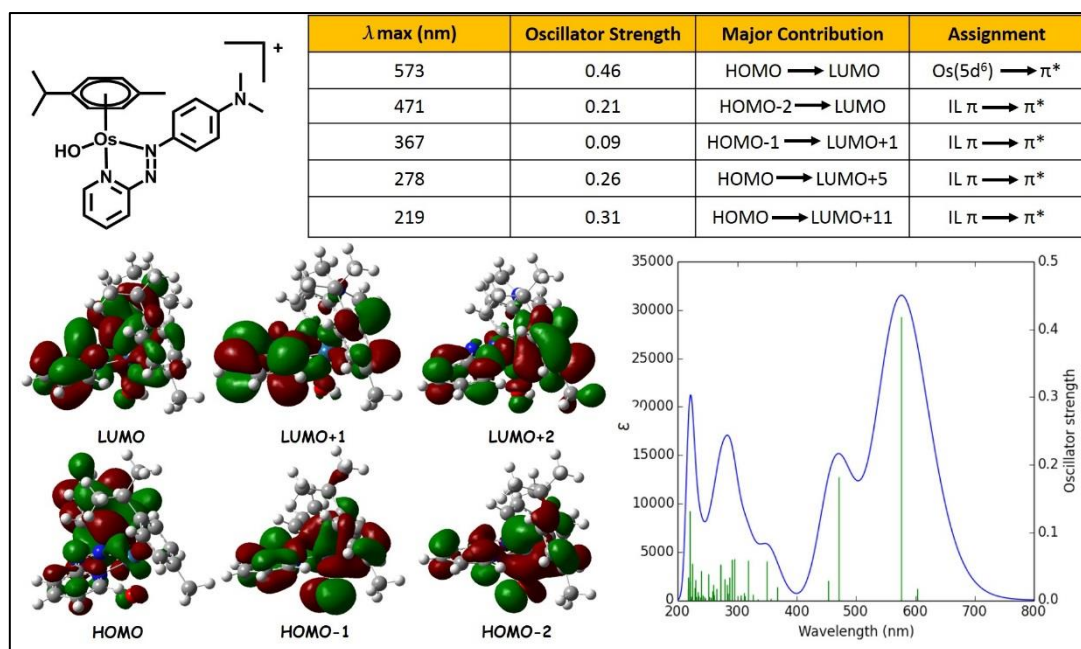


Figure 3.6. The HOMO and LUMO models, electronic spectrum (blue line) and assignments for $[\mathbf{2-OH}]^+$ from the TD-DFT calculations.

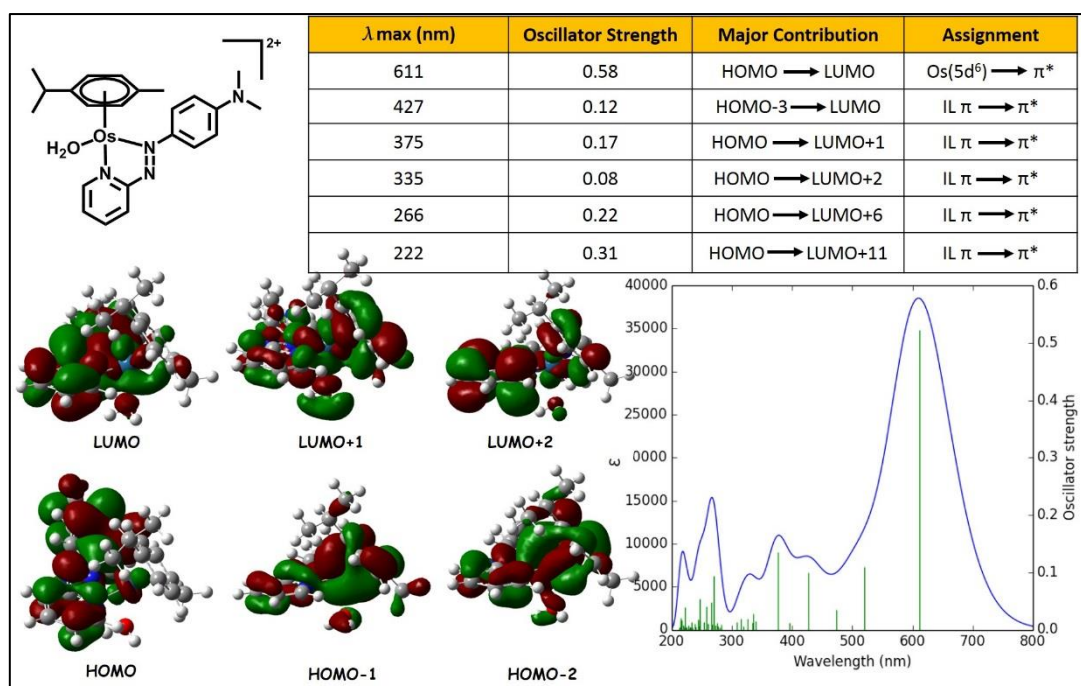


Figure 3.7. The HOMO and LUMO models, electronic spectrum (blue line) and assignments for [2-OH₂]²⁺ from the TD-DFT calculations.

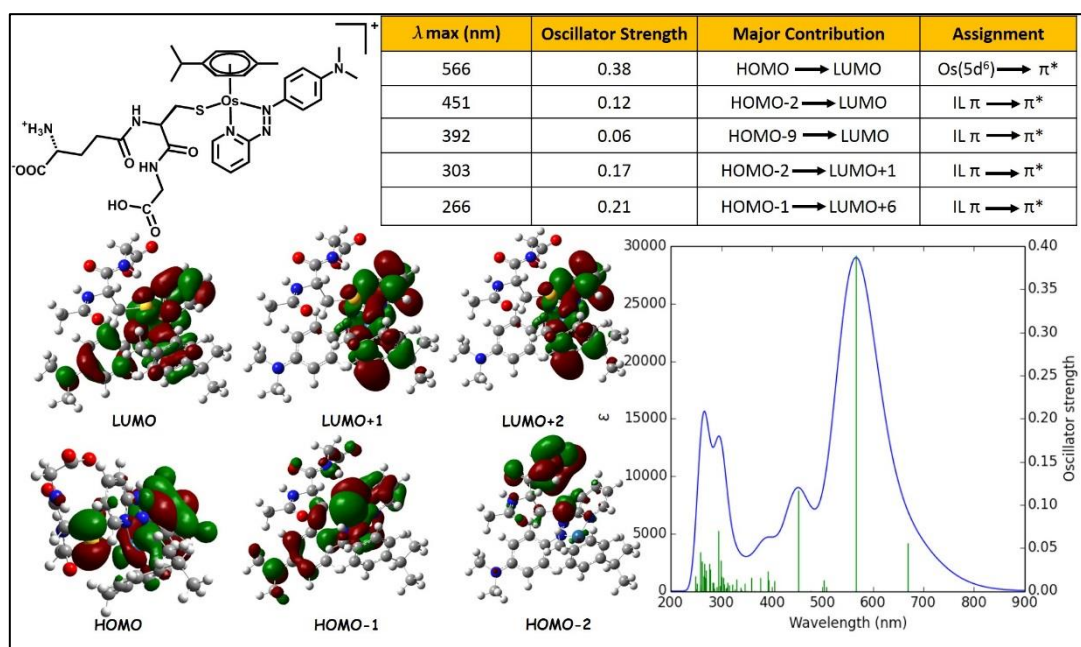


Figure 3.8. The HOMO and LUMO models, electronic spectrum (blue line) and assignments for 2-SG from the TD-DFT calculations.

3.3.4. Extinction Coefficients

The UV-vis spectra of complexes **[2-Cl]⁺**, **[2-I]⁺**, **2-NAC**, **2-SG**, **[2-OH]⁺** in fresh aqueous solutions in 75 mM phosphate buffer (pH 7.4) were acquired. These complexes possessed very similar UV-vis absorbance spectra and have three maxima at 610 nm, 475 nm and 290 nm, of which the absorbance at 610 nm is the highest for all complexes. The spectra (**Figure 3.9**) are consistent with the electronic spectra predicted from TD-DFT calculations.

Then concentrations of osmium in these stock solutions were determined using ICP-OES as $26.45 \pm 0.13 \mu\text{M}$ for **[2-Cl]⁺**, $17.02 \pm 0.09 \mu\text{M}$ for **[2-I]⁺**, $34.34 \pm 0.24 \mu\text{M}$ for **2-NAC**, $20.92 \pm 0.35 \mu\text{M}$ for **2-SG** and $22.32 \pm 0.19 \mu\text{M}$ for **[2-OH]⁺**. The extinction coefficients for each osmium complex at the above maxima were calculated based on the Beer–Lambert law.¹⁹ The results are summarized at **Table 3.3**. Notably, complex **[2-I]⁺** exhibits a higher extinction coefficient ($40000 \text{ M}^{-1} \text{ cm}^{-1}$ at 611 nm) than the other osmium complexes **[2-Cl]⁺** ($25000 \text{ M}^{-1} \text{ cm}^{-1}$ at 608 nm), **2-NAC** ($20000 \text{ M}^{-1} \text{ cm}^{-1}$ at 607 nm), **2-SG** ($26000 \text{ M}^{-1} \text{ cm}^{-1}$ at 613 nm), and **[2-OH]⁺** ($28000 \text{ M}^{-1} \text{ cm}^{-1}$ at 615 nm).

Table 3.3. Wavelengths of maximum absorbance, extinction coefficients, and assignments for osmium complexes [2-Cl]⁺, [2-I]⁺, 2-NAC, 2-SG, [2-OH]⁺.

Complexes	λ max (nm)	ϵ (M ⁻¹ cm ⁻¹)	Assignment
[2-Cl] ⁺	650 (sh ^a)	23085±113	Os(5d ⁶)→ π^*
	608	25016±122	Os(5d ⁶)→ π^*
	474	7476±37	IL ^b π → π^*
	283	7410±36	IL π → π^*
[2-I] ⁺	611	40971±217	Os(5d ⁶)→ π^*
	506	15225±81	IL π → π^*
	298	15136±80	IL π → π^*
2-NAC	607	20240±141	Os(5d ⁶)→ π^*
	467	5990±42	IL π → π^*
	291	8479±59	IL π → π^*
2-SG	613	26006±435	Os(5d ⁶)→ π^*
	462	5872±98	IL π → π^*
	295	8882±149	IL π → π^*
[2-OH] ⁺	615	27799±237	Os(5d ⁶)→ π^*
	475	8243±70	IL π → π^*
	293	8032±68	IL π → π^*

^a (sh) = shoulder. ^b(IL) = Intraligand.

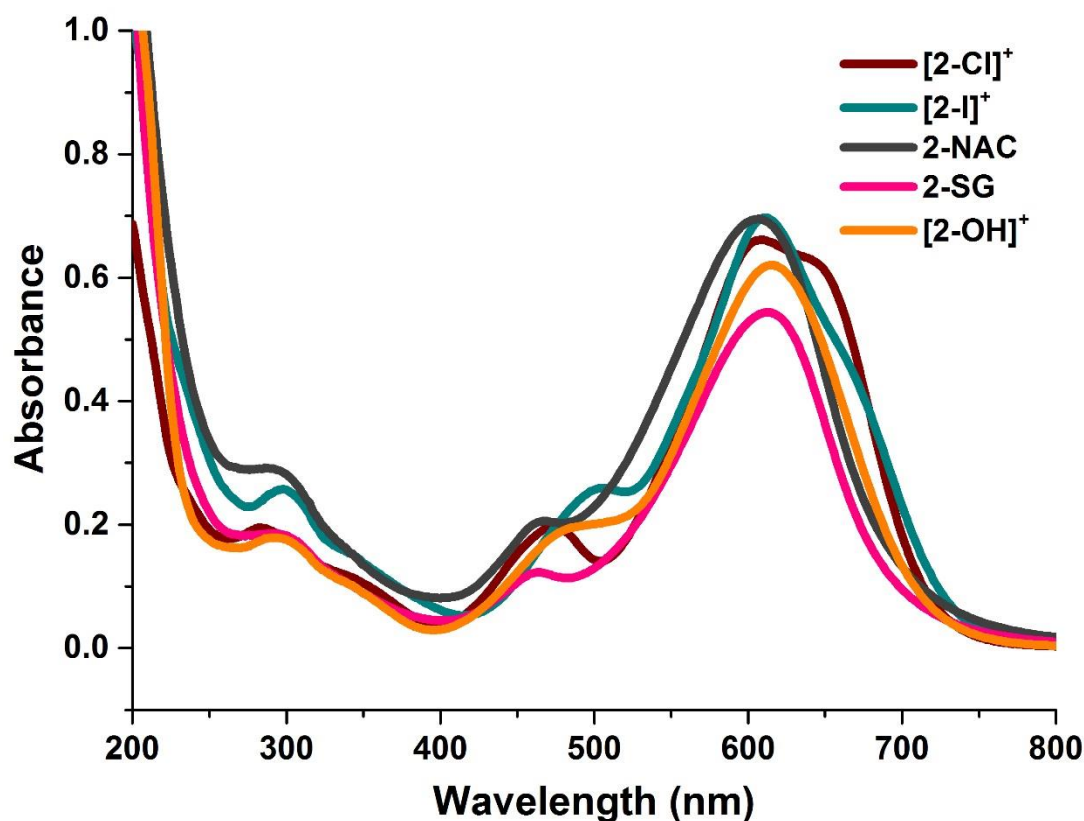


Figure 3.9. The UV-Vis spectrum for aqueous solutions of $[2-\text{Cl}]^+$ (26.45 μM), $[2-\text{I}]^+$ (17.02 μM), **2-NAC** aqueous solution (34.34 μM), **2-SG** (20.92 μM), $[2-\text{OH}]^+$ aqueous solution (22.32 μM), pH 7.4.

3.3.5. HPLC Retention Times and Mass Spectrometric Analysis for Osmium Species

Fresh aqueous solutions of osmium complexes **2-I**•PF₆, **2-Cl**•PF₆, **2-imp**-**Cl**•PF₆, **2-imp**-**I**•PF₆, **2-NO₃**•PF₆, $[2-\text{OH}]^+$, **2-SG**, **2-NAC** were prepared in phosphate buffer (75 mM, pH = 7.4) and analysed by HPLC and LC-MS to give their corresponding retention times and m/z of positive ions. HRMS was used to confirm the m/z values observed by

LC-MS for each species. The results are summarized in **Table 3.4**. The HPLC retention times for [2-I]⁺, [2-Cl]⁺, [2-imp-Cl]⁺, [2-imp-I]⁺, [2-NO₃]⁺, [2-OH]⁺, 2-SG, 2-NAC were 23.02, 19.67, 26.43, 41.42, 18.62, 15.68, 12.53, 13.29 (min), respectively and corresponding HRMS m/z values were 679.0952, 587.1594, 586.1633, 678.1028, 614.1809, 714.2149, 569.1941 and 858.2693, respectively.

Table 3.4. Species identified by HPLC/LC-MS/HRMS, their molecular formula, calculated and observed m/z values, and HPLC retention times.

Species	Molecular Formula	m/z	Observed m/z (LCMS)	Observed m/z (HRMS)	HPLC Retention Time (min)
[2-I] ⁺	C ₂₃ H ₂₈ IN ₄ Os ⁺	679.0969	679.02	679.0952	23.02
[2-Cl] ⁺	C ₂₃ H ₂₈ ClN ₄ Os ⁺	587.1602	587.21	587.1594	19.67
[2-imp-Cl] ⁺	C ₂₄ H ₂₉ ClN ₃ Os ⁺	586.1649	586.23	586.1633	26.43*
[2-imp-I] ⁺	C ₂₄ H ₂₉ IN ₃ Os ⁺	678.1016	678.17	678.1028	41.42*
[2-NO ₃] ⁺	C ₂₃ H ₂₈ N ₅ O ₃ Os ⁺	614.1802	614.11	614.1809	18.62
[2-NAC + H ⁺] ⁺	C ₂₈ H ₃₆ N ₅ O ₃ SOs ⁺	714.2147	714.16	714.2149	15.68
[2-OH] ⁺	C ₂₃ H ₂₉ N ₄ OOs ⁺	569.1951	569.17	569.1941	12.53
[2-SG + H ⁺] ⁺	C ₃₃ H ₄₄ N ₇ O ₆ OsS ⁺	858.2682	858.19	858.2693	13.29

* The HPLC methods for imino complexes and azo complexes are different, see **Table 3.1**.

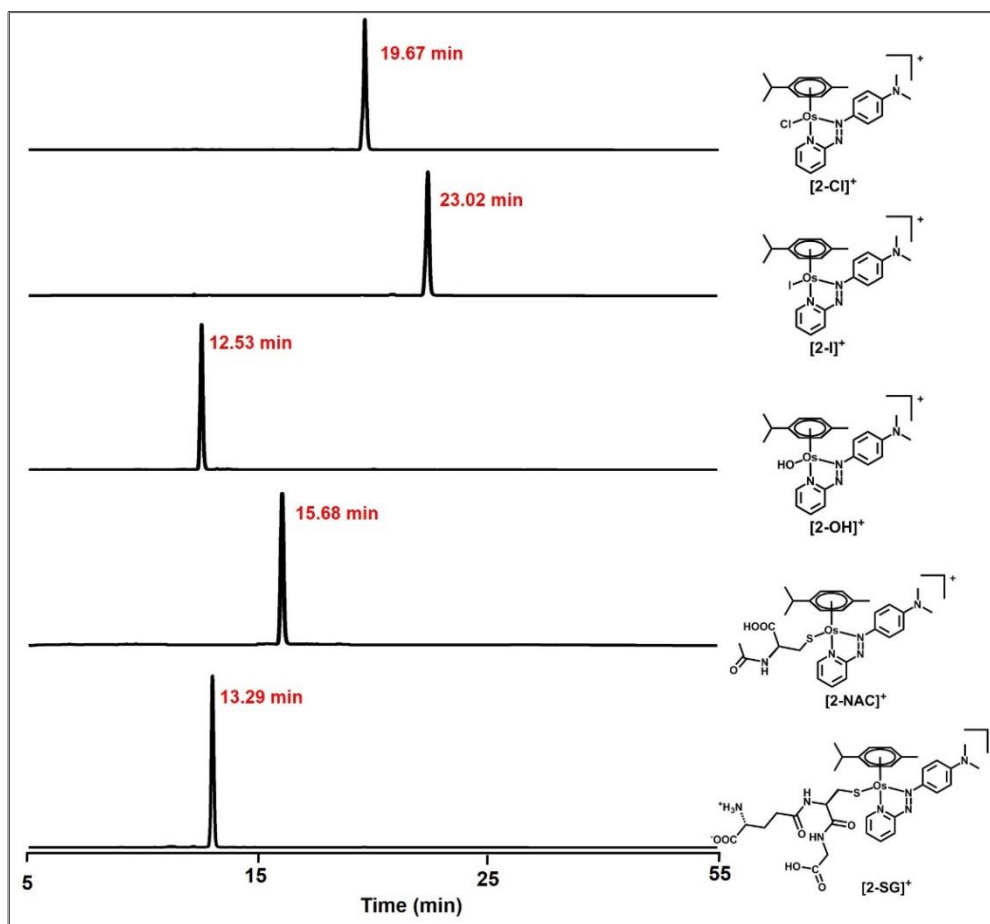


Figure 3.10. HPLC chromatography retention times for osmium azo complexes in aqueous solution with concentration of *ca.* 100 μM.

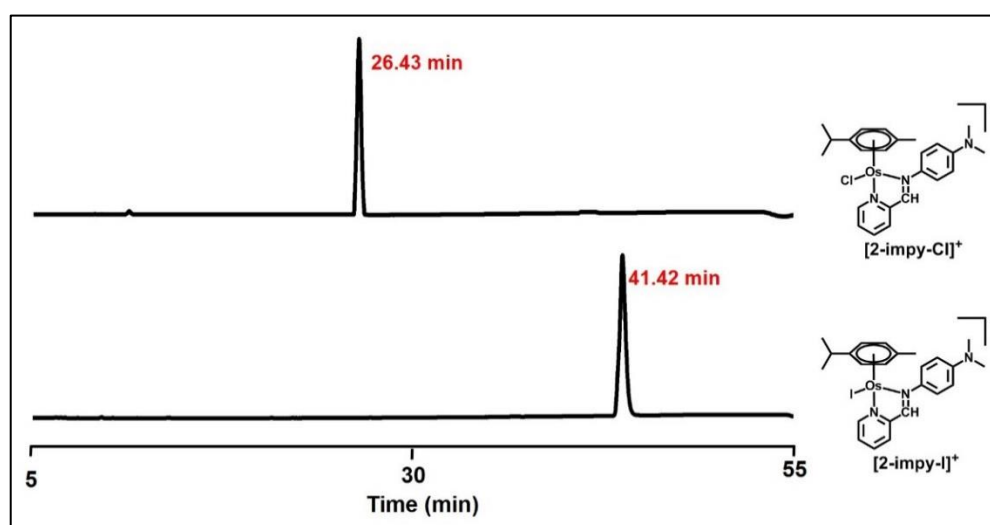


Figure 3.11. HPLC chromatography retention times for osmium imino complexes in aqueous solution with concentration of *ca.* 100 μM.

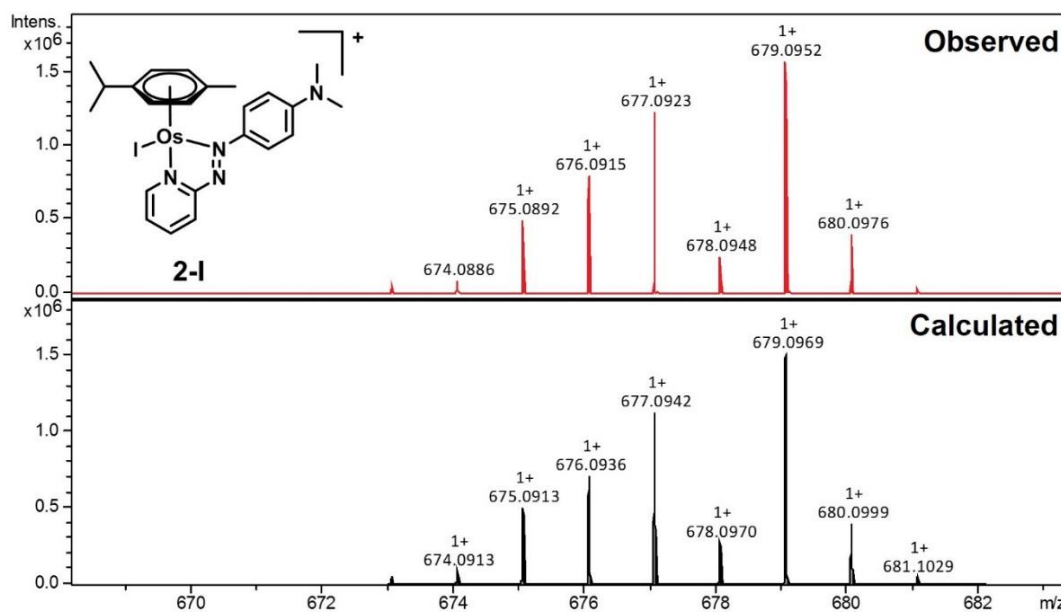


Figure 3.12. HRMS spectra for **2-I**. Molecular formula: C₂₃H₂₈IN₄Os⁺, calculated m/z: 679.0969, observed m/z: 679.0952, (error: 2.5 ppm).

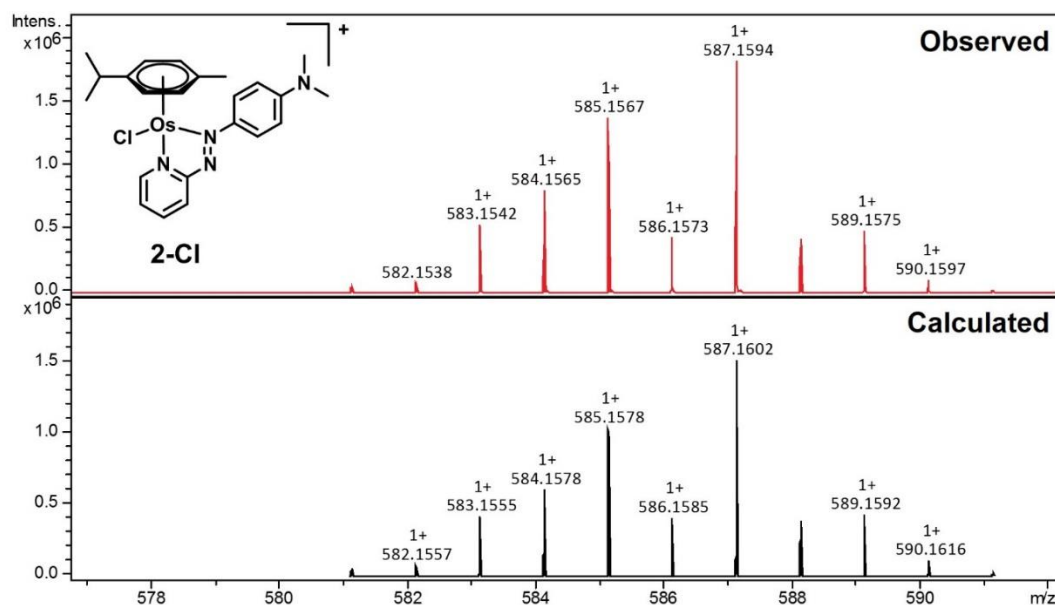


Figure 3.13. HRMS spectra for **2-Cl**. Molecular formula: C₂₃H₂₈ClN₄Os⁺, calculated m/z: 587.1602, observed m/z: 587.1594, (error: 1.4 ppm).

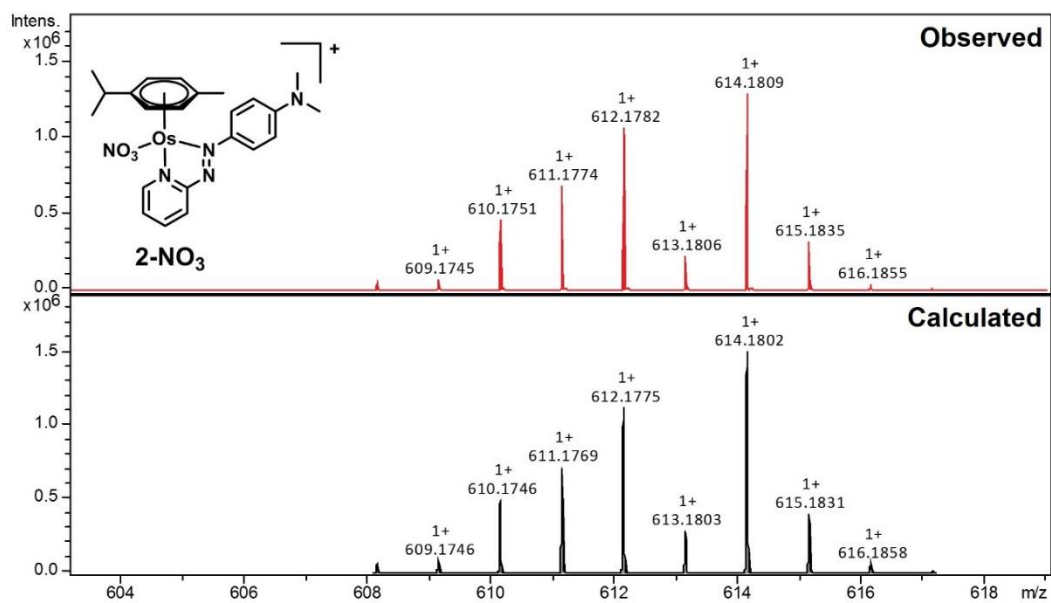


Figure 3.14. HRMS spectra for **2-NO₃**. Molecular formula: C₂₃H₂₈N₅O₃Os⁺, calculated m/z: 614.1802, observed m/z: 614.1809, (error: 1.2 ppm).

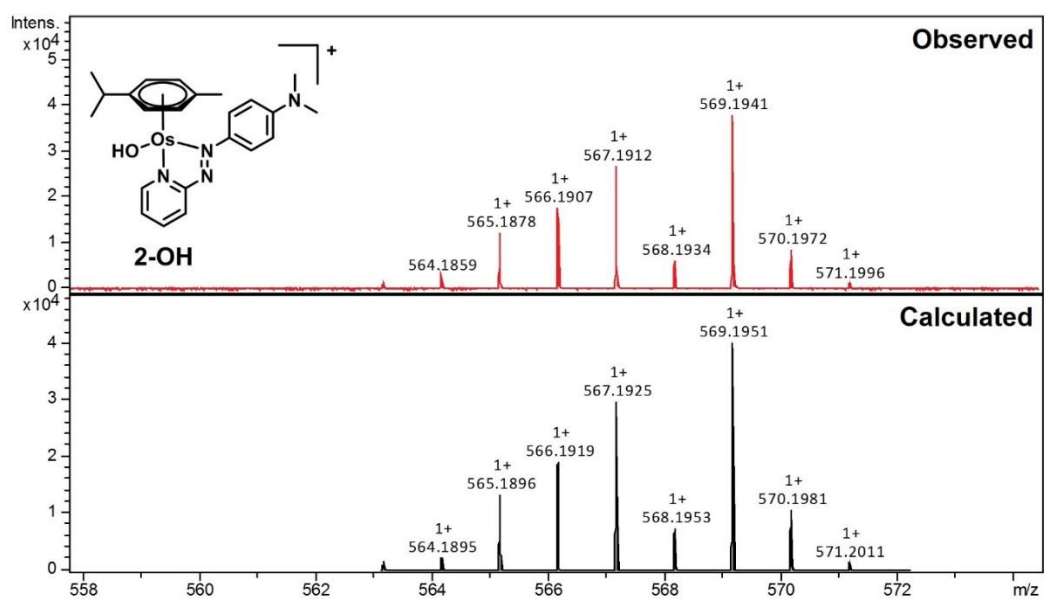


Figure 3.15. HRMS spectra for **2-OH**. Molecular formula: C₂₃H₂₉N₄OOs⁺, calculated m/z: 569.1951, observed m/z: 569.1941, (error: 1.8 ppm).

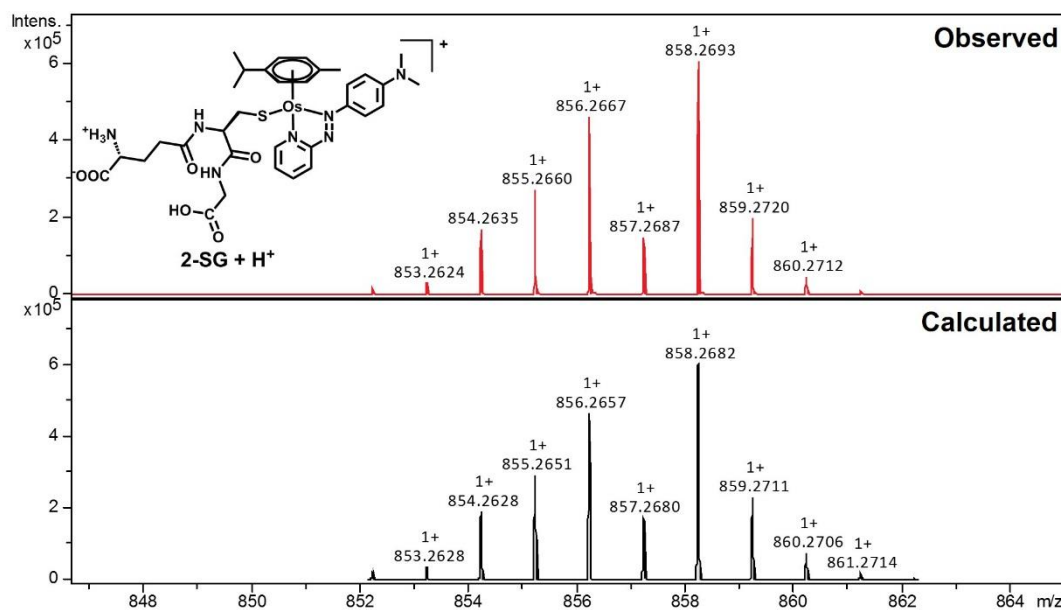


Figure 3.16. HRMS spectra for **2-SG + H⁺**. Molecular formula: C₃₃H₄₄N₇O₆OsS⁺, calculated m/z: 858.2682, observed m/z: 858.2693, (error: 1.3 ppm).

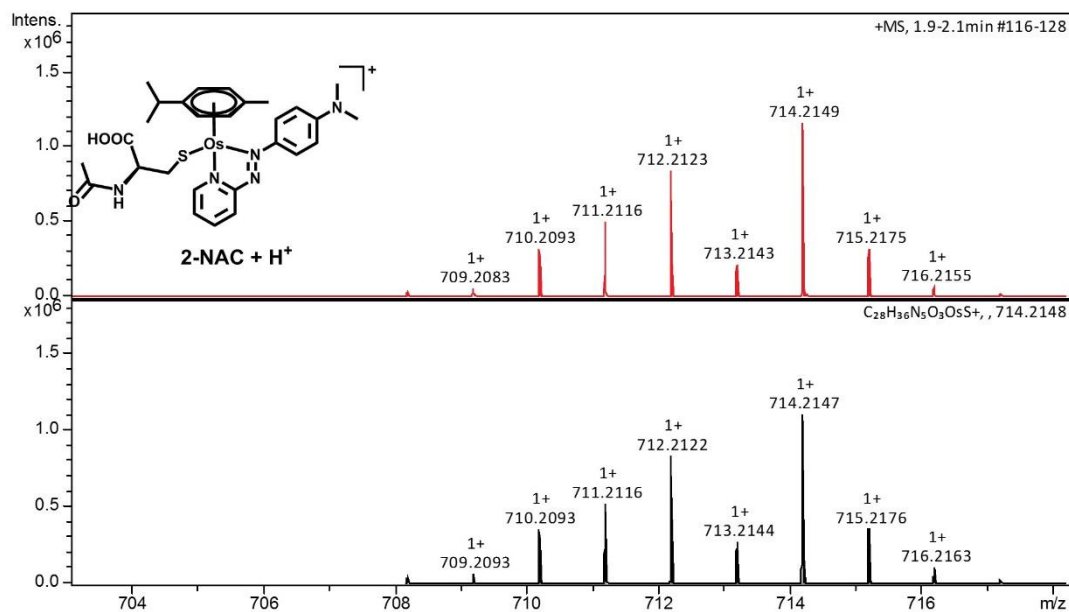


Figure 3.17. HRMS spectra for **2-NAC + H⁺**. Molecular formula: C₂₈H₃₆N₅O₃OsS⁺, calculated m/z: 714.2147, observed m/z: 714.2149, (error: 0.3 ppm).

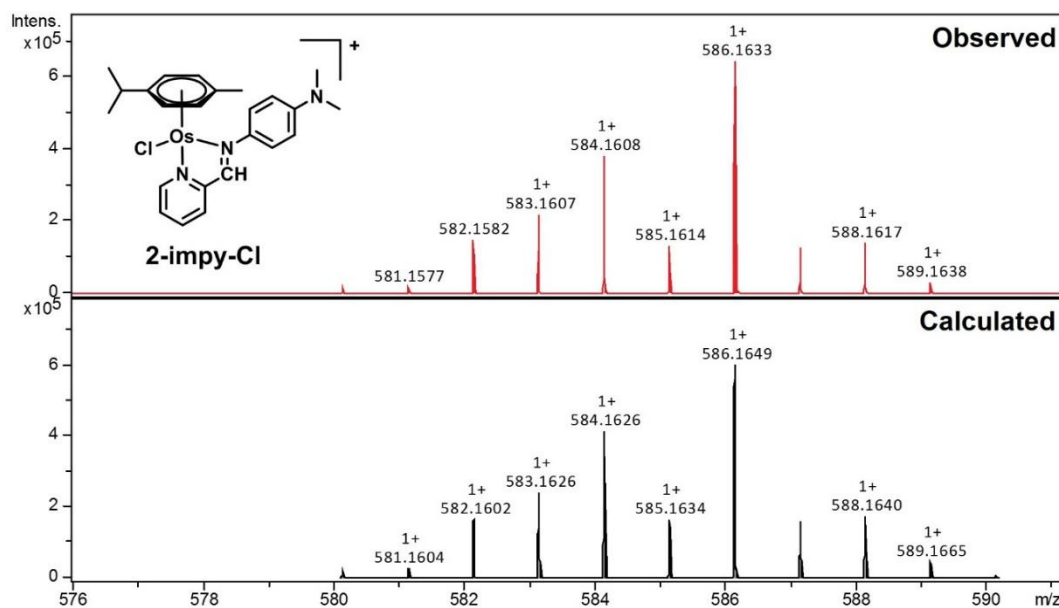


Figure 3.18. HRMS spectra for **2-impy-Cl**. Molecular formula: $C_{24}H_{29}ClN_3Os^+$, calculated m/z : 586.1649, observed m/z : 586.1633, (error: 2.7 ppm).

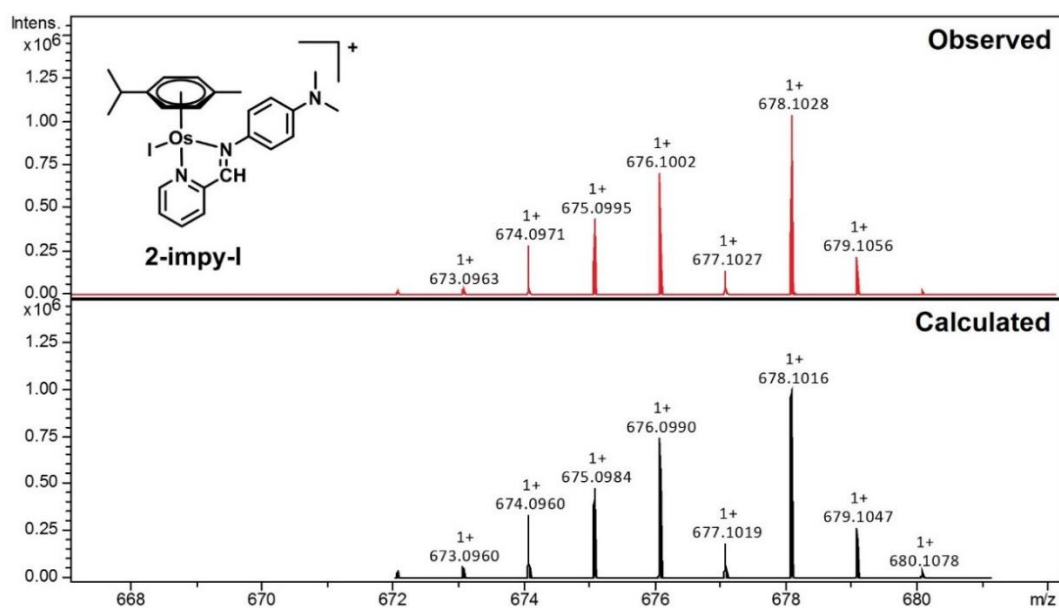


Figure 3.19. HRMS spectra for **2-impy-I**. Molecular formula: $C_{24}H_{29}IN_3Os^+$, calculated m/z : 678.1016, observed m/z : 678.1028, (error: 1.8 ppm).

3.3.6. The Proportionality of HPLC Peak Areas with Concentrations

Fresh aqueous solutions of **2-I•PF₆**, **2-Cl•PF₆**, **[2-OH]⁺**, **2-SG** in phosphate buffer (75 mM, pH = 7.4) were prepared with a concentration of *ca.* 100 μ M and diluted 1 \times , 2 \times or 4 \times times. All these samples were analysed on HPLC at a wavelength of 610 nm and their corresponding integrated peak areas were recorded. Subsequently, ICP-OES was used to determine the concentration of osmium for each stock solution. The results are summarized in **Table 3.5** and the linear relationship between the peak area in HPLC traces and concentration of osmium complexes were obtained for **[2-Cl]⁺** is $y = (81.47 \pm 0.11)x - (4.38 \pm 6.33)$; for **[2-I]⁺** is $y = (103.00 \pm 0.85)x - (126.09 \pm 16.61)$; for **[2-OH]⁺** is $y = (81.95 \pm 0.68)x - (28.86 \pm 34.96)$; for **2-SG** is $y = (84.63 \pm 0.048)x - (81.96 \pm 32.96)$.

Table 3.5. The HPLC peak area of osmium complexes at 610 nm and corresponding osmium concentrations.

Complexes	Concentration (μ M) ^a	Peak Area ^b
[2-Cl]⁺	71.72 \pm 0.22	5838 \pm 173
	35.86 \pm 0.11	2921 \pm 86
	17.93 \pm 0.05	1450 \pm 43
[2-I]⁺	23.93 \pm 0.12	2340 \pm 69
	11.96 \pm 0.06	1186 \pm 34
	5.98 \pm 0.03	594 \pm 17
[2-OH]⁺	63.64 \pm 0.35	5190 \pm 154
	31.82 \pm 0.18	2554 \pm 75
	15.91 \pm 0.09	1307 \pm 38
2-SG	84.61 \pm 0.29	7075 \pm 210
	42.31 \pm 0.15	3521 \pm 104
	21.15 \pm 0.08	1676 \pm 49

^a mean \pm sd from three independent determinations by ICP-OES; ^b mean \pm sd from three independent injections.

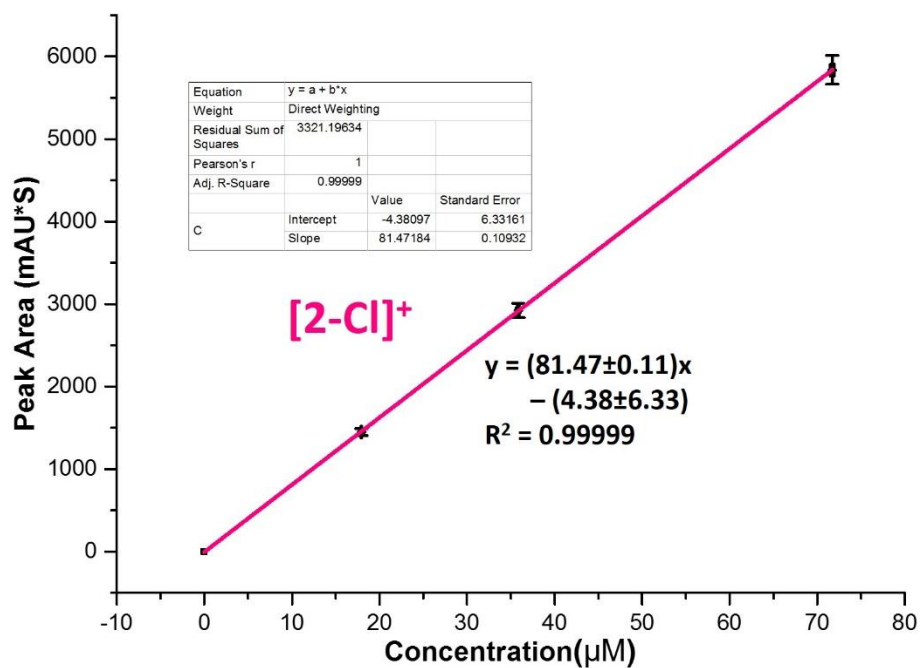


Figure 3.20. Linear relationship between HPLC peak area (610 nm) and concentration of **[2-Cl]⁺**.

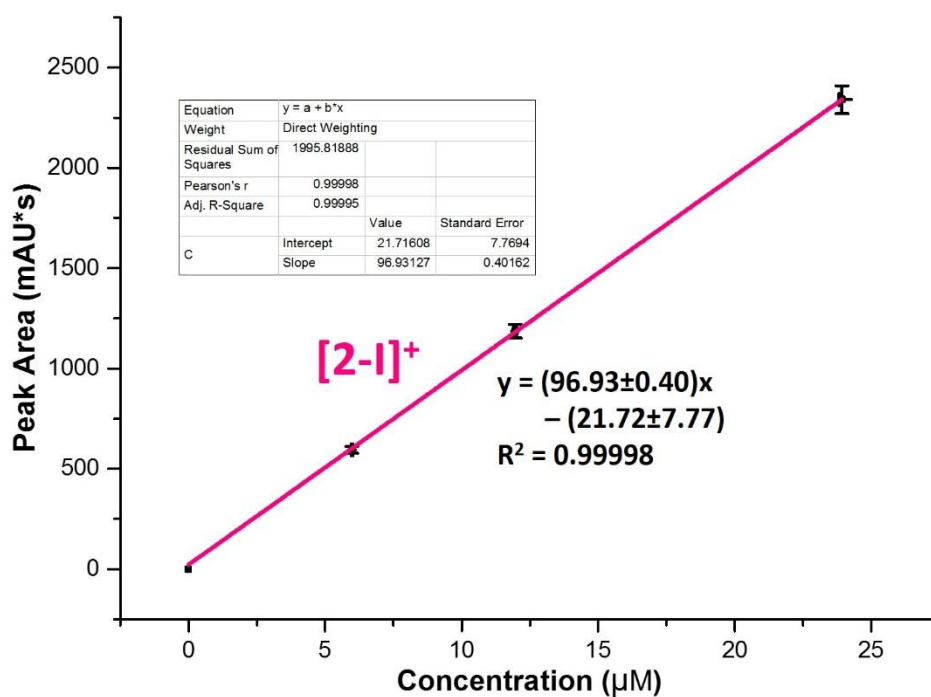


Figure 3.21. Linear relationship between HPLC peak area (610 nm) and concentration of **[2-I]⁺**.

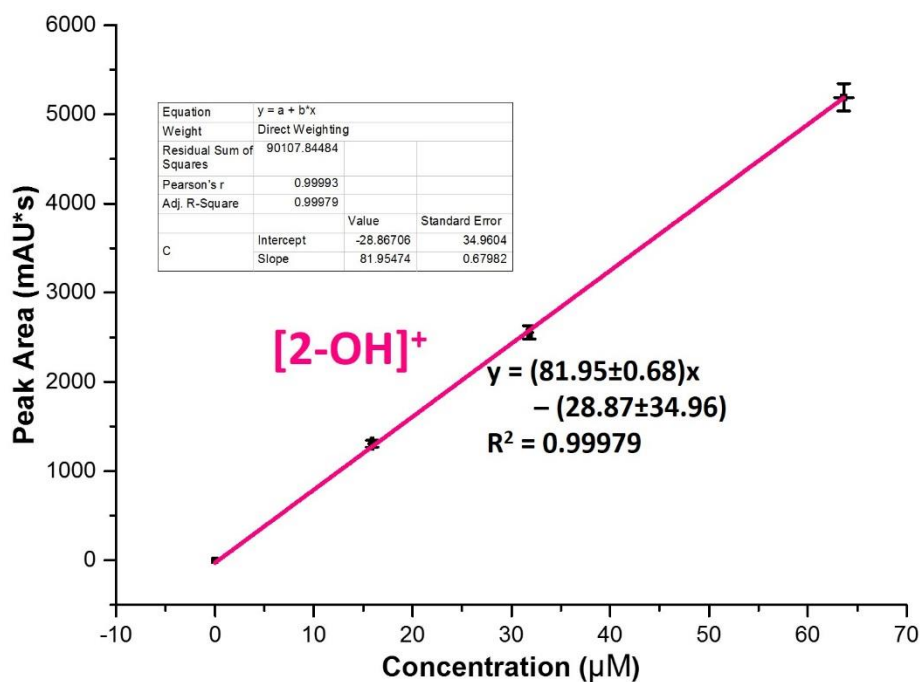


Figure 3.22. Linear relationship between HPLC peak area (610 nm) and concentration of [2-OH]⁺.

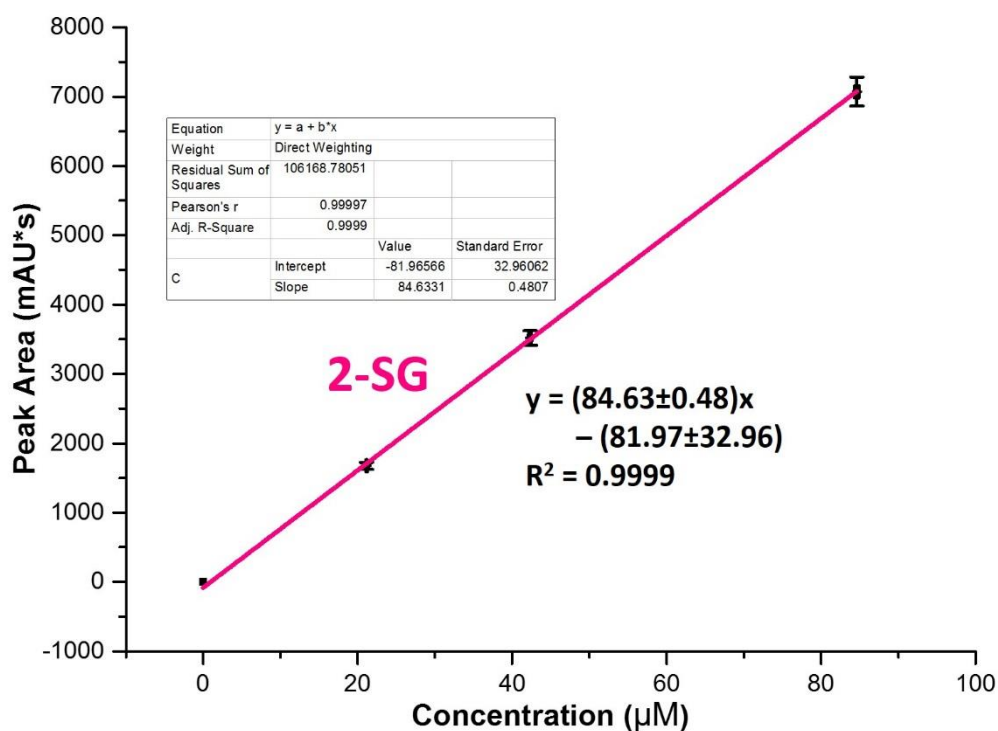


Figure 3.23. Linear relationship between HPLC peak area (610 nm) and concentration of 2-SG.

3.4. Discussion

The half-sandwich osmium azo complex [Os (η^6 -*p*-cymene) (4-(2-pyridylazo)-*N,N*-dimethylaniline)I]PF₆ **FY26** (termed **2-I•PF₆** in this thesis) has been reported as a very promising anticancer drug candidate. This thesis is aimed to explore the mechanism of action of **2-I•PF₆**, especially studying the reactions between **2-I•PF₆** with intracellular biomolecule GSH. Contributions towards the aim for the whole thesis, the work in this **Chapter 3** includes the synthesis and characterization of **2-I•PF₆** and its analogue complexes including chloride analogue **2-Cl•PF₆**, non-substituted template complex **1-Cl•PF₆**, imino analogue complexes **2-impy-I•PF₆** and **2-impy-Cl•PF₆**, hydrolysis product complex **[2-OH]⁺** (solution), N-acetyl-cysteine adduct **2-NAC**, glutathione adduct **2-SG**.

Complexes	X	Y	Z	R
1-Cl•PF₆	-Cl	N	PF ₆	-H
2-I•PF₆	-I	N	PF ₆	-NMe ₂
2-I•PF₆	-I	N	PF ₆	-NMe ₂
2-impy-Cl•PF₆	-Cl	CH	PF ₆	-NMe ₂
2-impy-I•PF₆	-I	CH	PF ₆	-NMe ₂
2-NO₃•PF₆	-O ₃ N	N	PF ₆	-NMe ₂
[2-OH]⁺	-OH	N	+1	-NMe ₂
2-NAC	-NAC	N	0	-NMe ₂
2-SG	-SG	N	0	-NMe ₂

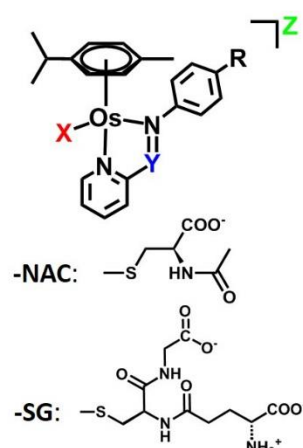


Figure 3.24. Structures of the complexes synthesised and studied in this chapter.

After obtaining these complexes, some of their properties were studied, such as the pK_a value of the aqua complex, electronic absorption spectra, extinction coefficients, liquid chromatography and mass spectrometry identification, proportionality between HPLC peak areas and concentrations. **[2-I]⁺** has been found to lose the monodentate iodido ligand significantly once uptaken by cancer cells⁹ and its hydrolysis product **[2-OH]⁺** appears to be the key active species to the anticancer cytotoxicity. The measurement of the pK_a value of **[2-OH₂]²⁺** helps to uncover which form hydroxido **[2-OH]⁺** or aqua **[2-OH₂]²⁺** predominates under the physiological condition (pH = 7.4). The result of pK_a = 5.20 ± 0.02 demonstrates that **[2-OH]⁺** predominates in cells and its low pK_a value is consistent with its Ru analogue [Ru (η⁶-*p*-cymene) (4-(1*H*-pyrazol-3-ylazo)-NMe₂)OH]⁺ (pK_a = 4.60). The azo ligand bearing in **[2-OH]⁺** is a strong π-acceptor ligand that draws electron density away from the metal centre rendering it more electropositive and making the H₂O ligand more acidic (lower pK_a).²⁰ In contrast, anionic ligands such as acetylacetonate and picolinate produce an opposite effect of making the H₂O ligand less acidic through placing more electron density around the metal centre.^{21,22} In general, Os(II) aqua adducts tend to have a lower pK_a than the Ru(II) analogue.²³ The pK_a value is a crucial factor to the stability and reactivity of metal aqua complexes because pK_a value determined aqua (M-OH₂) or hydroxido analogue (M-OH) predominates

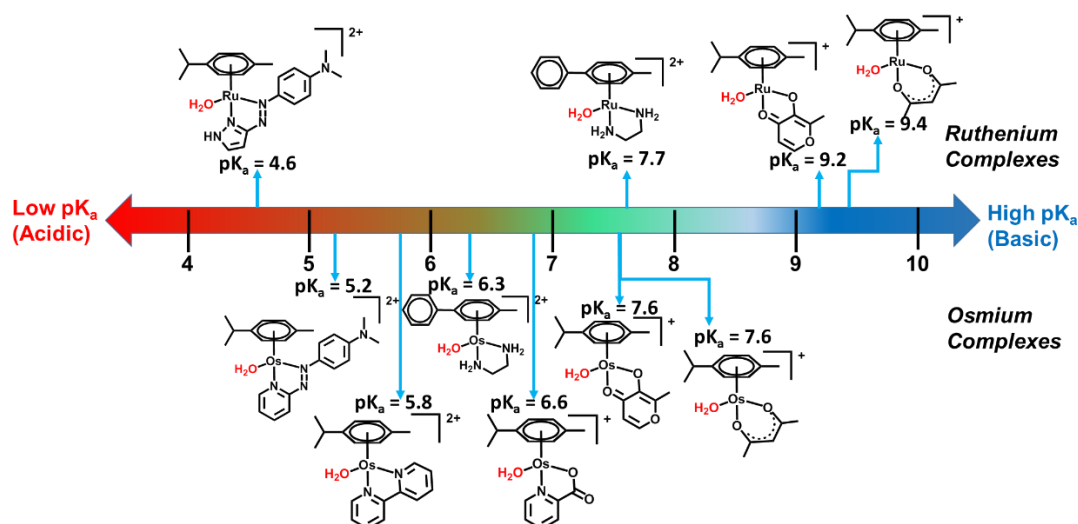


Figure 3.25. Comparison of pK_a values for Os(II) and Ru(II) arene aqua species with different bidentate ligands.^{11,21-27}

under physiological conditions and M-OH is generally more stable than M-OH₂ to various intracellular molecules.²⁸⁻³⁰ For example, cisplatin aqua analogue $[cis\text{-Pt}(\text{OH}_2)_2(\text{NH}_3)_2]^{2+}$ is more reactive than hydroxido analogue $[cis\text{-Pt}(\text{OH})_2(\text{NH}_3)_2]$ on reacting with glycine to form $[cis\text{-Pt}(\text{NH}_3)_2(\text{glyH-O})(\text{H}_2\text{O})]^{2+}$.³¹ In the ion exchange reaction with solvent, $[(\text{NH}_3)_5\text{CoOH}_2]^{3+}$ exhibits 40 times faster exchange rate than hydroxido analogue $[(\text{NH}_3)_5\text{CoOH}]^{2+}$ and $[\text{Co}(\text{cyclen})(\text{NH}_3)\text{OH}_2]^{3+}$ is two orders of magnitude faster than its hydroxido analogue $[\text{Co}(\text{cyclen})(\text{NH}_3)\text{OH}]^{2+}$.^{28,32,33}

Continued to the cytotoxicity of complexes $[\mathbf{1}\text{-Cl}]^+$, $[\mathbf{2}\text{-Cl}]^+$, $[\mathbf{2}\text{-I}]^+$ that have been measured and reported,^{6,34} the novel thiolate complexes **2-NAC** and **2-SG** are inactive, similar to the corresponding Pt(II) and Ir(III)

thiolate adducts.^{35,36} These thiol adducts may be too inert to react targets in the cancer cell and GS-X pump in cell membrane might lead low accumulation of thiol adducts into cancer cells.³⁷⁻³⁹ Complex **[2-OH]⁺** (IC₅₀ = 9.1 ± 0.7) was less cytotoxicity than **[2-Cl]⁺** (IC₅₀ = 1.4 μM) and **[2-I]⁺** (IC₅₀ = 0.14 μM),⁶ although **[2-OH]⁺** was considered as the active species of **[2-I]⁺** in the cancer cell line.⁹ This could be attributed to the too high reactivity of **[2-OH]⁺** and its reactions with intracellular targets and non-target species. The hydroxido analogue of cisplatin is able to react with many intracellular species, including DNA bases, amino acids and even phosphate buffer.^{29,40,41} This may lead to drug inactivation, and minimise the amount of active species reaching its cellular targets.

In terms of the UV-vis spectra and extinction coefficients of osmium complexes **[2-Cl]⁺**, **[2-I]⁺**, **2-NAC**, **2-SG**, and **[2-OH]⁺**, maximum absorbance bands at around 610, 475 and 290 nm were observed while the maximum absorbance of the free ligand (Azpy-NMe₂) are 432 nm and 272 nm.¹¹ Thus the bands at 610 nm for these osmium complexes can be assigned to metal-ligand charge transfer (MLCT) Os(5d⁶) → π* and the absorbance bands at 475 nm, 290 nm can be assigned to intra-ligand transitions. The TD-DFT calculations for the electronic spectra of these osmium complexes (**Section 3.3.**) suggest that the highest absorbance is mostly due to the excitation from HOMO to LUMO. Comparing the

electron density in the HOMO and LUMO models, it is clear to that charge transfer from the osmium(II) centre to the ligands, which also supports to assignment of most intense bands at 610 nm to metal-ligand charge transfer. Moreover, the TD-DFT calculations show that the MLCT of **[2-I]⁺** (excitation from HOMO to LUMO) involves phenyl and iodide ligands. However, the MLCT of other osmium complexes involves only the phenyl ligand. This difference might explain why the extinction coefficient of **[2-I]⁺** is higher than other osmium complexes studied.

The reversed-phase HPLC retention times of these osmium complexes reflect their hydrophobicities. The sequence of retention times is **[2-OH]⁺ < 2-SG < 2-NAC < [2-Cl]⁺ < [2-I]⁺ (Figure 3.10)**. The column used for HPLC was a C18 reverse column. Thus the hydrophobicity trend might be **[2-OH]⁺ > 2-SG > 2-NAC > [2-Cl]⁺ > [2-I]⁺**. Together with retention times, the mass spectrometry identification of these osmium complexes provides the basis of using HPLC/LC-MS to study the behaviour of these osmium complexes. In order to quantify the reactions by HPLC, proportionality between HPLC peak areas and concentrations of osmium complexes was established by combining with ICP-OES determinations.

3.5. Conclusions

In this chapter, **2-I•PF₆** and its chloride analogue **2-Cl•PF₆**, non-substituted template complex **1-Cl•PF₆**, imino analogue complexes **2-imp_y-I•PF₆** and **2-imp_y-Cl•PF₆**, hydrolysis product complex **[2-OH]⁺** (solution), N-acetyl-cysteine adduct **2-NAC**, and glutathione adduct **2-SG** were synthesized and characterized. The pK_a value of **[2-OH₂]²⁺** was determined as 5.20 ± 0.02 which indicates that under physiological conditions the more stable species **[2-OH]⁺** predominates. The IC₅₀ value of **[2-OH]⁺** towards A2780 ovarian cancer cells is 9.1 μM, less cytotoxic than **[2-Cl]⁺** and **[2-I]⁺**. The thiol adducts **2-NAC** and **2-SG** are completely inactive to cancer cells. The comparison between their cytotoxicity highlights the importance of halogen ligands. The acquisition of the electronic spectra and extinction coefficients for these osmium complexes presents the basis for further study of their reactions by UV-vis analysis. Their maximum absorbance at around 610 nm provides a useful detection wavelength in HPLC studies. The retention time and mass spectrometry identification of these osmium complexes renders it possible to analyse the reactions by HPLC/LC-MS. Moreover, the establishment of proportionality between HPLC peak area and concentrations provides a simple but sensitive method to quantitatively analyse the reactions of these osmium complexes in following chapters.

3.6. References

- (1) Sava, G.; Zorzet, S.; Turrin, C.; Vita, F.; Soranzo, M.; Zabucchi, G.; Cocchietto, M.; Bergamo, A.; DiGiovine, S.; Pezzoni, G. *Clin. Cancer. Res.* **2003**, *9*, 1898.
- (2) Kapitza, S.; Jakupec, M. A.; Uhl, M.; Keppler, B. K.; Marian, B. *Cancer Lett.* **2005**, *226*, 115.
- (3) Dougan, S. J.; Habtemariam, A.; McHale, S. E.; Parsons, S.; Sadler, P. J. *Proc. Natl. Acad. Sci. U.S.A.* **2008**, *105*, 11628.
- (4) Liu, Z.; Romero-Canelón, I.; Qamar, B.; Hearn, J. M.; Habtemariam, A.; Barry, N. P.; Pizarro, A. M.; Clarkson, G. J.; Sadler, P. J. *Angew. Chem. Int. Ed.* **2014**, *53*, 3941.
- (5) Fu, Y.; Romero, M. J.; Habtemariam, A.; Snowden, M. E.; Song, L.; Clarkson, G. J.; Qamar, B.; Pizarro, A. M.; Unwin, P. R.; Sadler, P. J. *Chem. Sci.* **2012**, *3*, 2485.
- (6) Fu, Y.; Habtemariam, A.; Pizarro, A. M.; van Rijt, S. H.; Healey, D. J.; Cooper, P. A.; Shnyder, S. D.; Clarkson, G. J.; Sadler, P. J. *J. Med. Chem.* **2010**, *53*, 8192.
- (7) Hearn, J. M.; Romero-Canelón, I.; Munro, A. F.; Fu, Y.; Pizarro, A. M.; Garnett, M. J.; McDermott, U.; Carragher, N. O.; Sadler, P. J. *Proc. Natl. Acad. Sci. U.S.A.* **2015**, *112*, E3800.

- (8) Shnyder, S. D.; Fu, Y.; Habtemariam, A.; van Rijt, S. H.; Cooper, P. A.; Loadman, P. M.; Sadler, P. J. *MedChemComm* **2011**, 2, 666.
- (9) Needham, R. J.; Sanchez-Cano, C.; Zhang, X.; Romero-Canelón, I.; Habtemariam, A.; Cooper, M. S.; Meszaros, L.; Clarkson, G. J.; Blower, P. J.; Sadler, P. J. *Angew. Chem. Int. Ed.* **2017**, 56, 1017.
- (10) Arthur, T.; Stephenson, T. A. *J. Organomet. Chem.* **1981**, 208, 369.
- (11) Dougan, S. J.; Melchart, M.; Habtemariam, A.; Parsons, S.; Sadler, P. J. *Inorg. Chem.* **2006**, 45, 10882.
- (12) Hindo, S. S.; Mancino, A. M.; Braymer, J. J.; Liu, Y.; Vivekanandan, S.; Ramamoorthy, A.; Lim, M. H. *J. Am. Chem. Soc.* **2009**, 131, 16663.
- (13) Gottlieb, H. E.; Kotlyar, V.; Nudelman, A. *J. Org. Chem.* **1997**, 62, 7512.
- (14) Krężel, A.; Bal, W. *J. Inorg. Biochem.* **2004**, 98, 161.
- (15) Becke, A. D. *J. Chem. Phys.* **1993**, 98, 5648.
- (16) Lee, C.; Yang, W.; Parr, R. G. *Phys. Rev. B* **1988**, 37, 785.
- (17) Grimme, S.; Antony, J.; Ehrlich, S.; Krieg, H. *J. Chem. Phys.* **2010**, 132, 154104.
- (18) Dunning, T. H.; Hay, P. J. In *Modern theoretical chemistry*; Plenum Press: New York, NY, 1977; Vol. 3, p 1.
- (19) Swinehart, D. F. *J. Chem. Educ.* **1962**, 39, 333.

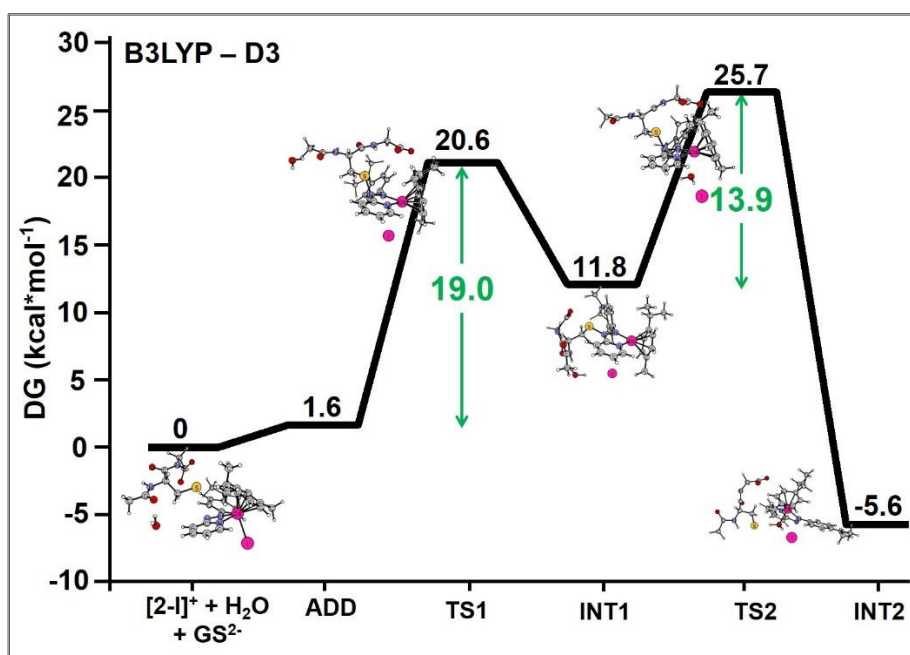
- (20) Pizarro, A. M.; Habtemariam, A.; Sadler, P. J. In *Medicinal Organometallic Chemistry. Topics in Organometallic Chemistry*; Jaouen, G., Metzler-Nolte, N., Eds.; Springer: Berlin, Heidelberg, 2010; Vol. 32, p 21.
- (21) Fernández, R.; Melchart, M.; Habtemariam, A.; Parsons, S.; Sadler, P. J. *Chem. Eur. J.* **2004**, *10*, 5173.
- (22) Peacock, A. F. A.; Parsons, S.; Sadler, P. J. *J. Am. Chem. Soc.* **2007**, *129*, 3348.
- (23) Peacock, A. F. A.; Melchart, M.; Deeth, R. J.; Habtemariam, A.; Parsons, S.; Sadler, P. J. *Chem. Eur. J.* **2007**, *13*, 2601.
- (24) Chen, H.; Parkinson, J. A.; Morris, R. E.; Sadler, P. J. *J. Am. Chem. Soc.* **2003**, *125*, 173.
- (25) Peacock, A. F. A.; Habtemariam, A.; Fernández, R.; Walland, V.; Fabbiani, F. P. A.; Parsons, S.; Aird, R. E.; Jodrell, D. I.; Sadler, P. J. *J. Am. Chem. Soc.* **2006**, *128*, 1739.
- (26) Peacock, A. F. A.; Habtemariam, A.; Moggach, S. A.; Prescimone, A.; Parsons, S.; Sadler, P. J. *Inorg. Chem.* **2007**, *46*, 4049.
- (27) Wang, F.; Chen, H.; Parsons, S.; Oswald, I. D. H.; Davidson, J. E.; Sadler, P. J. *Chem. Eur. J.* **2003**, *9*, 5810.
- (28) Helm, L.; Merbach, A. E. *Chem. Rev.* **2005**, *105*, 1923.

- (29) Berners-Price, S. J.; Appleton, T. G. In *Platinum-based drugs in cancer therapy*; Farrell, N. P., Kelland, L. R., Eds.; Humana Press Inc: Totawa, NJ, 2000, p 3.
- (30) Koelle, U. *Coord. Chem. Rev.* **1994**, *135*, 623.
- (31) Appleton, T. G.; Hall, J. R.; Ralph, S. F. *Inorg. Chem.* **1985**, *24*, 673.
- (32) Hunt, H. R.; Taube, H. *J. Am. Chem. Soc.* **1958**, *80*, 2642.
- (33) Buckingham, D. A.; Clark, C. R.; Rogers, A. J.; Simpson, J. *Inorg. Chem.* **1998**, *37*, 3497.
- (34) Fu, Y.; Habtemariam, A.; Basri, A. M.; Braddick, D.; Clarkson, G. J.; Sadler, P. J. *Dalton Trans.* **2011**, *40*, 10553.
- (35) Kasherman, Y.; Sturup, S.; Gibson, D. *J. Med. Chem.* **2009**, *52*, 4319.
- (36) Liu, Z.; Sadler, P. J. *Inorg. Chem. Front.* **2014**, *1*, 668.
- (37) Akimaru, K.; Kuo, M. T.; Furuta, K.; Suzuki, M.; Noyori, R.; Ishikawa, T. *Cytotechnology* **1996**, *19*, 221.
- (38) Senna, S. M.; Vidor, A. C.; Miyasaka, C. K.; Curi, R.; Williams, J. F. *Biochem. Mol. Biol. Int.* **1998**, *45*, 1243.
- (39) Ishikawa, T.; Akimaru, K.; Nakanishi, M.; Tomokiyo, K.; Furuta, K.; Suzuki, M.; Noyori, R. *Biochem. J.* **1998**, *336*, 569.
- (40) Heudi, O.; Cailleux, A.; Allain, P. *J. Inorg. Biochem.* **1998**, *71*, 61.

- (41) Appleton, T. G.; Berry, R. D.; Hall, J. R. *Inorg. Chim. Acta* **1982**, 64, L229.

Chapter 4

Hydrolysis Studies on Azopyridine Osmium Arene Complexes



4.1. Introduction

Half-sandwich organo-osmium complex $[\text{Os}(\eta^6\text{-p-cym})(4\text{-(2-pyridylazo)-}N,N\text{-dimethylaniline)I}]\text{PF}_6$ (**2-I•PF₆**, also known as **FY26**, **Figure 4.2**) has been reported to exhibit 49× times higher potency than cisplatin in >800 cancer cell lines whilst still retaining cytotoxicity to cisplatin-resistant cancer cells.¹⁻³ Thus, **2-I•PF₆** is considered as a very promising anticancer drug candidate to overcome the drug-resistance induced by platinum drugs. Understanding the mechanism of action of **2-I•PF₆**, an aim of this thesis, is a key process to contribute to its advancement to clinical application and ultimately lead the development of new analogues with improved performance.

For many anticancer metallodrugs, the hydrolysis process should not be ignored when considering their reactions with intracellular targets and exploration of anticancer mechanism. Cisplatin is known to undergo hydrolysis before binding to DNA.⁴⁻⁶ In the mechanism of action of cisplatin, H₂O attacks the Pt centre and replaces the chlorido ligand to form aquated products. This class of aquated product is a potent electrophile that can react with nucleophiles like nitrogen donor atoms on DNA base residues and then cause DNA damage.⁶ A similar mechanism action involving hydrolysis also has been observed for Ru(II) RAPTAs anticancer complexes (**Figure 4.1**). The liable Ru-Cl bonds in

the complex can be attacked by H₂O to form aquated Ru(II) adducts which can pH-dependently bind to DNA.^{7,8}

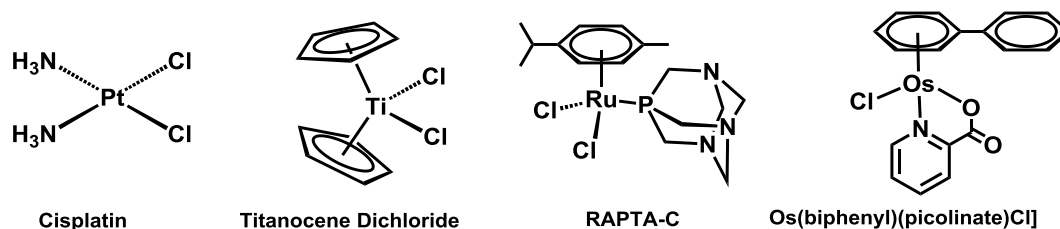


Figure 4.1. The molecular structures of anticancer complexes with their hydrolysis-mediated mechanism of action.

Moreover, the hydrolysis rate and reactivity of aquated adducts are crucial to the cytotoxicity of anticancer complexes. Inappropriate hydrolysis rates and reactivities of such hydrolysis products might limit their anticancer applications. The clinical trials of anticancer candidate drug titanocene dichloride were terminated at phase II in view of hydrolytic instability.^{9,10} During the development of organo-osmium anticancer complexes, N,N-chelators (e.g. ethylenediamine) and O,O-chelators (e.g. acetylacetonate) were introduced. However, both these two series of osmium complexes are inactive towards cancer cells in view of their excessive stability towards hydrolysis for N,N-chelating complexes or because of the excessive stability towards hydrolysis for O,O-chelating complexes.^{11,12} Finally, N,O-chelating osmium complexes (e.g. [Os(η^6 -biphenyl)(picolinate)Cl]) provide a balanced compromise for facile hydrolysis and acquiring activity comparable to that of

cisplatin.^{13,14} Overall, many examples can be given to highlight the importance of the hydrolysis process in the mechanism of action of metal-based anticancer complexes. The aim of this thesis is to explore the mechanism action of **2-I•PF₆**, and its hydrolysis is studied in this Chapter. Before these studies, Dr. Russell Needham (University of Warwick) found that **[2-I]⁺** is stable under physiological conditions. But once taken up by cancer cells, 99% of **[2-I]⁺** rapidly loses its iodide ligand.¹⁵ The intracellular tripeptide glutathione (γ -L-Glu-L-Cys-Gly, GSH) was indicated to be involved in this process and promoted the hydrolysis of **[2-I]⁺**. GSH is well known as the most abundant low molecular weight thiol with a concentration range 0.1-10 mM in cells and a key molecule in the redox system in cells (further introduction to GSH is in **Section 1.5** of **Chapter 1**).^{16,17}

Hence in this **Chapter 4**, the hydrolysis of **[2-I]⁺** in presence of GSH is studied in detail by techniques HPLC and LC-MS, including reactions of **[2-I]⁺** with various concentrations of GSH, and time- and pH-dependent reactions of **[2-I]⁺** with GSH. Based on the proportionality between the HPLC peak area and concentration of osmium species (**Section 3.3.6** of **Chapter 3**), these reactions were quantitatively analysed. Reactions of osmium complexes **[2-I]⁺** with GSH were also studied by NMR spectroscopy under an N₂ atmosphere to avoid the auto-oxidation of GSH

to GSSG in the air. In addition to GSH, the reactions of other free thiols such as N-acetyl-L-cysteine (NAC) and 1,4-dithiothreitol (DTT) were also with $[2-I]^+$ were also studied. In order to better understand the hydrolysis of $[2-I]^+$ in presence of GSH, reactions of GSH with analogues of $[2-I]^+$ including chlorido analogue $[2-Cl]^+$, hydroxido analogue $[2-OH]^+$ (hydrolysis product of $[2-I]^+$), glutathione adduct **2-SG**, imino analogue $[2-impy-I]^+$ were also investigated. After analysing the experimental results and investigating related literature, three possible mechanistic pathways for the hydrolysis of $[2-I]^+$ in presence of GSH were proposed and then probed using a computational approach based on density functional theory (DFT).

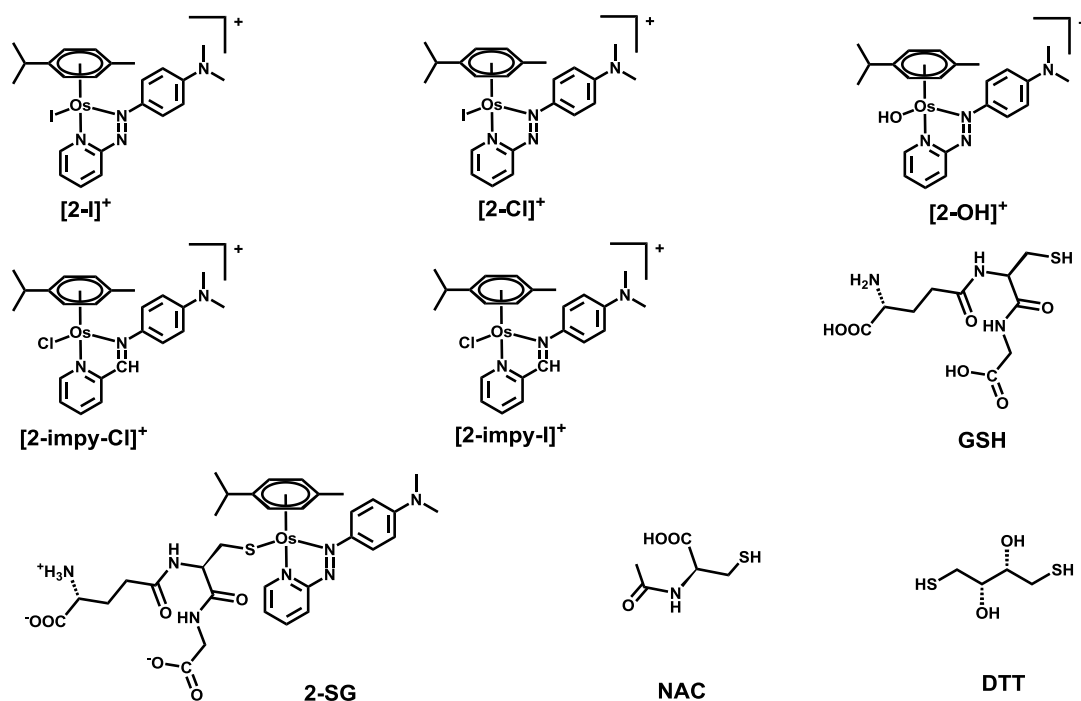


Figure 4.2. Molecular structures of the compounds studied in this chapter.

4.2. Experimental Section

4.2.1. Materials

The osmium complexes **2-I•PF₆**, **2-Cl•PF₆**, **2-impy-I•PF₆**, **[2-OH]⁺** (solution), **2-SG**, **2-NAC** were synthesised and characterized by procedures described in **Section 3.2.3 of Chapter 3**. The more soluble complex **2-I•Cl** was provided by Dr. Russell Needham (University of Warwick) for NMR experiments. In aqueous solution, both **2-I•PF₆** and **2-I•Cl** dissociate to **[2-I]⁺**. Phosphate buffer solutions (including deuterated phosphate buffer solution) were prepared as described in **Chapter 2, Section 2.12**. Reduced glutathione (**GSH**), N-acetyl-L-cysteine (**NAC**), and 1,4-dithiothreitol (**DTT**) were purchased from Sigma Aldrich. Sodium hydroxide, sodium chloride, sodium phosphate dibasic (Na₂HPO₄), sodium phosphate monobasic dehydrate (H₂NaPO₄·2H₂O), and trifluoroacetic acid were purchased from Fisher Scientific. Solvents used for high performance liquid chromatography (HPLC) and liquid chromatography-mass spectrometry (LC-MS) were purchased from Fisher Scientific. Analysis grade doubly deionised water (18 MΩ cm⁻¹) was obtained from either a Millipore Simplicity UV, or an USF Elga UHQ PS purification system. All other solvents and reagents for synthesis and analysis were purchased from commercial suppliers and used as received.

4.2.2. General Samples Preparation for HPLC Analysis

The osmium complexes was generally dissolved in doubly deionised water to prepare solutions of osmium complexes (100 μ M). GSH or other thiols (NAC, DTT) were dissolved in phosphate (300 mM) with sodium chloride (100 mM) buffer solution (pH = 7.40) with GSH concentrations of 0.3 mM - 30 mM. Then 3 mL osmium complex solution (100 μ M in H₂O) was mixed with 1 mL GSH solution (required concentration of GSH in 300 mM phosphate with 100 mM NaCl buffer solution) to give the experimental samples (75 μ M osmium complex with increasing concentrations of GSH in 75 mM phosphate buffer and 25 mM NaCl, pH = 7.40 solution). The experimental samples were incubated at 310 K for the required time.

4.2.3. pH-Dependent Reaction Studies by HPLC

The experimental solutions containing [2-I]⁺ (100 μ M) with GSH (200 μ M) in phosphate buffer (1 mM) at various pH values 2.43, 6.86 and 10.05. All the solutions were incubated at 310 K for the required time (3 h or 6 h). Due to the effect of different pH values on the performance of HPLC, each experimental solution (3 mL) was mixed with a high concentration phosphate buffer (1 mL, 300 mM phosphate buffer, pH = 7.40) to modify the pH value to 7.40 prior to injection onto the HPLC instrument.

4.2.4. HPLC Analysis Methods

An Agilent HPLC instrument with an Agilent ZORBAX Eclipse Plus C18 250×4.6 mm column was used to analyse the samples and reactions in this thesis. Mobile phases consisted of: (A) H₂O with 0.1 % TFA, and (B) MeCN with 0.1 % TFA at 1 mL/min. In view of the different polarity of organo-osmium bearing azo ligands and imino ligands, the solvent gradient methods are different for these two kinds of complexes. Osmium imino complexes were analysed at a detection wavelength of 254 nm with reference wavelengths set to 360 nm and 510 nm while osmium azo complexes were analysed at 610 nm with a reference wavelength set to 360 nm.

Table 4.1. The solvent B (acetonitrile) gradient used in HPLC for analysing osmium azo and imino complexes.

Time (min)	% (B) for azo complexes	% (B) for imino complexes
0	10	20
30	80	60
40	80	60
41	10	20
55	10	20

4.2.5. Quantitative Analysis of HPLC Traces

After acquiring the HPLC traces (detection wavelength is 610 nm and reference wavelength is 360 nm) for each samples, the peak areas on HPLC were integrated. The proportionality between HPLC peak area (y)

and concentrations of osmium complexes (x) was analysed in **Section 3.3.6 of Chapter 3**. These proportions were:

for **[2-Cl]⁺** is $y = (81.47 \pm 0.11)x - (4.38 \pm 6.33)$;

for **[2-I]⁺** is $y = (103.00 \pm 0.85)x - (126.09 \pm 16.61)$;

for **[2-OH]⁺** is $y = (81.95 \pm 0.68)x - (28.86 \pm 34.96)$;

for **2-SG** is $y = (84.63 \pm 0.048)x - (81.96 \pm 32.96)$.

Based on the proportionality for each complexes, concentrations of each osmium species were calculated from integrated peak areas and the percentage of each osmium species was then determined. The results were presented with error bar which was calculated from the uncertainty of equations.

4.2.6. Reactions under N₂ Atmosphere Studied by NMR

The reactions of **[2-I]⁺** with GSH were studied by ¹H NMR analysis under N₂ with to avoid its auto-oxidation of GSH by atmospheric O₂. The N₂-protected NMR experiments was carried out with a specific NMR tube with a screw cap. The osmium complex **2-I•Cl** (in aqueous solution, both **2-I•PF₆** and **2-I•Cl** dissociate to **[2-I]⁺**) for experiments were transferred into the NMR tube first, which was then placed in a long two-neck glass flask. A vacuum pump was used to remove the air from both NMR tube and long glass flask, then refilled with N₂. After repeating three times,

the NMR solvent was added and NMR tube cap was screwed while the N_2 was kept flowing. In this reaction, samples containing $[2-I]^+$ (2 mM) with GSH (200 μ M) in deuterated phosphate buffer solution (pH 7.40) were analysed in NMR experiments. The pH value of deuterated phosphate buffer solution was recorded as a pH meter reading pH^* and corrected to pH using the equation $pH = 0.929pH^* + 0.4^{18}$ due to effect of deuterium on the glass pH electrode.

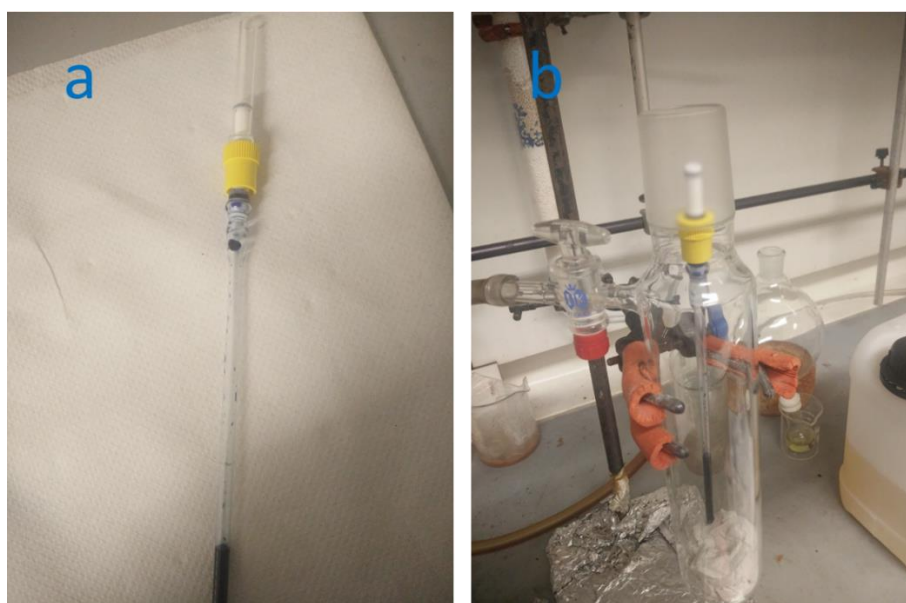


Figure 4.3. (a) The specific NMR tube, and (b) long two-neck flask for N_2 -protection in NMR experiments (from **Chapter 2**).

4.2.7. DFT Calculations

All the computational calculations were carried out by Prof. Emilia Sicilia (Università della Calabria, Italy). The Gaussian 09 program was employed to carry out all calculations in the framework of the density

functional theory using the hybrid Becke three-parameter exchange functional¹⁹ and the Lee–Yang–Parr correlation functional, B3LYP.²⁰ Dispersion corrections for nonbonding interactions have been included through the Grimme approach using atom pair-wise additive schemes,²¹ DFT-D3 method.

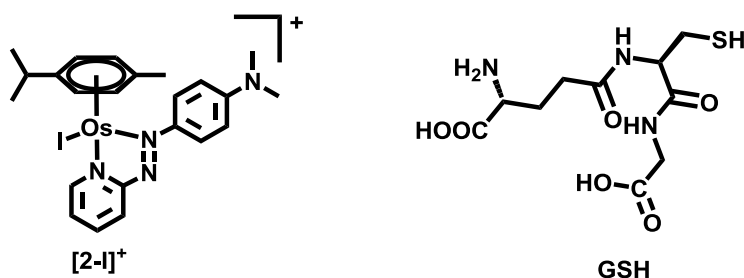
LANL2DZ effective core potential has been used for the Os atom,²² along with the split valence basis set. The standard triple- ζ quality 6-311+G** basis sets of Pople and coworkers have been used for the atoms directly participating in the process, whereas in order to reduce the computational effort, the 6-31G* basis sets have been employed for peripheral atoms. Vibrational frequencies at the same level of theory have been calculated for both establishing the nature of intercepted stationary points as minima and transition states and calculating zero-point energy (ZPE) and Gibbs free energy corrections. The intercepted transition states are first order saddle points on a potential energy surface (PES) and their vibrational spectrum is characterized by one imaginary frequency, corresponding to a negative force constant, which means that in one direction, in the nuclear configuration space, the energy has a maximum, while in all the other directions the energy has a minimum. Furthermore, transition states have been carefully checked to be properly connected to the correct minima by IRC (intrinsic reaction coordinate) analysis.^{23,24}

The Tomasi's implicit Polarizable Continuum Model (PCM)^{25,26} as implemented in Gaussian 09 has been used to include the effects due to the presence of the solvent and the UFF set of radii has been used to build-up the cavity in which the solute molecules are accommodated. Solvation Gibbs free energies have been calculated performing single-point calculations for all *in vacuum* stationary points structures in implicit water ($\epsilon=78.4$) at the same level of theory. Enthalpies and Gibbs free energies have been obtained using standard statistical procedures²⁷ at 298 K and 1 atm from total energies, including zero-point, thermal and solvent corrections. As the free energy corrections in the Gaussian's default standard state corresponds to an ideal gas at a standard pressure of 1 atm, the computed free energies have been converted²⁸ to yield Gibbs energies with a solution phase standard state of 1 mol L⁻¹ for all the species except water solvent. For water molecules a standard state of 55.5 M has been used. That is, to the free energy of each species, as computed in Gaussian, a free energy correction term equal to $RT \ln(V_{\text{molar gas}}/V_{\text{molar solution}})$, (R = gas constant, T = absolute temperature) has been added, where $V_{\text{molar gas}}$ is the volume occupied by one mole of ideal gas at the considered temperature, and $V_{\text{molar solution}}$ is the volume occupied by one mole of species in a standard solution of concentration of 1 mol L⁻¹.

4.3. Results

In this section, the results of quantitatively studying the hydrolysis of **[2-I]⁺** in presence of GSH under various conditions (different reagent ratios, reaction time, pH values) are presented. However, the influence of other free thiols (N-acetyl-L-cysteine and 1,4-dithiothreitol) on the hydrolysis of **[2-I]⁺** were explored. For comparison with **[2-I]⁺**, the behaviours of chlorido analogue **[2-Cl]⁺**, imino analogue **[2-imp_y-I]⁺**, hydroxido analogue **[2-OH]⁺** and thiolato analogue **2-SG** with GSH are also studied. Finally, three possible pathways for the hydrolysis of **[2-I]⁺** in presence of GSH are probed by DFT calculations.

4.3.1. Reactions of **[2-I]⁺** with GSH



Reactions of **[2-I]⁺ with various concentrations GSH.** The [Os (η^6 -*p*-cymene) (4-(2-pyridylazo)-*N,N*-dimethylaniline)I]⁺ (**[2-I]⁺**) (75 μ M) was incubated with various concentrations of GSH in phosphate (75 mM), NaCl (25 mM) buffer solution (pH = 7.40) for 24 h at 310 K. The concentrations of GSH are 0 mM, 0.08 mM, 0.38 mM, 0.75 mM, 0.94

mM, 1.88 mM, 3.75 mM, and 7.50 mM. As shown in **Figure 4.4**, several peaks were observed in the HPLC traces of the experimental samples and these peaks were identified based on their retention times, m/z values of LC-MS and HRMS. The characterisation data for each osmium species are summarized in **Table 4.2**. The HPLC peaks for each osmium species were integrated and quantified based on the proportionality between HPLC peak area and concentrations of osmium complexes (**Section 4.2.5**). The quantitative analysis results are shown in **Figure 4.5**.

From these results, it was shown that $[2-I]^+$ was very stable under physiological conditions and that less than 1% of $[2-I]^+$ was hydrolysed in absence of GSH, which indicated that $[2-I]^+$ was inert towards H_2O , phosphate and NaCl present. However, mixing with GSH dramatically decreased the percentage of $[2-I]^+$. 83% $[2-I]^+$ was left with 1 molar equivalent of GSH and only 22% $[2-I]^+$ was left with 5 molar equivalent GSH. However, an increase of $[2-OH]^+$ was observed with more added GSH. 15% $[2-OH]^+$ with 1 mole equiv GSH and the percentage of $[2-OH]^+$ was up to 80 % with 10 mole equiv GSH. Surprisingly, when 25 mole equiv GSH was added, the percentage of $[2-OH]^+$ decreased to 35% and no $[2-OH]^+$ was detected with neither 50 nor 100 mole equiv GSH. The decrease of $[2-OH]^+$ was mainly due to the increase of the thiolato adduct **2-SG** when co-incubated with higher concentrations of GSH. 35 %

2-SG was observed with 25 mole equiv GSH, and more than 95% **2-SG** predominated when adding 50 or 100 mole equiv GSH. Besides, other osmium species like chlorido analogue **[2-Cl]⁺** (due to presence of 25 mM NaCl mimicking cytoplasmic physiological conditions) and formation of the sulfenate analogue **2-SOG** was also observed.

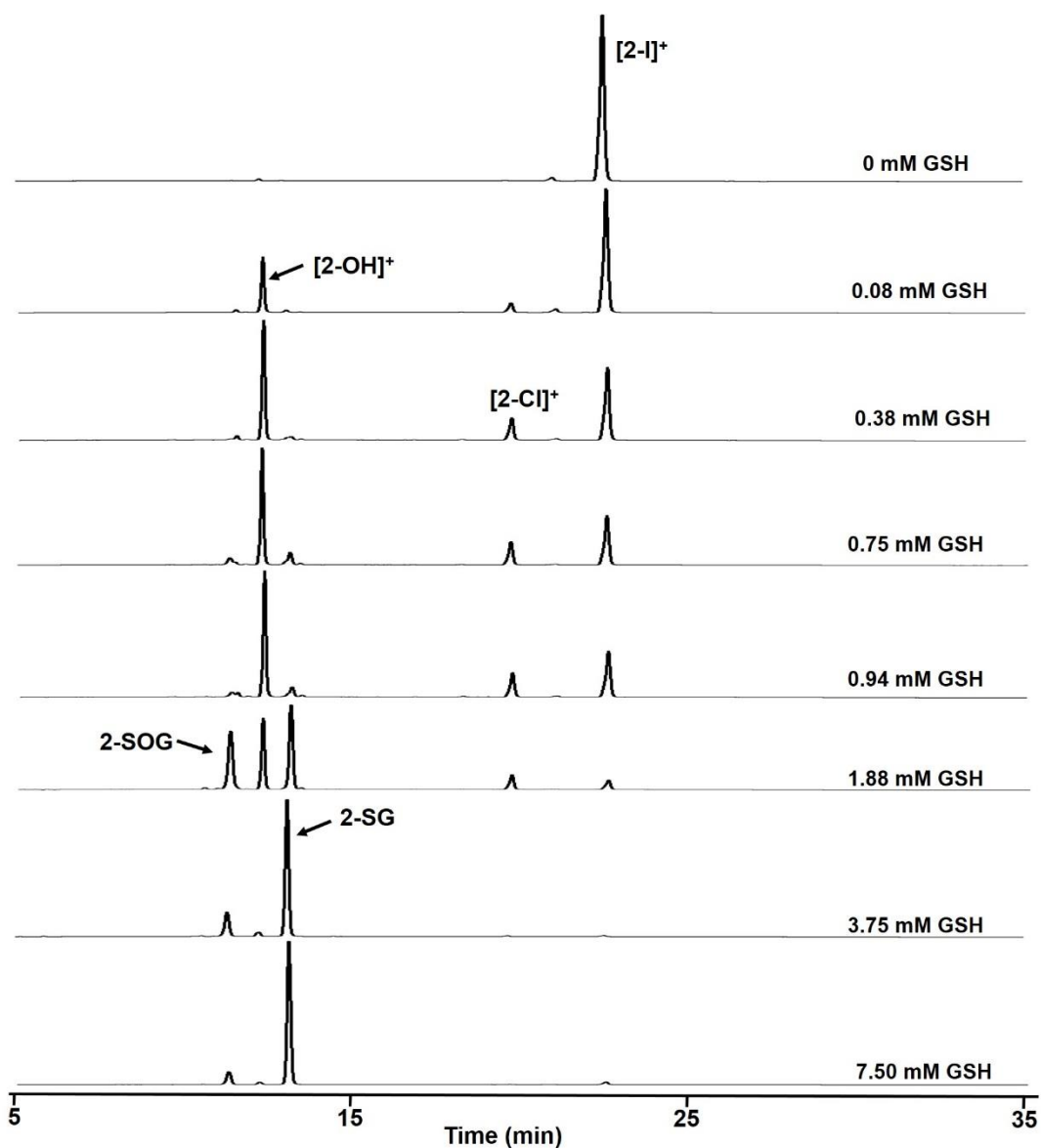
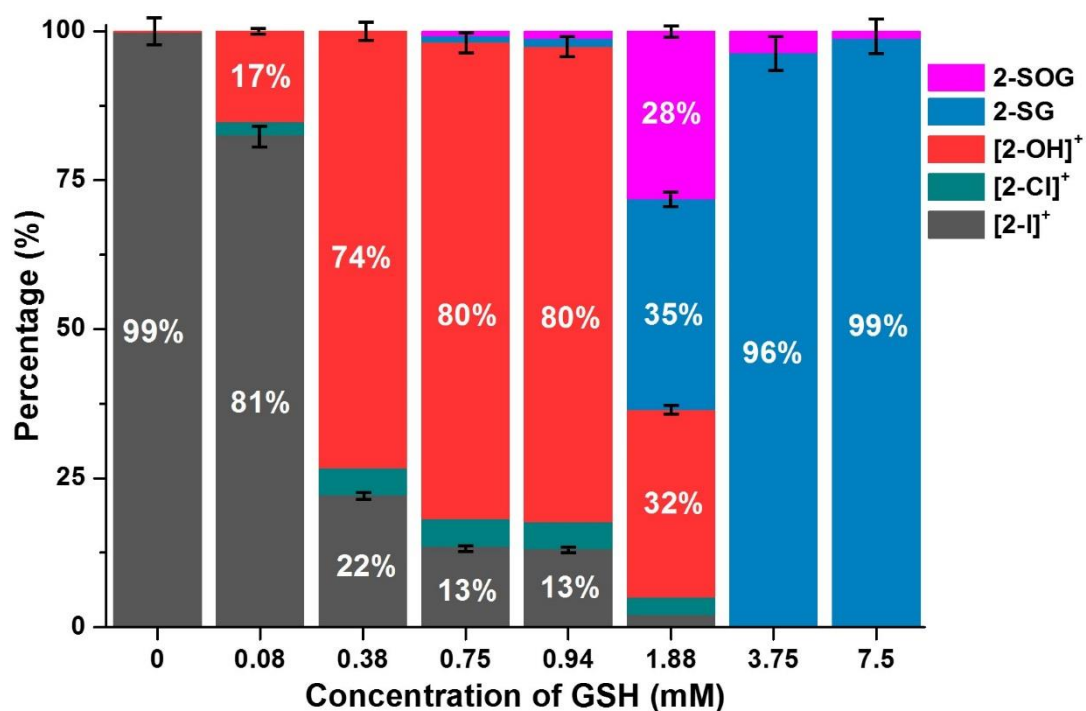


Figure 4.4. HPLC traces for reactions of complex **[2-I]⁺** (75 μ M) with various concentrations of GSH (0 - 7.5 mM) after incubation for 24 h at 310 K in phosphate buffer (75 mM, pH 7.40) with NaCl (25 mM).



GSH (mM)	Percentage of Osmium Species (%) ^a				
	[2-I] ⁺	[2-OH] ⁺	[2-Cl] ⁺	2-SG	2-SOG
0	98.65±3.45	1.65±0.05	0	0	0
0.08	80.64±2.82	17.15±0.54	2.21±0.08	0	0
0.38	21.68±0.76	73.6±2.31	4.72±0.17	0	0
0.75	13.34±0.47	80.18±2.52	4.65±0.16	0.97±0.04	0.86±0.04
0.94	13.08±0.46	80.24±2.52	4.26±0.16	0.99±0.04	1.43±0.06
1.88	2.1±0.07	31.51±0.99	2.91±0.11	35.31±1.59	28.17±1.27
3.75	0	0.23±0.07	0	96.17±4.33	3.60±0.15
7.50	0	0.13±0.04	0	98.67±4.44	1.20±0.05

^a mean±sd from uncertainty of the equations (Section 4.2.5)

Figure 4.5. Bar chart (top) and table (bottom) showing the percentage (%) of osmium species ([2-I]⁺, [2-Cl]⁺, [2-OH]⁺, 2-SG and 2-SOG) observed in reactions of [2-I]⁺ (75 μM) with various concentrations of GSH (0 - 7.5 mM) after incubation for 24 h at 310 K in phosphate buffer (75 mM, pH 7.40) with NaCl (25 mM).

Table 4.2. Species identified by HPLC/LC-S/HRMS, their molecular formulae, calculated and observed m/z values, and HPLC retention times (RT).

Species	Formula	Calculated m/z	Observed m/z (LCMS)	Observed m/z (HRMS)	HPLC RT (min)
[2-I] ⁺	C ₂₃ H ₂₈ IN ₄ Os ⁺	679.0969	679.02	679.0952	23.02
[2-Cl] ⁺	C ₂₃ H ₂₈ ClN ₄ Os ⁺	587.1602	587.21	587.1594	19.67
[2-imp-Cl] ⁺	C ₂₄ H ₂₉ ClN ₃ Os ⁺	586.1649	586.23	586.1633	26.43*
[2-imp-I] ⁺	C ₂₄ H ₂₉ IN ₃ Os ⁺	678.1016	678.17	678.1028	41.42*
[2-NO ₃] ⁺	C ₂₃ H ₂₈ N ₅ O ₃ Os ⁺	614.1802	614.11	614.1809	18.62
[2-NAC + H ⁺] ⁺	C ₂₈ H ₃₆ N ₅ O ₃ SOs ⁺	714.2147	714.16	714.2149	15.68
[2-OH] ⁺	C ₂₃ H ₂₉ N ₄ OOs ⁺	569.1951	569.17	569.1941	12.53
[2-imp-OH] ⁺	C ₂₄ H ₃₀ N ₃ OOs ⁺	568.1999	568.23	568.1999	11.30*
[2-SG + H ⁺] ⁺	C ₃₃ H ₄₄ N ₇ O ₆ OsS ⁺	858.2682	858.19	858.2693	13.29
[2-imp-SG + H ⁺] ⁺	C ₃₄ H ₄₅ N ₆ O ₆ OsS ⁺	857.2730	857.11	857.2738	12.44*
[2-SOG + H ⁺] ⁺	C ₃₃ H ₄₄ N ₇ O ₇ OsS ⁺	874.2632	874.15	874.2634	11.54

*The method applied in HPLC separations for imino complexes is different from that for azo complexes (Section 4.2.4).

Time-dependent reactions of [2-I]⁺ with GSH. [2-I]⁺ (75 μ M) was incubated with 25 mole equiv GSH (1.88 mM) in phosphate (75 mM), NaCl (25 mM) buffer solution (pH 7.40) at 310 K and this reaction was analysed at different time points (5 min, 1 h, 3 h, 6 h, 18 h and 24 h). The reaction started with 100% [2-I]⁺, but after 1 h incubation periods, the percentage of [2-I]⁺ dramatically decreased to 83% with 16% hydrolysis product [2-OH]⁺ together with 1% of the chlorido analogue [2-Cl]⁺ (**Figure 4.6**). With increasing reaction time, 16% of the glutathione adduct 2-SG was observed after 6 h incubation. The sulfenate adduct 2-SOG was the last osmium species to appear after a 18 h incubation period.

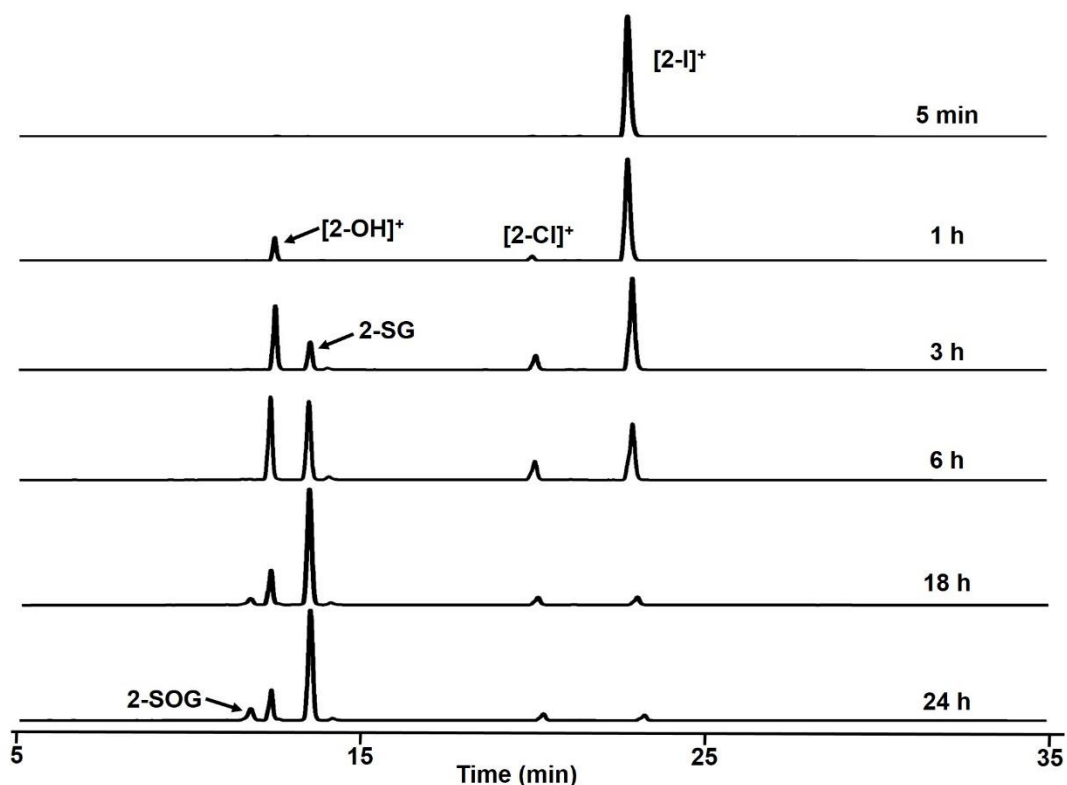
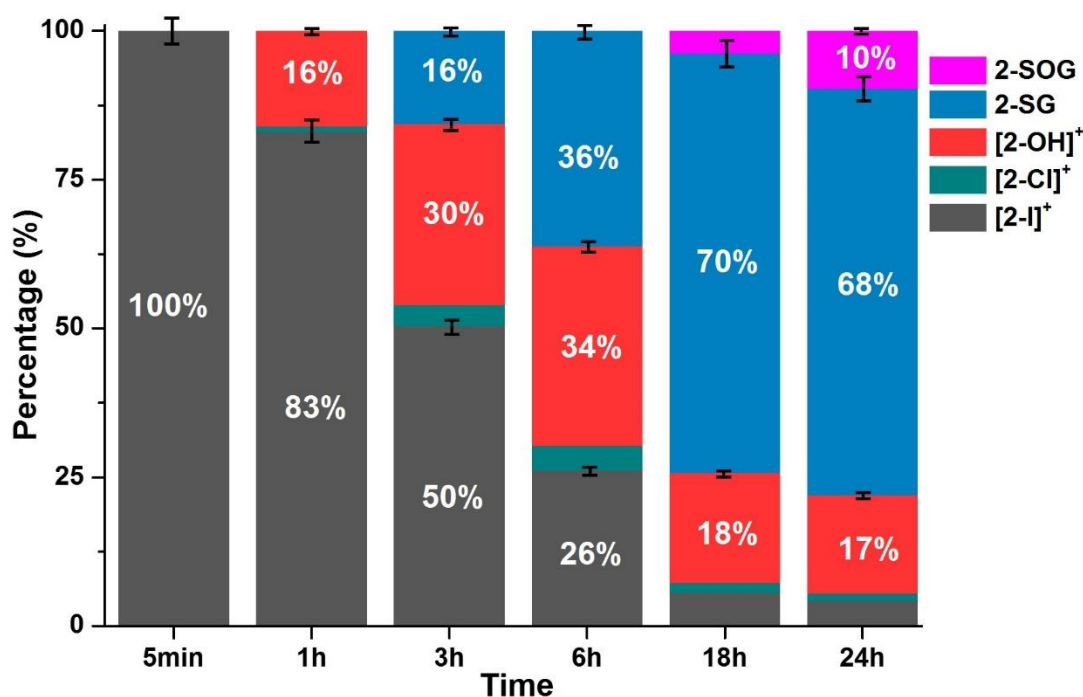


Figure 4.6. HPLC traces for kinetic reactions of [2-I]⁺ (75 μ M) with GSH (1.88 mM) at 310 K in phosphate buffer (75 mM, pH 7.40) with NaCl (25 mM).



Time	Percentage of Osmium Species (%) ^a				
	[2-I] ⁺	[2-Cl] ⁺	[2-OH] ⁺	2-SG	2-SOG
5 min	100.00±3.50	0	0	0	0
1 h	83.09±2.91	0.88±0.03	16.03±0.59	0	0
3 h	50.45±1.77	3.58±0.11	30.38±1.12	15.59±0.70	0
6 h	26.22±0.92	4.08±0.13	33.63±1.24	36.07±1.62	0
18 h	5.62±0.20	1.69±0.05	18.47±0.68	70.47±3.17	3.75±0.17
24 h	4.23±0.19	1.35±0.04	16.54±0.61	68.23±3.07	9.65±0.43

^a mean±sd from uncertainty of the equations (Section 4.2.5)

Figure 4.7. Bar chart (top) and table (bottom) showing the percentage (%) of osmium species ([2-I]⁺, [2-Cl]⁺, [2-OH]⁺, 2-SG and 2-SOG) observed in the reaction of [2-I]⁺ (75 μM) with GSH (1.88 mM) after 5 min, 1 h, 3 h, 6 h, 18 h, 24 h incubation at 310 K in phosphate buffer (75 mM, pH 7.40) with NaCl (25 mM).

pH-dependent reactions of $[2-I]^+$ with GSH. $[2-I]^+$ (100 μM) was incubated with 2 mol equiv of GSH (200 μM) under various pH values (pH = 2.43, 6.86 and 10.05) at 310 K and analysed with HPLC after 3 h or 6 h incubation. Less than 1% of the hydrolysis product $[2-OH]^+$ was observed at pH 2.43 after either 3 h or 6 h incubation. However, 14% of $[2-OH]^+$ was observed at a pH 6.86, and 45% $[2-OH]^+$ at pH 10.05 after 3 h incubation (**Figure 4.10**). It seems that acidic conditions inhibited the hydrolysis of $[2-I]^+$ by reaction with GSH while basic conditions promoted the reaction. In control experiments of $[2-I]^+$ incubated at pH 10.05 without GSH, little hydrolysis was observed after 24 h (**Figure 4.9**).

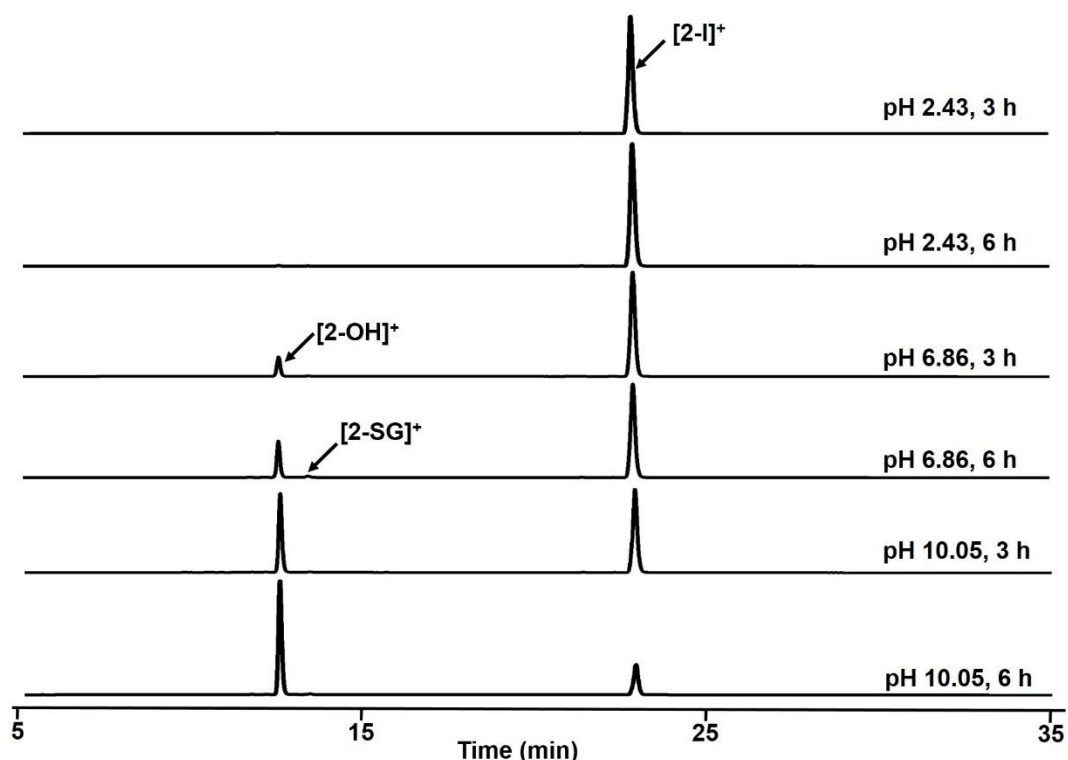


Figure 4.8. HPLC traces for the reactions of $[2-I]^+$ (100 μM) with GSH (200 μM) at various pH values (2.43, 6.86, 10.05) in phosphate buffer (1 mM) after 3 h or 6 h incubation at 310 K.

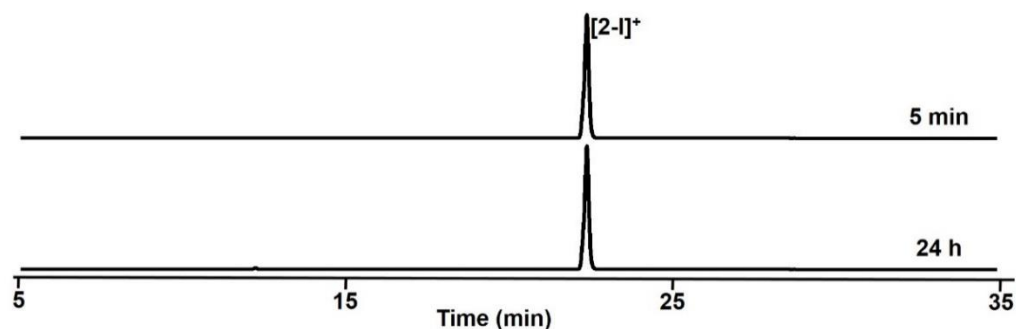
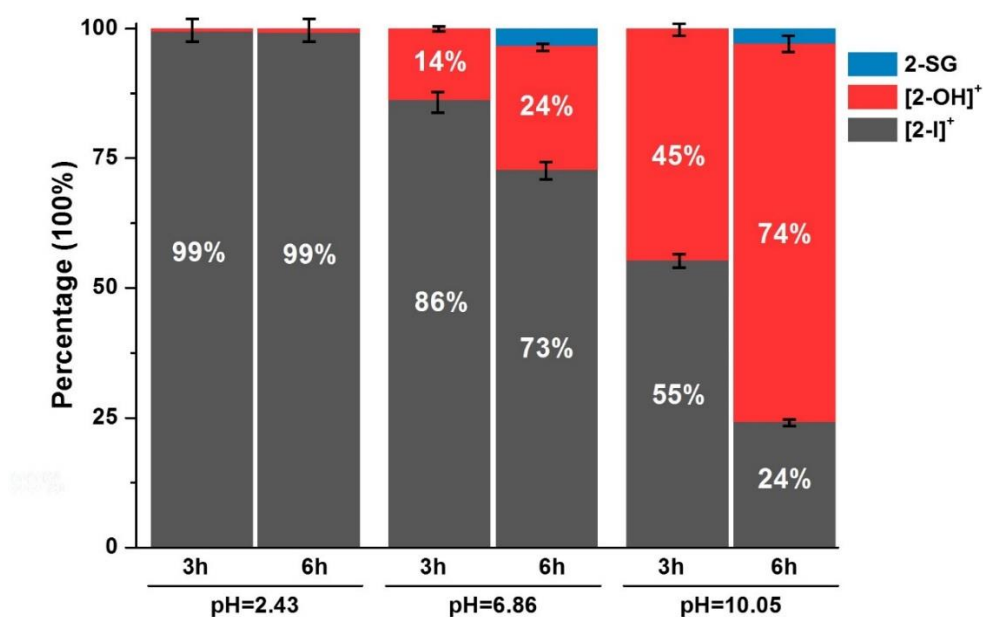


Figure 4.9. HPLC traces for complex $[2-I]^+$ ($100\ \mu\text{M}$) after 5 min or 24 h incubation at 310 K for in basic phosphate buffer (1 mM, pH 10.05) solution.



Time	pH value	Percentage of Osmium Species (%) ^a		
		$[2-I]^+$	$[2-OH]^+$	2-SG
3 h	2.43	99.40±3.48	0.60±0.02	0
	6.86	86.22±3.02	13.78±0.51	0
	10.05	55.39±1.94	44.61±1.65	0
6 h	2.43	99.26±3.47	0.74±0.03	0
	6.86	72.83±2.55	23.87±0.88	3.30±0.15
	10.05	24.24±0.85	72.85±2.70	2.91±0.13

^a mean±sd from uncertainty of the equations (Section 4.2.5)

Figure 4.10. Bar chart (top) and table (bottom) showing percentage (%) of osmium species ($[2-I]^+$, $[2-OH]^+$ and 2-SG) observed in the reaction of $[2-I]^+$ ($100\ \mu\text{M}$) with GSH ($200\ \mu\text{M}$) under different pH (2.43, 6.86 and 10.05) in phosphate buffer (1 mM) after 3 h or 6 h incubation at 310 K.

NMR studies of reactions of $[2-I]^+$ with GSH under N_2 . The reaction of $[2-I]^+$ (2 mM) with 0.1 mole equiv GSH (0.2 mM) in deuterated phosphate buffer (75 mM, pH 7.40) with NaCl (25 mM) was studied under an N_2 atmosphere. Each spectrum for the reaction was recorded every 5 min on a AV-400 spectrometer at 298 K for 2 h. The spectra show significant level of $[2-OH]^+$ (525 μ M) was generated while little GSH was consumed. This suggests that the thiol might be regenerated during the reaction, playing a catalytic role in the hydrolytic process with a turn over frequency number of 1.97 h^{-1} (200 μ M GSH catalyses 525 μ M $[2-I]^+$ to hydrolyse in 90 min).

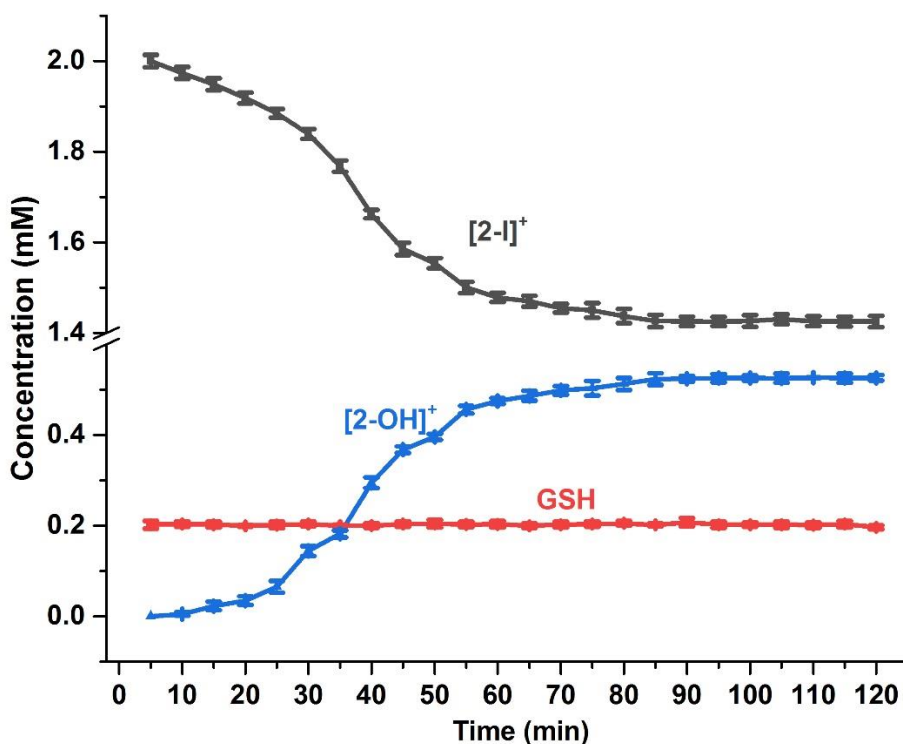


Figure 4.11. The change in concentrations of GSH, $[2-I]^+$ and $[2-OH]^+$ through a 2 h for the reaction of $[2-I]^+$ (2 mM) with GSH (200 μ M, 10% mole equiv) in phosphate buffer (75 mM, pH 7.40) at 298 K under N_2 (mean \pm sd is based on three independently NMR peak integration).

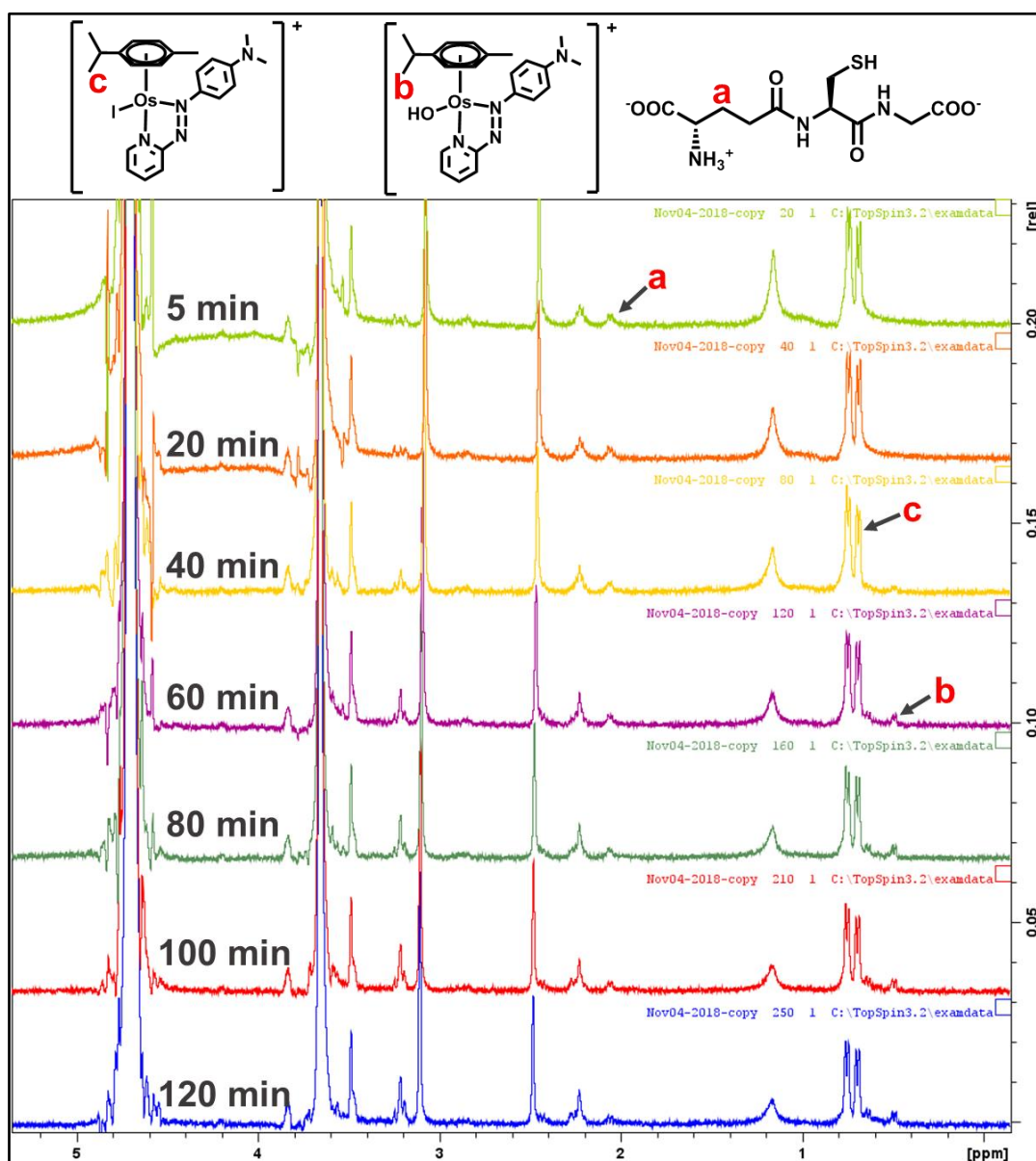
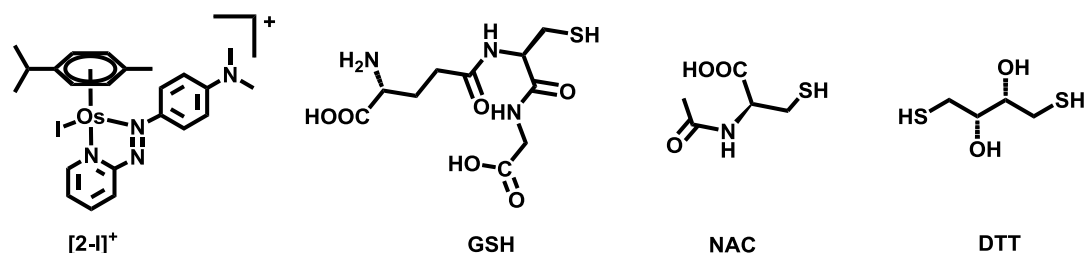


Figure 4.12. The NMR spectra and assignment for the reactions of $[2-I]^+$ (2 mM) with GSH (200 μ M, 10% mole equiv) in phosphate buffer (75 mM, pH 7.40) after different reaction times at 298 K under N_2 .

4.3.2. Reactions of $[2-I]^+$ with Various Thiols

The reactions of $[2-I]^+$ (75 μ M) with 10 mole equiv GSH, NAC or DTT (0.75 mM) in phosphate buffer (75 mM, pH 7.40) with NaCl (25 mM) were studied after 24 h incubation at 310 K. Significant amounts of the hydrolysis product $[2-OH]^+$ were observed in all the reactions with free thiols GSH, NAC and DTT, which indicated that the thiol group (-SH) is the key functional group in reactions with $[2-I]^+$.

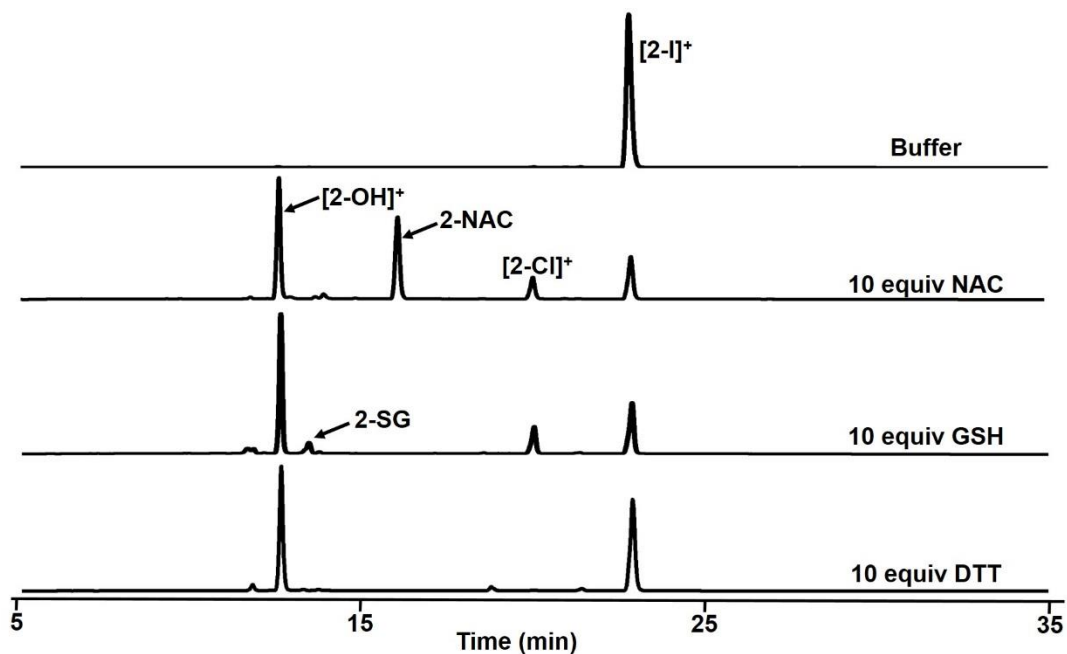
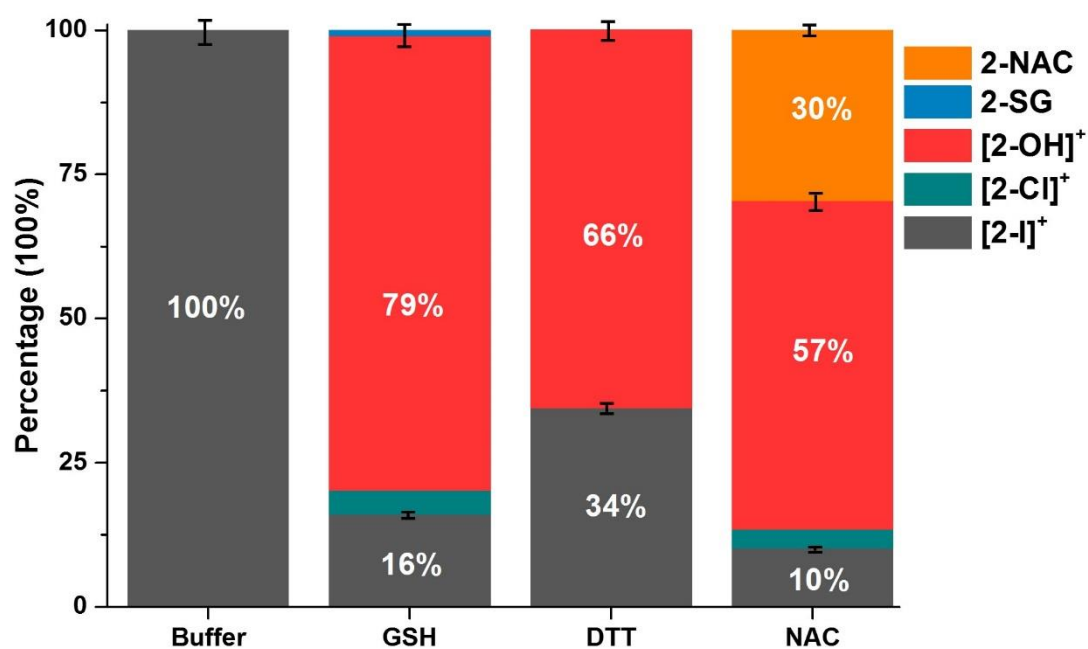


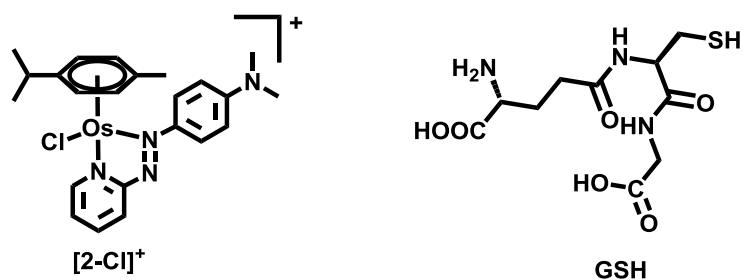
Figure 4.13. HPLC traces for the reactions of $[2-I]^+$ (75 μ M) with the thiols NAC, GSH or DTT (0.75 mM) in phosphate buffer (75 mM, pH 7.4) with NaCl (25 mM) after 24 h incubation at 310 K.



^a mean±sd from uncertainty of the equations (Section 4.2.5)

Figure 4.14. Bar chart (top) and table (bottom) showing percentage (%) of osmium species ([2-I]⁺, [2-Cl]⁺, [2-OH]⁺, 2-SG and 2-NAC) observed in the reaction of [2-I]⁺ (75 μM) with thiols GSH, NAC or DTT (0.75 mM) in phosphate buffer (75 mM, pH 7.4) with NaCl (25 mM) after 24 h incubation at 310 K.

4.3.3. Reactions of Chlorido Complex $[2-\text{Cl}]^+$ with GSH



Reaction of $[2-\text{Cl}]^+$ with various concentrations of GSH. $[\text{Os}(\eta^6\text{-p-cymene})(4\text{-(2-pyridylazo)-}N,N\text{-dimethylaniline})\text{Cl}]^+$ ($[2-\text{Cl}]^+$) (75 μM) was incubated with various concentrations of GSH in phosphate (75 mM), NaCl (25 mM) buffer solution (pH = 7.40) for 24 h at 310 K. The concentrations of GSH were 0, 0.08, 0.38, 0.75, 0.94, 1.88, 3.75, and 7.50 mM. All these reactions were quantitatively analysed based on the proportionality between HPLC peak area and concentrations of osmium complexes (**Section 4.2.5**). The identification of each peak observed in HPLC traces is summarized in **Table 4.2**.

Similar to the behaviour of $[2-\text{I}]^+$ in reactions with GSH observed in **Section 4.3.1**, $[2-\text{Cl}]^+$ was stable under physiological conditions but GSH significantly induced the hydrolysis of $[2-\text{Cl}]^+$. Co-incubation with 1 mole equiv GSH dramatically induced 91% $[2-\text{Cl}]^+$ to hydrolyse. With addition of more GSH, the thiolate adduct **2-SG** and sulfenate adduct **2-SOG** started to be observed. The highest percentage of **2-SOG** (27%)

appeared when $[2\text{-Cl}]^+$ was incubated with 25 mole equiv GSH and **2-SG** predominated when $[2\text{-Cl}]^+$ reacted with 50 or 100 mole equiv GSH.

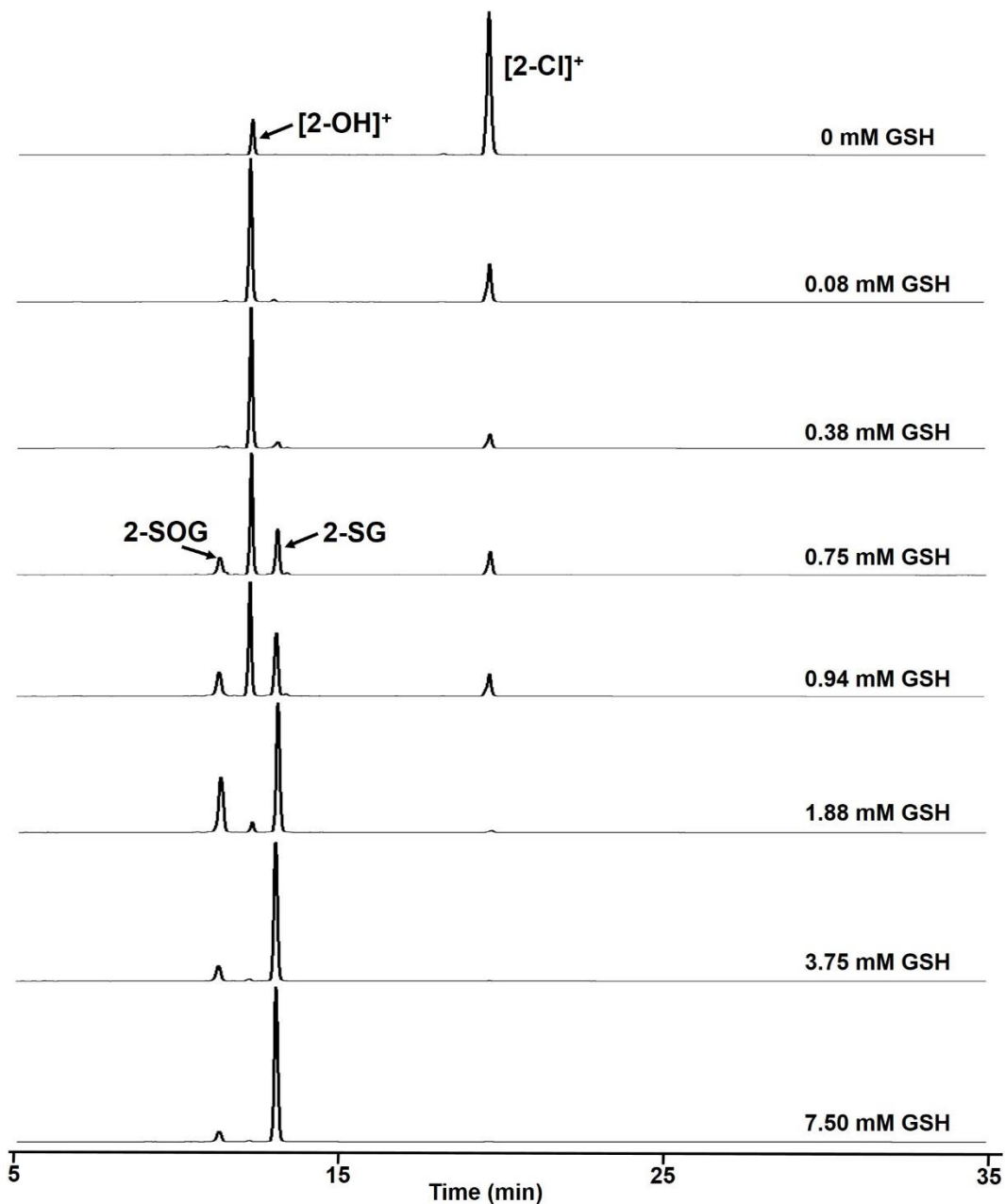
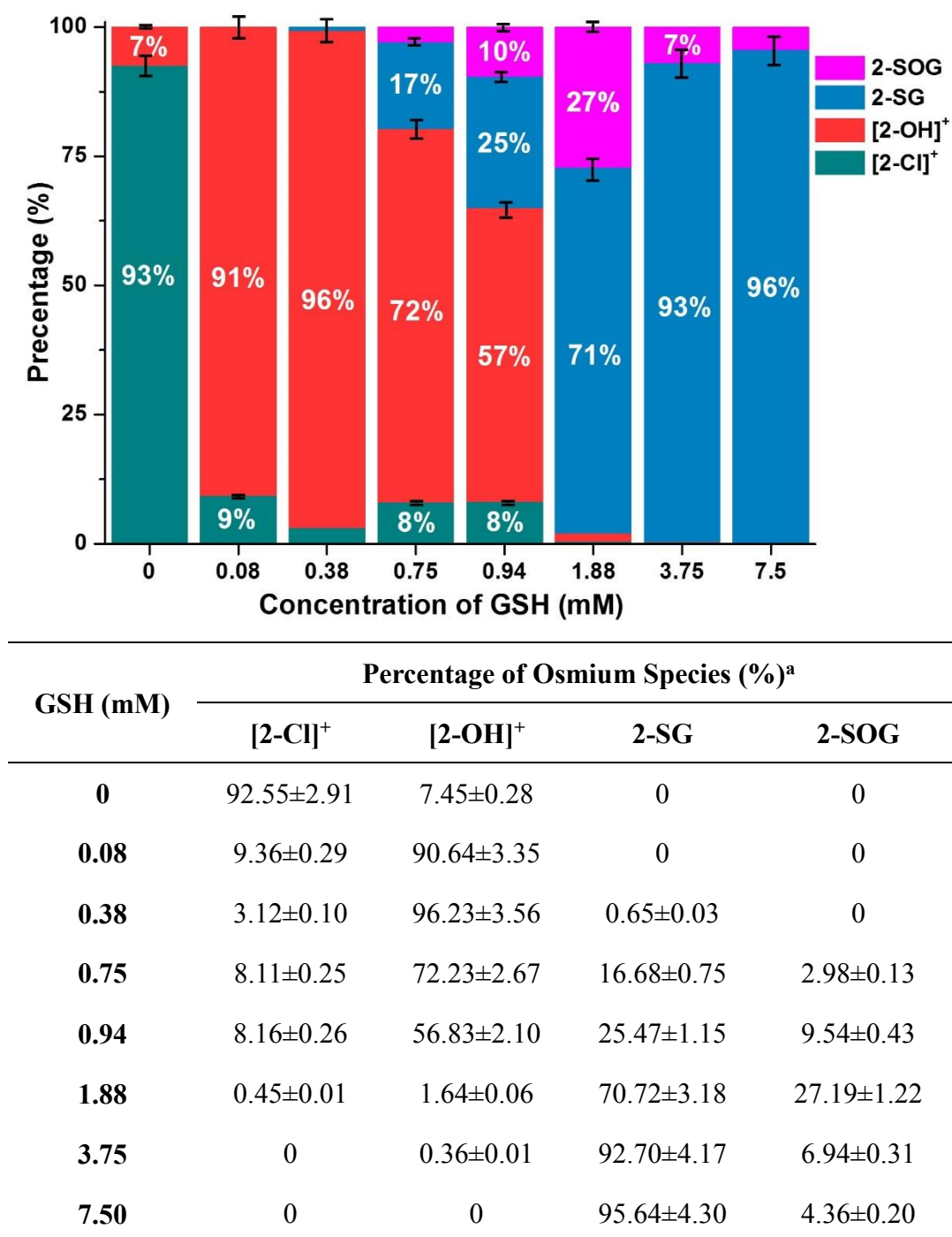


Figure 4.15. HPLC traces for reactions of complex $[2\text{-Cl}]^+$ (75 μM) with various concentrations of GSH (0 - 7.5 mM) in phosphate buffer (75 mM, pH 7.40) with NaCl (25 mM) after 24 h incubation at 310 K.



^a mean±sd from uncertainty of the equations (Section 4.2.5)

Figure 4.16. Bar chart (top) and table (bottom) showing percentage (%) of osmium species ([2-Cl]⁺, [2-OH]⁺, 2-SG and 2-SOG) observed in the reaction of [2-Cl]⁺ (75 μM) with various concentrations of GSH (0 - 7.5 mM) in phosphate buffer (75 mM, pH 7.40) with NaCl (25 mM) after 24 h incubation at 310 K.

Time-dependent reactions of $[2\text{-Cl}]^+$ with GSH. $[2\text{-Cl}]^+$ ($75\ \mu\text{M}$) was incubated with 12.5 mole equivalent GSH ($0.94\ \text{mM}$) in phosphate ($75\ \text{mM}$), NaCl ($25\ \text{mM}$) buffer solution (pH 7.40) at $310\ \text{K}$ and this reaction was analysed at different time points (5 min, 1 h, 3 h, 6 h, 18 h and 24 h) by HPLC. After 1 h incubation more than 80% $[2\text{-Cl}]^+$ underwent hydrolysis to generate $[2\text{-OH}]^+$ and after 3 h incubation 14% **2-SG** formed. The sulfenate complex **2-SOG** was the last specie to appear after 18 h incubation and there was still 28% **2-SOG** present after 24 h incubation (**Figure 4.17** and **Figure 4.18**).

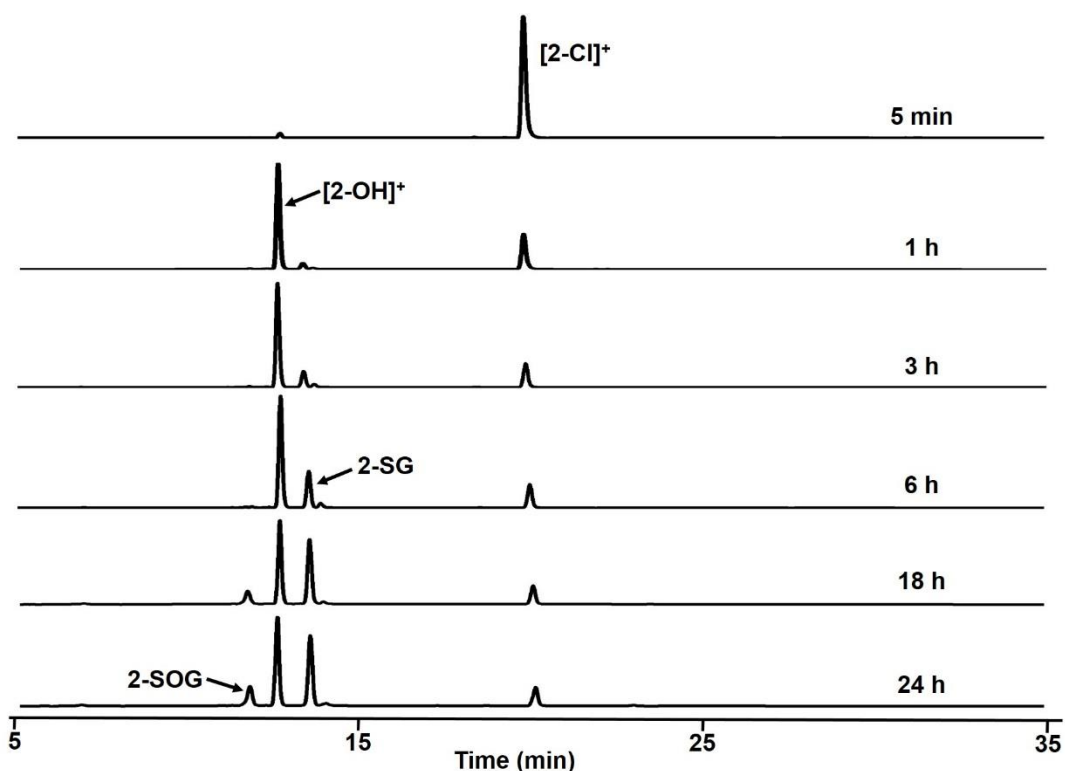
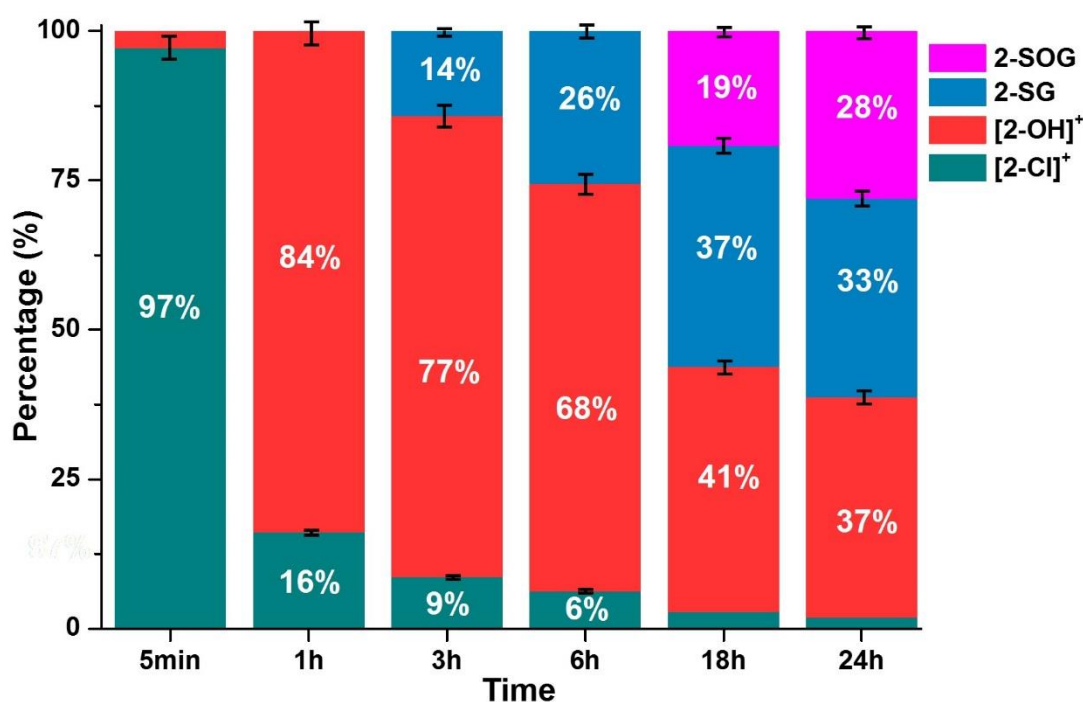


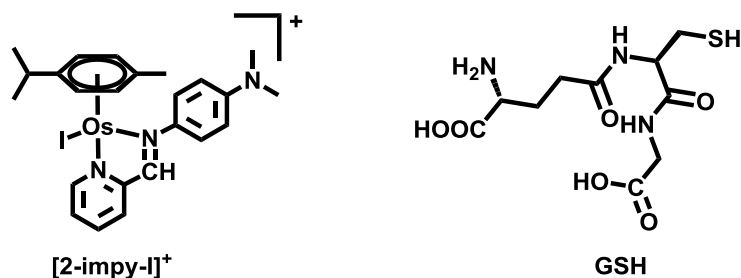
Figure 4.17. HPLC traces for kinetic reaction of $[2\text{-Cl}]^+$ ($75\ \mu\text{M}$) with GSH ($0.94\ \text{mM}$) at $310\ \text{K}$ in phosphate buffer ($75\ \text{mM}$, pH 7.40) with NaCl ($25\ \text{mM}$).



Time	Percentage of Osmium Species (%) ^a			
	[2-Cl] ⁺	[2-OH] ⁺	2-SG	2-SOG
5 min	97.17±3.05	2.83±0.11	0	0
1 h	16.21±0.51	83.79±3.10	0	0
3 h	8.70±0.27	77.09±2.85	14.21±0.64	0
6 h	6.34±0.20	68.10±2.52	25.56±1.15	0
18 h	2.87±0.09	41.01±1.52	36.92±1.66	19.20±0.86
24 h	1.96±0.06	36.81±1.36	33.25±1.50	27.98±1.26

^a mean±sd from uncertainty of the equations (Section 4.2.5)

Figure 4.18. Bar chart (top) and table (bottom) showing the percentages (%) of osmium species ([2-Cl]⁺, [2-OH]⁺, 2-SG and 2-SOG) observed in the reaction of [2-Cl]⁺ (75 μM) with GSH (0.94 mM) after 5 min, 1 h, 3 h, 6 h, 18 h, 24 h incubation at 310 K in phosphate buffer solution (75 mM, pH 7.40) with NaCl (25 mM).

4.3.4. Reactions of Imino Analogue [2-imp π -I]⁺ with GSH

[2-imp π -I]⁺ (75 μ M) was incubated with 1 or 2 mole equiv GSH (75 μ M or 150 μ M) in phosphate (75 mM), NaCl (25 mM) buffer solution (pH 7.40) at 310 K and these reactions were analysed at different time points (5 min, 3 h, 24 h) by HPLC analysis. In view of the different chemical properties of imino analogue, the method applied for HPLC analysis of these reactions was different from the method for analysing reactions of azo complexes ([2-I]⁺, [2-Cl]⁺) (Section 4.2.4). The peaks observed in the HPLC traces were identified and assigned based on the retention time and HRMS spectrometry which have been summarized at **Table 4.2**.

The imino analogue [2-imp π -I]⁺ showed a completely different behaviour to the azo complex [2-I]⁺ during its hydrolysis and reactions with GSH. Firstly, [2-imp π -I]⁺ is not as stable as [2-I]⁺ under physiological conditions. After 3 h incubation in absence of GSH, almost half [2-imp π -I]⁺ hydrolysed to [2-imp π -OH]⁺. More surprisingly, co-incubation with GSH did not increase the extent of hydrolysis of [2-imp π -I]⁺ after either 3 h or 24 h. However, the extent of formation of the thiolate adduct 2-imp π -SG dramatically increased even with 1 mole

equiv GSH. In presence of 2 mole equiv GSH, thiolate adduct **2-impy-SG** completely predominated in the reactions while similar predomination of **2-SG** needed 50 mole equiv GSH to react with $[2-I]^+$. Besides, no glutathione sulfenate adduct could be detected in the reaction of $[2\text{-impy-I}]^+$ with GSH.

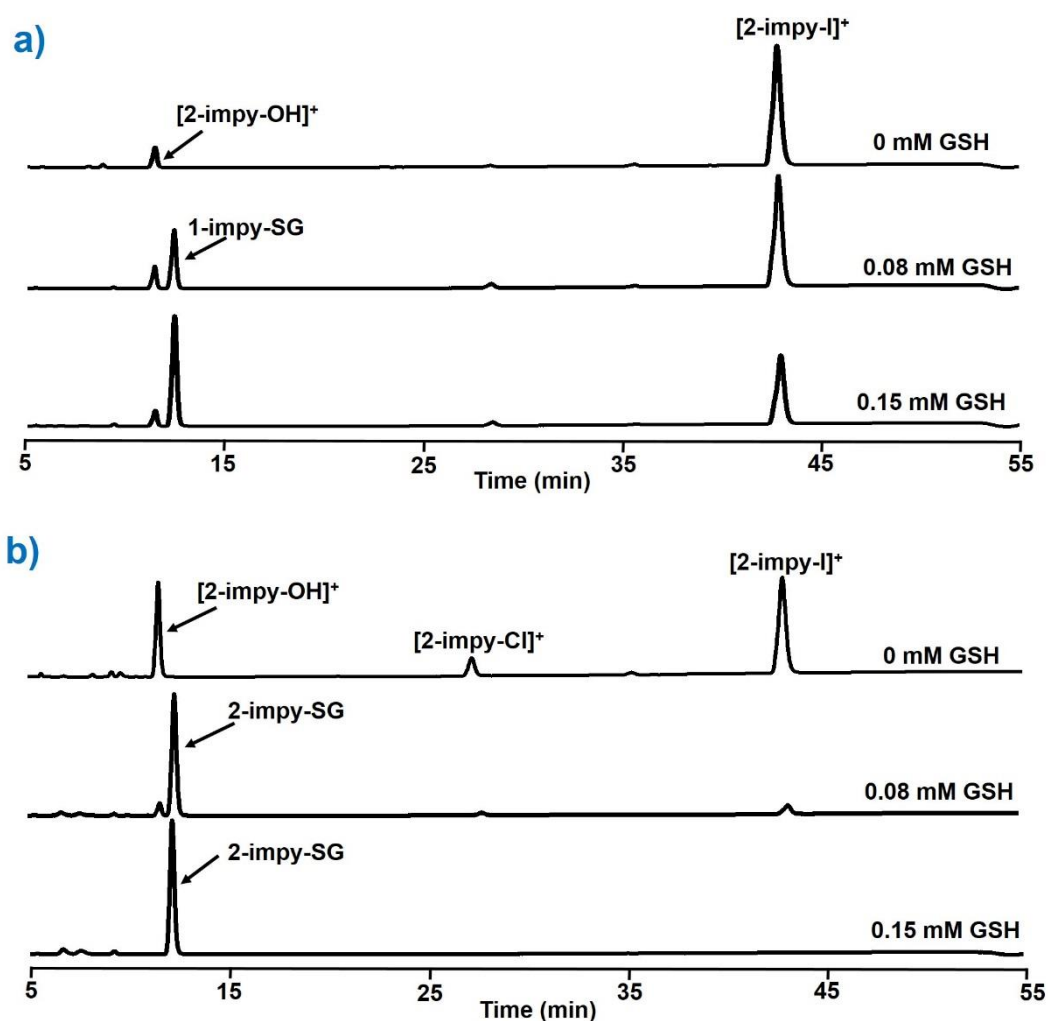
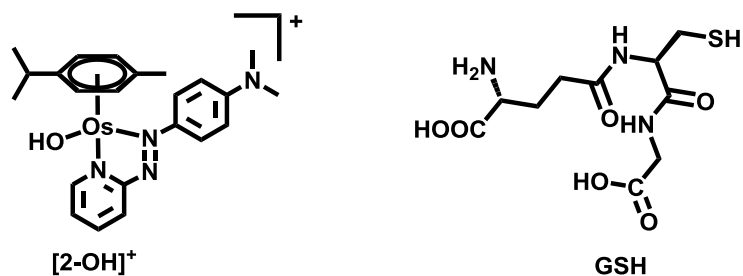


Figure 4.19. HPLC traces for the reaction of $[2\text{-impy-I}]^+$ (75 μM) with GSH (0 mM, 0.08 mM, 0.15 mM) after (a) 3 h and (b) 24 h incubation at 310 K in phosphate buffer (75 mM, pH 7.40) with NaCl (25 mM).

4.3.5. Reactions of Hydroxido Complex $[2\text{-OH}]^+$ with GSH

In the reactions of GSH with $[2\text{-I}]^+$ or $[2\text{-Cl}]^+$, the hydrolysis product $[2\text{-OH}]^+$ was normally observed. Therefore the behaviour of $[2\text{-OH}]^+$ was also explored in reactions with GSH. Thus the reactions of $[2\text{-OH}]^+$ (75 μM) with various concentration GSH (0, 0.08, 0.38, 0.75, 0.94, 1.88, 3.75, 7.5 mM) in phosphate (75 mM), NaCl (25 mM) buffer solution (pH 7.40) were analysed after 24 h incubation at 310 K. All the peaks observed in HPLC traces were identified and assigned based on retention times and mass spectrometry (**Table 4.2**). Complex $[2\text{-Cl}]^+$ was observed when $[2\text{-OH}]^+$ was incubated in NaCl (25 mM) solution without GSH, which demonstrated that $[2\text{-OH}]^+$ could react with Cl^- to generate $[2\text{-Cl}]^+$. Then $[2\text{-OH}]^+$ was incubated in KI (25 mM) in phosphate (75 mM) buffer solution (pH 7.40) and $[2\text{-I}]^+$ was observed after 24 h incubation at 310 K. In presence of more than 10 mole equiv GSH, thiolate adduct **2-SG** and sulfenate adduct **2-SOG** were observed during the reactions (**Figure 4.20**), similar to the reaction of $[2\text{-I}]^+$ with GSH.

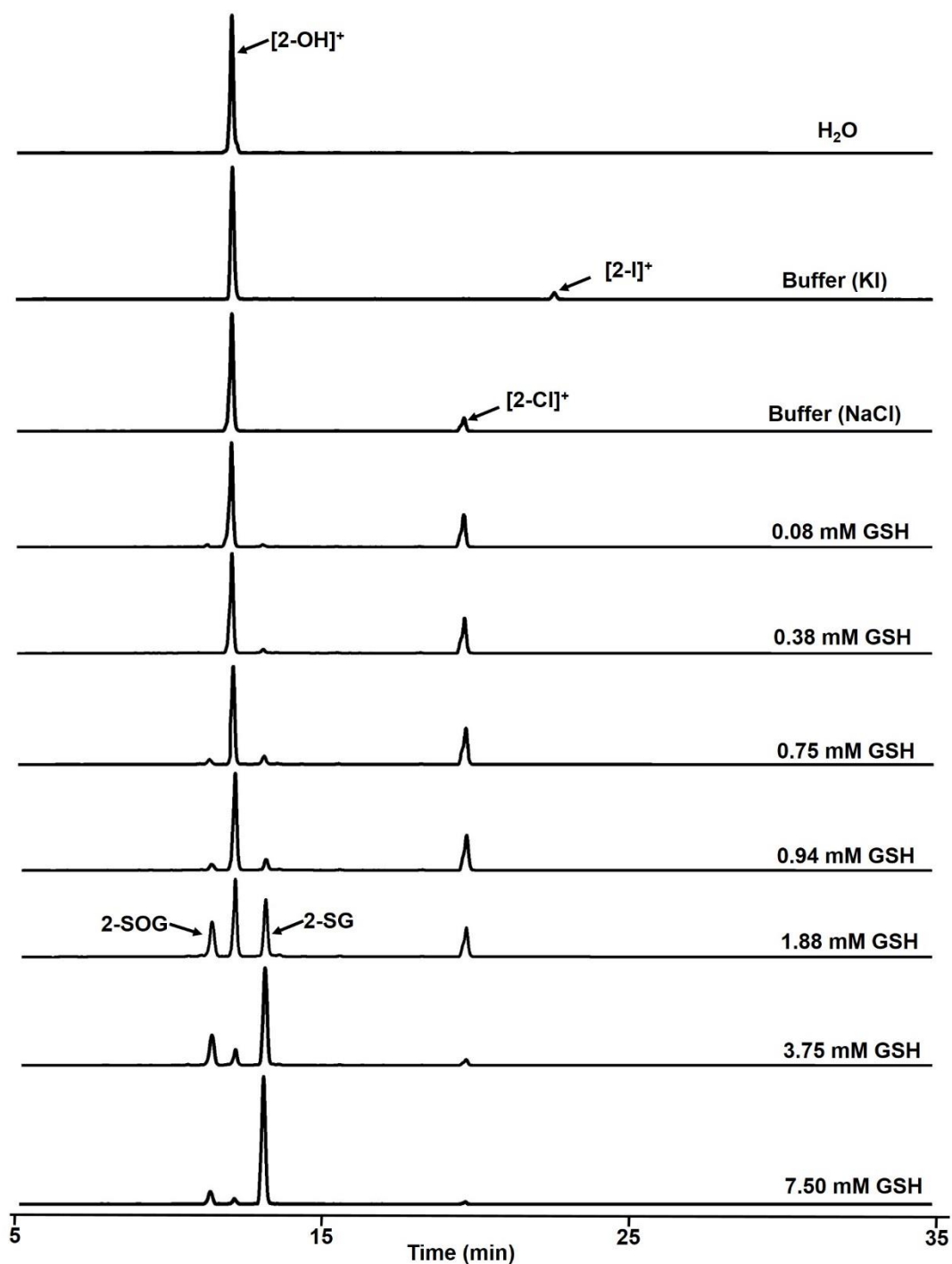
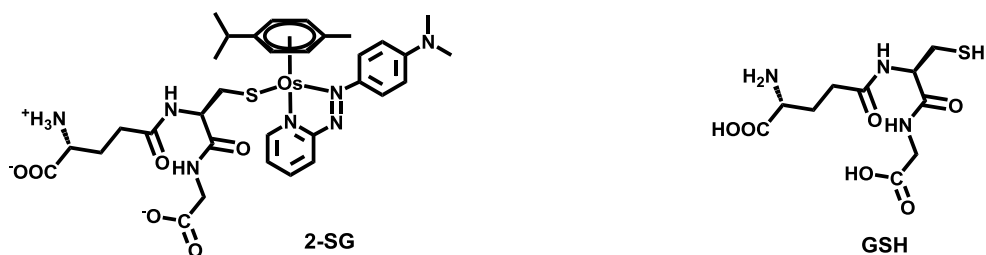


Figure 4.20. HPLC traces for reactions of complex $[2\text{-OH}]^+$ (75 μM) with KI (25 mM), NaCl (25 mM) or various concentrations of GSH (0 - 7.5 mM) with NaCl (25 mM) after incubation for 24 h at 310 K in phosphate buffer (75 mM, pH 7.40).

4.3.6. Reactions of the Glutathione Adduct 2-SG with GSH



Reactions of **2-SG** with **GSH** in phosphate (75 mM), NaCl (25 mM) buffer solution (pH 7.40) were analysed after 24 h incubation at 310 K. All the peaks observed were identified and assigned based on retention times and mass spectrometry (**Table 4.2**). Complex **2-SG** is quite stable in absence of GSH under physiological relevant conditions, but when mixed with GSH, the sulfenate analogue **2-SOG** was observed, which might cause by the oxidative species from the reaction of GSH with dioxygen in the air. However, it was surprising that the hydroxido adduct **[2-OH]⁺** was also observed during this reaction with GSH (**Figure 4.21**).

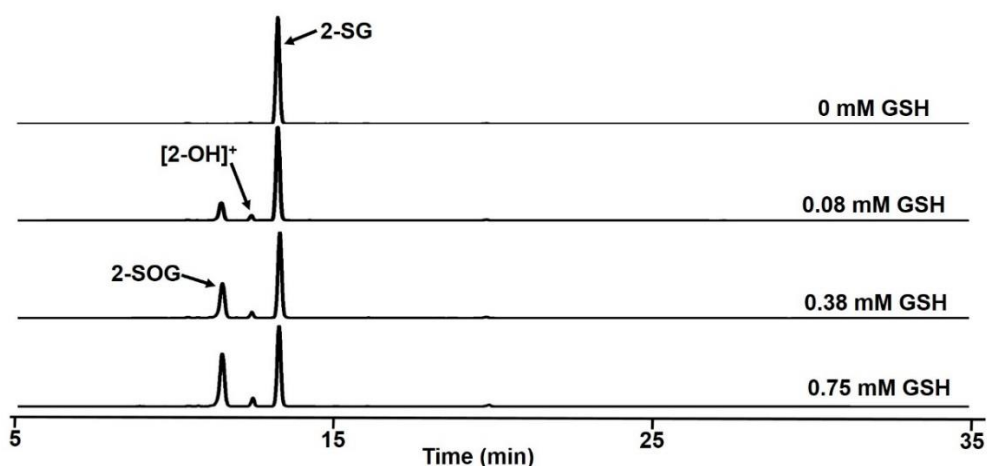


Figure 4.21. HPLC traces for the reactions of [2-SG]⁺ (75 μM) with GSH (0 mM, 0.08 mM, 0.38 mM, 0.75 mM) after 24 h incubation at 310 K in phosphate buffer (75 mM, pH 7.40) with NaCl (25 mM).

4.3.7. Hydrolysis Mechanism and DFT Calculations

The hydrolysis of $[2-I]^+$ in presence of GSH was probed using a computational approach based on DFT calculations carried out by Prof. Emilia Sicilia (Università della Calabria, Italy). Three different possible reaction mechanisms were analysed. These were chosen since they have been previously reported to occur in molecules related to $[2-I]^+$, and included:

- 1) Direct hydrolysis of the Os-I bond in presence of water, which occurs at normal physiological conditions for several organometallic complexes of the type $[M(\text{arene})(L-L')X]^+$ (where M is, Os, Ru, Rh or Ir; arene, a polyhapto arene; L-L', a chelating ligand; and X an halide);^{13,29-32}
- 2) Direct interaction of the metal ion centre with GSH, For example, $[Ru(\text{arene})(\text{ethylenediammine})Cl]PF_6$ and its analogues form Ru-SG adducts through direct interaction with GSH, displacing the coordinated halide in the process. Thiolate adducts can then be oxidised in presence of O_2 , forming unstable Ru-SOG species that are easily hydrolysed.³³
- 3) Hydrolysis through redox mediation by the azo group, as organic diazenes structurally similar to the chelating ligand present in $[2-I]^+$ are known to catalyse the oxidation of GSH in presence of O_2 ,

generating hydrazines and H_2O_2 during the process.^{34,35} This reaction has also been observed when diazenes are coordinated to Ru(II) or Ir(III).³⁶⁻³⁸

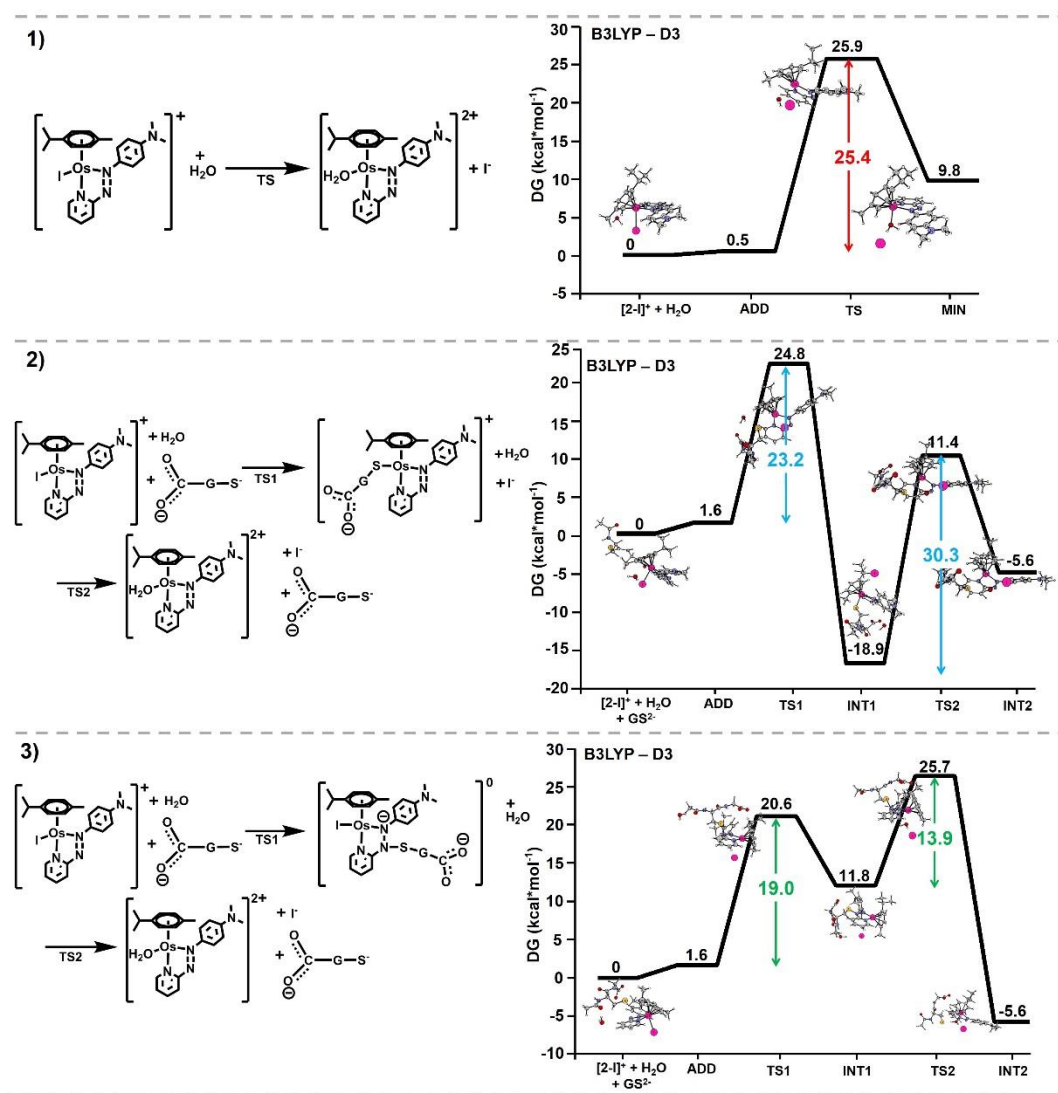


Figure 4.22. DFT analysis of the different reaction pathways for $[2-\text{I}]^+$ with GSH (GS^{2-} is deprotonated form of GSH).

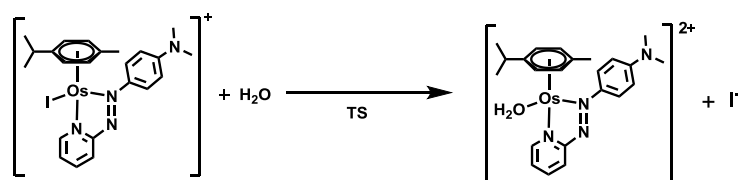
Results obtained from DFT calculations showed differences in the energy barriers obtained for the three pathways proposed for the reaction (**Figure 4.22**). Direct hydrolysis in the presence of water and interaction with GSH had relatively high energy barriers (25.4 and 23.2 kcal/mol, respectively). Moreover, direct interaction of GSH with Os(II) led to stable Os-SG adducts, and a possible hydrolysis of those species presented a much higher energy barrier (30.3 kcal/mol). On the contrary, the hydrolysis pathway considering the redox interaction between GSH and the azo ligand present in **[2-I]⁺** showed the lowest initial energy barrier (19.4 kcal/mol). This allowed formation of a direct bond between GSH and the -N=N- bond present in **[2-I]⁺**, generating an area of high electronic density close to the Os centre which appeared to destabilise the Os-I bond, and therefore facilitate hydrolysis (modelled as a second step with an energy barrier of 13.9 kcal/mol as shown in **Figure 4.22**).

4.4. Discussion

The organo-osmium anticancer complex $[\text{Os}(\eta^6\text{-p-cym})(4\text{-(2-pyridylazo)-}N,N\text{-dimethylaniline})\text{I}]\text{PF}_6$ (**2-I•PF₆**, also known as **FY26**) has been reported as a very promising next generation anticancer drug in view of its high potency *in vitro* and *in vivo*.^{2,3} **[2-I]⁺** was relatively inert in solution under physiological conditions, but surprisingly released the iodido monodentate ligand very fast once uptaken into cancer cells.¹⁵ The intracellular tripeptide glutathione (**GSH**) was thought to be involved into this process and activate the prodrug **[2-I]⁺** to the more reactive hydroxido adduct **[2-OH]⁺**.¹⁵ As part of the aim of exploring the mechanism of action of **[2-I]⁺** in this thesis, hydrolysis studies of **[2-I]⁺** in presence of GSH were studied in this **Chapter**, combining experimental (HPLC, NMR) and theoretical (DFT calculation) approaches. Based on the fundamental work in **Chapter 3** of synthesis and characterization of the osmium complexes (**[2-I]⁺**, **[2-Cl]⁺**, **[2-OH]⁺**, **2-SG**) related to the reaction of **[2-I]⁺** with GSH and build-up the proportionality between the HPLC peak area *versus* concentration of osmium species, the hydrolysis of **[2-I]⁺** in presence of GSH was systematically studied and quantitatively analysed. On the basis of previous studies of the hydrolysis of metal complexes, three different hydrolysis modes were proposed for **[2-I]⁺** and then these three possible

pathways were probed and analysed based on DFT calculations. Finally, the energy barriers of each pathway from the DFT calculations and the results of experiments were combined to present a reasonable mechanism for the hydrolysis of **[2-I]⁺**.

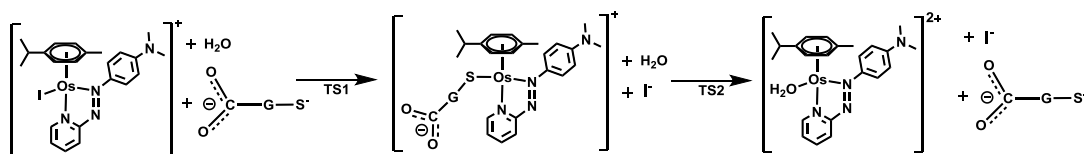
Pathway 1



The first pathway proposed for the hydrolysis of **[2-I]⁺** involved the direct attack on the Os-I bond by H₂O (**Pathway 1**), which occurs in many coordination complexes, such as cisplatin,^{39,40} and several organometallic complexes of the type [M (arene) (L-L') X]⁺ (where M is, Os, Ru, or Ir; arene, a polyhapto arene or Cp*; L-L', a chelating ligand; and X an halide).^{29,32} The DFT calculations demonstrated that this pathway was thermodynamically possible with an energy barrier of 25.4 kcal/mol. Meanwhile, the experimental results obtained for **[2-I]⁺** and its chlorido analogue **[2-Cl]⁺** in the absence of GSH were consistent with the DFT calculations performed. After 24 h incubation under physiological conditions, there was 0.13% (**Figure 4.5**) and 7.45% (**Figure 4.16**) hydrolysis of **[2-I]⁺** and **[2-Cl]⁺**, respectively. However, the degree of

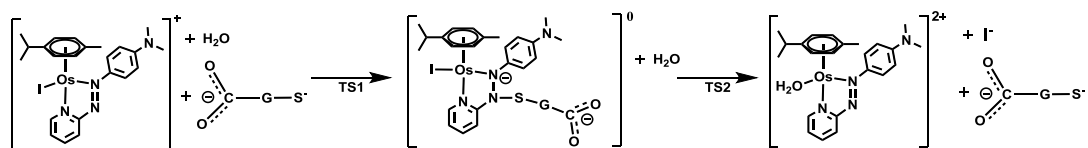
hydrolysis is quite low, and the energy barrier for this pathway seems relatively too high to contribute the whole hydrolysis of **[2-I]⁺** within cells. Especially in comparison with the dramatically increased hydrolysis in presence of GSH, there should be other more feasible pathways which contribute to the hydrolysis of **[2-I]⁺** involving GSH.

Pathway 2



The second pathway proposed for the hydrolysis of **[2-I]⁺** with GSH present involves GS^{2-} (deprotonated GSH) attacking the Os-I bond to form thiolate adduct **2-SG** and then the H_2O attacking the Os-S bond to generate the hydrolysis product **[2-OH]⁺** (**Pathway 2**). This pathway is inspired from reported studies on $[\text{Ru}(\text{arene})(\text{ethylenediamine})\text{Cl}]\text{PF}_6$ and its analogues which form Ru-SG adducts through its direct interaction with GSH, displacing the coordinated halide ligand in the process. Thiolato adducts can then be oxidised in presence of O_2 , forming unstable Ru-SOG species that are easily hydrolysed.³³ The DFT calculations indicated that this pathway is thermodynamically possible with an energy barrier 23.2 kcal/mol for GS^{2-} attacking Os-I bond and

30.3 kcal/mol for H₂O attack on the Os-S bond. The experimental results appear to support this pathway. **2-SG** was observed in the reaction of [**2-I**]⁺ with GSH (**Figure 4.5**), which suggested that it was possible for GSH to attack the Os-I bond. The sulfenate analogue **2-SOG** and hydrolysis product [**2-OH**]⁺ were observed as products from the co-incubation of **2-SG** with GSH (**Figure 4.21**), which was quite similar to reactions of a Ru arene thiolate adduct^{33,41} and indicated that [**2-I**]⁺ can undergo hydrolysis through this pathway. However, the energy barrier for H₂O attack on the Os-S bond in this pathway was even higher than that for H₂O directly attacking Os-I in **Pathway 1**. Only a very small amount (less than 2%) hydrolysis product [**2-OH**]⁺ was observed from the reaction of **2-SG** with or without GSH. The same problem was observed for **Pathway 2** as with **Pathway 1** with H₂O directly attacking Os-I. Both these two pathways were thermodynamically possible, but quite a small percentage hydrolysis product would be generated from them due to their high energy barriers. In the kinetic reaction of [**2-I**]⁺ with GSH, [**2-OH**]⁺ was observed at the 5 min time point ahead of **2-SG** which was observed at the 3 h time point. This result did not agree with **Pathway 2** in which [**2-OH**]⁺ was generated from H₂O attacking Os-S bond in **2-SG**. Thus **Pathway 2** was not the main contributor to [**2-I**]⁺ hydrolysis and a more novel mechanism of hydrolysis of [**2-I**]⁺ to give [**2-OH**]⁺ in presence of GSH was expected.

Pathway 3

The third pathway proposed for the hydrolysis of **[2-I]⁺** with GSH involved attack by **GS²⁻** (deprotonated GSH) on the -N=N- azo bond to form sulfenylhydrazide intermediates **2-GS/NN** followed by attack of **H₂O** to the **Os^{II}** centre to produce the hydrolysis product **[2-OH]⁺** (**Pathway 3**). The reduction of the azo bond potentially affected the strength of Os-I bond and made it easier to be attacked by **H₂O**. As the DFT calculations for **Pathway 3** have shown, this pathway was thermodynamically possible with an energy barrier 19.0 kcal/mol for **GS²⁻** attacking the -N=N- azo bond and 13.9 kcal/mol for **H₂O** attacking the Os-I bond in the sulfenylhydrazide intermediate **2-GS/NN** to produce the hydrolysis product **[2-OH]⁺**. It was very clear that the energy barriers in **Pathway 3** (19.0 kcal/mol, 13.9 kcal/mol) were much lower than those of **Pathway 1** (25.4 kcal/mol) and **Pathway 2** (23.2 kcal/mol, 30.3 kcal/mol), which indicated the **Pathway 3** was more likely for the reaction of **[2-I]⁺** with GSH and mainly contribute to the hydrolysis of **[2-I]⁺** in cells. Meanwhile, the proposed mechanism in **Pathway 3** could also reasonably explain the behaviours observed in HPLC and NMR experiments. The key step in **Pathway 3** is the thiol group in GSH

attacking the -N=N- azo bond. Other thiols like N-acetyl-cysteine (NAC) and dithiothreitol (DTT) also dramatically induce hydrolysis of $[2-I]^+$ confirming the importance of thiol group in the reaction. For confirming the importance of -N=N- azo group, reactions of chlorido $[2-Cl]^+$ and imino $[2\text{-impy-I}]^+$ complexes with GSH were also studied to compare with $[2-I]^+$. Indeed, $[2-Cl]^+$ had a similar hydrolysis behaviour as $[2-I]^+$. The difference between $[2-Cl]^+$ and $[2-I]^+$ was that the chlorido complex seemed to be more active in view of the different strength of the Os-halide bond. On the contrary, co-incubation with GSH does not increase the degree of hydrolysis of imino complex $[2\text{-impy-I}]^+$. The pH influence on the reaction of $[2-I]^+$ with GSH demonstrated that little hydrolysis occurred at low pH (2.43) and an increase of pH to 6.86 or 10.05 can induce a higher extent of hydrolysis of $[2-I]^+$ in reactions with GSH. The inhibition in acidic conditions might be related to the lack of deprotonation of GSH to GS^{2-} which is a key species to react with $[2-I]^+$ according to **Pathway 3**. The thiol group in GSH has a relatively high pK_a value of 9.65^{42,43} and little deprotonated GS^{2-} (dissociation percentage is less than 10^{-6}) would be present at pH 3 to attack $[2-I]^+$ and induce hydrolysis. While at pH 6.86 (0.16 % deprotonated GS^{2-}) and at pH 10.05 (71 % deprotonated GS^{2-}), there are enough active deprotonated GS^{2-} to attack azo bond to induce its hydrolysis. Moreover, the catalytic nature of GSH-induced hydrolysis of $[2-I]^+$ proposed has been

demonstrated in the NMR experiments and the catalytic nature (TOF = 1.97 h^{-1}) of GSH inducing the hydrolysis of $[2-I]^+$ was observed (**Figure 4.11**), which is consistent with the mechanism of action proposed in **Pathway 3**.

On considering the computational and experimental results, the **Pathway 3** of deprotonated GS^{2-} attacking the azo bond in $[2-I]^+$ seems more likely to mainly contribute the hydrolysis of $[2-I]^+$. This pathway provides a novel mechanism of hydrolysis based on azo ligands in coordinated complexes. Azo compounds have a wide range of medical applications. For example, phenazopyridine is used in conjunction with an antibiotic or other anti-infective medication at the beginning of treatment to help provide immediate symptomatic relief (more information regarding azo compounds can be found in **Section 1.4.1** of **Chapter 1**).⁴⁴ The phenomenon of thiols attacking -N=N- azo bonds has been observed for both organic and inorganic azo compounds.^{35,36,38} Through being attacked by thiols, diamide $(\text{CH}_3)_2\text{NCON}=\text{NCON}(\text{CH}_3)_2$ and azoester I were reported to rapidly oxidize GSH to GSSG within human red blood cells.⁴⁵⁻⁴⁷ Due to being attacked by the cysteine residue, the diamide $(\text{CH}_3)_2\text{NCON}=\text{NCON}(\text{CH}_3)_2$ was found to inactivate active transport in the *E.coli* membrane vesicle.⁴⁸ Based on a similar behaviour of azo bond being attacked by thiols, azo group linked dinuclear Ir(III) and Ru(II)

complexes have been developed as intracellular thiol probes.^{36,49,50} Azo ligands bearing half-sandwich ruthenium arene complex $[\text{Ru}(\eta^6\text{-p-cym})(4\text{-(2-pyridylazo)-}N,N\text{-dimethylaniline})\text{I}]^+$ catalyse the oxidation of GSH to increase the intracellular ROS level and exhibit a high level of cytotoxicity towards cancer cells. In the mechanism of action, GSH reduces the azo bond in the ruthenium complexes and is a key step for the catalysis process.³⁸ Although many systems of thiols attacking azo bond were reported, the key sulfenylhydrazide intermediates were rarely detected, which may be ascribable to short half-life. It is not surprising that the sulfenylhydrazide intermediate **2-GS/NN** for the reaction of **[2-I]**⁺ with GSH studied in this chapter has not been detected by chromatographic and NMR experiments. However, advanced X-ray absorption spectroscopy will be used to probe **2-GS/NN** to confirm the mechanism of action presented here and related work will be introduced in **Chapter 6**.

4.5. Conclusions

The mechanism of hydrolysis of **[2-I]⁺** in presence of GSH has been explored in this **Chapter 4** based on the fundamental work in **Chapter 3**. The proposed pathway, in which deprotonated GSH, the thiolato form GS^{2-} reduces -N=N- azo bond to form the sulfenylhydrazide intermediate **2-GS/NN** and then H_2O attacks the Os-I bond in the intermediate **2-GS/NN** to induce hydrolysis, has the lowest energy barrier according to DFT calculations, and is consistent with all the experimental data. As in the proposed pathway, the experimental results show the importance of the thiolate group and involvement of -N=N- function in the reaction with GSH, activating the hydrolysis of **[2-I]⁺**, and consistent with the behaviour of different free thiols and analogues of **[2-I]⁺**. Meanwhile, acidic conditions inhibit the hydrolysis process for **[2-I]⁺** induced by GSH and basic conditions promote this reaction because of the presence of GSH's deprotonated form GS^{2-} , which is a key factor for attack on **[2-I]⁺**. Then GSH can be regenerated after attacking -N=N- and plays a catalytic role to activate the hydrolysis of **[2-I]⁺**. Based on all the experimental and computational approaches, the pathway for GSH attack on the -N=N- bond seems more likely to be the main contributor to the hydrolysis of **[2-I]⁺** in the cellular-systems.

4.6. References

- (1) Fu, Y.; Habtemariam, A.; Pizarro, A. M.; van Rijt, S. H.; Healey, D. J.; Cooper, P. A.; Shnyder, S. D.; Clarkson, G. J.; Sadler, P. J. *J. Med. Chem.* **2010**, *53*, 8192.
- (2) Hearn, J. M.; Romero-Canelón, I.; Munro, A. F.; Fu, Y.; Pizarro, A. M.; Garnett, M. J.; McDermott, U.; Carragher, N. O.; Sadler, P. *J. Proc. Natl. Acad. Sci. U.S.A.* **2015**, *112*, E3800.
- (3) Shnyder, S. D.; Fu, Y.; Habtemariam, A.; van Rijt, S. H.; Cooper, P. A.; Loadman, P. M.; Sadler, P. J. *MedChemComm* **2011**, *2*, 666.
- (4) Arnesano, F.; Natile, G. *Coord. Chem. Rev.* **2009**, *253*, 2070.
- (5) Dasari, S.; Tchounwou, P. B. *Eur. J. Pharmacol.* **2014**, *740*, 364.
- (6) Brabec, V.; Hrabina, O.; Kasparkova, J. *Coord. Chem. Rev.* **2017**, *351*, 2.
- (7) Allardyce, C. S.; Dyson, P. J.; Ellis, D. J.; Salter, P. A.; Scopelliti, R. *J. Organomet. Chem.* **2003**, *668*, 35.
- (8) Scolaro, C.; Bergamo, A.; Brescacin, L.; Delfino, R.; Cocchietto, M.; Laurenczy, G.; Geldbach, T. J.; Sava, G.; Dyson, P. J. *J. Med. Chem.* **2005**, *48*, 4161.
- (9) Köpf, H.; Köpf-Maier, P. *Angew. Chem. Int. Ed. Engl.* **1979**, *18*, 477.

- (10) Lümme, G.; Sperling, H.; Luboldt, H.; Otto, T.; Rübber, H. *Cancer Chemother. Pharmacol.* **1998**, *42*, 415.
- (11) Peacock, A. F. A.; Habtemariam, A.; Moggach, S. A.; Prescimone, A.; Parsons, S.; Sadler, P. J. *Inorg. Chem.* **2007**, *46*, 4049.
- (12) Peacock, A. F. A.; Melchart, M.; Deeth, R. J.; Habtemariam, A.; Parsons, S.; Sadler, P. J. *Chem. Eur. J.* **2007**, *13*, 2601.
- (13) Peacock, A. F. A.; Parsons, S.; Sadler, P. J. *J. Am. Chem. Soc.* **2007**, *129*, 3348.
- (14) Kostrhunova, H.; Florian, J.; Novakova, O.; Peacock, A. F. A.; Sadler, P. J.; Brabec, V. *J. Med. Chem.* **2008**, *51*, 3635.
- (15) Needham, R. J.; Sanchez-Cano, C.; Zhang, X.; Romero-Canelón, I.; Habtemariam, A.; Cooper, M. S.; Meszaros, L.; Clarkson, G. J.; Blower, P. J.; Sadler, P. J. *Angew. Chem. Int. Ed.* **2017**, *56*, 1017.
- (16) Zhang, S.; Ong, C.-N.; Shen, H.-M. *Cancer Lett.* **2004**, *208*, 143.
- (17) Moran, L. K.; Gutteridge, J.; Quinlan, G. J. *Curr. Med. Chem.* **2001**, *8*, 763.
- (18) Krężel, A.; Bal, W. *J. Inorg. Biochem.* **2004**, *98*, 161.
- (19) Becke, A. D. *J. Chem. Phys.* **1993**, *98*, 5648.
- (20) Lee, C.; Yang, W.; Parr, R. G. *Phys. Rev. B* **1988**, *37*, 785.
- (21) Grimme, S.; Antony, J.; Ehrlich, S.; Krieg, H. *J. Chem. Phys.* **2010**, *132*, 154104.

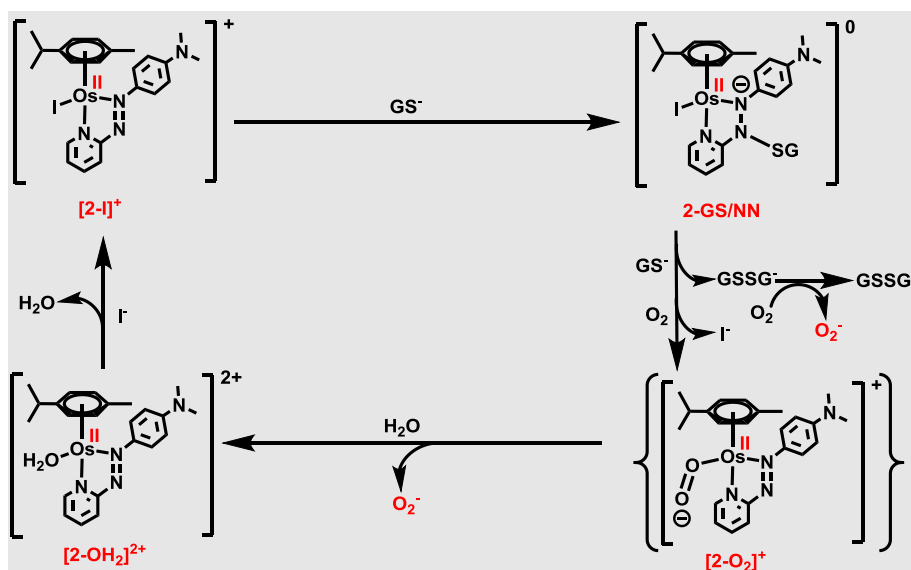
- (22) Dunning, T. H.; Hay, P. J. In *Modern theoretical chemistry*; Plenum Press: New York, NY, 1977; Vol. 3, p 1.
- (23) Fukui, K. *J. Phys. Chem.* **1970**, 74, 4161.
- (24) Gonzalez, C.; Schlegel, H. B. *J. Chem. Phys.* **1989**, 90, 2154.
- (25) Miertuš, S.; Scrocco, E.; Tomasi, J. *Chem. Phys.* **1981**, 55, 117.
- (26) Pascual-ahuir, J.-L.; Silla, E.; Tunon, I. *J. Comput. Chem.* **1994**, 15, 1127.
- (27) McQuarrie, D. A.; Simon, J. D. *Molecular Thermodynamics. University Science Books, Sausalito, CA* **1999**, 581.
- (28) Ashcraft, R. W.; Raman, S.; Green, W. H. *J. Phys. Chem. B* **2007**, 111, 11968.
- (29) Guo, L.; Zhang, H.; Tian, M.; Tian, Z.; Xu, Y.; Yang, Y.; Peng, H.; Liu, P.; Liu, Z. *New J. Chem.* **2018**, 42, 16183.
- (30) Tian, M.; Li, J.; Zhang, S.; Guo, L.; He, X.; Kong, D.; Zhang, H.; Liu, Z. *Chem. Commun.* **2017**, 53, 12810.
- (31) Mukhopadhyay, S.; Gupta, R. K.; Paitandi, R. P.; Rana, N. K.; Sharma, G.; Koch, B.; Rana, L. K.; Hundal, M. S.; Pandey, D. S. *Organometallics* **2015**, 34, 4491.
- (32) Peacock, A. F. A.; Habtemariam, A.; Fernández, R.; Walland, V.; Fabbiani, F. P. A.; Parsons, S.; Aird, R. E.; Jodrell, D. I.; Sadler, P. J. *J. Am. Chem. Soc.* **2006**, 128, 1739.

- (33) Wang, F.; Xu, J.; Habtemariam, A.; Bella, J.; Sadler, P. J. *J. Am. Chem. Soc.* **2005**, *127*, 17734.
- (34) Kosower, E. M.; Miyadera, T. *J. Med. Chem.* **1972**, *15*, 307.
- (35) Kosower, E. M.; Kanety-Londner, H. *J. Am. Chem. Soc.* **1976**, *98*, 3001.
- (36) Li, G.; Chen, Y.; Wu, J.; Ji, L.; Chao, H. *Chem. Commun.* **2013**, *49*, 2040.
- (37) Zhou, Q.-X.; Zheng, Y.; Wang, T.-J.; Chen, Y.-J.; Li, K.; Zhang, Y.-Y.; Li, C.; Hou, Y.-J.; Wang, X.-S. *Chem. Commun.* **2015**, *51*, 10684.
- (38) Dougan, S. J.; Habtemariam, A.; McHale, S. E.; Parsons, S.; Sadler, P. J. *Proc. Natl. Acad. Sci. U.S.A.* **2008**, *105*, 11628.
- (39) Wang, D.; Lippard, S. J. *Nat. Rev. Drug Discov.* **2005**, *4*, 307.
- (40) Lau, J. K.-C.; Ensing, B. *PCCP* **2010**, *12*, 10348.
- (41) Petzold, H.; Sadler, P. J. *Chem. Commun.* **2008**, 4413.
- (42) Corazza, A.; Harvey, I.; Sadler, P. J. *Eur. J. Biochem.* **1996**, *236*, 697.
- (43) Picart, P.; Sevenich, M.; de María, P. D.; Schallmeyer, A. *Green Chem.* **2015**, *17*, 4931.
- (44) Thomas, B. H.; Whitehouse, L. W.; Solomonraj, G.; Paul, C. J. *J. Pharm. Sci.* **1990**, *79*, 321.

- (45) Kosower, N. S.; Kosower, E. M.; Wertheim, B.; Correa, W. S. *Biochem. Biophys. Res. Commun.* **1969**, 37, 593.
- (46) Kosower, N. S.; Kosower, E. M. *Methods Enzymol.* **1987**, 143, 264.
- (47) Kosower, N. S.; Song, K.-R.; Kosower, E. M. *Biochim. Biophys. Acta Gen. Subj.* **1969**, 192, 1.
- (48) Kaback, H. R.; Patel, L. *Biochemistry* **1978**, 17, 1640.
- (49) Li, G.; Chen, Y.; Wang, J.; Lin, Q.; Zhao, J.; Ji, L.; Chao, H. *Chem. Sci.* **2013**, 4, 4426.
- (50) Li, G.; Chen, Y.; Wang, J.; Wu, J.; Gasser, G.; Ji, L.; Chao, H. *Biomaterials* **2015**, 63, 128.

Chapter 5

Free Radical Detection



5.1. Introduction

DNA is the target of many anticancer metallodrugs, ¹⁻⁷ for example cisplatin,⁸⁻¹¹ but the non-selectivity of such drugs to normal cells causes many side effects.^{12,13} This intracellular redox system is considered to be a novel target of anticancer drugs with higher selectivity. All cells require a strict redox balance and reactive oxygen species (ROS) play important roles in the function of cell metabolism and signal transduction.^{14,15} The characterization of cancer cells that undergo increased metabolism for higher energy and nutritional requirements requires a higher level of oxidative stress compared to healthy cells.^{16,17} Oxidative therapy is a method to increase significantly intracellular ROS levels and push cancer cells above a cellular tolerability threshold, while normal cells at lower ROS levels appear to have higher capacity to cope with additional ROS-generating insults.¹⁸⁻²⁰

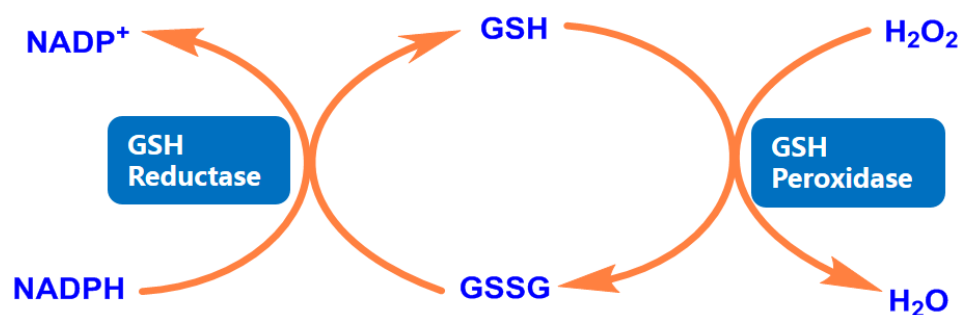


Figure 5.1. Intracellular redox system.

The intracellular redox balance is normally maintained through a cell redox system in which glutathione (GSH, γ -Glu-L-Cys-Gly) reacts with ROS (H_2O_2 in **Figure 5.1**) and itself is oxidized to GSSG. Then GSH reductase catalyses electron transfer from NAD(P)H to GSSG producing NAD(P)⁺ and GSH.²¹⁻²³ GSH is a tripeptide with a gamma peptide linkage between the carboxyl group of the L-glutamate side chain and the amine group of L-cysteine (**Figure. 5.2**).²⁴ It is generally maintained at an approximately 5 mM concentration level in mammal ion cells.²⁵ The thiol group of GSH is the major source of non-protein thiols in the cell and reacts with ROS and complexes metal ions (**Chapter 1, Section 1.6**).²⁶ [Os (η^6 -p-cymene)(4-(2-pyridylazo)-*N,N*-dimethylaniline)I] PF₆ (**FY26**, also named **2-I•PF₆**, which is dissociated to [**2-I**]⁺ in aqueous solution) was found to be involved in intracellular redox modulation and induce the superoxide production to kill cancer cells.^{27,28} The modification of intracellular glutathione level was able to affect the potency of **2-I•PF₆**²⁹ and so interactions between **2-I•PF₆** and GSH have become of significant interest. Thus this thesis is mainly concerned with studies of reactions between GSH with **2-I•PF₆** as well as its related compounds. In **Chapter 4**, studies of GSH promoting the hydrolysis of **2-I•PF₆** were conducted and it was concluded that GS⁻ catalysed the hydrolysis of **2-I•PF₆** through attacking the azo bond -N=N- to form azo bond reduced intermediates in which the monodentate halide ligand was more readily replaceable

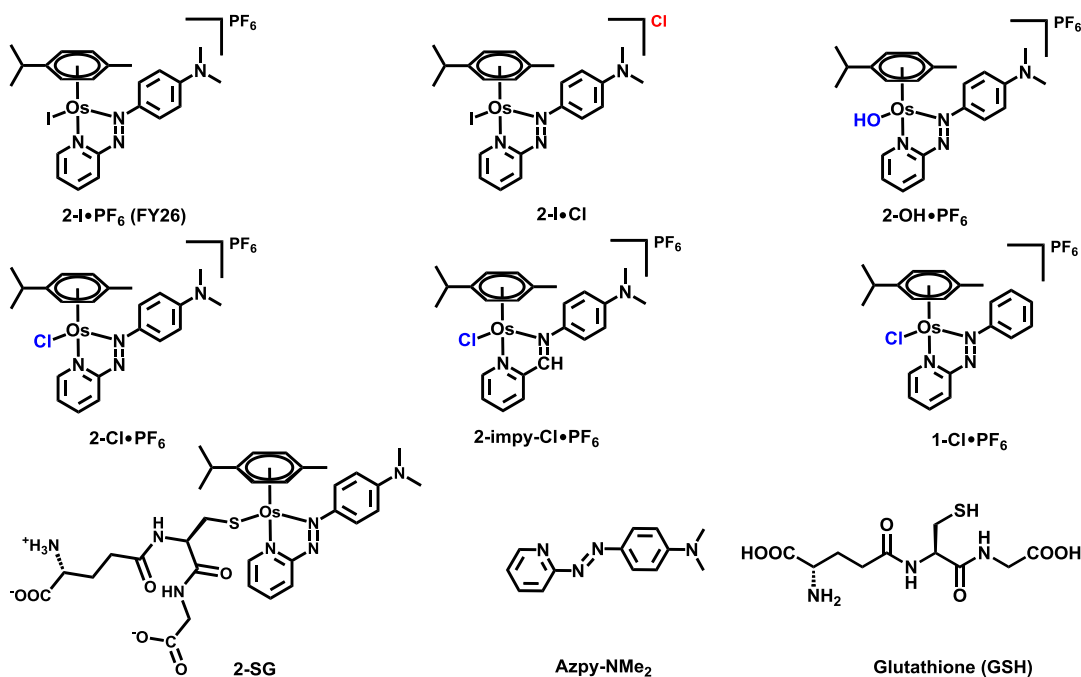


Figure 5.2. The structures of compounds studied in EPR experiments.

by H₂O. It was interesting that under N₂ protection, little GSH is consumed during the **2-I•PF₆** hydrolysis process, but when the reaction was exposed to air GSH consumption was much faster (**Chapter 4**), even faster than the auto-oxidation of GSH without the osmium complex. Such results suggested that dioxygen plays important roles in the reaction of **2-I•PF₆** with GSH and free radicals could be generated. Following from the work in **Chapter 4**, in this **Chapter 5**, reactions between GSH with **2-I•PF₆** as well as related compounds are studied by electron paramagnetic resonance (EPR) to detect the free radicals. A problem for these studies was the poor solubility of **2-I•PF₆** in aqueous solution. In order to improve its solubility, the anion of **2-I•PF₆** was exchanged with Cl⁻

through anion-exchange chromatography to produce **2-I•Cl** to replace **2-I•PF₆** (in aqueous solution, both **2-I•Cl** and **2-I•PF₆** dissociate to **[2-I]⁺**). The reactions of GSH with the chlorido analogue **2-Cl•PF₆**, hydroxido analogue **[2-OH]⁺**, imino analogue **2-imp_y-Cl•PF₆**, glutathione adduct **2-SG**, non-substituted analogue **1-Cl•PF₆** and free ligand **AZPY-NMe₂** are also studied by EPR. Apart from free radicals, other proposed products such as oxidized glutathione (GSSG) and hydrogen peroxide are also detected. Then DFT calculations were used to probe the possible intermediates for the free radicals production and finally a potential mechanism of action is proposed.

EPR, also called ESR (electron spin resonance), is widely applied in the studying chemical species with unpaired electrons. It was developed by Yevgeny Zavoisky at Kazan State University and Brebis Bleaney at the University of Oxford in 1944.^{30,31} The basic concepts of EPR are analogous to those of NMR (nuclear magnetic resonance), but EPR is concerned the interaction of the electron spin with the microwave magnetic vector whilst NMR studies the spin of atomic nuclei. Basically, EPR spectra are characterised with two parameters: hyperfine coupling constants and g values. The g value is equivalent to the chemical shift (δ) parameter in NMR spectroscopy. It is independent of the microwave frequency and determined from the equation below where h is Plank's constant (6.626×10^{-34} J.s), ν is the frequency (MHz), β is the Bohr

Magneton constant ($9.274 \times 10^{-24} \text{ J.T}^{-1}$) and B_0 is the magnetic field (G). The g value is the centre of the EPR spectrum and normally close to the value of free electron $g_E = 2.0023$. But every radical has its own g value that is considered as a radical “fingerprint”.

$$g = \frac{h\nu}{\beta B_0}$$

Hyperfine coupling, which is equivalent to the J coupling in NMR, is caused by the coupling of an unpaired electron with a magnetically active nuclei with spin (I) greater than zero such as ^1H ($1/2$), ^{15}N (1) and ^{31}P ($1/2$). The number of expected lines in an EPR spectrum can be deduced from $2nI+1$, where n refers to the number of equivalent magnetically active nuclei. The standard free radical 4-hydroxy-2,2,6,6-tetramethylpiperidine-1-oxyl (Tempol) generates a triplet EPR spectrum, which is produced from the coupling of the unpaired electron with the nitroxidic nitrogen (^{14}N) (**Figure 5.3**).

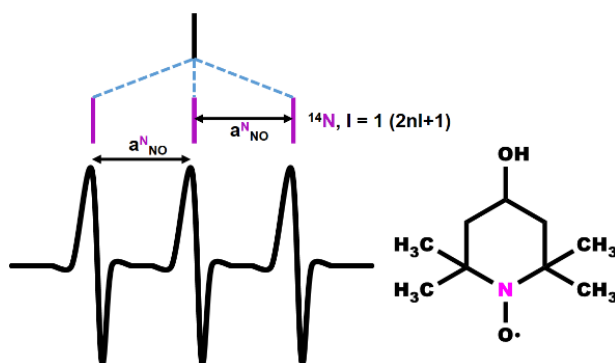


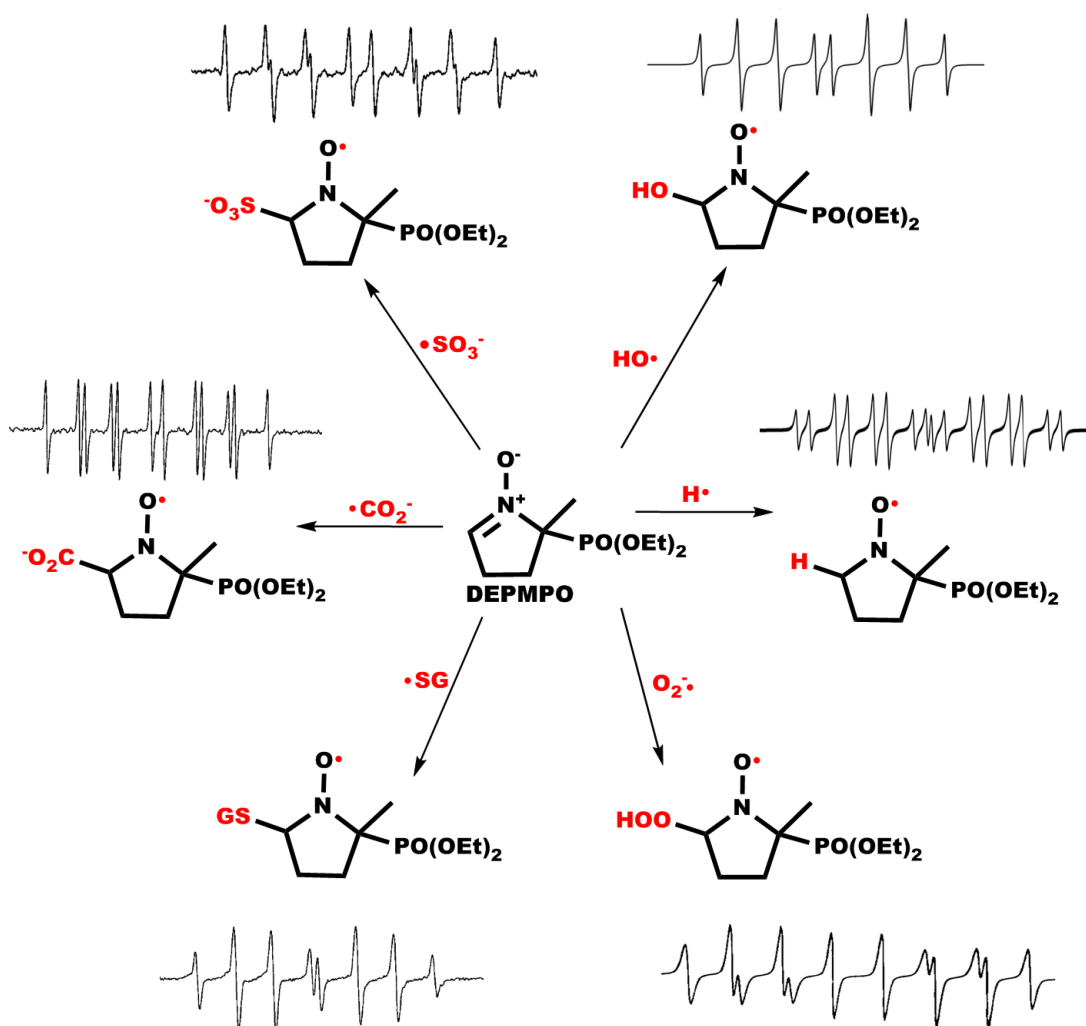
Figure 5.3. Triplet EPR spectrum of the standard free radical Tempol, with hyperfine coupling to ^{14}N indicated.

5.2. Experimental Section

5.2.1. Materials

Osmium complexes **2-I•PF₆** (**FY26**), **2-Cl•PF₆** (**FY025**), **[2-OH]⁺**, **2-impy-Cl•PF₆** and **1-Cl•PF₆** were synthesized and characterised as described in **Chapter 3, Section 3.2**. **2-I•Cl** was provided by Dr. Russell Needham from the Sadler Group. **AZPY-NMe₂** (pyridine-2-azo-*p*-dimethylaniline) was purchased from Alfa Aesar. L-glutathione (GSH), ammonium molybdate and bovine superoxide dismutase (SOD) were purchased from Sigma Aldrich (Gillingham, UK). Peroxide analytical test strips were purchased from Merck KGaA. The trapping agent 5-(diethoxyphosphoryl)-5-methyl-1-pyrroline-N-oxide (DEPMPO) was purchased from Enzo Life Sciences. EPR tubes were purchased from Wilmad Labglass. Phosphate buffer solution containing sodium chloride was prepared by dissolving disodium hydrogen phosphate (3.45 g, 24.3 mmol), sodium dihydrogen phosphate dehydrate (0.89 g, 5.7 mmol) and sodium chloride (0.58 g, 10 mmol) (all purchased from Fisher Scientific) together in deionised water (100 mL). The pH of the phosphate buffer solution was measured using a bench top pH meter (**Chapter 2**) with glass electrode and read pH = 7.4(±0.1). If necessary, the pH of the buffer solution was adjusted by aqueous sodium hydroxide (100 mM) or nitric acid (3.6%) to pH = 10.8(±0.1) or pH = 3.8(±0.1), respectively. The

deuterated phosphate buffer solution for NMR experiments was prepared according to the description provided in **Chapter 2**. Sodium hydroxide and nitric acid were purchased from Fisher Scientific. Metal trace basis salts including disodium hydrogen phosphate, sodium dihydrogen phosphate dehydrate and sodium chloride were purchased from Sigma-Aldrich and the no-metal absolute buffer solution was prepared in the same manners as the general buffer solution.



Scheme 5.1. Structures and spectral appearances of radicals $\text{HO}\cdot$, $\text{H}\cdot$, $\text{O}_2^{\cdot-}$, $\text{GS}\cdot$, $\cdot\text{SO}_3^-$ and $\cdot\text{CO}_2^-$ trapped by DEPMPO.

5.2.2. Radical Trapping

In all the free radical detection experiments described in this chapter, DEPMPO was used as spin trap.³²⁻³⁴ As shown in **Scheme 5.1**, DEPMPO is capable of trapping HO• radical yielding an 8-peak spectrum (DEPMPO-OH),^{32,35} O₂• radical yielding a 12-peak spectrum (DEPMPO-OOH),³⁵ H• radical yielding a 16-peak spectrum (DEPMPO-H),³⁵ GS• (DEPMPO-SG) radical yielding an 8-peak spectrum,³⁶ (the structure of GSH is provided in **Figure 5.2**), •SO₃⁻ (DEPMPO-SO₃⁻) radicals yielding a 12-peak spectrum³⁶ and •CO₂⁻ (DEPMPO-CO₂⁻) radicals yielding a 12-peak spectrum.^{34,36}

5.2.3. Sample Preparation

The samples were generally prepared by mixing 3 mL of 1.33 mM osmium compounds (**2-I•PF₆**, **2-I•Cl**, **2-Cl•PF₆**, **[2-OH]⁺**, **2-imp-Cl•PF₆** and **1-Cl•PF₆**) in deionised water with 1 mL of a 4 mM GSH solution in stock phosphate buffer solution (**Chapter 5, Section 5.2.1**). The solutions were heated at 310 K for 1 h (samples of **1-Cl•PF₆** were incubated for 30 min since it is unstable in aqueous solution) and the air bubbling into the solution was achieved with a long needle during the incubation (**Figure 5.4a**). When the samples needed to be protected by N₂, a vacuum pump was used to remove all the air from the two-neck flask which was then refilled with N₂.

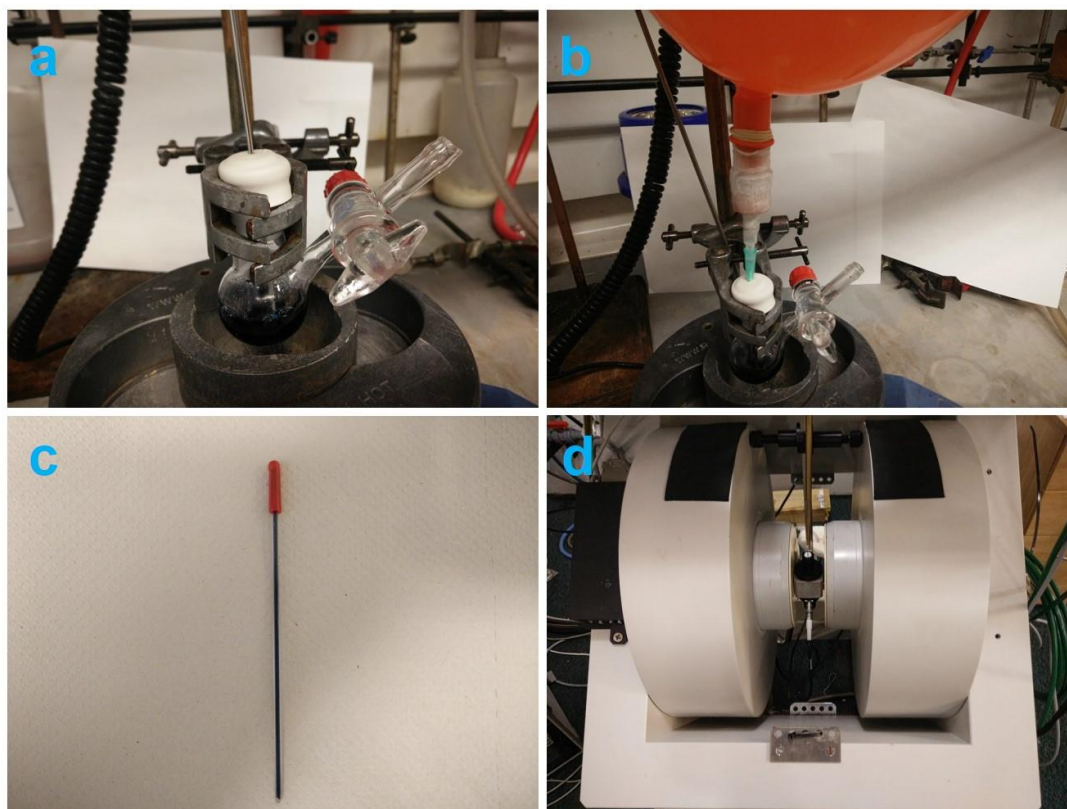


Figure 5.4. a) Preparation of samples with bubbling air; b) Preparation of sample with N₂ protection; c) The EPR tube filled with sample; d) The EPR instrument.

The osmium complex and GSH solutions were bubbled with N₂ separately for more than 1 h to remove the dissolved air from the solutions. Under N₂ flow, the degassed osmium complex solution and the degassed GSH solution were mixed in the N₂-filled two-neck flask. Finally a closed one neck of the flask and the other neck were protected by a balloon which was filled with N₂ (**Figure 5.4b**). Solutions were heated at 310 K for 1 h. Subsequently, the solution was transferred to the EPR lab and 1 mL solution was taken out with a syringe to mix with DEPMPO (4.72 mg, 20 μ mol). Immediately, the solution with DEPMPO

was transferred to quartz capillary EPR tube (I.D. 1.0 mm; O.D. 1.2 mm; Wilmad Labglass; **Figure 5.4c**) for loading on the EPR instrument (**Figure 5.4d**). In the experiments involving reaction of **2-I•PF₆**, **2-Cl•PF₆** and **AZPY-NMe₂** with GSH, in view of their poor solubility in water, ultrasonic irradiation was used to promote dissolution of the compounds. If the compounds could not be dissolved completely, turbid **2-I•PF₆**, **2-Cl•PF₆** or **AZPY-NMe₂** solutions were mixed with GSH solution for EPR experiments.

5.2.4. Spectrum Acquisition and Simulation

Dr. Ben Breeze from Department of Physics of the University of Warwick provided much help and guidance with the operation of the EPR instrument. All EPR spectra were recorded on a 9.5 GHz X-band EPR spectrometer at ambient temperature (ca. 291 K). The sweep time for each scanning was 83.89 seconds and every 10 scans produced an average spectrum which was recorded. Thus in the kinetic EPR experiments, one spectrum took about 15 min to be recorded. More specific details are described in **Chapter 2**. All the spectra were analysed and simulated using the EASYSPIN software.³⁷ Three independent experiments and simulations combining spectra resolution (2048 data points in 200 G) were used to calculate error bars.

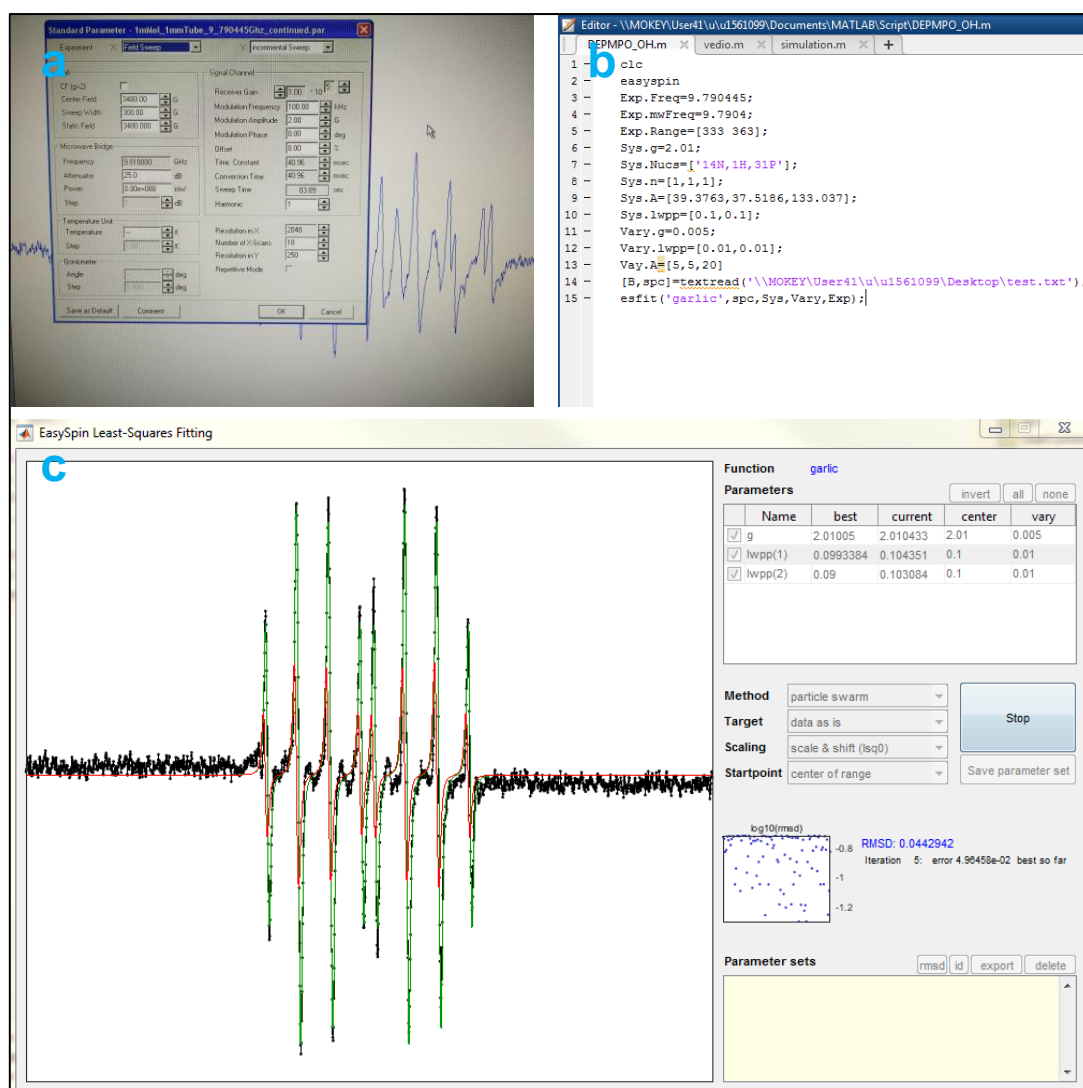


Figure 5.5. a) The parameters for EPR spectrum acquisition; b) The command for EPR spectrum (DEPMPO-OH) simulation; c) The parameters for EPR spectrum simulation.

5.2.5. Effect of Superoxide Dismutase on Radical Generation

The buffer solution used in this experiment was phosphate (75 mM) buffer solution with sodium chloride (25 mM), pH 7.4. Bovine superoxide dismutase (SOD) was dissolved in the buffer solution and its concentration (60 μ M) was calculated from UV-vis absorbance at 258

nm ($\epsilon^{\text{mM}} = 10.3$) from with Beer–Lambert law.³⁸ Then 2 mL of SOD solution (60 μM) was mixed with 1.5 mL of **[2-OH]⁺** (2.66 mM) and 0.5 mL GSH solution (8 mM) to prepare the experimental sample and the control sample was prepared by mixing 2 mL buffer solution with 1.5 mL **[2-OH]⁺** (2.66 mM) and 0.5 mL GSH solution (8 mM). Samples were incubated at 310 K for 1 h; 1 mL of the solution was then mixed with DEPMPO (4.72 mg, 20 μmol), transferred to a quartz EPR tube, and then loaded into the EPR instrument (i.e., the same procedure as that described in **Section 5.2.3**).

5.2.6. H₂O₂ Measurements

5.2.6.1. H₂O₂ Test Strips

The buffer solution used in this experiment was phosphate (75 mM) buffer solution with sodium chloride (25 mM), pH value 7.4. **2-I•PF₆** solution (200 μM) and GSH solution (600 μM) were prepared, and 5 mL of **2-I•PF₆** solution (200 μM) and 5 mL GSH solution (600 μM) mixed to prepare the experimental sample. Then 5 mL **2-I•PF₆** solution (200 μM) was mixed with 5 mL buffer solution, and 5 mL GSH solution (600 μM) with 5 mL buffer solution to prepare two control samples. These three samples were incubated at 310 K for 3 h and then peroxide test strips were left to soak in the samples for 15 s. The colours of the test strips were then compared to a standard chart.

5.2.6.2. Ammonium Molybdate Method

The buffer solution used in this experiment is the phosphate (75 mM) buffer solution with sodium chloride (25 mM), pH 7.4. **2-I•PF₆** solution (200 μ M), GSH solution (600 μ M) and ammonium molybdate solution (32.4 mM) were prepared. Then 5 mL **2-I•PF₆** solution (200 μ M) and 5 mL GSH solution (600 μ M) were mixed to prepare the experimental sample. To prepare the two control samples 5 mL **2-I•PF₆** solution (200 μ M) was mixed with 5 mL buffer solution, and 5 mL GSH solution (200 μ M) with 5 mL buffer solution. Incubated These three sample were incubated at 310 K for 5 min, 1 h, 2 h, 3 h and 4 h, and then 0.5 mL sample was removed and mixed with 0.5 mL ammonium molybdate solution (32.4 mM), and scanned by UV-vis to determine the absorbance

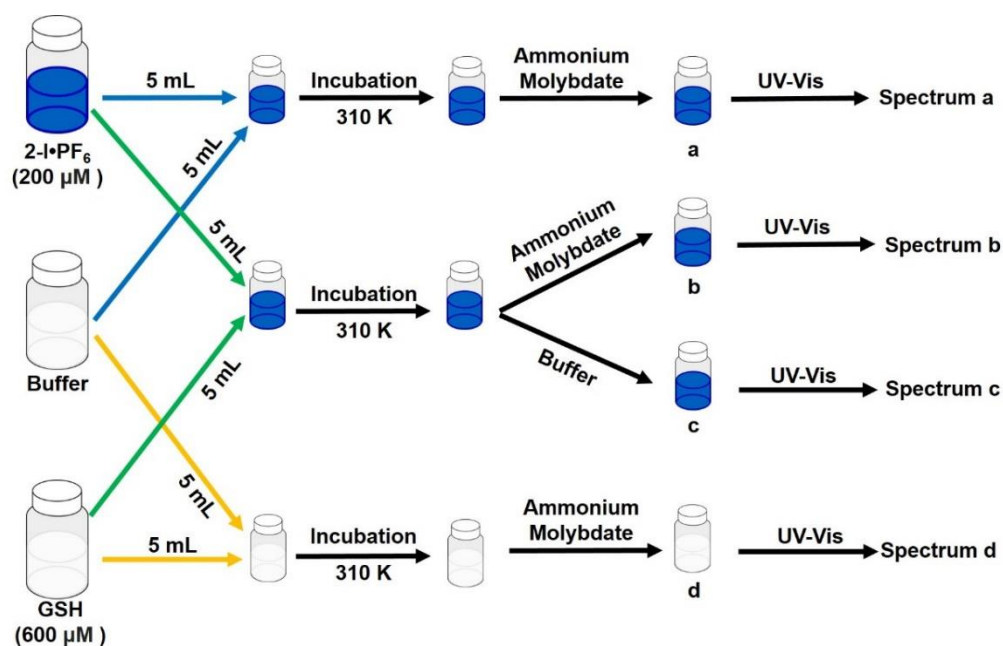


Figure 5.6. The procedure for using ammonium molybdate to detect the H_2O_2 production during the reactions of **2-I•PF₆** with GSH.

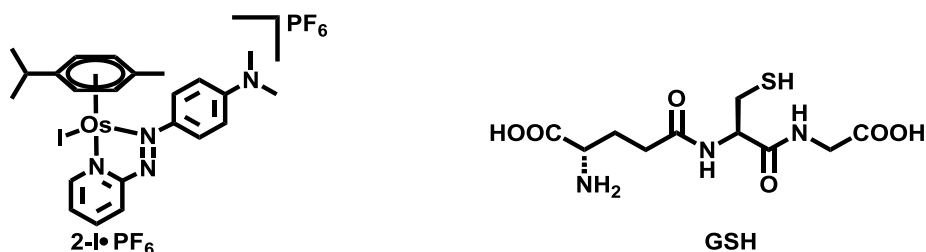
changes at 405 nm in order to determine the amount of H₂O₂ presented.³⁹

The calibration curve for the relationship between concentration of H₂O₂ (y AU) and the absorbance change at 405 nm (x μ M) was $y = 0.0123x + 0.0305$ ($r = 0.9996$, $n = 11$).⁴⁰ The sample containing **2-I•PF₆** and GSH but no ammonium molybdate solution were also scanned by UV-Vis as the control sample. This experimental procedure is summarized in **Figure 5.6**.

5.3. Results

In this section, the results of free radicals detection using the spin-trap DEPMPO trapping radicals generated from the reactions of osmium complexes (as well as free ligands) with GSH under various conditions (different pHs, air or N₂ atmosphere) is presented. The osmium complexes include **2-I•PF₆**, chloride-counterion form **2-I•Cl** (Improved solubility), chlorido analogue **2-I•PF₆**, hydroxido analogue **[2-OH]⁺**, imino analogue **2-impy-Cl•PF₆** and no-substituted analogue **1-Cl•PF₆**. Apart from free radicals, other proposed products such as oxidized glutathione (GSSG) and hydrogen peroxide were also detected, and finally a favourable mechanism for this reaction system is proposed.

5.3.1. Reactions of 2-I•PF₆ with GSH



5.3.1.1 pH = 7.4

A turbid solution of **2-I•PF₆** (1 mM) with GSH (1 mM) in sodium chloride (25 mM) and phosphate buffer (75 mM), pH 7.4, was prepared. This was incubated at 310 K for 1 h and then DEPMPO (20 mM) was

added as a spin trap. The sample was then scanned by EPR for 3 h at 298 K, but no free radical spectrum was observed (**Figure 5.7**).

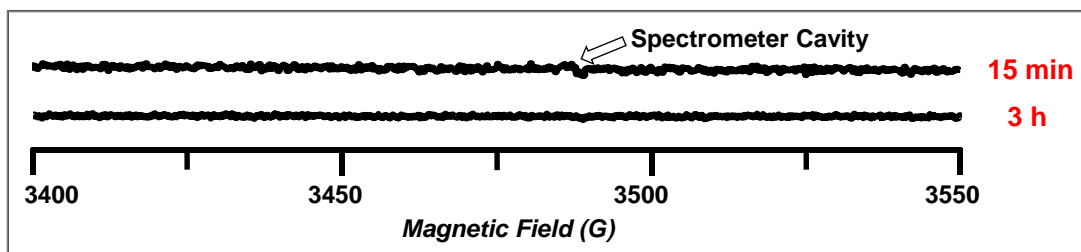


Figure 5.7. Spectra after 15 min and 3 h EPR scanning for sample of **2-I•PF₆** (1 mM) with GSH (1 mM) and DEPMPO (20 mM) in sodium chloride (25 mM) and phosphate buffer (75 mM) at pH = 7.4.

5.3.1.2 pH = 10.8

A turbid solution of **2-I•PF₆** (1 mM) with GSH (1 mM) in sodium chloride (25 mM) and phosphate buffer (75 mM) at pH = 10.8 was prepared. Then the solution was incubated at 310 K for 1 h and DEPMPO (20 mM) was added as spin trap. The sample was scanned by EPR for 3 h at 298 K, but no free radical spectrum was observed (**Figure 5.8**).

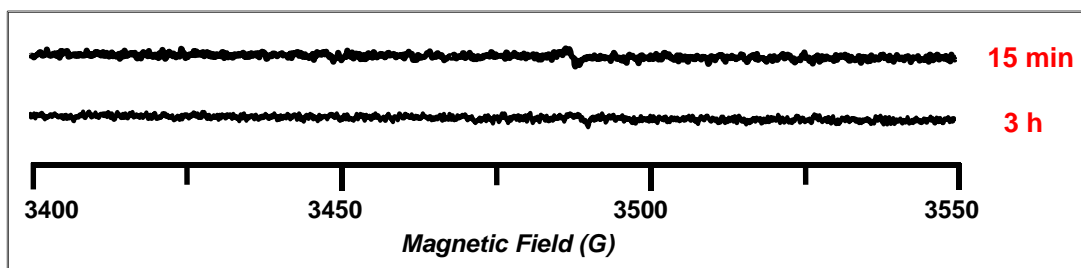
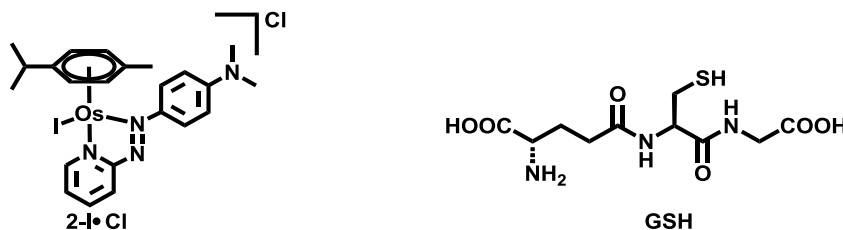


Figure 5.8. Spectra after 15 min and 3 h EPR scanning for sample of **2-I•PF₆** (1 mM) with GSH (1 mM) and DEPMPO (20 mM) in sodium chloride (25 mM) and phosphate buffer (75 mM) at pH = 10.8.

5.3.2. Reactions of 2-I•Cl with GSH



5.3.2.1. pH = 3.8

A solution of **2-I•Cl** (1 mM) with GSH (1 mM) in sodium chloride (25 mM) and phosphate buffer (75 mM) at pH = 3.8 was prepared and incubated at 310 K for 1 h before DEPMPO (20 mM) was added as a spin trap. The sample was then kinetically scanned on EPR for 3 h at 298 K but no free radical spectrum was observed (**Figure 5.9**)

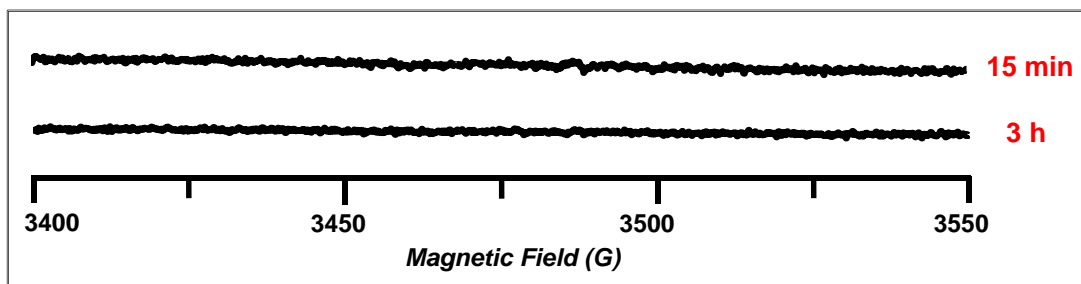


Figure 5.9. Spectra after 15 min and 3 h scanning for sample of **2-I•Cl** (1 mM) with GSH (1 mM) and DEPMPO (20 mM) in sodium chloride (25 mM) and phosphate buffer (75 mM) at pH = 3.8.

5.3.2.2. pH = 7.4

A solution of **2-I•Cl** (1 mM) with GSH (1 mM) in sodium chloride (25 mM) and phosphate buffer (75 mM) at pH = 7.4 was incubated at 310 K for 1 h and then DEPMPO (20 mM) was added as spin trap. The sample

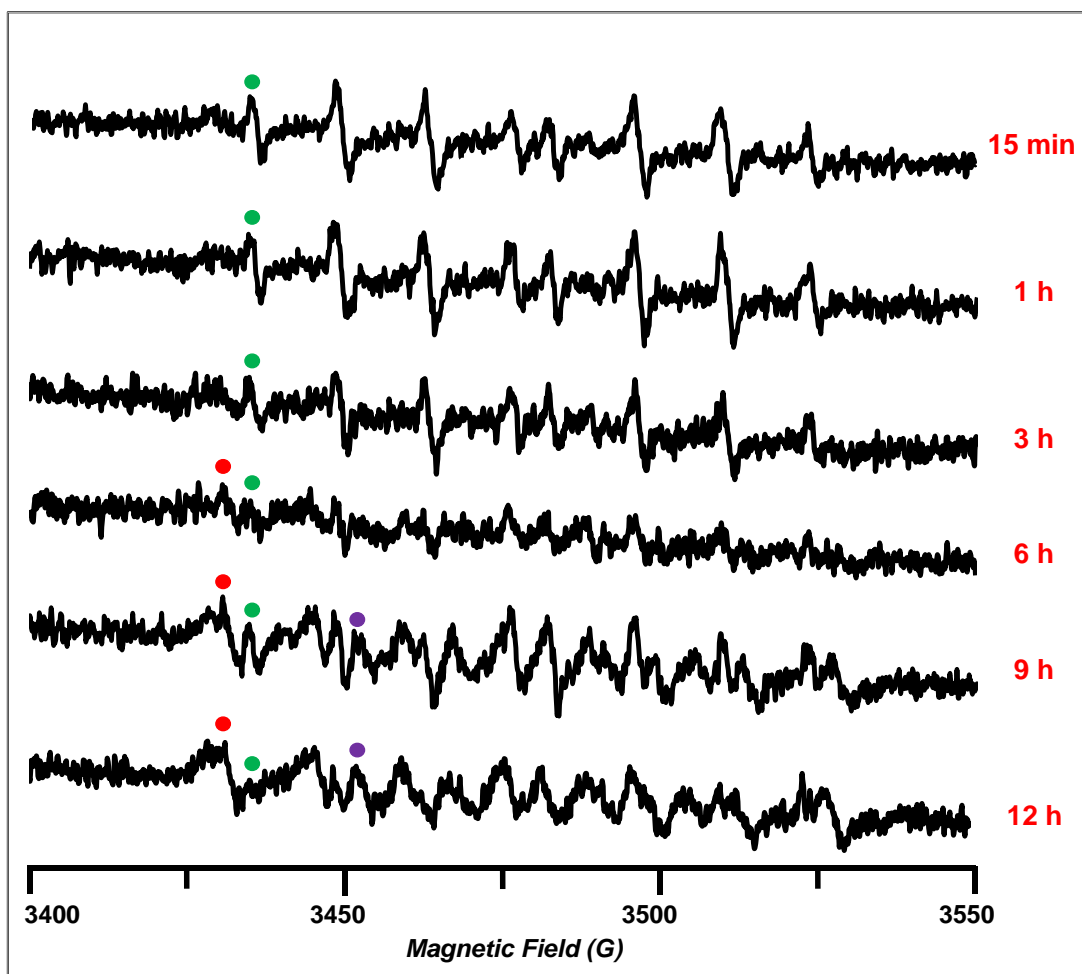


Figure 5.10. EPR spectra for sample of **2-I•Cl** (1 mM) with GSH (1 mM) and DEPMPO (20 mM) in sodium chloride (25 mM) and phosphate buffer (75 mM) at pH = 7.4 after 15 min, 1 h, 3 h, 6 h, 9 h and 12 h scanning at 298 K. The set of signal labelled with green ● was assigned to DEPMPO-OH, the set of signal labelled with red ● was assigned to DEPMPO-H and the set of signal labelled with purple ● was assigned to DEPMPO-OOH.

was scanned by EPR for 12 h at 298 K. An 8-peak spectrum was observed at the beginning (from 15 min to 3 h) and then an 18-peak spectrum started to be observed after 9 h scanning (**Figure 5.10**). From the simulation results (**Section 5.3.9**), the 8-peak spectrum was assigned to DEPMPO-OH (green ●) and the 18-peak spectrum was assigned to mixture of DEPMPO-OH (green ●), DEPMPO-H (red ●) and DEPMPO-OOH (purple ●).

5.3.2.3. pH = 10.8

A solution of **2-I•Cl** (1 mM) with GSH (1 mM) in sodium chloride (25 mM) and phosphate buffer (75 mM) at pH = 10.8 was incubated at 310 K for 1 h and then DEPMPO (20 mM) was added as spin trap. The concentration of osmium complex was confirmed by ICP-OES (detection of Os) as 1.054 mM (more details of ICP-OES are provided in **Chapter 2**). The sample had been scanned on EPR for 12 h at 298 K. During the scanning period, an 18-peak spectrum was continuously observed (**Figure 5.11**). From the simulation results (**Section 5.3.9**), the 18-peak spectrum was assigned to a mixture of DEPMPO-OH (green ●), DEPMPO-H (red ●) and DEPMPO-OOH (purple ●).

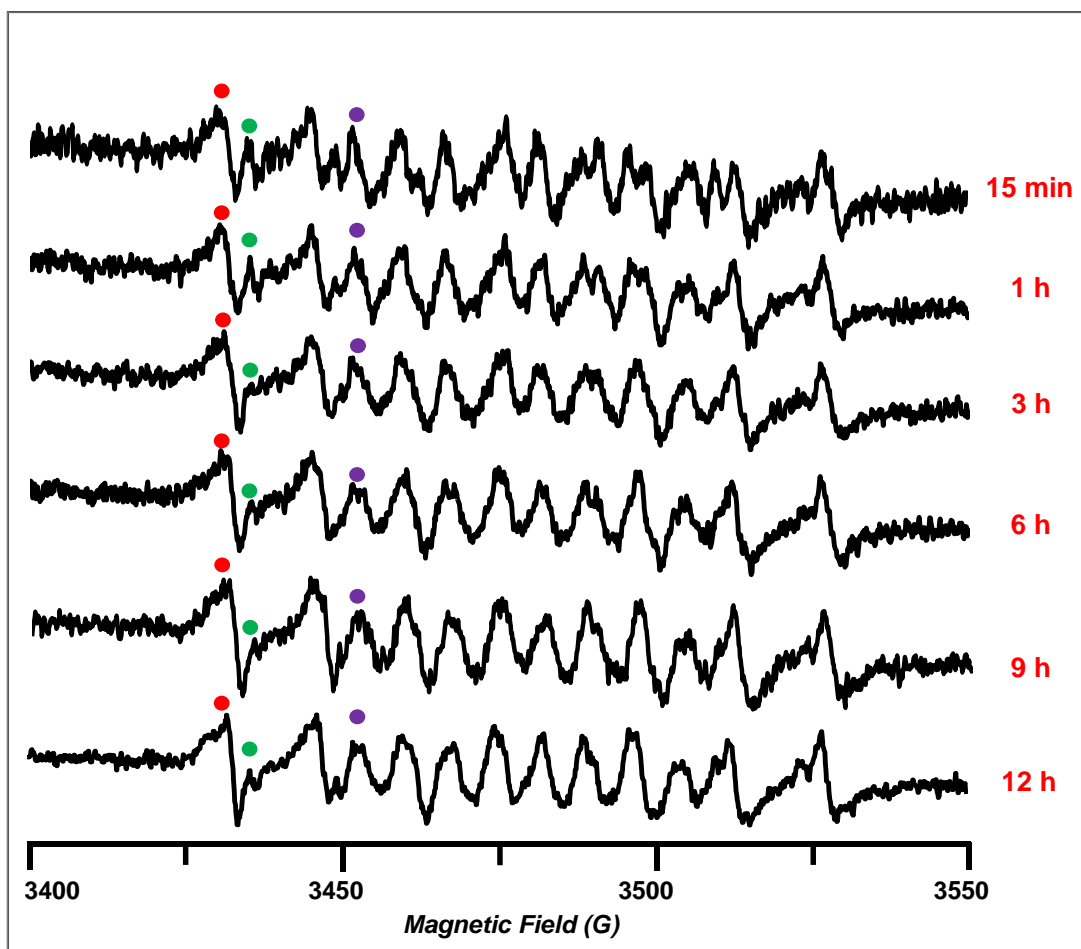


Figure 5.11. EPR spectra for sample of **2-I•Cl** (1 mM) with GSH (1 mM) and DEPMPO (20 mM) in sodium chloride (25 mM) and phosphate buffer (75 mM) at pH = 10.8 after 15 min, 1 h, 3 h, 6 h, 9 h and 12 h scanning periods at 298 K. The set of signal labelled with green ● was assigned to DEPMPO-OH, the set of signals labelled with red ● was assigned to DEPMPO-H and the set of signals labelled with purple ● was assigned to DEPMPO-OOH.

5.3.2.4. Under N₂

Solutions of **2-I•Cl** (1 mM) with GSH (1 mM) in sodium chloride (25 mM) and phosphate buffer (75 mM) at pH = 3.8, 7.4 and 10.8 were prepared separately under N₂ protection and then incubated at 310 K for

1 h before DEPMPO (20 mM) was added as spin trap. The samples were scanned by EPR for 3 h at 298 K, but no free radical spectra were observed (**Figure 5.12**).

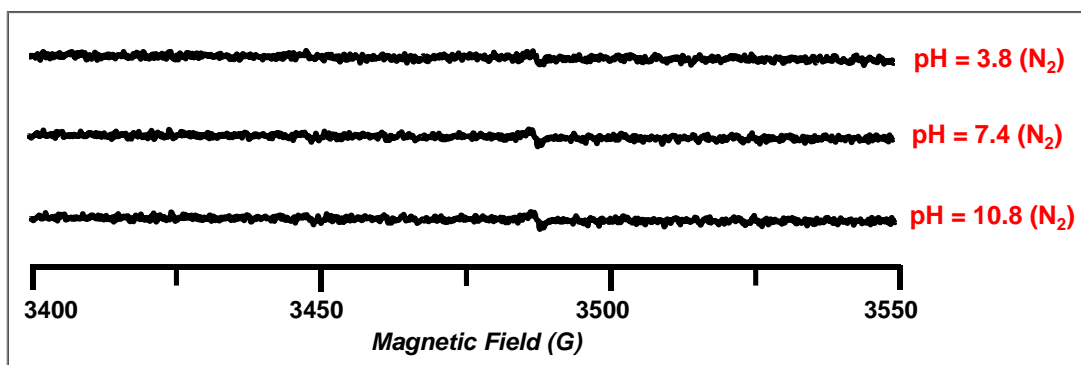


Figure 5.12. EPR spectra for sample of **2-I•Cl** (1 mM) with GSH (1 mM) and DEPMPO (20 mM) in sodium chloride (25 mM) and phosphate buffer (75 mM) at pH = 3.8, 7.4 and 10.8 with the protection from N₂ after 3 h scanning at 298 K.

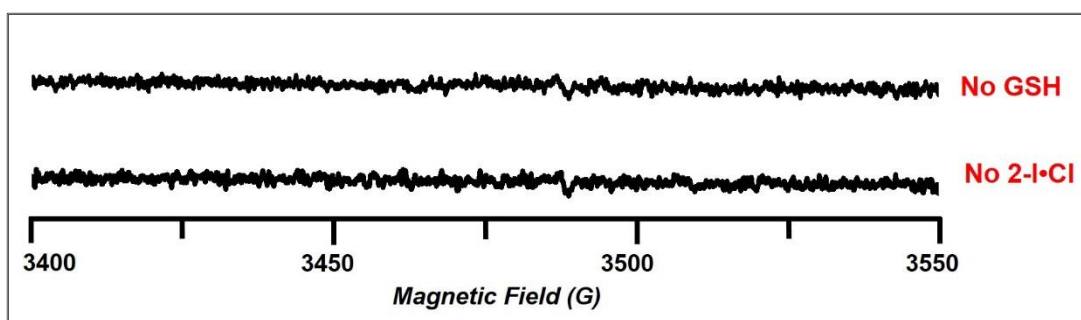


Figure 5.13 EPR spectra samples of **2-I•Cl** (1 mM) in absence of GSH or GSH (1 mM) in absence of **2-I•Cl** with DEPMPO (20 mM) in sodium chloride (25 mM) and phosphate buffer (75 mM) at pH = 10.83 after 3 h scanning at 298 K.

5.3.2.5 GSH Absence or 2-I•Cl Absence Controls

A solution of **2-I•Cl** (1 mM) without GSH (1 mM) in sodium chloride (25 mM) and phosphate buffer (75 mM) at pH = 10.8 and a solution of GSH (1 mM) without **2-I•Cl** in sodium chloride (25 mM) and phosphate buffer (75 mM) at pH = 10.8 were incubated at 310 K for 1 h and then DEPMPO (20 mM) was added as spin trap. The sample was scanned by EPR for 3 h at 298 K, but no free radical spectrum was observed (**Figure 5.13**).

5.3.2.6. In Trace Metal Basis Buffer

Metal ions especially Cu^{2+} are reported to catalyse the oxidation of GSH by dioxygen.⁴¹ In general phosphate buffer solution, there are residual trace metal ion which have the potential to affect the reactions of osmium complexes with GSH. To eliminate the interference of residual metal ions, a sample of **2-I•Cl** (1 mM) with GSH (1 mM) in sodium chloride (25 mM) and phosphate trace metal basis buffer (75 mM) solution at pH = 10.8 was incubated at 310 K for a 1 h duration and then DEPMPO (20 mM) was added as a spin trap. The sample was scanned by EPR for a period of 12 h at 298 K. The same result as for the corresponding sample in

general buffer solution with residual metal ions, an 18-peak spectrum, was continuously observed (**Figure 5.14**). From the simulation results (**Section 5.3.9**), this 18-peak spectrum was assigned to a mixture of DEPMPO-OH (green ●), DEPMPO-H (red ●) and DEPMPO-OOH (purple ●).

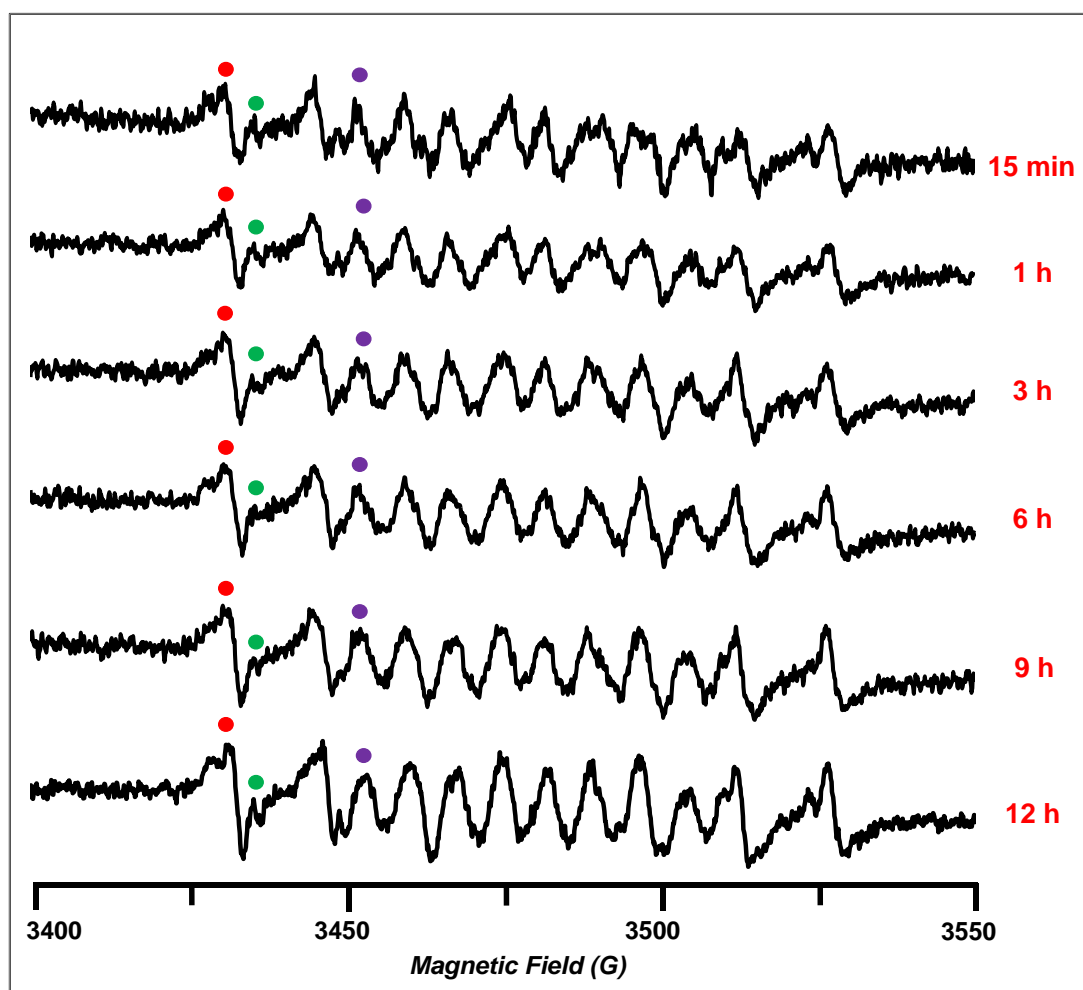
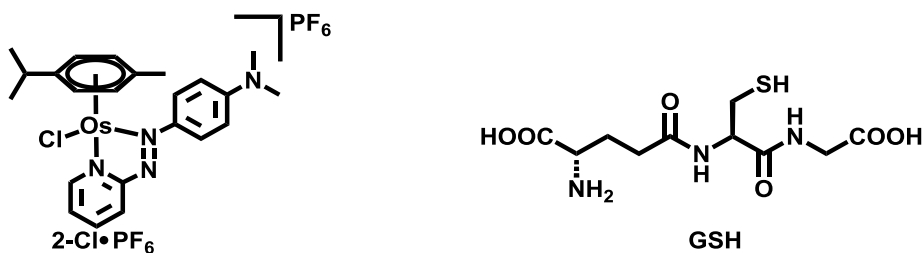


Figure 5.14. EPR spectra for sample of **2-I•Cl** (1 mM) with GSH (1 mM) and DEPMPO (20 mM) in trace metal basis sodium chloride (25 mM) and phosphate buffer (75 mM) solution at pH = 10.83 after 15 min, 1 h, 3 h, 6 h, 9 h and 12 h scanning at 298 K. The set of signals labelled with green ● was assigned to DEPMPO-OH, the set of signals labelled with red ● was assigned to DEPMPO-H and the set of signals labelled with purple ● was assigned to DEPMPO-OOH.

5.3.3. Reactions of 2-Cl•PF₆ with GSH



5.3.3.1. pH = 3.8

A solution containing **2-Cl•PF₆** (1 mM) with GSH (1 mM) in sodium chloride (25 mM) and phosphate buffer (75 mM) at pH = 3.8 was incubated at 310 K for 1 h and then DEPMPO (20 mM) was added as spin trap. The sample was scanned by EPR for 3 h at 298 K, but no free radical spectrum was observed (**Figure 5.15**).

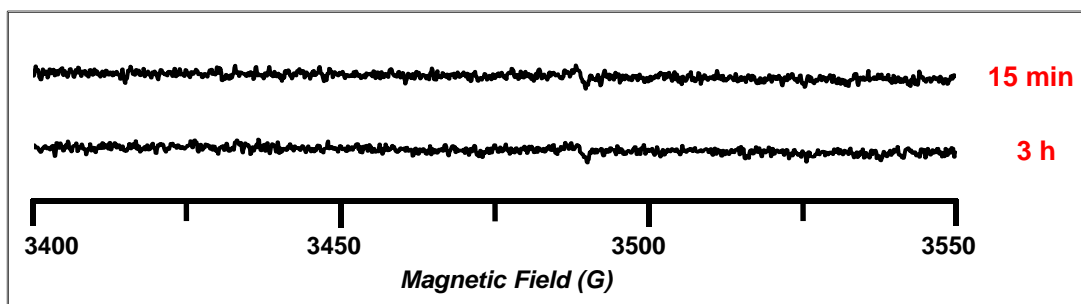


Figure 5.15. EPR spectra of a sample of **2-Cl•PF₆** (1 mM) with GSH (1 mM) and DEPMPO (20 mM) in sodium chloride (25 mM) and phosphate buffer (75 mM) solution at pH = 3.8 after 15 min and 3 h of scanning at 298 K.

5.3.3.2. pH = 7.4

A solution of **2-Cl•PF₆** (1 mM) with GSH (1 mM) in sodium chloride (25 mM) and phosphate buffer (75 mM) at pH = 7.4 was incubated at 310 K for 1 h and then DEPMPO (20 mM) was added as spin trap. The sample scanned on EPR for 12 h at 298 K and an 8-peak spectrum was observed

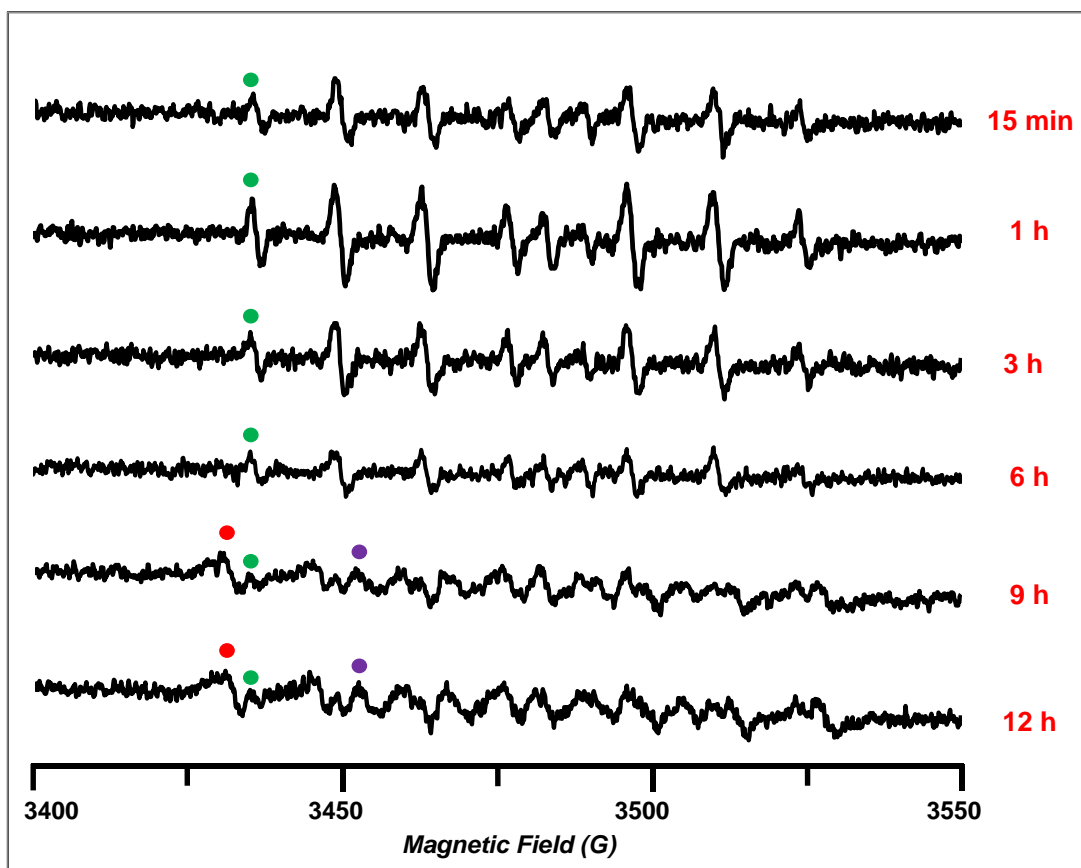


Figure 5.16. EPR spectra for sample of **2-Cl•PF₆** (1 mM) with GSH (1 mM) and DEPMPO (20 mM) in sodium chloride (25 mM) and phosphate buffer (75 mM) at pH = 7.40 after 15 min, 1 h, 3 h, 6 h, 9 h and 12 h scanning at 298 K. The set of signal labelled with green ● was assigned to DEPMPO-OH, the set of signal labelled with red ● was assigned to DEPMPO-H and the set of signal labelled with purple ● was assigned to DEPMPO-OOH.

from 15 min to 6 h scanning along with an 18-peak spectrum appearing after 9 h scanning (**Figure 5.16**). From the simulation results (**Section 5.3.9**), the 8-peak spectrum was assigned to DEPMPO-OH (green ●) and the 18-peak spectrum was assigned to mixture of DEPMPO-OH (green ●), DEPMPO-H (red ●) and DEPMPO-OOH (purple ●).

5.3.3.3. pH = 10.8

A solution of **2-Cl•PF₆** (1 mM) with GSH (1 mM) in sodium chloride (25 mM) and phosphate buffer (75 mM) solutions at pH = 10.8 was incubated at 310 K for 1 h and then DEPMPO (20 mM) was added as spin trap. The sample was scanned by EPR for 12 h at 298 K. At the beginning, an 18-peak spectrum was observed but later some peaks (red ● and purple ●) decreased in intensity whilst that of others (green ●) increased. Finally, a 12-peak spectrum was observed (**Figure 5.17**). From the simulation (**Section 5.3.9**), the 18-peak spectrum was assigned to mixture of DEPMPO-OH (green ●), DEPMPO-H (red ●) and DEPMPO-OOH (purple ball ●) and the 12-peak spectrum was assigned to mixture DEPMPO-OH (green ball ●) and DEPMPO-H (red ●).

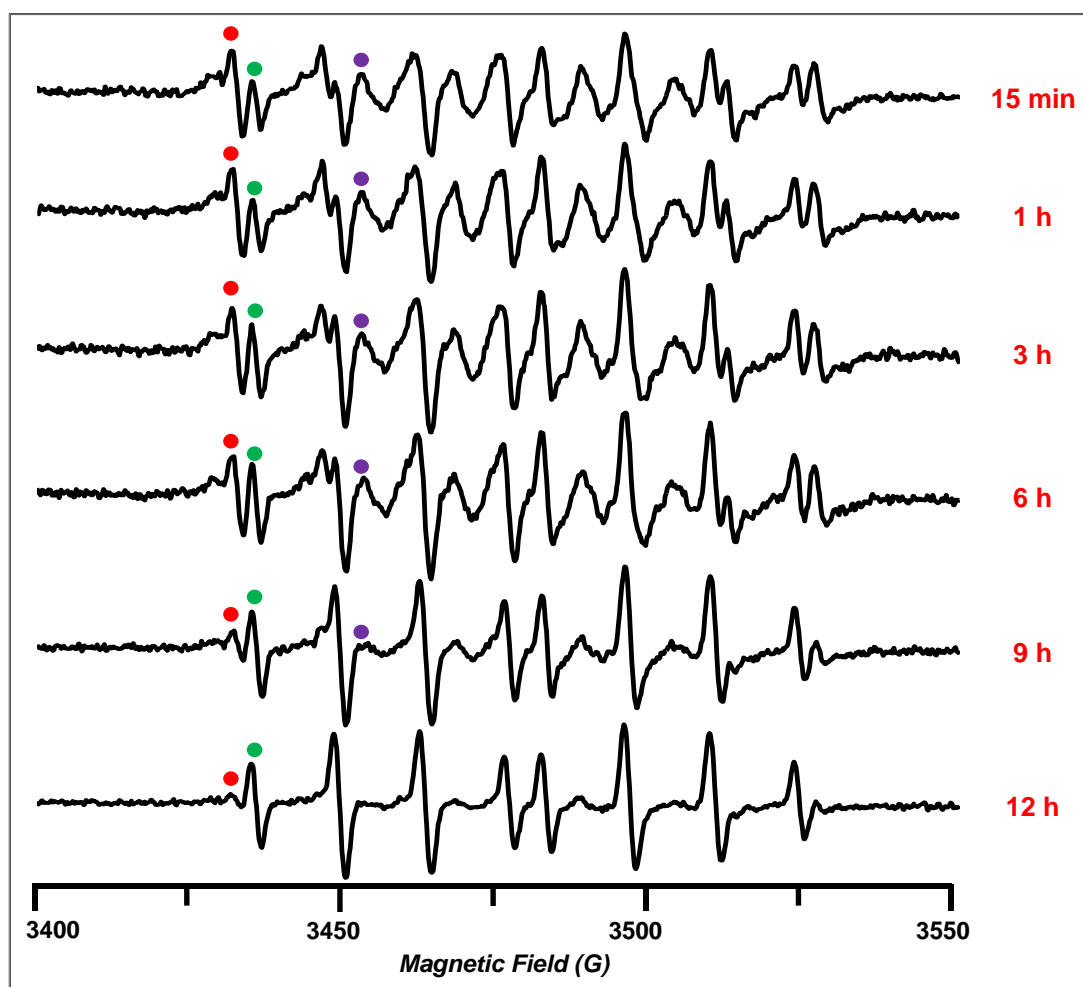


Figure 5.17. EPR spectra for a sample of $2\text{-Cl}\cdot\text{PF}_6$ (1 mM) with GSH (1 mM) and DEPMPO (20 mM) in sodium chloride (25 mM) and phosphate buffer (75 mM) at pH = 10.8 after 15 min, 1 h, 3 h, 6 h, 9 h and 12 h scanning at 298 K. The set of signal labelled with green ● was assigned to DEPMPO-OH, the set of signal labelled with red ● was assigned to DEPMPO-H and the set of signal labelled with purple ● was assigned to DEPMPO-OOH.

5.3.3.4. Under N₂

Solutions of **2-Cl•PF₆** (1 mM) with GSH (1 mM) in sodium chloride (25 mM) and phosphate buffer (75 mM) solution at pH values of 3.8, 7.4 and 10.8 was prepared under N₂ protection and incubated at 310 K for 1 h and then DEPMPO (20 mM) was added as spin trap. The sample was scanned by EPR for 3 h, but no free radical spectrum was observed (**Figure 5.18**).

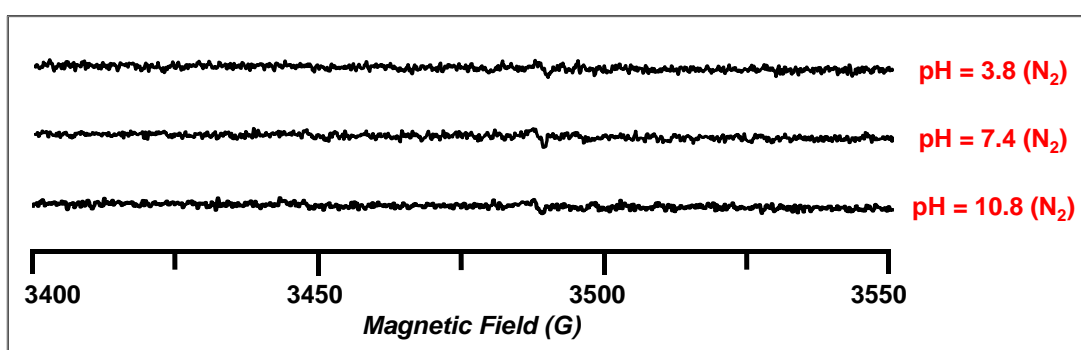
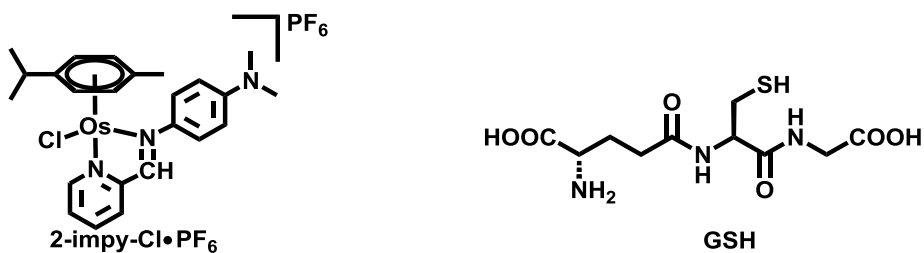


Figure 5.18. EPR spectra for sample of **2-Cl•PF₆** (1 mM) with GSH (1 mM) and DEPMPO (20 mM) in sodium chloride (25 mM) and phosphate buffer (75 mM) solution at pH values of 3.8, 7.4 and 10.8 with the protection of N₂ after 3 h scanning at 298 K.

5.3.4. Reactions of 2-impy-Cl•PF₆ with GSH



Solutions of **2-impy-Cl•PF₆** (1 mM) with GSH (1 mM) in sodium chloride (25 mM) and phosphate buffer (75 mM) at pH = 3.8, 7.4 and 10.8 were incubated at 310 K for 1 h and then DEPMPO (20 mM) was added as spin trap. The sample was scanned by EPR for 3 h but no free radical spectrum was observed (**Figure 5.19**).

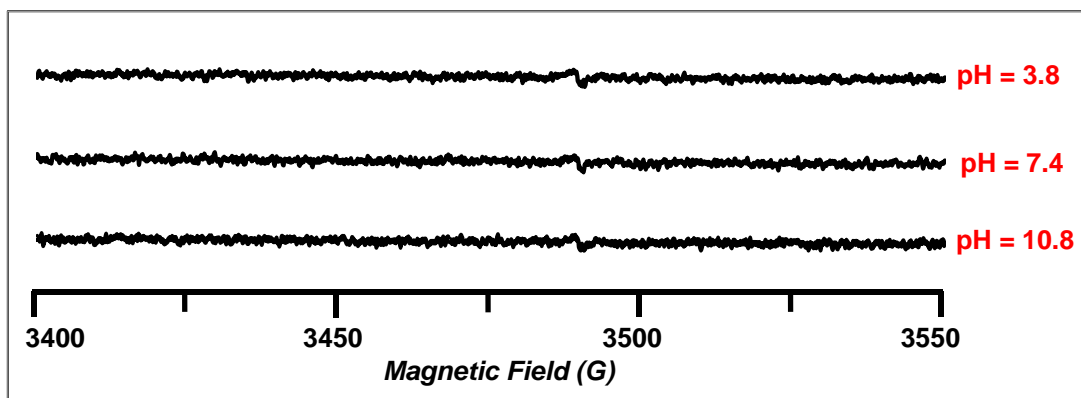
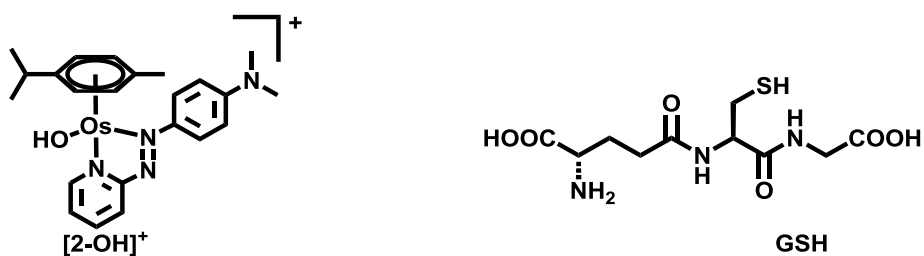


Figure 5.19. EPR spectra for sample of **2-impy-Cl•PF₆** (1 mM) with GSH (1 mM) and DEPMPO (20 mM) in sodium chloride (25 mM) and phosphate buffer (75 mM) at pH = 3.8, 7.4 and 10.8 after 3 h EPR scanning at 298 K.

5.3.5. Reactions of $[2\text{-OH}]^+$ with GSH



5.3.5.1. pH = 3.8

A solution of $[2\text{-OH}]^+$ (1 mM) with GSH (1 mM) in sodium chloride (25 mM) and phosphate buffer (75 mM) at pH = 3.8 was incubated at 310 K for 1 h and then DEPMPO (20 mM) was added as spin trap. The sample was scanned by EPR for 3 h at 298 K, but no free radical spectrum was observed (**Figure 5.20**).

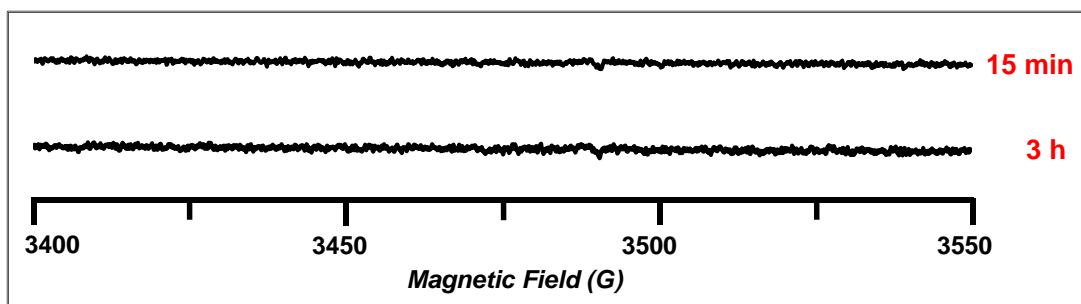


Figure 5.20. EPR spectra for sample of $[2\text{-OH}]^+$ (1 mM) with GSH (1 mM) and DEPMPO (20 mM) in sodium chloride (25 mM) and phosphate buffer (75 mM) at pH = 3.8 after 15 min and 3 h EPR scanning at 298 K.

5.3.5.2. pH = 7.4

A solution of $[2\text{-OH}]^+$ (1 mM) with GSH (1 mM) in sodium chloride (25 mM) and phosphate buffer (75 mM) solutions at pH = 7.4 was incubated at 310 K for 1 h. Then DEPMPO (20 mM) added as spin trap.

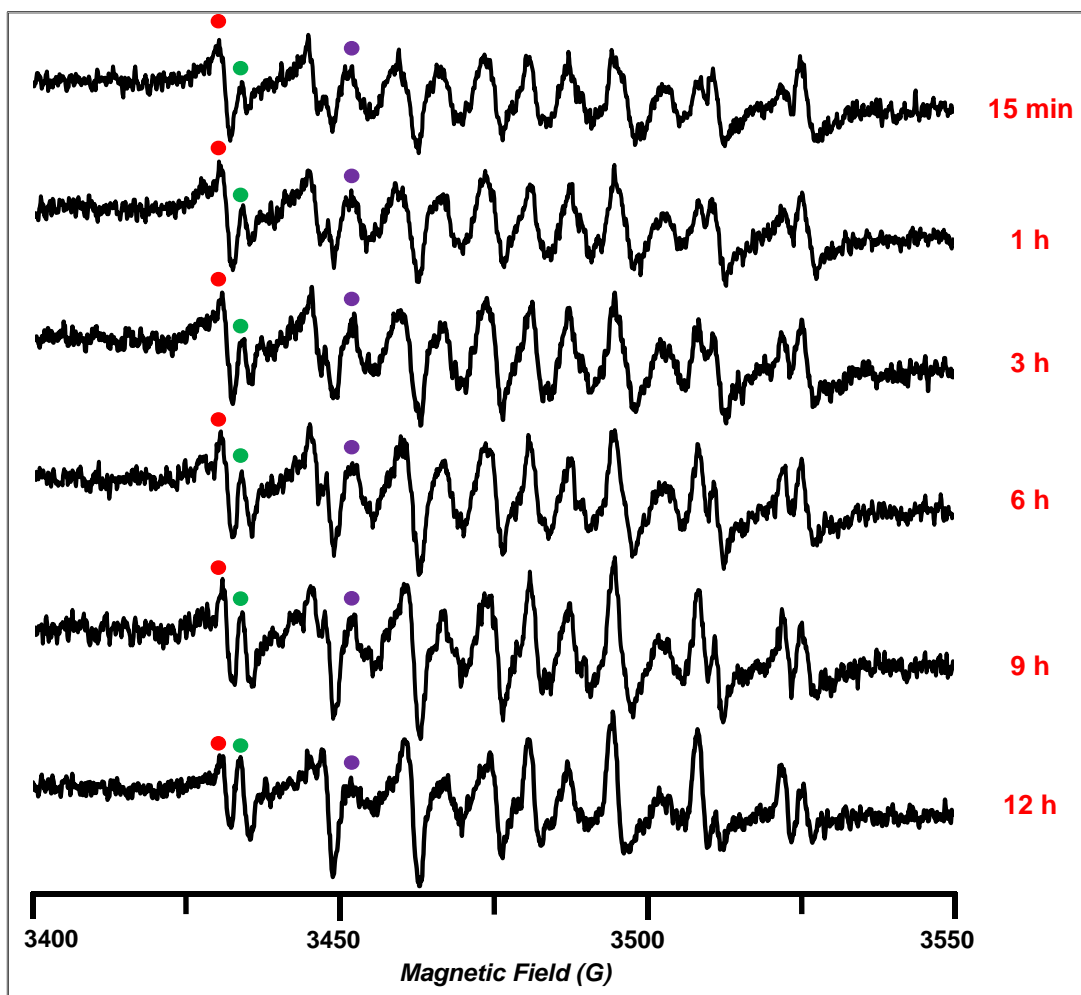


Figure 5.21. EPR spectra for sample of $[2\text{-OH}]^+$ (1 mM) with GSH (1 mM) and DEPMPO (20 mM) in sodium chloride (25 mM) and phosphate buffer (75 mM) at pH = 7.4 after 15 min, 1 h, 3 h, 6 h, 9 h and 12 h scanning at 298 K. The set of signal labelled with green ● was assigned to DEPMPO-OH, the set of signal labelled with red ● was assigned to DEPMPO-H and the set of signal labelled with purple ● was assigned to DEPMPO-OOH.

The sample was scanned by EPR for 12 h. An 18-peak spectrum was continuously observed (**Figure 5.21**) but as the reaction progressed one set of peaks (green ●) increased in intensity whilst and the rest of the peaks decreased (red ● and purple ●). There was still an 18-peak spectrum even after 12 h. From the simulation results (**Section 5.3.9**), this 18-peak spectrum was assigned to mixture of DEPMPO-OH (green ●), DEPMPO-H (red ●) and DEPMPO-OOH (purple ●).

5.3.5.3. Effect of Superoxide Dismutase (SOD)

A solution of [2-OH]⁺ (1 mM) with GSH (1 mM) in sodium chloride (25 mM) and phosphate buffer (75 mM) at pH = 7.4 was prepared and divided into two. To one portion, was added superoxide dismutase (30 μM) and to the other, which served as a control, was added buffer. After incubation of these two samples at 310 K for 1 h was added DEPMPO (20 mM) as spin trap. These two samples were scanned by EPR. An 18-peak spectrum was observed for the control sample and a 12-peak spectrum was observed for the sample containing superoxide dismutase (**Figure 5.22**). As the simulation results (**Section 5.3.9**) showed, the 18-peak spectrum can be assigned to a mixture of DEPMPO-OH (green ●), DEPMPO-H (red ●) and DEPMPO-OOH (purple ●) and the 12-peak spectrum observed for the sample containing SOD can be assigned to a

mixture of DEPMPO-OH (green ●) and DEPMPO-H (red ●), with an absence of peaks for DEPMPO-OOH. This result supported the assignment of peaks labelled with purple ● to DEPMPO-OOH.

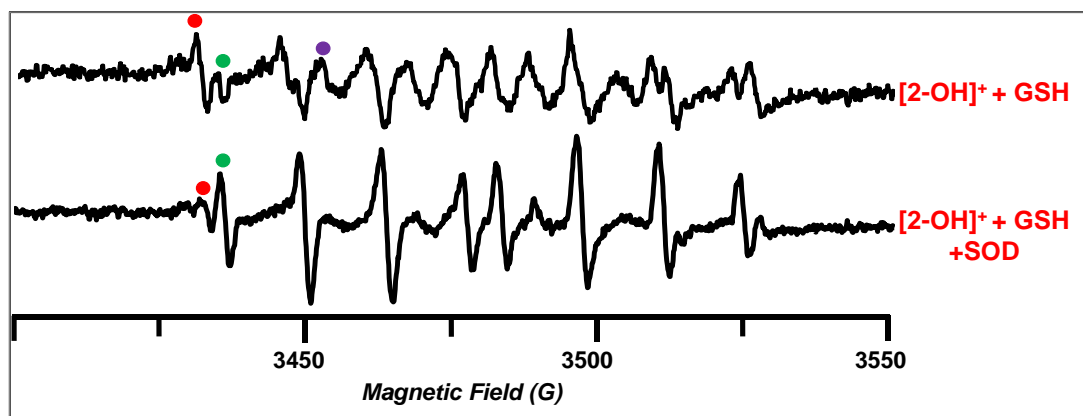


Figure 5.22. Comparison of EPR spectra for samples of $[2\text{-OH}]^+$ (1 mM) with GSH (1 mM) and DEPMPO (20 mM) in presence or absence of SOD (30 μM) in sodium chloride (25 mM) and phosphate buffer (75 mM) at pH = 7.4.

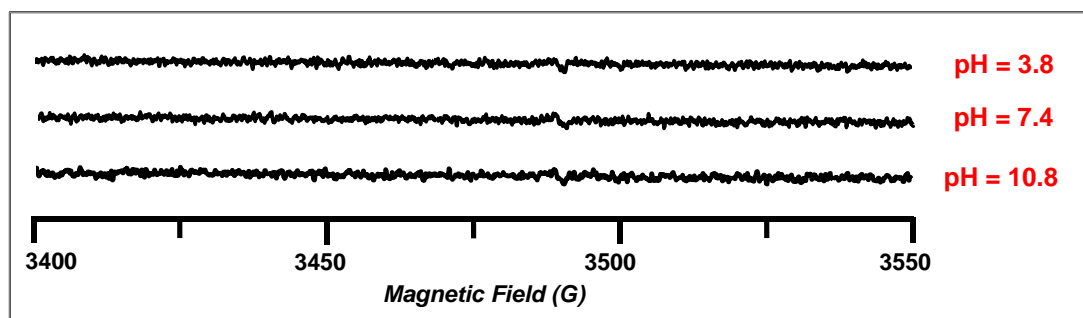
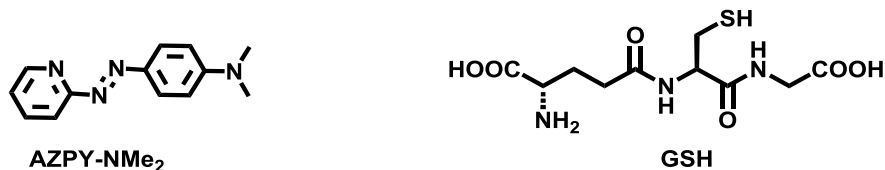


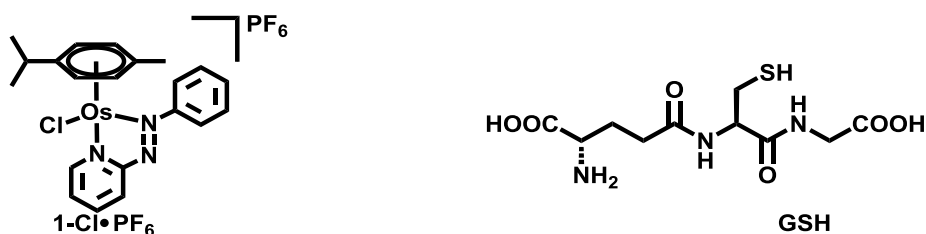
Figure 5.23. EPR spectra for samples of AZPY-NMe₂ (1 mM) with GSH (1 mM) and DEPMPO (20 mM) in sodium chloride (25 mM) and phosphate buffer (75 mM) at pH = 3.8, 7.4 and 10.8 after 3 h scanning at 298 K.

5.3.6. Reactions of AZPY-NMe₂ with GSH



Solutions of free ligand **AZPY-NMe₂** (1 mM) with GSH (1 mM) in sodium chloride (25 mM) and phosphate buffer (75 mM) at pH = 3.8, 7.4 and 10.8 were prepared and incubated at 310 K for 1 h and then DEPMPO (20 mM) was added as spin trap. The samples were scanned by EPR for 3 h, but no free radical species were observed (**Figure 5.23**).

5.3.7. Reactions of 1-Cl•PF₆ with GSH



A solution of **1-Cl•PF₆** (1 mM) with GSH (1 mM) in sodium chloride (25 mM) and phosphate buffer (75 mM) solutions at pH = 10.8 was prepared, incubated at 310 K for 30 min, and then DEPMPO (20 mM) was added as spin trap. The sample was scanned by EPR for 12 h. An 18-peak spectrum was observed after 15 min scanning at 310 K and then the spectrum decayed very rapidly (this may be ascribable the instability of **1-Cl•PF₆** in aqueous solution²⁷). After a 9 h scanning period, only very

weak signals for radicals were observed (**Figure 5.24**). From the simulation results (**Section 5.3.9**), the 18-peak spectrum was assigned to the mixture of DEPMPO-OH (green ●), DEPMPO-H (red ●) and DEPMPO-OOH (purple ●).

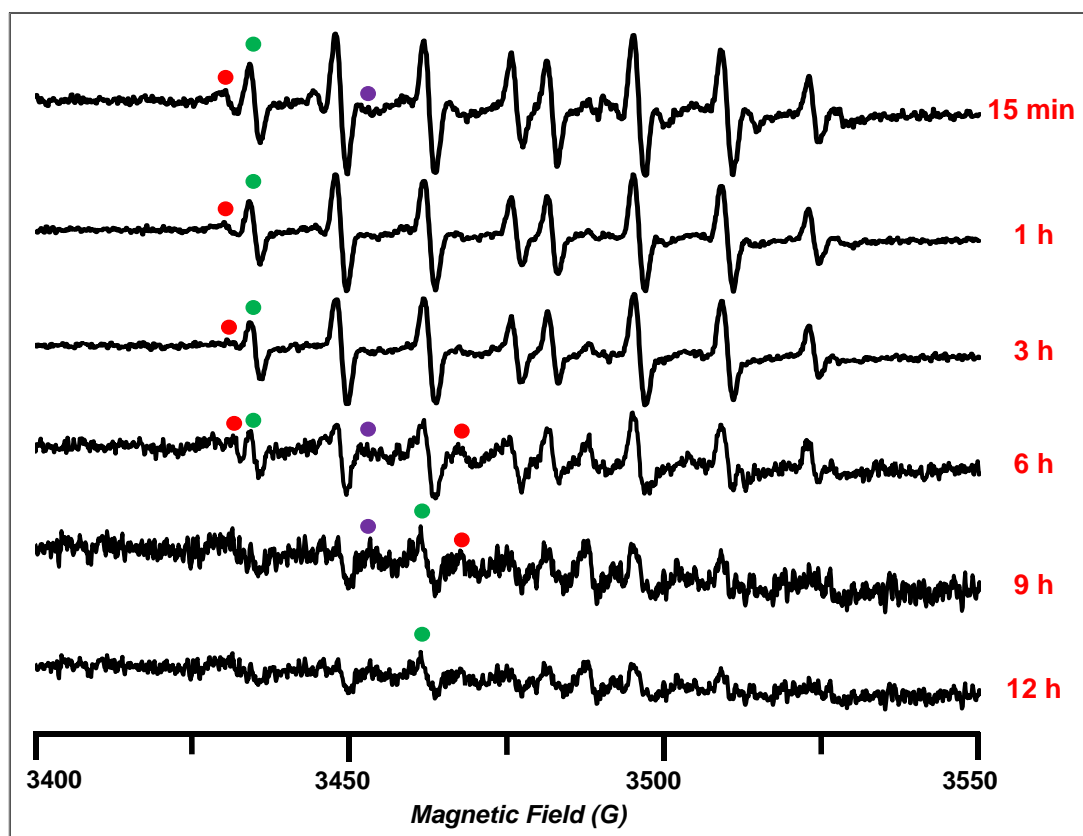


Figure 5.24. EPR spectra for sample of $\mathbf{1\text{-Cl}\cdot\text{PF}_6}$ (1 mM) with GSH (1 mM) and DEPMPO (20 mM) in sodium chloride (25 mM) and phosphate buffer (75 mM) at pH = 10.8 after 15 min, 1 h, 3 h, 6 h, 9 h and 12 h scanning at 298 K. The set of signal labelled with green ● was assigned to DEPMPO-OH, the set of signal labelled with red ● was assigned to DEPMPO-H and the set of signal labelled with purple ● was assigned to DEPMPO-OOH.

5.3.9. Simulation of EPR Spectra

EPR experiments were conducted in this chapter to study reactions of the osmium complexes with GSH. An 8-peak spectrum was observed in the reactions of **2-I•Cl** with GSH at pH = 7.4 (Section 5.3.2.2) and **2-Cl•PF₆** with GSH at pH = 7.4 (Section 5.3.3.2). An 18-peak spectrum was observed in the reactions of **2-I•Cl** with GSH at pH = 7.4 (Section 5.3.2.2) and pH = 10.8 (Section 5.3.2.3), **2-Cl•PF₆** with GSH at pH = 7.4 (Section 5.3.3.2) and pH = 10.8 (Section 5.3.3.3), **[2-OH]⁺** with GSH at pH = 7.4 (Section 5.3.5.2). These spectra were analysed and simulated with the EASYSPIN.³⁷ Three independent experiments and simulation combining spectral resolution (2048 data points at 200 G) were used to calculate error bars.

5.3.9.1. 8-Peaks Spectrual Simulation

The experimental spectrum for the reaction of **2-I•Cl** (1 mM) with GSH (1 mM) at pH = 7.4 with spin trap DEPMPO (20 mM) after 1 h reaction time at 310 K and a further 1 h EPR scanning at 298 K was used as a typical 8-peak spectrum for simulation. The spectrum was fitted with parameters $\alpha^P=47.52$ G, $\alpha^N=14.02$ G, $\alpha^H=13.06$ G, which can be assigned to DEPMPO-OH (Figure 5.26).³⁵

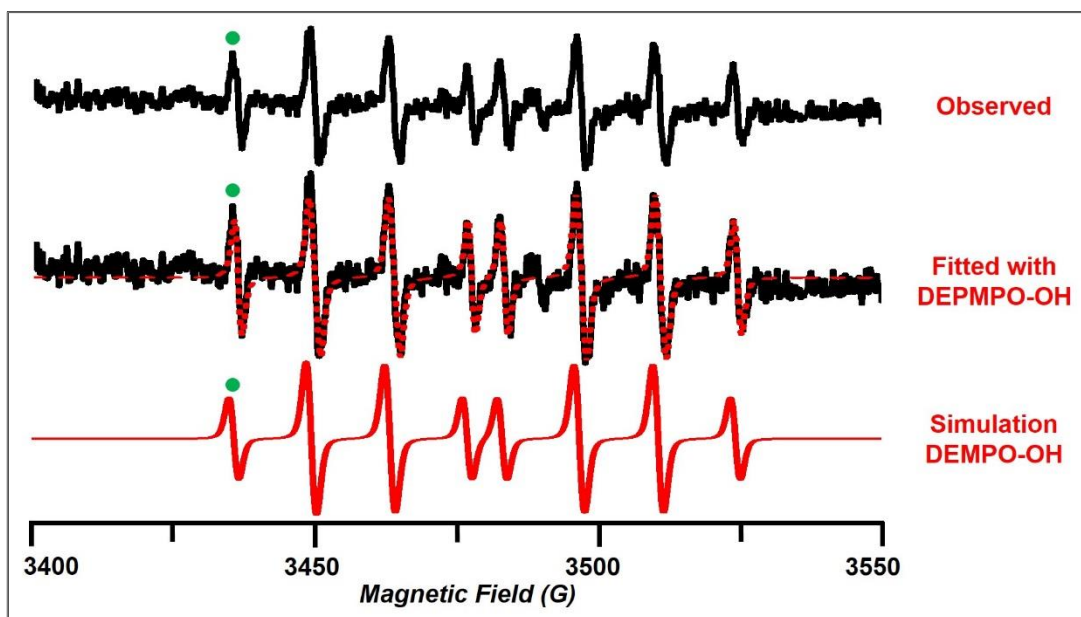


Figure 5.26. The simulation result for the typical 8-peaks spectrum (green ●) observed in the reaction of **2-I•Cl** (1 mM) with GSH (1 mM) at pH = 7.4 in presence of DEPMPO (20 mM), which was assigned to DEPMPO-OH.

5.3.9.2. Simulation of the 18-peak Spectrum

The experimental spectrum of **2-Cl•PF₆** (1 mM) on reaction with GSH (1 mM) at pH = 10.8 in presence of DEPMPO (20 mM) after 1 h reaction time at 310 K and a further 6 h EPR scanning at 298 K was used as a typical 18-peak spectrum for simulation. It was fitted as a mixture of peaks for DEPMPO-OH, DEPMPO-H and DEPMPO-OOH (**Figure 5.27**). The simulation result showed the experimental spectrum contained DEPMPO-OH ($\alpha^P = 47.52$, $\alpha^N = 14.02$, $\alpha^H = 13.06$), DEPMPO-H ($\alpha^P = 49.91$, $\alpha^H = 15.12$, $\alpha^N = 13.58$, $\alpha^H = 3.21$, $\alpha^H = 0.29$) and DEPMPO-OOH

(Isomer I, 44%, $\alpha^P = 47.3$, $\alpha^N = 13.72$, $\alpha^H = 12.26$, $\alpha^H = 0.93$, $\alpha^H = 0.42$, $\alpha^H = 0.43$; Isomer II, 42%, $\alpha^P = 47.52$, $\alpha^N = 13.72$, $\alpha^H = 10.18$, $\alpha^H = 0.92$, $\alpha^H = 1.02$, $\alpha^H = 0.48$; Isomer III, 14%, $\alpha^P = 37.13$, $\alpha^N = 15.14$, $\alpha^H = 9.8$, $\alpha^H = 1.38$).^{33,35} The ratio of DEPMPO-OH (green ●), DEPMPO-H (red ●) and DEPMPO-OOH (purple ●) signal intensities was 3:2:2.

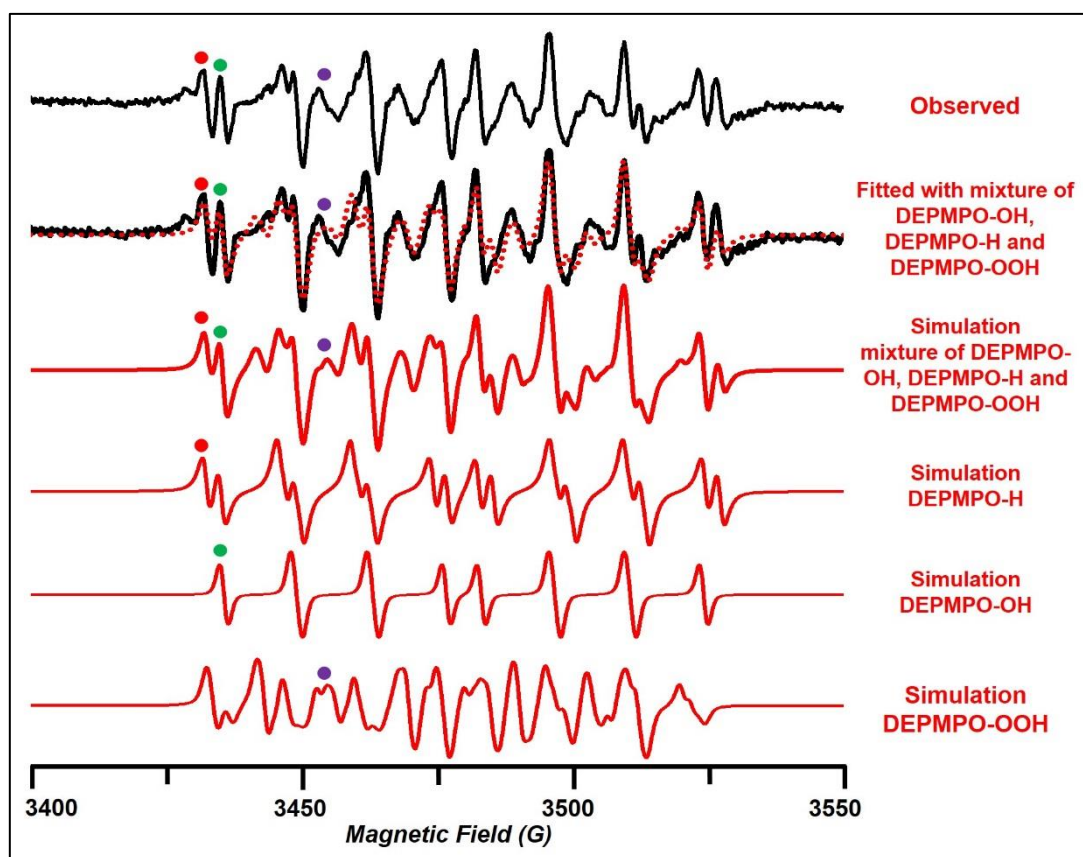


Figure 5.27. The simulation result for the typical 18-peaks spectrum (mixture of red ●, green ● and purple ●) observed in the reaction of **2-Cl•PF₆** (1 mM) with GSH (1 mM) at pH = 10.8 in presence of DEPMPO (20 mM), which was assigned to a spectral mixture of DEPMPO-OH, DEPMPO-H and DEPMPO-OOH. The ratio of DEPMPO-OH (green ●) : DEPMPO-H (red ●) : DEPMPO-OOH (purple ●) signal intensities is 3:2:2 based on simulation weight.

Table 5.1. The comparison between observed parameters fitted by simulation for the spectra for reaction of **2-I•Cl** with GSH (**Figure 5.27**) and reported parameters³⁵ of DEPMPO-OH, DEPMPO-H.

	Reported (G) ^b	Observed (G) ^a
DEPMOP-H	$\alpha^P = 47.50$	$\alpha^P = 48.62 \pm 1.15$
	$\alpha^N = 14.00$	$\alpha^N = 13.93 \pm 0.36$
	$\alpha^{H_a} = 15.00$	$\alpha^{H_a} = 15.09 \pm 0.18$
	$\alpha^{H_a} = 3.00$	$\alpha^{H_a} = 3.10 \pm 0.19$
	$\alpha^{H_b} = 0.27$	$\alpha^{H_b} = 0.27 \pm 0.11$
DEPMPO-OH	$\alpha^P = 46.70$	$\alpha^P = 46.77 \pm 0.66$
	$\alpha^N = 13.90$	$\alpha^N = 13.99 \pm 0.17$
	$\alpha^{H_a} = 13.50$	$\alpha^{H_a} = 13.40 \pm 0.51$

^a means \pm the standard deviation of three independent experiments with parameters fitted by simulation.

^b from reference 35

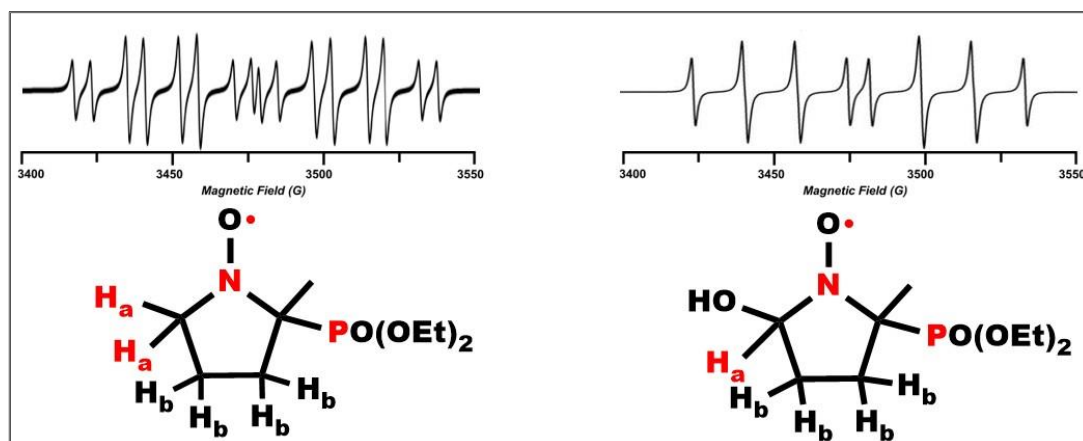


Figure 5.28. The EPR spectra (top) and structures of DEPMPO-H and DEPMPO-OH (bottom). The atoms H ($I = 1/2$), N ($I = 1$), P ($I = 1/2$), causing hyperfine coupling are shown in red.

Table 5.2. The comparison between parameters fitted by simulation for the spectra the reaction of **2-Cl•PF₆** with GSH (**Figure 5.27**) and reported parameters³⁵ of DEPMPO-OOH.

	Reported (G) ^b	Observed (G) ^a
Isomer I	$\alpha^P = 50.15$	$\alpha^P = 49.97 \pm 2.06$
	$\alpha^N = 13.00$	$\alpha^N = 13.25 \pm 0.43$
	$\alpha^{H_a} = 11.30$	$\alpha^{H_a} = 11.55 \pm 1.15$
	$\alpha^{H_b} = 0.85$	$\alpha^{H_a} = 0.86 \pm 0.16$
	$\alpha^{H_b} = 0.35$	$\alpha^{H_b} = 0.37 \pm 0.13$
	$\alpha^{H_b} = 0.53$	$\alpha^{H_b} = 0.49 \pm 0.15$
Isomer II	$\alpha^P = 48.68$	$\alpha^P = 47.54 \pm 1.39$
	$\alpha^N = 13.08$	$\alpha^N = 13.29 \pm 0.41$
	$\alpha^{H_a} = 10.20$	$\alpha^{H_a} = 10.27 \pm 0.33$
	$\alpha^{H_b} = 0.88$	$\alpha^{H_a} = 0.97 \pm 0.24$
	$\alpha^{H_b} = 0.41$	$\alpha^{H_b} = 0.62 \pm 0.32$
	$\alpha^{H_b} = 0.34$	$\alpha^{H_b} = 0.47 \pm 0.16$
Isomer III	$\alpha^P = 40.08$	$\alpha^P = 39.13 \pm 1.61$
	$\alpha^N = 13.30$	$\alpha^N = 14.24 \pm 0.78$
	$\alpha^{H_a} = 10.00$	$\alpha^{H_a} = 9.81 \pm 0.40$
	$\alpha^{H_b} = 1.50$	$\alpha^{H_b} = 1.27 \pm 0.30$

^a mean \pm the standard deviation of three independent experiments with parameters fitted by simulation.

^b from reference 35

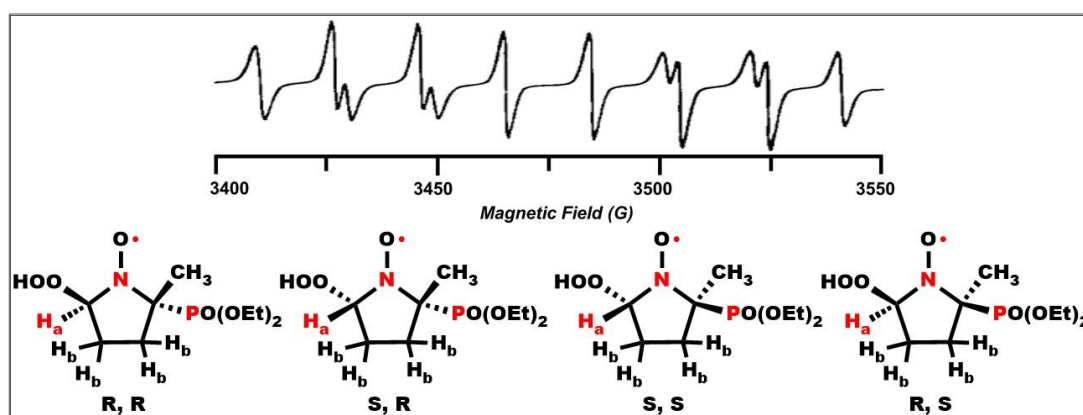


Figure 5.29. The structures of four possible diastereoisomers of DEPMPO-OOH (bottom) and assumed EPR spectrum contribution from three of these four diastereoisomers.⁴² The atoms H ($I = 1/2$), N ($I = 1$), P ($I = 1/2$), causing hyperfine coupling are shown in red.

5.3.10. H₂O₂ Detection

5.3.10.1. H₂O₂ Test Strips

Three samples of [2-I]⁺ (100 μM) alone, GSH (300 μM) alone and [2-I]⁺ (100 μM) mixing with GSH (300 μM) in sodium chloride (25 mM) and phosphate buffer (75 mM) solution at pH = 7.4 were incubated at 310 K for 3 h and then left in contact with the H₂O₂ test strips for 15 s. The result showed that there was below 2 mg/L (50 μM) hydrogen peroxide generated in the reaction [2-I]⁺ with GSH. There was a faint blue colour in the H₂O₂ test strip for the solution [2-I]⁺ (100 μM), which could be caused by the blue colour of [2-I]⁺ itself (**Figure 5.30**).

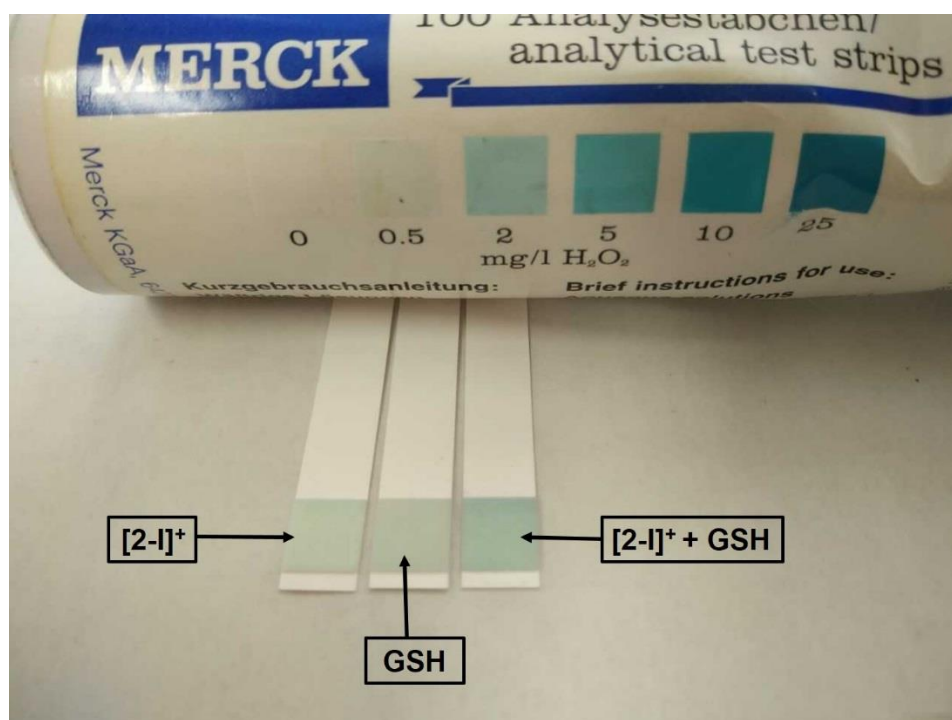


Figure 5.30. Colour change of H₂O₂ test strips for samples of [2-I]⁺ (100 μM), GSH (300 μM) and [2-I]⁺ (100 μM) reacting with GSH (300 μM) in sodium chloride (25 mM) and phosphate buffer (75 mM) at pH = 7.4 after 3 h incubation at 310 K.

5.3.10.2. Ammonium Molybdate Method

Three solutions containing **2-I•PF₆** (100 μ M), GSH (300 μ M) and **2-I•PF₆** (100 μ M) mixed with GSH (300 μ M) were prepared in sodium chloride (25 mM) and phosphate buffer (75 mM) at pH = 7.4, and incubated at 310 K for 5 min, 1 h, 2 h, 3 h and 4 h. Then 0.5 mL of these three solutions was mixed with 0.5 mL ammonium molybdate solution (32.4 mM), and the reaction sample in absence of ammonium molybdate was also prepared as control.

The concentration of hydrogen peroxide for these four samples was determined from the change in absorbance at 405 nm using the calibration equation $y = 0.0123x + 0.0305$ (y is the absorbance change and x is the concentration of hydrogen peroxide in μ M). The absorbance at 405 nm for sample of **2-I•PF₆** (100 μ M) on reaction with GSH (300 μ M) changed by 0.28 after 2 h incubation and the concentration of hydrogen peroxide was therefore ca. 20 μ M (**Figure 5.31**).

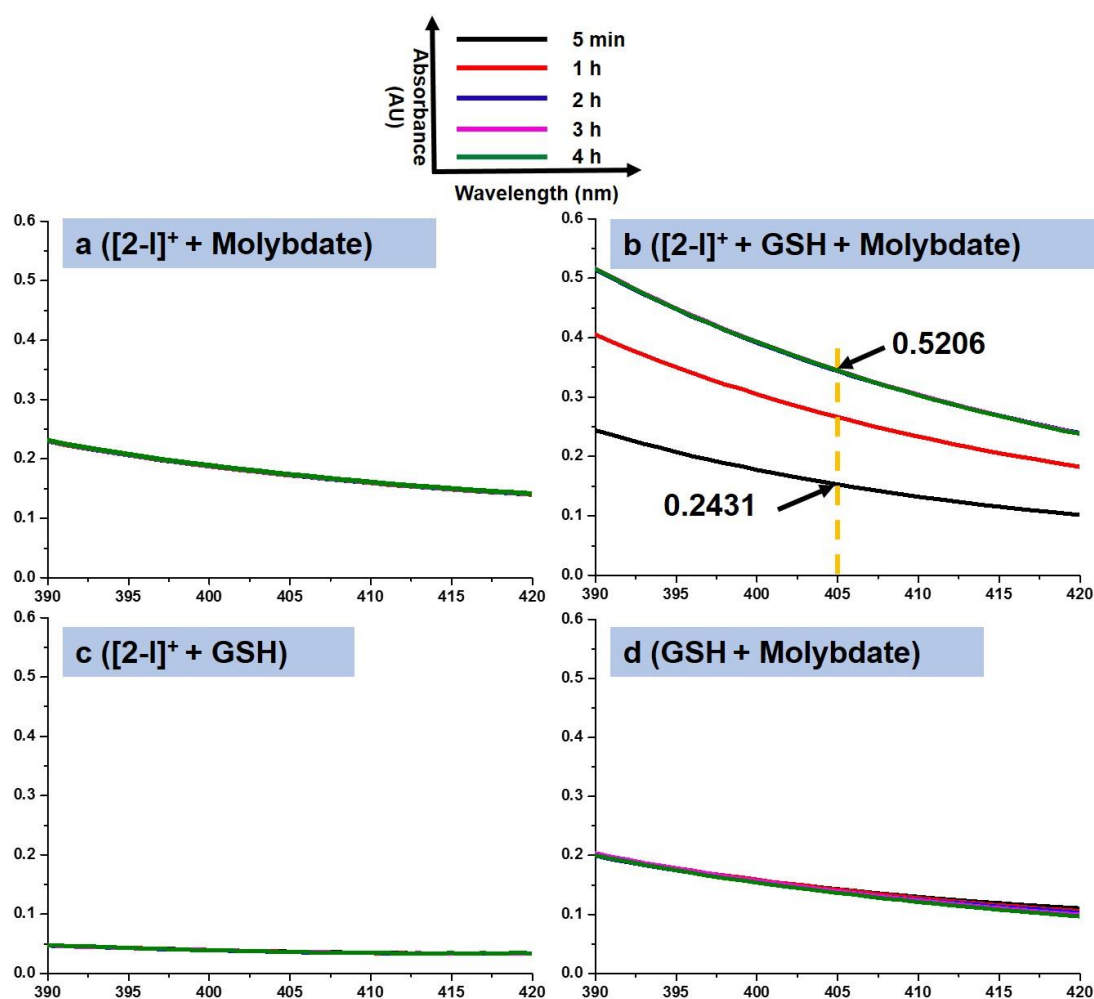


Figure 5.31. UV-vis spectra of samples a) mixture of $[2-I]^+$ (100 μM) with ammonium molybdate (32.4 mM); b) mixture of $[2-I]^+$ (100 μM) with GSH (300 μM) and ammonium molybdate (32.4 mM); c) mixture of $[2-I]^+$ (100 μM) with GSH (300 μM); d) mixture of GSH (300 μM) with ammonium molybdate (32.4 mM). All samples were prepared in sodium chloride (25 mM) and phosphate buffer (75 mM) at pH = 7.4, and were incubated at 310 K for 5 min, 1 h, 2 h, 3 h and 4 h.

5.3.11. GSSG Detection

The oxidation of GSH in the reaction with $[2-I]^+$ was determined through ^1H NMR experiments. The result (**Figure 5.32**) showed that 60% GSH was oxidized to GSSG in the reaction of $[2-I]^+$ (2 mM) with 1 mole equiv GSH (2 mM) while little GSSG was observed in the sample of GSH (2 mM) without **2-I** after 3 h incubation at 310 K in deuterated phosphate buffer (75 mM, pH 7.4). GSSG solution (6 mM) in deuterated phosphate buffer (75 mM, pH 7.4) was also scanned as references. This result demonstrated that GSH may represent a source of electrons for the production of superoxide from dioxygen.

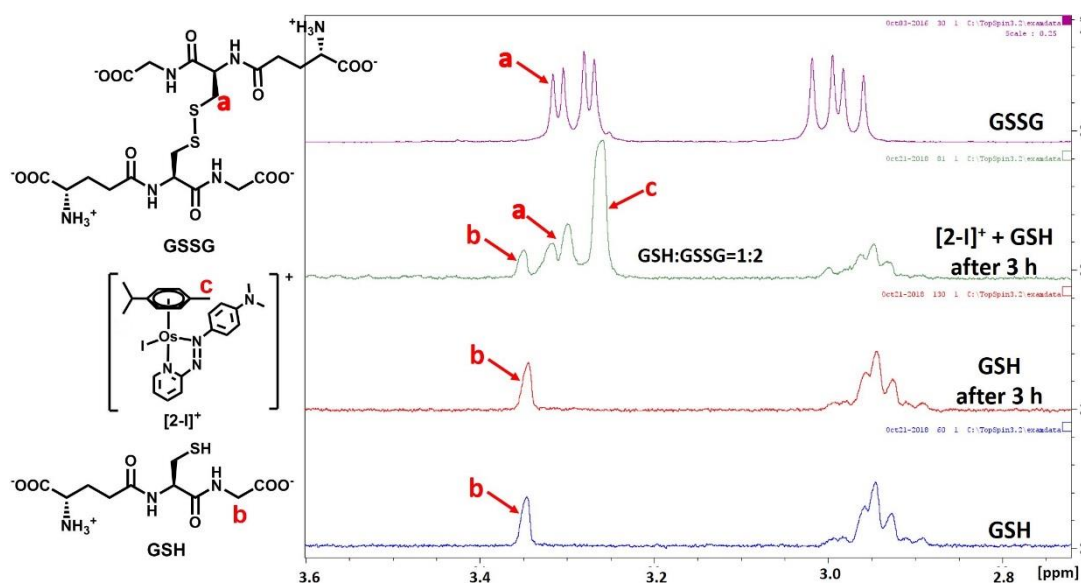


Figure 5.32. The ^1H NMR spectra for GSH (2 mM), GSSG (4 mM) references without incubation as well as reactions of GSH (2 mM) exposed to air and GSH with $[2-I]^+$ (2 mM) exposed to air after 3 h incubation at 310 K in deuterated phosphate buffer (75 mM, pH 7.4).

5.4. Discussion

GSH (γ -Glu-L-Cys-Gly) is a tripeptide with a *ca.* 5 mM intracellular concentration providing free thiol and electrons for many reactions including cell signalling and metabolism, especially reactions with free radicals to maintain the cellular redox balance, and binding to heavy metal ions to reduce metal-induced stress in cells.^{22,23,26} When transition metal ions as including metallodrugs enter into the cells, they are likely to bind to GSH and form metal-SG adducts which can be pumped out of the cell through the glutathione S-conjugate export pump (GS-X pump).⁴³⁻⁴⁵ As a result, GSH exhibits a ‘double-edged sword’ function that protects healthy cells from the heavy metal toxicity as well as reducing the activity of metallodrugs in cancer cells. It is a challenge to take advantage of the properties of GSH in anticancer metallodrug development. There are several good examples that GSH promoting rather than blocking the activity of metallodrugs. The anticancer complex $\text{Pt}^{\text{II}}(\text{ethylenediamine})\text{Cl}_2$ was reported to react with GSH and form a glutathione-bridged diplatinum(II) macrochelate. This dinuclear intermediate may play a role in allowing platinum drug to reach the nucleus and bind to DNA.⁴⁶ GSH was also found to promote the binding of $[(\eta^6\text{-bip})\text{Ru}(\text{en})\text{Cl}]^+$ (bip = biphenyl, en = ethylenediamine) to DNA with a mechanism in which GSH firstly binds to Ru ions to form the

thiolato adduct which was then very easily oxidized to the ruthenium sulfenate complex. Compared to the original Ru(II) complex, the sulfenate complex had a stronger ability to bind to DNA.⁴⁷

$[\text{Os}(\eta^6\text{-}p\text{-cymene})(4\text{-(2-pyridylazo)-}N,N\text{-dimethylaniline})\text{I}]^+$ (**FY26**, [**2-I**]⁺) is about 49 times more toxic to >800 cancer cell lines than cisplatin and retains potency towards cisplatin-resistant cancer cells with a novel mechanism of action. [**2-I**]⁺ dramatically increased the level of intracellular ROS especially superoxide.²⁸ Further studies showed that GSH promotes the hydrolysis process of [**2-I**]⁺ and activates this osmium pro-drug.⁴⁸ The mechanism of this activation process was explored in **Chapter 4**. Results acquired indicated that deprotonated GS⁻ (the pK_a of -SH in GSH is 9.65⁴⁹) attacked on the -N=N- bond in the osmium azo complex and formed an sulfenylhydrazide intermediate in which the monodentate iodide ligand is easily replaced by H₂O to produce aqua analogue [**2-OH**]²⁺ and further hydroxido analogue [**2-OH**]⁺.

In this **Chapter 5**, EPR experiments were conducted to detect free radicals in the reactions of GSH with several osmium complexes including lead complex [**2-I**]⁺, chloride analogue [**2-Cl**]⁺, hydroxido analogue [**2-OH**]⁺, imino analogue [**2-impy-Cl**]⁺, no-substituted [**1-Cl**]⁺, thiolate adduct **2-SG** and free ligand **AZPY-NMe₂**. The reaction

conditions including dioxygen concentration and pHs were modified since such conditions affect the hydrolysis reactions (**Chapter 4**).

Table 5.3. The summary of free radicals production in the reactions of compounds with GSH at various conditions.

Complexes	pH			Under N ₂
	3.8	7.4	10.8	
[2-I] ⁺	×	✓	✓✓	×
[2-Cl] ⁺	×	✓	✓✓	×
[2-OH] ⁺	×	✓✓	✓✓	○
[1-Cl] ⁺	○	○	✓✓	○
[2-imp-Cl] ⁺	×	×	×	○
2-SG	×	×	×	○

× no free radicals observed; ✓ only hydroxyl radical (•OH) observed; ✓✓ mixed free radicals superoxide (O₂^{•−}), hydroxyl radical (•OH) and hydrogen atom (•H) observed; ○ not determined.

pH effect

For **2-I•PF₆** (**FY26**), no free radicals were observed in the reaction with GSH because of its poor solubility but in the reactions of the solubility-improved complex **2-I•Cl** (in aqueous solution, both **2-I•PF₆** and **2-I•Cl** dissociate to [2-I]⁺) with GSH, at pH = 10.8, an 18-peak spectrum was observed which can be assigned to a mixture of DEPMPO-OH, DEPMPO-OOH and DEPMPO-H, at pH = 7.4, only an 8-peak spectrum was observed which can be assigned to DEPMPO-OH, and at pH = 3.8, no radicals were detected. The influence of pH on free radical generation

can be explained by the conclusion that in the reaction of GSH with **[2-I]⁺**, **GS⁻** rather than GSH attacked the complexes (**Chapter 4**). The pK_a value of thiol group in GSH is 9.65⁴⁹ and the pH value of the reaction determined the ratio of GSH and **GS⁻**. When the pH = 3.8, there was too low level **GS⁻** (dissociation percentage is less than 10⁻⁶) to attack osmium complex and little free radicals were detected by EPR. However, when pH value was increased to pH = 7.4 (1 % deprotonated **GS⁻**) and pH = 10.8 (94 % deprotonated **GS⁻**), more **GS⁻** is present to be involved in the reaction and free radicals were observed.

Attacking site for GSH on osmium complex

In terms of the reaction site, the DFT calculations (**Chapter 4**) suggested that **GS⁻** attacks the -N=N- azo bond and activate **[2-I]⁺**. In order to confirm the importance of -N=N- azo bond, the detection of free radicals from the reactions of **[2-Cl]⁺**, **[2-OH]⁺**, **[2-imp-Cl]⁺** and **[1-Cl]⁺** with GSH were explored. Similar to **[2-I]⁺**, all the osmium azo complexes **[2-Cl]⁺**, **[2-OH]⁺** and **[1-Cl]⁺** gave rise to free radicals at neutral or alkaline pH values (7.4 or 10.8). However no radicals were trapped from the reaction of osmium imino complex **[2-imp-Cl]⁺** with GSH no matter the pH value, 3.8, 7.4 or 10.8. Such results confirmed that -N=N- bond plays a critical role in the free radical generation and is likely to be the attack site for GSH as the DFT calculations suggested. The key

sulphenylhydrazide intermediate **2-GS/NN** of GSH attacking azo bond in **[2-I]⁺** was detected using X-ray absorption spectroscopy in **Chapter 6**. Similar attacking of GSH on the azo bond in metal coordinated complexes have been observed for Ru (II)⁵⁰ and Ir (III)⁵¹ complexes.

Special behaviour of [2-OH]⁺

It is interesting to compare the different behaviours of **[2-I]⁺**, **[2-Cl]⁺** and **[2-OH]⁺** in the reaction with GSH at pH=7.4. After the first 6 h of EPR scanning, **[2-I]⁺/[2-Cl]⁺** induced only the 8-peak spectrum of DEPMPO-OH, but **[2-OH]⁺** was able to induce mixed radical species of DEPMPO-OH, DEPMPO-OOH and DEPMPO-H. This result indicates that **[2-OH]⁺** was more active than **[2-I]⁺/[2-Cl]⁺** in the reaction with GSH to induce free radicals, especially superoxide. After 6 h scanning time, the superoxide radical was observed in the samples of all osmium complexes **[2-I]⁺**, **[2-Cl]⁺** and **[2-OH]⁺** after reaction with GSH. This was resulted from the hydrolysis of **[2-I]⁺/[2-Cl]⁺** to **[2-OH]⁺**. Thus in the cell living under physiological conditions (pH = 7.4), osmium arene halide complexes **[2-I]⁺** and **[2-Cl]⁺** may not be able to induce significant amounts of superoxide radicals but GSH can activate the hydrolysis of **[2-I]⁺** and **[2-Cl]⁺** to generate more active **[2-OH]⁺** first (**Chapter 4**) and then GSH again reacts with **[2-OH]⁺** to produce superoxide. This

mechanism provides a reasonable explanation of how $[2-I]^+$ (FY26) increases the intracellular superoxide level.²⁸

How are the free radicals produced?

In control experiments, no free radicals were observed when neither GSH nor osmium complexes were absent. The metal trace basis buffer solution had no effect on the free radical generation which confirmed that no residual metal ions in the buffer are involved in the radical production. In the reactions with $[2-I]^+$, 60% GSH was rapidly oxidized to GSSG within 3 h. From GSH to GSSG, 2 electrons can be released with O_2 accepting one of them to give superoxide which can be trapped by DEPMPO. But the formed DEPMPO-OOH adduct is very easily decomposed to the more stable DEPMPO-OH.^{52,53} As a consequence, only DEPMPO-OH spectrum was observed for the reaction of $[2-I]^+$ with GSH at pH = 7.4. At pH = 10.8, the higher concentration of GS^- increases the reaction rate and more O_2 is converted to superoxide. Even with decomposition to DEPMPO-OH, enough DEPMPO-OOH was present to detect by EPR. The superoxide generation was also supported by the effect of superoxide dismutase. To explain DEPMPO-H production, the superoxide O_2^- could also react with GSH and generate hydrogen peroxide H_2O_2 ^{54,55} which is reported to react with organo-osmium azo complexes to produce $\bullet H$ and $\bullet OH$ radicals.⁴⁸ To confirm hydrogen peroxide production, H_2O_2 test

strips and the ammonium molybdate test were used to measure the concentration of H_2O_2 . The result showed about 20 μM hydrogen peroxide was produced by 100 μM **[2-I]**⁺ in the reaction with GSH.

What role does O_2 play in the reactions?

It seems likely that the free radicals observed in the reactions of osmium azo complexes with GSH are generally produced through the process in which they promote the electron transfer from GSH to O_2 and generates GSSG and O_2^- . Then the generated O_2^- can give rise to other free radicals, $\bullet\text{H}$ and $\bullet\text{OH}$. GSH is also involved in attack as GS^- on the $-\text{N}=\text{N}-$ azo bond to donate its electrons to the system but the mechanism by which dioxygen accept an electron is still unknown. Literature investigations suggest two possible pathways, one in which dioxygen can directly accept an electron from negatively-charged azo anions which is the intermediate from GS^- reduction of the azo bond.^{56,57} However, the free azo ligand **AZPY-NMe₂** and thiolate adduct **2-SG** cannot induce free radicals. This result does not support that dioxygen accept electron from negatively-charged azo anions. Thus osmium metal centre is critical to free radicals production and dioxygen involvement. The other pathway is that dioxygen could bind to the osmium centre to form an osmium- η^1 -superoxo complex (**[2-O₂]**⁺) as a reaction intermediate. Similar intermediate complexes have been observed in the activation of dioxygen

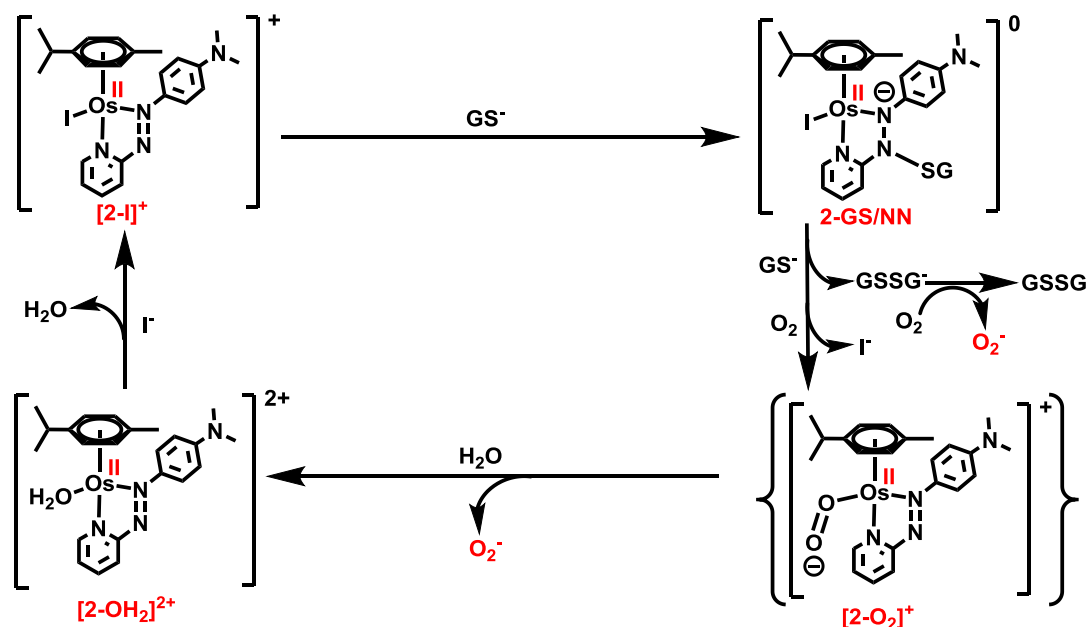
by Fe(II), Cu(II), Cr (III), Mn(III) and Ni(III) complexes.⁵⁸⁻⁶¹ DFT calculations indicated the plausibility of $[2-O_2]^+$ for superoxide production.

Proposed Mechanism for Radical Generation

Overall, from all the experimental studies, DFT calculations and literature reports, a mechanism for the reaction of organo-osmium azo complex $[2-I]^+$ and $[2-Cl]^+$ with GSH can be proposed (**Scheme 5.2**). Firstly, GSH is deprotonated to GS^- in aqueous solution at an alkaline pH value and then GS^- attacks the $-N=N-$ bond in osmium azo complexes to form a sulfonylhydrazide intermediate (**2-GS/NN**) that has been probed by DFT calculations in **Chapter 4** and detected by X-ray absorption spectroscopy in **Chapter 6**.

In this sulfonylhydrazide intermediate **2-GS/NN**, the bond between the osmium centre and monodentate halide becomes labile because attacking of GS^- changes the electron density in this region. In the whole reaction system, O_2 is the most electrophilic group compared with OH^- , GS^- and H_2O to react with **2-GS/NN** so that O_2 attacks the liable bond between osmium centre and monodentate halide ligand to form an osmium- η^1 -superoxo intermediate complex ($[2-O_2]^+$) with release of the halide ligand (I^- or Cl^-). Then $[2-O_2]^+$ is also very liable and another GS^- can attack the $-N-SG$ bond in $[2-O_2]^+$ to generate $GSSG^-$ which is reported to

transfer electron to O_2 producing superoxide $O_2^{\cdot-}$ and GSSG.^{54,55} H_2O can attack the osmium-dioxygen bond to release another superoxide $O_2^{\cdot-}$ forming aqua adduct $[2-OH_2]^{2+}$ which then was deprotonated to $[2-OH]^+$ with pK_a 5.20 (**Chapter 3**). $[2-OH]^+$ can react with halide anions Cl^- and I^- to reform $[2-Cl]^+$ and $[2-I]^+$ and the azo bond in $[2-OH]^+$ can also be attacked by GS^- to produce superoxide with a similar mechanism to that of $[2-Cl/2-I]^+$. The superoxide can be trapped by DEPMPO to form DEPMPO-OOH which is very easily to be decomposed to DEPMPO-OH. If more superoxide is generated, the DEPMPO-OOH can be detected and superoxide can also react with GSH to produce H_2O_2 . The osmium azo complexes can be attacked by H_2O_2 to induce $\bullet OH$ and $\bullet H$,⁴⁸ both of which can be trapped by DEPMPO.



Scheme 5.2. Proposed mechanism for free radicals generation induced by osmium azo complexes in reactions with GSH in the presence of O_2 .

5.5. Conclusions

In this **Chapter 5**, the results show that recycling of osmium azo complexes $[2-I]^+$, $[2-Cl]^+$ and $[2-OH]^+$ promotes electron transfer from GS^- to O_2 and produces GSSG and superoxide that can give rise to other free radicals, $\bullet H$ and $\bullet OH$. For the whole reaction, the osmium azo complex catalyses the oxidation of GSH to GSSG and activation of O_2 to superoxide which provides a plausible explanation of how the osmium azo complex increases the superoxide level and may alter the redox balance within cells, contributing to their toxicity to cancer cells. GSH is usually considered to be an antioxidant which consumes free radicals but herein it works with osmium azo complexes to induce free radicals production. Based on all the experimental results, DFT calculations and literature reports, a novel mechanism of action of osmium azo anticancer drugs catalysing the GSH oxidation and dioxygen activation is proposed, in which dioxygen chelated to the osmium arene complex is an intermediate. This mechanism provides a new view on research on dioxygen activation, glutathione oxidation and metallodrug development.

5.6 References

- (1) Overington, J. P.; Al-Lazikani, B.; Hopkins, A. L. *Nat. Rev. Drug Discov.* **2006**, 5, 993.
- (2) Mjos, K. D.; Orvig, C. *Chem. Rev.* **2014**, 114, 4540.
- (3) Yıldırım, M. A.; Goh, K.-I.; Cusick, M. E.; Barabási, A.-L.; Vidal, M. *Nat. Biotechnol.* **2007**, 25, 1119.
- (4) Hurley, L. H.; Boyd, F. L. *Trends Pharmacol. Sci.* **1988**, 9, 402.
- (5) Hurley, L. H. *Nat. Rev. Cancer.* **2002**, 2, 188.
- (6) Hurley, L. H. *J. Med. Chem.* **1989**, 32, 2027.
- (7) Ge, R.; Sun, H. *Acc. Chem. Res.* **2007**, 40, 267.
- (8) Dasari, S.; Tchounwou, P. B. *Eur. J. Pharmacol.* **2014**, 740, 364.
- (9) Arnesano, F.; Natile, G. *Coord. Chem. Rev.* **2009**, 253, 2070.
- (10) Brabec, V.; Hrabina, O.; Kasparkova, J. *Coord. Chem. Rev.* **2017**, 351, 2.
- (11) Jamieson, E. R.; Lippard, S. J. *Chem. Rev.* **1999**, 99, 2467.
- (12) Oun, R.; Moussa, Y. E.; Wheate, N. J. *Dalton Trans.* **2018**, 47, 6645.
- (13) Yao, X.; Panichpisal, K.; Kurtzman, N.; Nugent, K. *Am. J. Med. Sci.* **2007**, 334, 115.
- (14) Circu, M. L.; Aw, T. Y. *Free Radic. Biol. Med.* **2010**, 48, 749.

- (15) Thannickal, V. J.; Fanburg, B. L. *Am. J. Physiol. Lung Cell Mol. Physiol.* **2000**, 279, L1005.
- (16) Khandrika, L.; Kumar, B.; Koul, S.; Maroni, P.; Koul, H. K. *Cancer Lett.* **2009**, 282, 125.
- (17) Hanahan, D.; Weinberg, R. A. *Cell* **2011**, 144, 646.
- (18) Gorrini, C.; Harris, I. S.; Mak, T. W. *Nat. Rev. Drug Discov.* **2013**, 12, 931.
- (19) Ozben, T. *J. Pharm. Sci.* **2007**, 96, 2181.
- (20) López-Lázaro, M. *Cancer Lett.* **2007**, 252, 1.
- (21) Das, K. C.; White, C. W. *Proc. Natl. Acad. Sci. U.S.A.* **2002**, 99, 9617.
- (22) Filomeni, G.; Rotilio, G.; Ciriolo, M. R. *Biochem. Pharmacol.* **2002**, 64, 1057.
- (23) Pompella, A.; Visvikis, A.; Paolicchi, A.; De Tata, V.; Casini, A. *F. Biochem. Pharmacol.* **2003**, 66, 1499.
- (24) Meister, A. *J. Biol. Chem.* **1988**, 263, 17205.
- (25) Petzold, H.; Sadler, P. J. *Chem. Commun.* **2008**, 4413.
- (26) Meister, A.; Anderson, M. E. *Annu. Rev. Biochem.* **1983**, 52, 711.
- (27) Fu, Y.; Habtemariam, A.; Pizarro, A. M.; van Rijt, S. H.; Healey, D. J.; Cooper, P. A.; Shnyder, S. D.; Clarkson, G. J.; Sadler, P. J. *J. Med. Chem.* **2010**, 53, 8192.

- (28) Hearn, J. M.; Romero-Canelón, I.; Munro, A. F.; Fu, Y.; Pizarro, A. M.; Garnett, M. J.; McDermott, U.; Carragher, N. O.; Sadler, P. J. *Proc. Natl. Acad. Sci. U.S.A.* **2015**, *112*, E3800.
- (29) Romero-Canelón, I.; Mos, M.; Sadler, P. J. *J. Med. Chem.* **2015**, *58*, 7874.
- (30) Zavoisky, E. *J. Phys. USSR* **1945**, *9*, 211.
- (31) Al'Tshuler, S. A.; Kozyrev, B. M. In *Electron Paramagnetic Resonance*; Poole, C. P., Ed.; Academic Press: New York, 2013; Vol. 1, p 3.
- (32) Frejaville, C.; Karoui, H.; Tuccio, B.; le Moigne, F.; Culcasi, M.; Pietri, S.; Lauricella, R.; Tordo, P. *J. Chem. Soc., Chem. Commun.* **1994**, *15*, 1793.
- (33) Liu, K. J.; Miyake, M.; Panz, T.; Swartz, H. *Free Radic. Biol. Med.* **1999**, *26*, 714.
- (34) Stolze, K.; Udilova, N.; Nohl, H. *Free Radic. Biol. Med.* **2000**, *29*, 1005.
- (35) Mojović, M.; Spasojević, I.; Bačić, G. *J. Chem. Inf. Model* **2005**, *45*, 1716.
- (36) Karoui, H.; Hogg, N.; Fréjaville, C.; Tordo, P.; Kalyanaraman, B. *J. J. o. B. C. J. Biol. Chem.* **1996**, *271*, 6000.
- (37) Stoll, S.; Schweiger, A. *J. Magn. Reson.* **2006**, *178*, 42.
- (38) McCord, J. M.; Fridovich, I. *J. Biol. Chem.* **1969**, *244*, 6049.

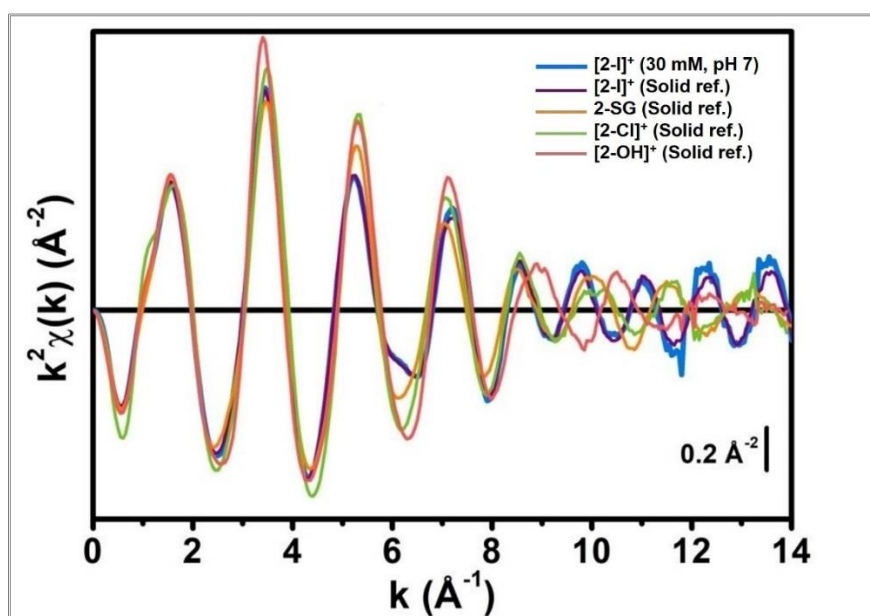
- (39) Milton, N. G. N. *Open Enzym. Inhib. J.* **2008**, *1*, 34.
- (40) Goth, L. *Clin. Chim. Acta* **1991**, *196*, 143.
- (41) Becke, A. D. *J. Chem. Phys.* **1993**, *98*, 5648.
- (42) Lee, C.; Yang, W.; Parr, R. G. *Phys. Rev. B* **1988**, *37*, 785.
- (43) Dunning, T. H.; Hay, P. J. In *Modern theoretical chemistry*; Plenum Press: New York, NY, 1977; Vol. 3, p 1.
- (44) Ngamchuea, K.; Batchelor-McAuley, C.; Compton, R. G. *Chem. Eur. J.* **2016**, *22*, 15937.
- (45) Vásquez-Vivar, J.; Martasek, P.; Hogg, N.; Masters, B. S. S.; Pritchard, K. A.; Kalyanaraman, B. *Biochemistry* **1997**, *36*, 11293.
- (46) Ishikawa, T.; Wright, C. D.; Ishizuka, H. *J. Biol. Chem.* **1994**, *269*, 29085.
- (47) Ishikawa, T.; Bao, J.-J.; Yamane, Y.; Akimaru, K.; Frindrich, K.; Wright, C. D.; Kuo, M. T. *J. Biol. Chem.* **1996**, *271*, 14981.
- (48) Ishikawa, T.; Li, Z.-S.; Lu, Y.-P.; Rea, P. A. *Biosci. Rep.* **1997**, *17*, 189.
- (49) del Socorro Murdoch, P.; Kratochwil, N. A.; Parkinson, J. A.; Patriarca, M.; Sadler, P. J. *Angew. Chem. Int. Ed.* **1999**, *38*, 2949.
- (50) Wang, F.; Xu, J.; Habtemariam, A.; Bella, J.; Sadler, P. J. *J. Am. Chem. Soc.* **2005**, *127*, 17734.

- (51) Needham, R. J.; Sanchez-Cano, C.; Zhang, X.; Romero-Canelón, I.; Habtemariam, A.; Cooper, M. S.; Meszaros, L.; Clarkson, G. J.; Blower, P. J.; Sadler, P. J. *Angew. Chem. Int. Ed.* **2017**, *56*, 1017.
- (52) Corazza, A.; Harvey, I.; Sadler, P. J. *Eur. J. Biochem.* **1996**, *236*, 697.
- (53) Dougan, S. J.; Habtemariam, A.; McHale, S. E.; Parsons, S.; Sadler, P. J. *Proc. Natl. Acad. Sci. U.S.A.* **2008**, *105*, 11628.
- (54) Li, G.; Chen, Y.; Wu, J.; Ji, L.; Chao, H. *Chem. Commun.* **2013**, *49*, 2040.
- (55) Bačić, G.; Spasojević, I.; Šećerov, B.; Mojović, M. *Spectrochim. Acta. A Mol. Biomol. Spectrosc.* **2008**, *69*, 1354.
- (56) Zhu, H. *React. Oxyg. Species.* **2016**, *1*, 65.
- (57) Winterbourn, C. C.; Metodiewa, D. *Arch. Biochem. Biophys.* **1994**, *314*, 284.
- (58) Winterbourn, C. C. *Free Radic. Biol. Med.* **1993**, *14*, 85.
- (59) Mason, R. P.; Peterson, F. J.; Holtzman, J. L. *Mol. Pharmacol.* **1978**, *14*, 665.
- (60) Mason, R. P.; Peterson, F. J.; Holtzman, J. L. *Biochem. Biophys. Res. Commun.* **1977**, *75*, 532.
- (61) Harata, M.; Jitsukawa, K.; Masuda, H.; Einaga, H. *J. Am. Chem. Soc.* **1994**, *116*, 10817.
- (62) Cho, J.; Woo, J.; Nam, W. *J. Am. Chem. Soc.* **2010**, *132*, 5958.

- (63) Kieber-Emmons, M. T.; Annaraj, J.; Seo, M. S.; Van Heuvelen, K. M.; Tosha, T.; Kitagawa, T.; Brunold, T. C.; Nam, W.; Riordan, C. *G. J. Am. Chem. Soc.* **2006**, *128*, 14230.
- (64) Liu, L.-L.; Li, H.-X.; Wan, L.-M.; Ren, Z.-G.; Wang, H.-F.; Lang, J.-P. *Chem. Commun.* **2011**, *47*, 11146.

Chapter 6

X-ray Absorption Spectroscopy (XAS) Studies



6.1. Introduction

The half-sandwich organo-osmium complex $[\text{Os}(\eta^6\text{-p-cym})(4\text{-(2-pyridylazo)-}N,N\text{-dimethylaniline})\text{I}]^+$ (**[2-I]**⁺ (**FY26**)) is being developed as a promising anticancer drug candidate with $49 \times$ times higher potency than cisplatin.^{1,2} Interestingly, **[2-I]**⁺ is inert under physiological conditions, but can be activated to release its iodido ligand once taken up by cancer cells.³ The abundant intracellular tripeptide glutathione (GSH, $\gamma\text{-L-Glu-L-Cys-Gly}$) appears to play a key role in the activation process of **[2-I]**⁺.³ Thus the aim of this thesis is to explore the mechanism of action of **[2-I]**⁺, especially to study the reaction **[2-I]**⁺ with GSH. From the work in **Chapter 4**, GSH can catalyse the hydrolysis of **[2-I]**⁺ to produce hydroxido analogue **[2-OH]**⁺ through a pathway of reducing the -N=N- azo bond in the complex (**Figure 6.1**). Similar behaviours of thiols reducing the azo bond has been observed to both organic diazenes^{4,5} and diazenes coordinated to Ru(II) or Ir(III).⁶⁻⁸ However, the sulfenylhydrazide intermediate **2-GS/NN** in the reaction of GSH with **[2-I]**⁺ has not been characterised even after much attempts using HPLC, NMR, UV-vis and Raman technology. The work in this **Chapter 6** seeks to provide some experimental evidence for the **2-GS/NN** intermediate from the X-ray absorption spectroscopy (XAS) studies of **[2-I]**⁺ in reactions with GSH.

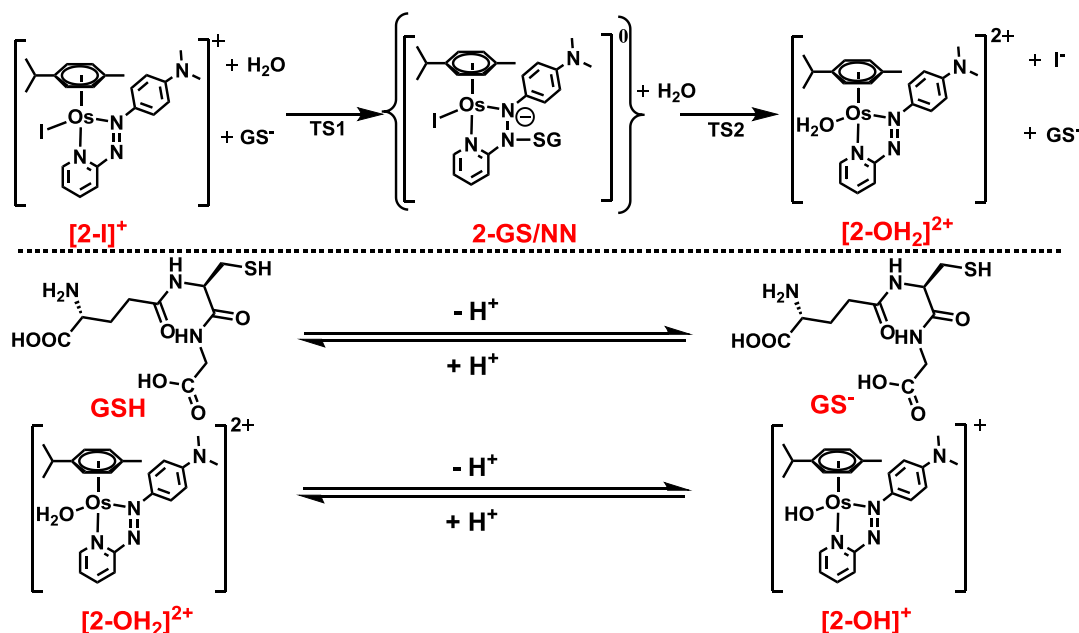


Figure 6.1. The proposed pathway for GSH attack on the azo bond to promote the hydrolysis of $[2-I]^+$ described in **Chapter 4**.

X-ray absorption spectroscopy (XAS) has been developed since the 1970s^{9,10} and is now widely used for determining the local geometric and electronic structures of matter, including organometallic complexes. The samples for XAS can be gases, solutions or solids, and the experiment is usually performed with synchrotron radiation facilities which provide intense and tunable X-ray beams. The XAS experiments in this **Chapter 6** were carried on BM23 beamline at the European Synchrotron Radiation Facility (ESRF) located in Grenoble, France.¹¹ XAS data are obtained by tuning the photon energy (0.1-100 keV) to excite the core electrons using a crystalline monochromator. Corresponding to the quantum numbers ($n = 1, 2, 3$) of the excited electrons, the excitation edge is termed as a K-,

L- or M-edge. For example, excitation of a 1s electron occurs at the K-edge, while excitation of a 2s or 2p electron occurs at an L-edge.¹²

The spectrum generated from XAS data generally has two regions that are the X-ray absorption near-edge structure (XANES) and extended X-ray absorption fine structure (EXAFS) (**Figure 6.2**). XANES is related to the measurement of transitions from core electronic states to the lowest unoccupied molecular orbital (LUMO), which can provide detailed information regarding the oxidation state and coordination environment of metal atoms.^{13,14} Moreover, at energies somewhat greater than the LUMO level, the absorption of an X-ray provides sufficient energy to cause the absorbing atom excitation and the excess energy is given as an ejected photo-electron from the absorbing atom. With other atoms nearby, the ejected photo-electron can scatter from one or multi neighbouring atoms and then return back to the absorbing atom. The interference effect of the outgoing photo-electron wave and back-scattered photo-electron wave results in the X-ray absorption fine structure (XAFS). But the energy range of the photoelectron scattering cross-section between multi neighbouring atoms is weak. Thus the scattering of the ejected photoelectron by neighbouring atoms can be approximated by single scattering events, which dominate the extended X-ray absorption fine structure (EXAFS).^{12,14} EXAFS mainly provides information about the

distance between the absorbing and back-scattering atoms within a distance of about 5 Å, as well as the identity and number of the backscattering atoms.¹⁴

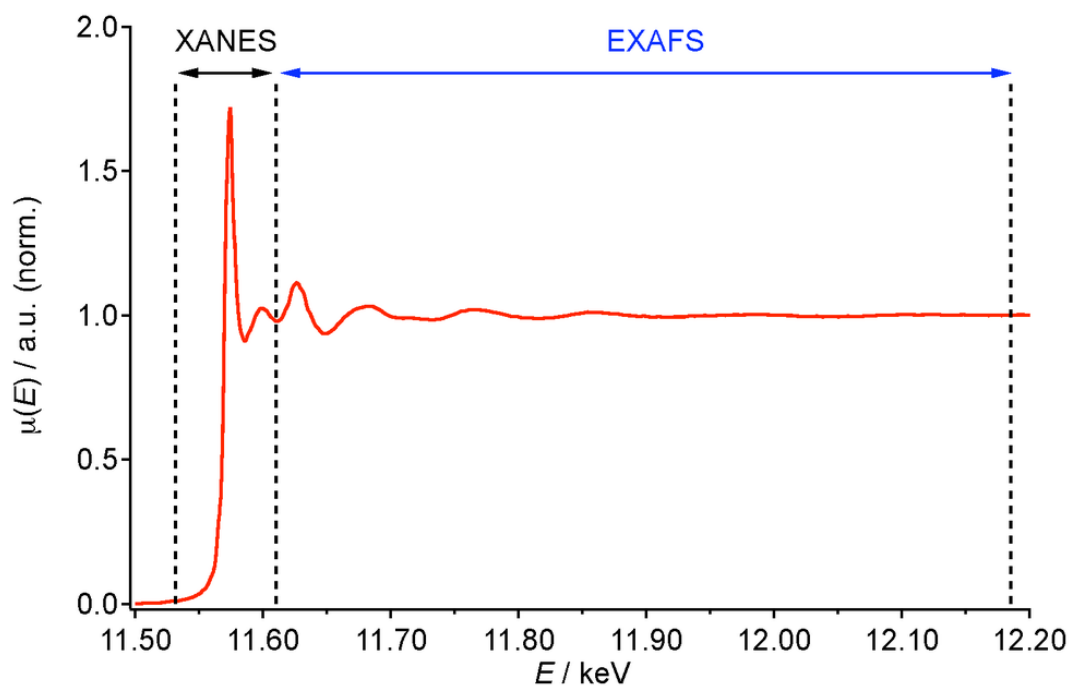


Figure 6.2. Two regions (XANES and EXAFS) in a XAS spectrum.

The advantages and limitations of XAS can be summarized as follows.¹⁴

16

Advantages

- XAS is element specific, so the focus can be on one element without interference from other elements present in the sample.
- There is no limitation of sample states. Gas, solution or solid samples can be studied with XAS because it is sensitive only to the local metal site structure.

- XAS is never “silent” to the metal of interest. The system could be ‘silent’ with respect to EPR, optical, or other spectroscopic methods, but the metal site structure can always be probed by XAS.
- The radiation damage to the samples caused in the XAS experiments can be precisely monitored and controlled, thus allowing data collection from an intact sample.

Limitations

- A frequent problem of XAS is the inability to distinguish between scattering atoms with little difference in atomic number (C, N, O, or S, Cl, or Mn, Fe).
- The presence of more than one metal centre limits the resolution of distance determinations to between 0.1 and 0.2 Å. It is difficult to determine whether a Fourier peak should be fit to one distance with a relatively large disorder parameter or to two distances, each having a small disorder parameter.
- Determination of coordination numbers or number of backscatterers is fraught with difficulties. The Debye-Waller factor (DWF, description of the attenuation of X-ray scattering caused by thermal motion) is strongly correlated with the coordination number and there must be recourse to other

information to narrow the range that is possible from curve-fitting analysis alone.

With these advantages and limitations, XAS has been widely applied to study metal-containing system including metallo-proteins, coordinated complexes, and inorganic catalytic systems and provides an excellent opportunity to identify redox states of metal-centre, determine distances of the metal centre with neighbouring atoms and detect the intermediates of metal-containing system reactions. An example of the development of XAS is the structural research on photosynthetic oxygen-evolving complex (OEC) in photosystem II (PS II) and the XAS studies focused on Mn_4Ca cluster in PS II which provide mechanistic information during the catalytic cycle.¹⁷⁻²⁰ In terms of small molecule coordinated complexes, XAS studies has demonstrated the reduction behaviour of Ru(III) to Ru(II),²¹ Pt(IV) to Pt(II)²² in cancer cells and characterized Pt-thiosulfate complex to confirm the strategy of reducing the toxicity of cisplatin by co-administering sodium thiosulfate. Similar to Pt-S bonds,²³ metal-sulphur bonds in Hg(II)- , Ni(II)- , Cr(III)- , and Mo(V)-cysteine complexes²⁴ and Au-cysteine bonds arising from the reaction of Au(III) complexes with a ‘zinc finger’ have been characterized by XAS.²⁵ Therefore, it appears attractive to use XAS to detect the intermediates in reactions of metal complexes with substrates. The key transient 7-

coordinate $\text{Ru}^{\text{V}}=\text{O}$ intermediate has been characterized with *in situ* EXFAS during the oxygen evolution reaction catalysed by Ru-bda type (bda is 2,2'-bipyridine-6,6'-dicarboxylate) complexes.²⁶ In XAS studies on osmium, many osmium-containing clusters and complexes has been investigated to characterize the redox states of osmium as well as the Os-Os, Os-Cu, Os-C, Os-O, Os-N bonds *etc.*²⁷⁻²⁹

Overall, XAS is a powerful tool to investigate the behaviours of coordinated complexes and complementary to the studies in this thesis which aim to explore the chemical mechanism of action of the anticancer complex $\text{Os}(\eta^6\text{-p-cym})(4\text{-(2-pyridylazo)-}N,N\text{-dimethylaniline})\text{I}]^+$ (**[2-I]**⁺). The redox state of **[2-I]**⁺ in cancer cells which may involve oxidation from Os(II) to Os(III) has been demonstrated by XANES³⁰ and the localization of **[2-I]**⁺ to mitochondria in cancer cells has been studied with a synchrotron X-ray fluorescence nanoprobe (SXRFN).³¹ Using such X-ray studies of **[2-I]**⁺, the work in this **Chapter 6** will focus on using XAS, especially EXAFS, to detect the sulfenylhydrazide intermediate **2-GS/NN** (**Figure 6.3**) which is a key intermediate in the reaction of **[2-I]**⁺ with GSH in the mechanism proposed in **Chapter 4**. For probing the intermediate **2-GS/NN**, references XAS spectra for complexes **[2-I]**⁺, **[2-Cl]**⁺, **[2-OH]**⁺, **2-SG** were first obtained and then DFT calculations used to validate the models of **[2-I]**⁺, **2-SG** against their

experimental EXFAS spectra, based on which the EXAFS signature corresponding to the DFT model of the intermediate **2-GS/NN** will be simulated. Finally, the EXAFS spectra for kinetic reactions of **[2-I]⁺** with GSH at pH 3, 5 and 7 (due to the pH influence to the reaction demonstrated at **Section 4.3.1** of **Chapter 4**) are analysed using a linear combination fit model and the contribution of **2-GS/NN** to the spectra is tracked.

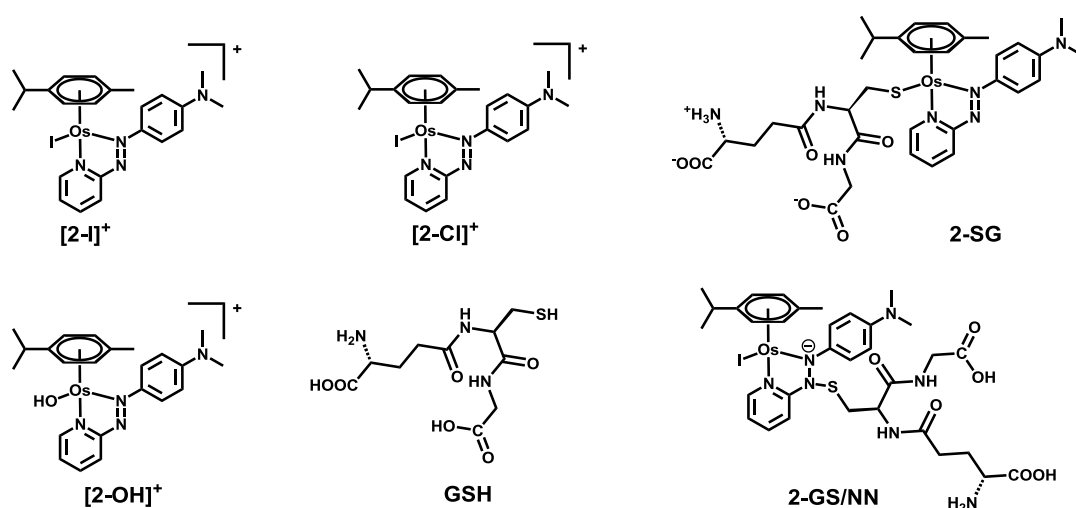


Figure 6.3. The molecular structures of compounds and intermediate (**2-GS/NN**) studied in this Chapter.

6.2. Experimental Section

6.2.1. Materials

Osmium complexes **2-Cl•PF₆**, [**2-OH**]⁺ (in solution), **2-SG** were synthesised and characterized as procedures described in **Section 3.2.3** of **Chapter 3**. A solid containing [**2-OH**]⁺ was prepared by freeze-drying to remove the solvent from the solution. The more soluble complex **2-I•Cl** (compared to the PF₆ salt) was provided by Dr. Russell Needham (University of Warwick, UK). The phosphate buffer (200 mM, pH 7) and citrate-phosphate buffer (200 mM, pH 5 or 3) were prepared as the described in **Section 2.1.2** of **Chapter 2**. Reduced glutathione (**GSH**) was purchased from Sigma Aldrich. Sodium hydroxide, sodium chloride, sodium phosphate dibasic (Na₂HPO₄), sodium phosphate monobasic dehydrate (H₂NaPO₄·2H₂O), and citric acid were purchased from Fisher Scientific. Analysis grade doubly deionised water (18 M Ω cm⁻¹) was obtained from USF Elga UHQ PS purification system. All other solvents and reagents for synthesis and analysis were purchased from commercial suppliers and used as received.

6.2.2. Methods

XAS experimental setup and data collection strategies. X-ray absorption (XAS) experiments at the Os L₃-edge (10871 eV) were performed at the BM23 beamline of the European Synchrotron Radiation Facility (ESRF, Grenoble, France).¹¹ The data was collected with the aid of Dr. Elisa Borfecchia (Università degli Studi di Torino, Italy). XAS experiments were conducted in transmission mode, using a Si(111) double crystal monochromator to select the incident X-ray energy. The intensity of the incident beam I_0 and the beam transmitted through the sample (I_1) and a reference Hf metal foil (I_2) was monitored by 30 cm ionization chambers. Such a setup allowed a precise energy calibration for each collected XAS spectrum. For static and *in situ* experiments in solution, a 4-mm thick EXAFS cell, specifically devoted to liquid samples, was filled with 30 mM solutions of **[2-I]**⁺ in pH 7.0 (200 mM phosphate buffer), pH 5.0 (200 mM citrate-phosphate buffer), or pH 3.0 (200 mM citrate-phosphate buffer) buffers, resulting in edge-jumps $\Delta\mu_x \sim 0.3$ for a total absorption after the edge $\mu_x \sim 2.2$. Initiation of the reaction for *in situ* experiments was obtained by injecting GSH into the cell at Os:GSH molar ratios of 1:2 or 2:1, depending on the specific experiment. The solid-state structure of **[2-I]**⁺, as well as of the **2-SG**, **[2-Cl]**⁺, **[2-OH]**⁺ and OsCl₃ model compounds, was also characterized with

transmission-mode XAS measurements, performed on self-supporting pellets of optimized mass.

For studies on solid-state model compounds, we employed higher-quality scans in the 10639 – 12107 eV range, requiring *ca.* 40 min of data collection per spectrum. The pre-edge region and XANES part of the spectra were acquired with a constant energy step of 5 and 0.5 eV, respectively, while the EXAFS part (up to 18 Å⁻¹) was collected with a $\Delta k = 0.035$ Å⁻¹, resulting in a variable sampling step in energy. The integration time was 1 s/point for the pre-edge region and XANES regions, and quadratically variable from 1 to 8 s/point in the EXAFS part of the spectrum. For *in situ* experiments during [2-I]⁺ hydrolysis reaction, we adopted shorter scans (20 min per spectrum) in the 10724 – 11619 eV range. In this case, the integration time in the EXAFS region quadratically increased from 1 to 4 s/point, up to 14 Å⁻¹, while the energy sampling parameters in the pre-edge and XANES region were the same as for the longer scans. Notably, the first accessible time point after GSH injection corresponded to 40 min, including *ca.* 20 min to safely set the measurement and 20 min to collect of the first scan.

Energy calibration and alignment, normalization to the edge jump, and extraction of the $\chi(k)$ functions for all the collected spectra was performed using the Athena program.³² For static experiments, two or

three consecutive EXAFS spectra were collected for each sample, and the corresponding $\mu x(E)$ curves were averaged, after checking the data reproducibility.

EXAFS fitting model and simulation strategy. The high-quality EXAFS spectra collected for **[2-I]⁺** and **2-SG** in the solid state, as well as for that in solution at pH 7.0, 5.0, and 3.0 buffered solutions of **[2-I]⁺**, were fitted starting from the available DFT models. EXAFS fits were performed by Dr. Elisa Borfecchia (Università degli Studi di Torino, Italy) using the Artemis software.³² The fits were performed in R-space in the $\Delta R = 1.2\text{--}5.0$ Å range, Fourier transforming the $k^2\chi(k)$ curves in the $2.0\text{--}15.5$ Å⁻¹ range, resulting in 42 independent points. Phase and amplitude functions of each path were calculated using as starting guess the geometry of **[2-I]⁺** or **2-SG** from computational analysis. To limit the number of optimized variables, the single scattering (SS) and multiple-scattering (MS) paths included in the fitting model were optimized with the same amplitude factor (S_0^2) and with the same energy shift (ΔE) parameter.

For both the Os-complexes, the fitting model included SS (single scattering) contribution from N₁ and C₁ sub-shells, involving two N atoms from the pyridylazolate unit and 6 C atoms from the *p*-cymene unit, respectively. The SS contributions from the I ligand in **[2-I]⁺** and for the

S ligand in **2-SG** were also included. For each of these coordination shells, the corresponding SS paths have been parametrized employing the same Debye-Waller (DW) factors σ_i^2 and bond distances R_i from the Os absorber, with coordination number fixed to the DFT geometry.

A lower-level parametrization strategy has been employed for the SS involving the distant C atoms of the pyridylazolate unit and the numerous MS paths falling in the 3.0–5.0 Å range from the Os center. These paths were parametrized by considering a common contraction/expansion factor α_{far} and a DW factor σ_{far}^2 increasing as the square root of the path length R_{eff} . This approach, allowing a significant reduction of the number of free fit parameters, has already been successfully used in the EXAFS analysis of metal complexes in solution as well as hosted in microporous matrixes, for which an initial structural model was available either from XRD or from computational modelling.³³⁻³⁵

The values of the optimized parameters obtained in these fits were employed to guide the simulation of the EXAFS signature for the **2-GS/NN** intermediate predicted by DFT. For the simulation, we calculated all the SS and MS paths resulting from the DFT geometry in the relevant R-space range 1.2–5.0 Å. Then, we parametrized the paths as described before for the fits, and fixed the eight relevant parameters (S_0^2 , ΔE , ΔR_{N1} , σ_{N1}^2 , ΔR_{C1} , σ_{C1}^2 , α_{far} , σ_{far}^2) based on the best-fit values obtained for **[2-I]⁺**

and **2-SG**. The simulation was hence obtained by summing all the parametrized paths.

k-space Linear Combination Fit (LCF) analysis of in situ EXAFS.

Linear combination fit (LCF) analysis of the k^2 -weighted time-dependent *in situ* EXAFS spectra was performed in k -space the 3.0–12.0 Å⁻¹ interval, using the Athena software from the Demeter package.³² Each experimental scan, $k^2\chi^{\text{EXP}}(k)$, was fitted as a linear combination of reference EXAFS spectra, $k^2\chi_i^{\text{REF}}(k)$, i.e.: $k^2\chi^{\text{LCF}}(k) = \sum_i w_i k^2\chi_i^{\text{REF}}(k)$, optimizing the weights w_i for each reference spectrum. LCF was performed by setting the total sum of the weights to unity, $\sum_i w_i = 1$ and constraining the weights in the [0 ; 1] interval ($0 \leq w_i \leq 1$). For each analysed scan, the corresponding LCF R-factor was computed as $\sum_j [k^2\chi_j^{\text{EXP}} - k^2\chi_j^{\text{LCF}}]^2 / \sum_j [k^2\chi_j^{\text{EXP}}]^2$, where j denotes each experimental point in fitted k -range, 3.0–12.0 Å⁻¹; R-factor = 0 corresponds to the ideal reproduction of the experimental curve: $k^2\chi^{\text{EXP}}(k) \equiv k^2\chi^{\text{LCF}}(k)$. Reference spectra were selected for each specific *in situ* experiment based on the examination of the EXAFS features of the experimental data series.

6.3. Results

6.3.1. XAS Spectra of Reference Complexes

The XAS spectra from the Os L₃-edge of solid state standards of OsCl₃, [2-I]⁺, [2-Cl]⁺, [2-OH]⁺, 2-SG, and an aqueous phase (30 mM, pH 7) standard of [2-I]⁺ were acquired. The complexes ([2-I]⁺, [2-Cl]⁺, [2-OH]⁺, 2-SG) have been observed in the reaction of [2-I]⁺ with GSH and their XAS (including XANES and EXAFS) spectra provide the references to study the reaction. Initial assessment of the spectra indicated discrimination between [2-I]⁺ and other Os-containing moieties ([2-Cl]⁺, [2-OH]⁺, 2-SG) could not rely on analysis of the XANES area due to the minor differences observed between the spectroscopic signatures of the different adducts. Nevertheless, EXAFS proved to be highly sensitive to the different ligands in the first coordination sphere of Os as shown in **Figure 6.5**. In particular, XAS spectra of [2-I]⁺ both in aqueous phase (pH 7 buffer) and in the solid state were virtually undistinguishable, whilst important differences in the EXAFS oscillations were noted for [2-I]⁺, especially when compared with [2-Cl]⁺, [2-OH]⁺ and 2-SG from $k = 10 \text{ \AA}^{-1}$ upward. On the contrary, [2-Cl]⁺ showed very similar spectra to 2-SG (most likely attributable to similarities in size and weight between Cl and S).

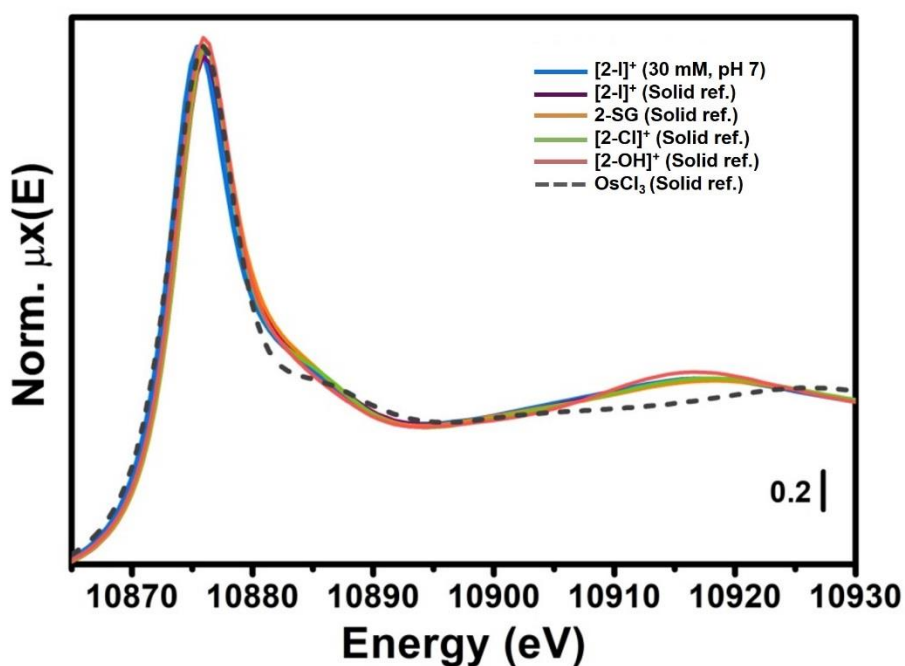


Figure 6.4. Os L₃-edge XANES spectra of reference compounds [2-I]⁺, 2-SG, [2-Cl]⁺, [2-OH]⁺, OsCl₃ in the solid state and [2-I]⁺ in the solution phase (30 mM, pH 7).

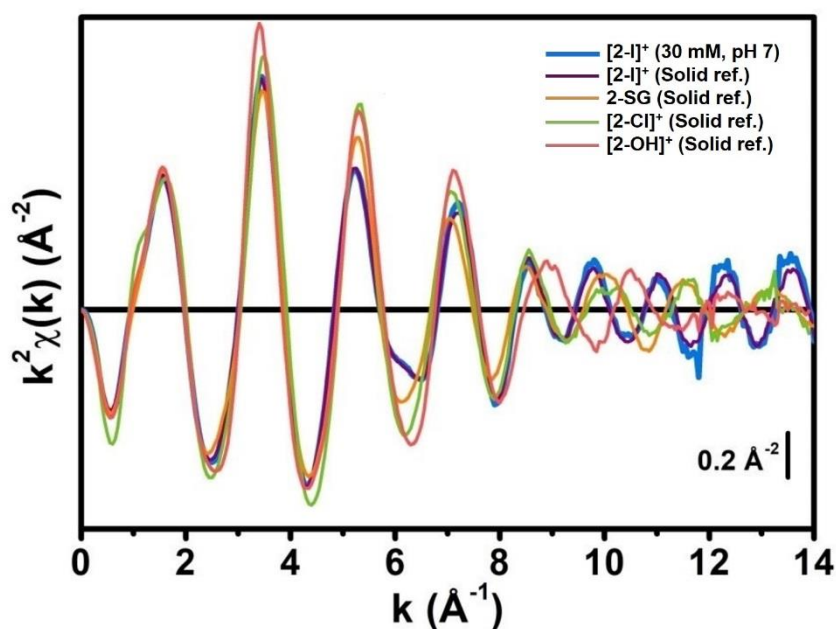


Figure 6.5. Os L₃-edge k²-weighted k²χ(k) EXAFS spectra of reference compounds [2-I]⁺, 2-SG, [2-Cl]⁺, [2-OH]⁺, OsCl₃ in the solid state and [2-I]⁺ in the solution phase (30 mM, pH 7).

6.3.2. FT-EXAFS Spectra of Reference Complexes

Fourier-transformed (FT-) EXAFS was able to provide direct information on the characteristic scattering contributions stemming from the atoms in the proximity of Os centres of the different complexes studied ($[2-I]^+$, $[2-Cl]^+$, $[2-OH]^+$ and **2-SG**). From this, it was possible to determine that the low-R ranges of the spectra of $[2-I]^+$, $[2-Cl]^+$ and **2-SG** (up to ~ 1.8 Å in the phase-uncorrected spectra) were mainly dominated by contributions from low-Z scatterers (N atoms from pyridylazo ligand and C atoms from *p*-cym unit), resulting in a similar EXAFS signal. $[2-OH]^+$ was instead characterised by a pronounced enhancement of the low-R ranges with respect to the other complexes. This was consistent with the presence of an Os–O single scattering (SS) contribution in addition to contributions from pyridylazolate N and *p*-cym C atoms. At higher distances from the Os centre, a prominent peak for $[2-I]^+$, centred at ~ 2.5 Å, arising from the Os–I single SS was observed. Smaller features at ~ 2.0 Å due to the presence of S or Cl atoms in the first coordination sphere of **2-SG**/ $[2-Cl]^+$ complexes were also observed. Finally, the exclusive presence of low-Z scatterers in $[2-OH]^+$ was also marked by a distinct shape of the FT-EXAFS signal in the 2–3 Å range, which was clearly discernible from what is observed for $[2-I]^+$ or **2-SG**/ $[2-Cl]^+$.

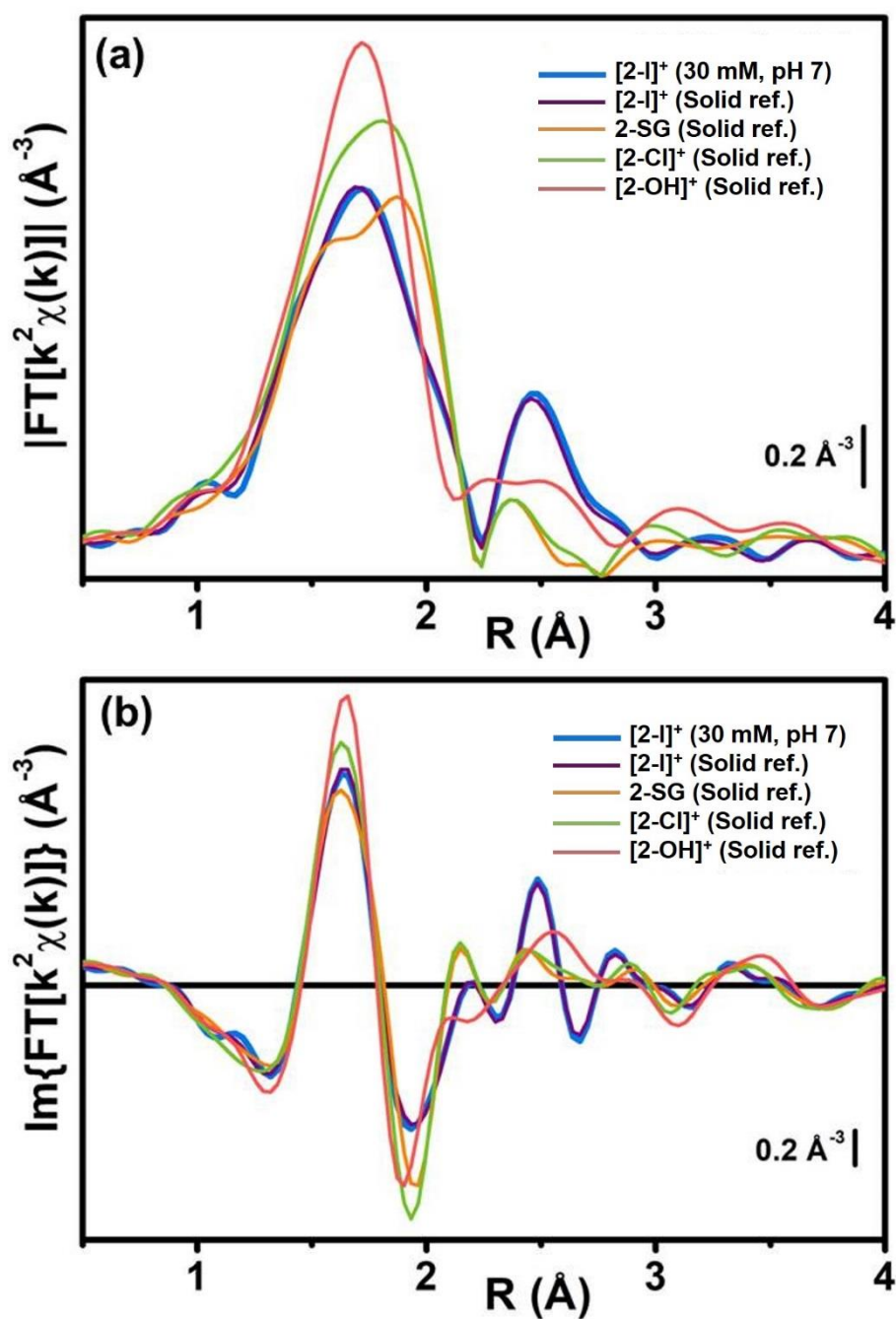


Figure 6.6. Phase-uncorrected (a) magnitude and (b) imaginary part of the Fourier Transformed (FT-) EXAFS functions for reference complexes [2-I]⁺, 2-SG, [2-Cl]⁺, [2-OH]⁺ (The part ranged 2.0-12.5 Å⁻¹ from the EXAFS spectra in **Figure 6.5** was selected for Fourier Transform for better comparison with *in situ* EXAFS spectra).

6.3.3. Validation of DFT Geometries against EXFAS Spectra

Based on the available EXAFS spectra of reference complexes, their structural models were validated from DFT (density functional theory) calculations. Initially, the computational models of **[2-I]⁺** and **2-SG** were used as the starting hypothesis to fit EXAFS spectra collected from solid-state standards, and results were assessed according to the quality and physical reliability of the optimised values of the structural parameters obtained. The best-fit curves shown in **Figure 6.7** showcase the quality of fit, as they adequately reproduced all the experimental features in the R-space range considered in the analysis, resulting in fit R-factors < 2% (**Table 6.1**). Furthermore, the optimised bond distances obtained were in substantial agreement with the x-ray crystal structure of **[2-I]⁺** and the DFT models for both complexes.³ However, EXAFS analysis revealed a slight elongation of the average Os–N₁ bond length (up to 0.03 Å) paralleled by a slight contraction of the average Os–C₁ distance (up to 0.08 Å) with respect to theoretical predictions. Moreover, the Os–I distance in **[2-I]⁺** was optimised at (2.708 ± 0.004) Å (in good agreement with x-ray crystal structure ³), whereas the S ligand in **2-SG** was refined at (2.39 ± 0.01) Å (corroborating the qualitative interpretation of the R-ranges between 2–2.5 Å of the FT-EXAFS proposed in **Figure 6.6**). Again, contractions in the order of 0.06 Å were noted in both cases with

respect to the respective DFT models. Nevertheless, all the other fitting parameters were optimised to physically reliable values, falling in their respective expectation intervals under the relevant experimental conditions. Finally, Debye-Waller (DW) factors for the N₁ and C₁ shells were higher for **2-SG** ($\sigma_{\text{N1}}^2 = 0.0024 \pm 0.0006 \text{ \AA}^2$; $\sigma_{\text{C1}}^2 = 0.004 \pm 0.001 \text{ \AA}^2$) with respect to **[2-I]⁺** ($\sigma_{\text{N1}}^2 = 0.0011 \pm 0.0008 \text{ \AA}^2$; $\sigma_{\text{C1}}^2 = 0.0015 \pm 0.0008 \text{ \AA}^2$), suggesting a higher degree of structural disorder for **2-SG**.

Based on these results, the EXAFS signature corresponding to the DFT model of **2-GS/NN** was able to be simulated. Interestingly, the signal simulated for **2-GS/NN** shows only small shifts to lower distances and a minor intensity enhancement at low-ranges R when compared to the experimental spectra of both **[2-I]⁺** and **2-SG**. Conversely, from 1.8 Å upward, the absence of scattering contribution from close high-Z atomic neighbours (in this case, S falls at ~ 4.5 Å from the Os centre), results into a distinct, unstructured, EXAFS signal. Such differences can also be clearly observed in the contrast in k-space EXAFS oscillations between the experimental spectra of **[2-I]⁺** and **2-SG** and the simulated spectrum of the synthetically inaccessible intermediate **2-GS/NN** (**Figure 6.7**). More importantly, the calculations based on experimentally-validated models allowed attempts to probe the presence of **2-GS/NN** when the reaction between **[2-I]⁺** and GSH was followed *in situ* EXAFS.

Table 6.1. Optimized parameters from EXAFS fitting of **[2-I]⁺** and **2-SG** in the solid state, employing as starting guess the respective DFT geometries. The fit was performed in R-space in the range (1.2-5.0) Å, Fourier-transforming the $k^2\chi(k)$ functions in the (2.0-15.5) Å⁻¹ range. Selected DFT bond distances were also presented in bold, for comparison. The last column reports spectroscopic and structural parameters employed in the DFT-assisted simulation of the EXAFS spectrum for the intermediate **2-GS/NN**. For each *i*th shell of scattering atoms, both the optimised (average) bond distances R_i and the corresponding radial shifts from DFT values [ΔR_i] are presented.

Parameters	[2-I]⁺		2-SG		2-GS/NN	
	DFT	Solid state ref.	DFT	Solid state ref.	DFT	Sim. parameters
S_0^2	–	0.72 ± 0.03	–	0.74 ± 0.4	–	0.75
ΔE (eV)	–	9 ± 1	–	9 ± 1	–	9
<i>R</i> -factor	–	0.00964	–	0.01588	–	–
$n^\circ \text{ par.}/n^\circ \text{ ind.}$	–	10/42	–	10/42	–	–
<i>Corr.</i> > 0.8	–	$\sigma_N^2 \text{ \& } \sigma_C^2 \rightarrow$ 0.8175	–	None	–	–
$\langle R_{\text{Ni}} \rangle$ [ΔR_{Ni}] (Å)	2.056	2.06 ± 0.03 [+ 0.004]	2.061	2.03 ± 0.01 [+ 0.03]	1.983	2.000 [+ 0.017] ^(a)
σ_{Ni}^2 (Å ²)	–	0.0011 ± 0.0008	–	$0.0025 \pm$ 0.0006	–	0.003 ^(d)
$\langle R_{\text{Cl}} \rangle$ [ΔR_{Cl}] (Å)	2.268	2.22 ± 0.01 [– 0.048]	2.297	2.22 ± 0.01 [– 0.077]	2.237	2.175 [– 0.062] ^(b)
σ_{Cl}^2 (Å ²)	–	0.0015 ± 0.0008	–	0.004 ± 0.001	–	0.004 ^(d)
R_{S} [ΔR_{S}] (Å)	–	–	2.443	2.39 ± 0.01 [– 0.059]	–	–
σ_{S}^2 (Å ²)	–	–	–	$0.0022 \pm$ 0.0006	–	–
R_{I} [ΔR_{I}] (Å)	2.765	2.708 ± 0.004 [– 0.057]	–	–	–	–
σ_{I}^2 (Å ²)	–	0.0022 ± 0.0003	–	–	–	–
α_{far}	–	-0.009 ± 0.005	–	$-0.022 \pm$ 0.006	–	-0.015 ^(c)
σ_{far}^2 (Å ²)	–	0.005 ± 0.002	–	0.006 ± 0.003	–	0.006 ^(d)

^(a) Obtained as the average of the ΔR_{Ni} best-fit values for the **[2-I]⁺** and **2-SG** solid-state references.

^(b) Obtained as the average of the ΔR_{Cl} best-fit values for the **[2-I]⁺** and **2-SG** solid-state references.

^(c) Obtained as the average of the α best-fit values for the **[2-I]⁺** and **2-SG** solid-state references.

^(d) Fixed for each sub-shell to the maximum best-fit value obtained in the fits of **[2-I]⁺** and **2-SG** solid-state references.

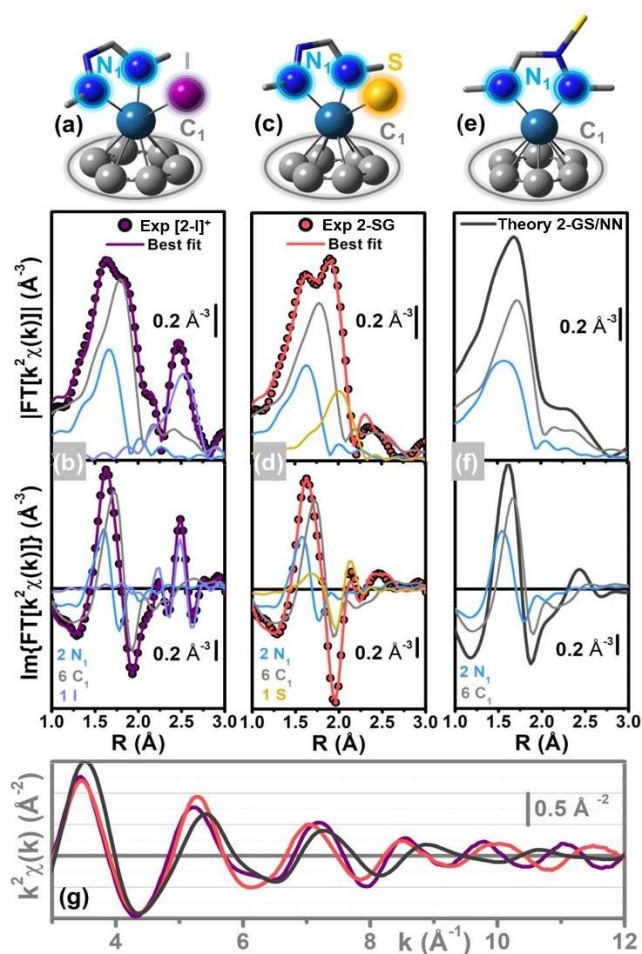


Figure 6.7. Structural refinement from static EXAFS. (a, c) DFT-optimised structural models of the first coordination sphere of Os in (a) **[2-I]⁺**, (b) **2-SG** and (c) **2-GS/NN** intermediate predicted by theory. Atom colour code: Os, indigo; N, blue; C, grey; S, yellow; I, purple. Coloured halos and corresponding labels denote the different sub-shells of scattering atoms employed for EXAFS fitting and simulation. (c, d) Comparison between experimental and best fit FT-EXAFS spectra (magnitude and imaginary part in top and bottom panels, respectively) for the solid-state references (b) **[2-I]⁺** and (d) **2-SG** using the DFT models in parts (a) and (c), respectively, as initial input in the EXAFS fit. (f) Simulated EXAFS spectrum of the **2-GS/NN** intermediate, obtained based on the DFT-optimised geometry in part (e) by exploiting the results of the EXAFS fits shown in parts (b, d) on reference compounds **[2-I]⁺** and **2-SG**. Parts (b, d, f) also report the principal contributions to the EXAFS signal, with the same colour code used to identify the different sub-shells of scattering atoms in parts (a, c, e). (g) Comparison between the experimental $k^2\chi(k)$ functions of the **[2-I]⁺** (purple) and **2-SG** (red) solid-state references and the simulated $k^2\chi(k)$ for the **2-GS/NN** intermediate (dark grey). The spectra were shown in the (3.0-12.0) \AA^{-1} k -space range, which were also employed for the analysis *in situ* of the reaction between **[2-I]⁺** and GSH using EXAFS.

6.3.4. Validation of Models of [2-I]⁺ in Aqueous Environments

Based on the DFT models validated, valuable structural information was obtained from the EXAFS spectra of [2-I]⁺ standards in three different aqueous environments (pH = 3, 5 and 7). This was of great importance as those were the main conditions used during our XAS experiments to study the hydrolysis of [2-I]⁺ in presence of GSH. Data analysis indicated that, when [2-I]⁺ was in solution, the closest Os coordination environment was substantially similar to the solid-state configuration, and adequately predicted by the DFT model (fit R-factor < 3% in all cases). This was particularly true for the spectra at pH 5 and 7, at which all the optimised values obtained for structural parameters were equivalent with those found from the solid-state standards. However, at pH 3, a slight contraction of the Os–N₁ bond length (2.02 ± 0.01 Å vs 2.06 ± 0.03 Å for the solid-state standard) was observed. EXAFS also provided evidence for a higher degree of structural disorder for [2-I]⁺ standards in solution, reflected by a global increase in DWs and fitting uncertainties with respect to the solid-state standards (**Table 6.2**). However, a remarkably good fitting quality is still attained (**Figure 6.8**).

Table 6.2. Best-fit parameters optimized in the EXAFS fit of the k^2 -weighted spectra of 30 mM buffer solutions of $[2-I]^+$ at pH 7, pH 5 and pH 3, employing as starting guess in the fitting procedure the DFT-optimized geometry. The fit was performed in R-space, in the range (1.2-5.0) Å, employing the k-range (2.0-15.5) Å⁻¹ for the FT-EXAFS. Selected bond distances from DFT were also presented for comparison.

EXAFS fit parameters	$[2-I]^+$ DFT	$[2-I]^+$ (30 mM, pH 7)	$[2-I]^+$ (30 mM, pH 5)	$[2-I]^+$ (30 mM, pH 3)
S_0^2	–	0.75 ± 0.07	0.81 ± 0.05	0.79 ± 0.05
ΔE (eV)	–	9 ± 1	9 ± 1	8 ± 1
R-factor	–	0.02960	0.01594	0.02586
N° par./ N° ind.	–	10/42	10/42	10/42
$Corr. > 0.8$		σ_N^2 & $\sigma_C^2 \rightarrow$ 0.8124	–	–
$\langle R_{Ni} \rangle$ (Å)	2.056	2.06 ± 0.03	2.06 ± 0.03	2.02 ± 0.01
σ_{Ni}^2 (Å ²)		0.003 ± 0.001	0.003 ± 0.001	0.002 ± 0.001
$\langle R_{Ci} \rangle$ (Å)	2.268	2.21 ± 0.01	2.21 ± 0.01	2.21 ± 0.01
σ_{Ci}^2 (Å ²)		0.003 ± 0.002	0.003 ± 0.001	0.002 ± 0.001
R_I (Å)	2.765	2.711 ± 0.007	2.704 ± 0.005	2.706 ± 0.008
σ_I^2 (Å ²)		$0.0027 \pm$ 0.0006	0.0026 ± 0.0004	0.0018 ± 0.0004
α		-0.01 ± 0.01	-0.010 ± 0.007	-0.02 ± 0.01
σ^2 (Å ²)		0.005 ± 0.004	0.006 ± 0.003	0.006 ± 0.004

Relevant parameters (S_0^2 , ΔE , R_{Ni} , σ_{Ni}^2 , R_{Ci} , σ_{Ci}^2 , σ_I^2 , R_I , α_{far} , σ_{far}^2) were fixed based on best-fitting results including amplitude factor (S_0^2), energy shift (ΔE), average length of Os-N/C/I bonds (R_{Ni} , R_{Ci} , R_I) and maximum best-fit value with solid references (σ_{Ni}^2 , σ_{Ci}^2 , σ_I^2), common contraction/expansion factor α and a DW factor σ^2 .

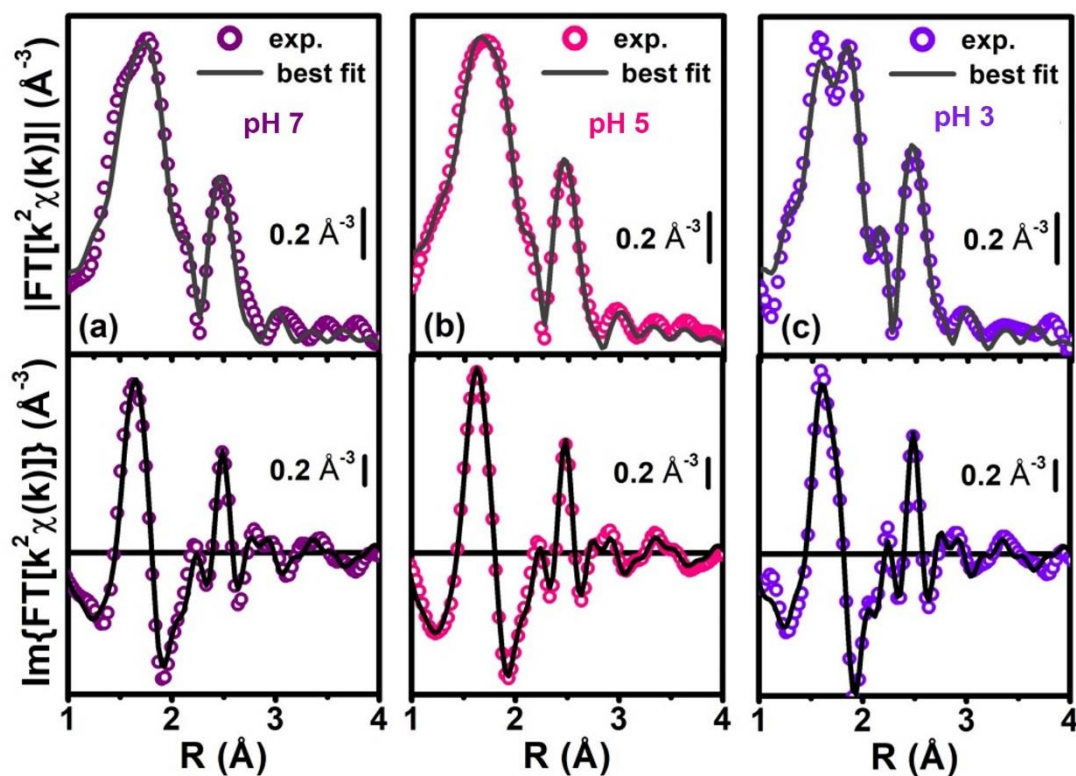


Figure 6.8. Comparison between experimental (colored circles) and best fit (dark grey solid lines) FT-EXAFS spectra for 30 mM buffer solution of $[2-I]^+$ at (a) pH 7, (b) pH 5 and (c) pH 3, using the DFT models as initial input in the EXAFS fit (see **Table 6.2** for quantitative results of the fits). Magnitude and imaginary parts of the FT-EXAFS were presented in top and bottom panels, respectively.

6.3.5. 2-GS/NN Tracking in Reactions of [2-I]⁺ with GSH

Experiments at pH 7. Initially, an *in situ* XAS experiment at pH 7, using a Os : GSH molar ratio of 1:2 was carried out. Under these experimental conditions (30 mM [2-I]⁺, 60 mM GSH, in 200 mM phosphate buffer pH 7, 298 K), the hydrolysis of Os-I bond was much faster than in the HPLC experiments performed previously (**Section 4.3.1 in Chapter 4**), and the reaction was mostly finished after 40 min from GSH being injected. Further minor spectral modifications were observed between 40-80 min, but EXAFS features were mostly stable at longer reaction times (80-220 min). A linear combination fit (LCF) analysis corroborated these observations, and indicated the dominant presence of **2-SG** and [2-Cl]⁺ after 80 min from GSH injection (accounting for over 80-90% of all the Os species found in the reaction mixture), together with contributions of < 10% from [2-I]⁺ and [2-OH]⁺ (**Table 6.3, Figure 6.9**). LCF analysis could provide the percentage of the individual chlorido and thiolate adducts (**Table 6.3**). However, only the combined total percentage of the two species should be considered because [2-Cl]⁺ and **2-SG** standards could not be easily discriminated by EXAFS analysis. Unfortunately, there no signal was tracked that could be assigned to the intermediate **2-GS/NN**, perhaps due to its high reactivity at pH 7 with Os : GSH molar ratio of 1:2.

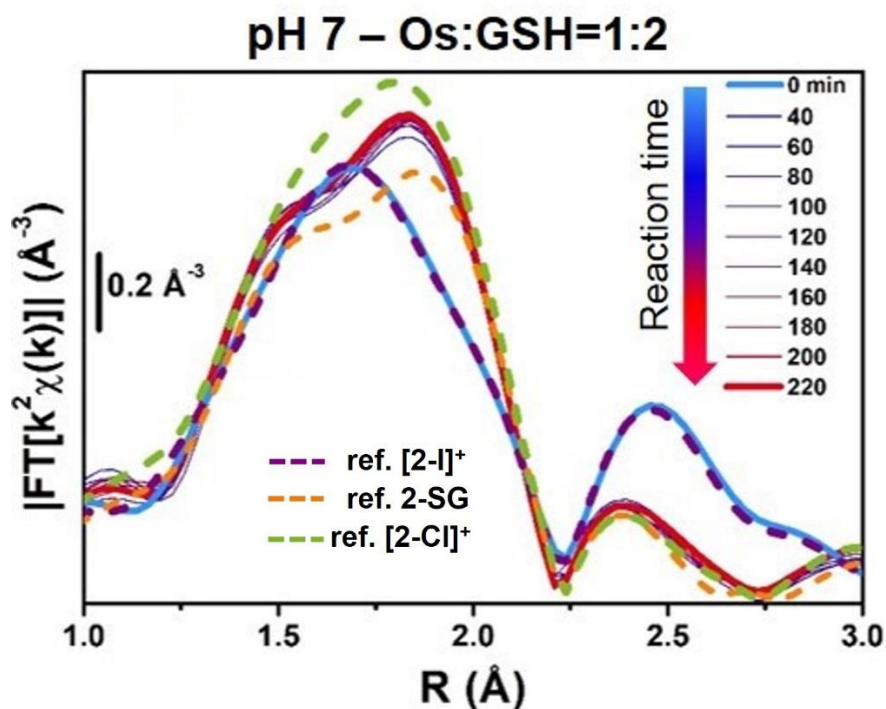


Figure 6.9. Time-resolved *in situ* FT-EXAFS (solid line) for reaction between $[2-I]^+$ (30 mM) and GSH (60 mM) at pH 7, Os : GSH = 1:2, compared with reference complexes (dashed lines).

Table 6.3. Os speciation during *in situ* XAS experiment on the reaction of $[2-I]^+$ (30 mM) with GSH (60 mM) at pH 7 from LCF analysis of the EXAFS scan collected at representative time points. LCF performed on $k^2\chi(k)$ curves, in the range (3.0-12.0) \AA^{-1} . Dominant contributions from **2-SG** and **$[2-Cl]^+$** are highlighted in bold font.

LCF results	Concentration (% total Os)		
	40 min	80 min	220 min
$[2-I]^+$	9 ± 3	8 ± 3	7 ± 3
2-SG	63 ± 5	54 ± 4	50 ± 5
$[2-Cl]^+$	22 ± 5	33 ± 4	42 ± 5
$[2-OH]^+$	6 ± 8	6 ± 7	2 ± 7
R-factor	0.0148	0.0093	0.0114

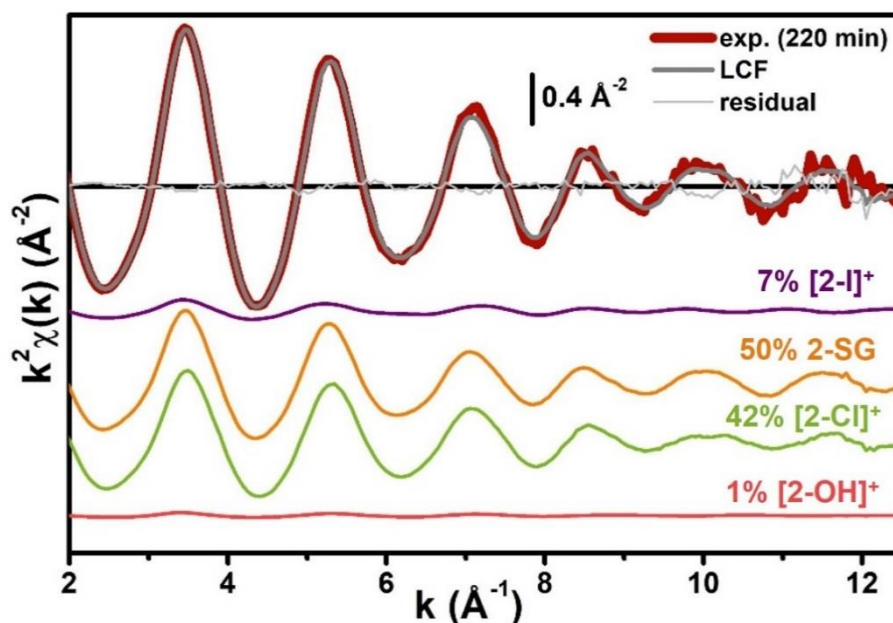


Figure 6.10. Comparison between experimental *in situ* EXAFS spectrum (thick dark red line) collected after 220 min for reaction of $[2-I]^+$ (30 mM) with GSH (60 mM) at pH 7 and the corresponding best fit curve (grey line), from LCF analysis in k-space. The scaled LCF contributions to the EXAFS signal related to $[2-I]^+$, 2-SG, $[2-Cl]^+$ and $[2-OH]^+$ were also presented, vertically translated for the sake of clarity.

Experiments at pH 3. An *in situ* XAS experiment under acidic conditions (30 mM $[2-I]^+$, 60 mM GSH, pH 3) was carried out. In contrast to pH 7, EXAFS spectra at pH 3 were almost identical to $[2-I]^+$ standards, and remained unchanged over the whole duration of the study (220 min from GSH injection). This was in line with the finding from chromatographic experiments (**Section 4.3.1** in **Chapter 4**). Furthermore, it meant that although no direct comparison could be made between the kinetics of the reactions studied by EXAFS and HPLC, they still followed the same trend as a function of pH. Intrinsically, this also suggested that

it may be possible to capture some dynamics related to the hydrolysis of $[2-I]^+$ in presence of GSH by careful tuning of the reaction conditions (i.e. pH, Os:GSH molar ratio).

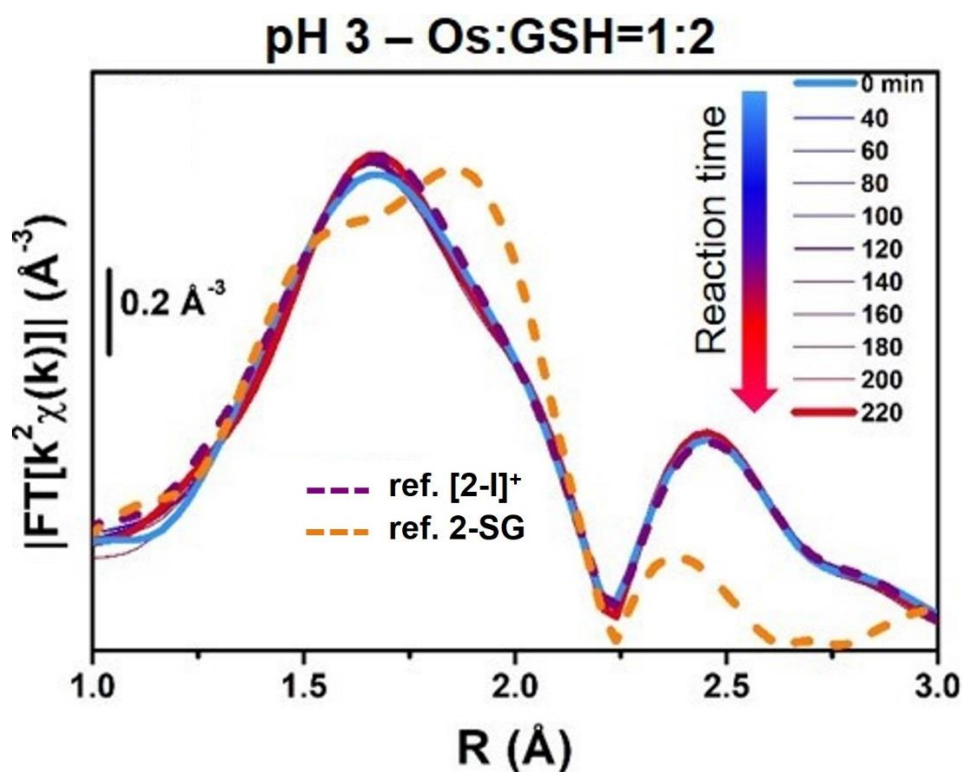


Figure 6.11. Time-resolved *in situ* FT-EXAFS (solid line) for reaction between $[2-I]^+$ (30 mM) and GSH (60 mM) at pH 3, Os : GSH = 1:2, comparing with reference complexes FT-EXAFS (dash line).

Experiments at pH 5. The reaction of $[2-I]^+$ with GSH was further studied at pH = 5, and using a new Os : GSH ratio of 2:1 (30 mM and 15 mM, respectively), in an attempt to moderate the reaction rate. Remarkably, EXAFS spectra collected in the 40-220 min time range from GSH injection under these conditions, showed the presence of an oscillatory behaviour within the reaction. It was observed that periodic

and opposite changes in the intensity of the peak at ca. 2.5 Å (Os-I SS contribution in $[2-I]^+$), and the shoulder at ca. 2.0 Å (Os-S SS contribution in **2-SG**) in the phase-uncorrected spectra. However, certain time points showed dampened contributions from Os-I SS (single scattering) without an increase in the characteristic Os-S SS (i.e. 200 min after GSH injection), suggesting the presence within the reaction mixture of additional unknown Os species. Furthermore, the cyclic behaviour may arise from alternated periods dominated by cleavage or formation of Os–I bonds. To check this, its Os-speciation was determined as a function of the reaction time by applying EXAFS LCF analysis in k-space.

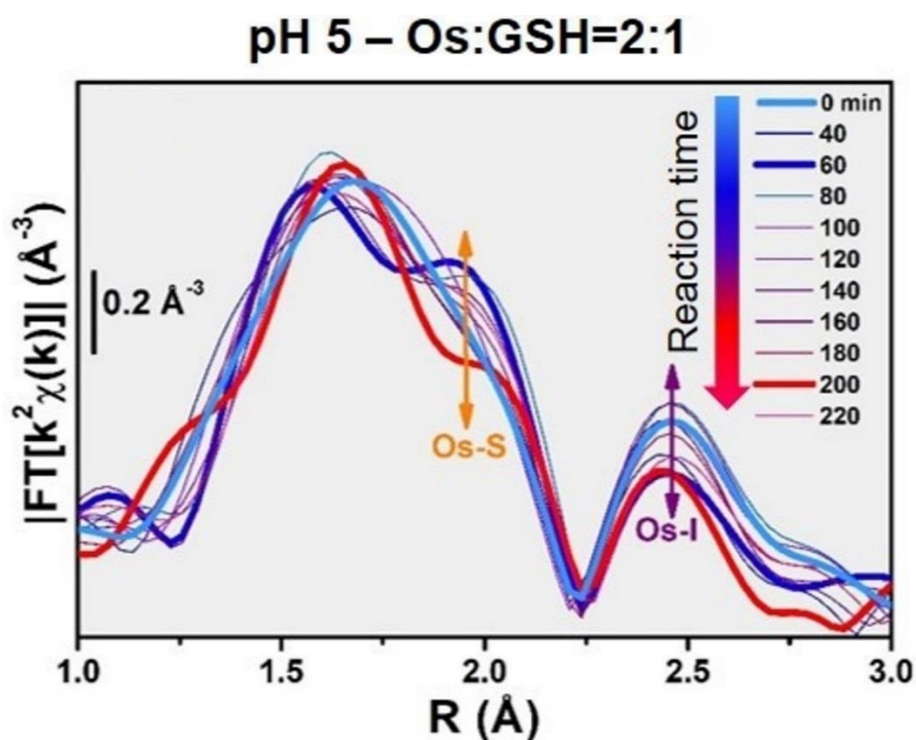


Figure 6.12. Time-resolved *in situ* FT-EXAFS for reaction between $[2-I]^+$ (30 mM) and GSH (15 mM) at pH 5, Os:GSH = 2:1.

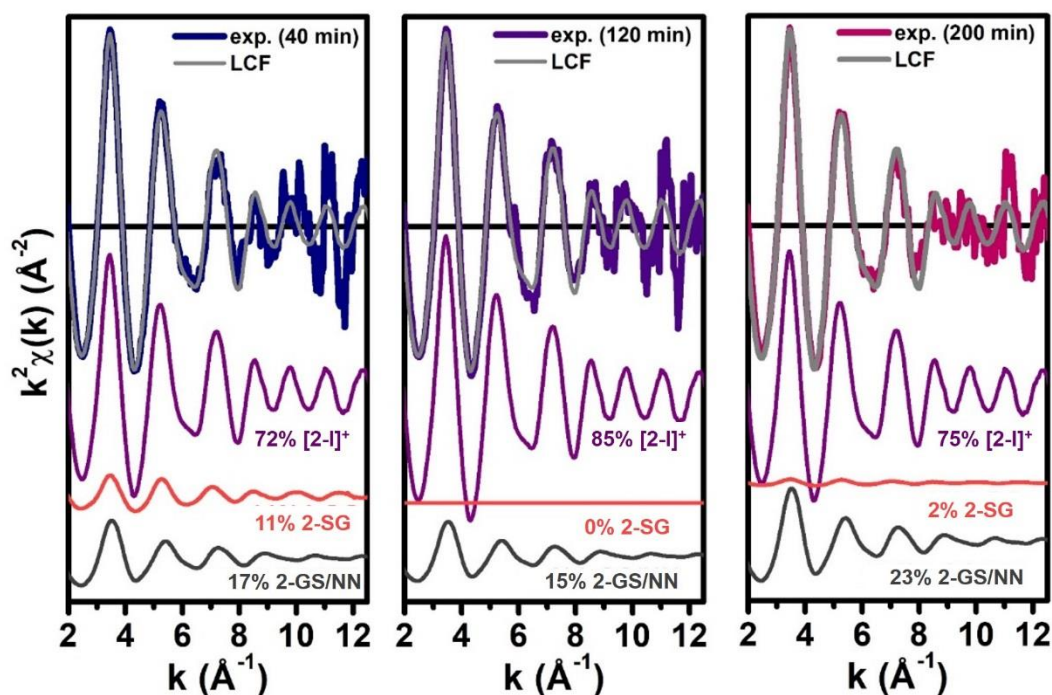


Figure 6.13. Comparison between experimental *in situ* EXAFS spectra (thick coloured lines) collected during reaction between [2-I]⁺ (30 mM) with GSH (15 mM) at pH 5, Os : GSH = 2:1 at selected reaction times and the corresponding best fit curves (grey lines), from LCF analysis in k-space. The three selected reaction time points 40 min (left panel), 120 min (middle panel), and 200 min (right panel), show the higher concentration of the 2-GS/NN intermediate in the reaction mixture. The scaled LCF contributions to the EXAFS signal related to [2-I]⁺, 2-SG and 2-GS/NN are also presented.

Three different components were used to generate the LCF model: the experimental references for [2-I]⁺ and 2-SG and the simulated EXAFS signature for the 2-GS/NN intermediate predicted by theory. The model adopted yielded a good reproduction of the experimental signals (**Figure 6.13**). Inclusion in the LCF model of the 2-GS/NN component resulted in a significant improvement of the fitting quality in the time points with

high concentrations of such species (marked by coloured arrows in **Figure 6.14**) with respect to a two-component model solely including $[2-I]^+$ and **2-SG** (**Figure 6.14**). Crucially, the maxima regarding the relative abundance of **2-GS/NN** (from 16 to 24% total Os) systematically precluded increases in the concentration of **2-SG**. This supported the presence of **2-GS/NN** species as part of the reaction mechanism, and was in line with their intermediate character defined by DFT (**Section 4.3.7** of **Chapter 4**).

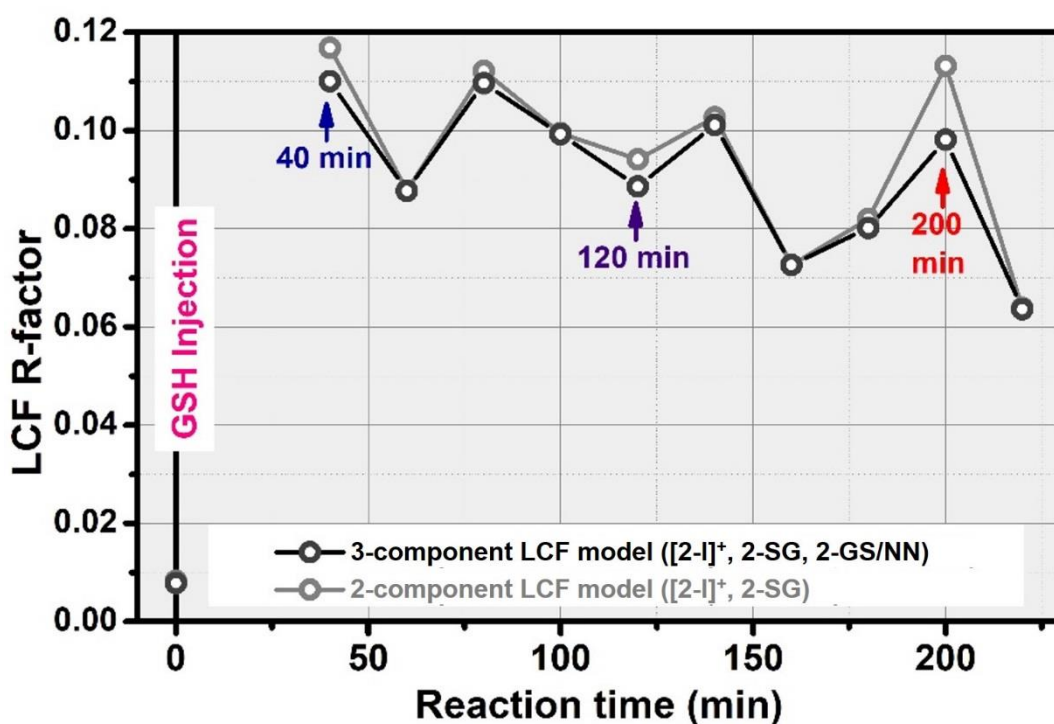


Figure 6.14. Comparison between the LCF R-factors obtained at each time point for the three-component model (reactant $[2-I]^+$; product **2-SG**, intermediate **2-GS/NN**) and for the two-component model (reactant $[2-I]^+$; product **2-SG**) reported in the top panel. The coloured arrows highlight the reaction times corresponding to the concentration of peaks for **2-GS/NN** (in the 16-24% total Os range), corresponding to systematic improvement of the LCF quality (lower R-factor values) for the three-component model.

LCF (linear combination fit) results highlighted the oscillating character of the reaction. $[2-I]^+$ was cyclically converted into **2-SG** (with a period of 60-80 min), which then was transformed again to $[2-I]^+$. This could be related to fluctuations in the concentrations of free I^- ions and free GSH as a result of the hydrolysis of Os-I bonds and the formation of new Os-SG species. Indeed, our chromatographic experiments have shown previously that the presence of high concentrations of chloride ions in the medium can alter the amount of the Os species (increase in $[2-Cl]^+$) found during the hydrolysis of $[2-I]^+$ in presence of GSH (**Section 4.3.1 in Chapter 4**). Moreover, a more complex four-component LCF model (using experimental $[2-I]^+$, **2-SG** and $[2-OH]^+$ and simulated **2-GS/NN** references) suggested negligible quantities of $[2-OH]^+$ in the reaction mixture (**Figure 6.15**). This might indicate the presence of high concentrations of free I^- ions and free GSH in the reaction. By calculating the concentrations of free I^- ions and free GSH (from amounts of $[2-I]^+$ and **2-SG** species indicated by LCF), an alternation between long periods of low I^- /GSH ratios and short periods of I^- /GSH ratios (every 60-80 min) is observed. Remarkably, the highest concentrations of free I^- ions would always be found just before periods dominated by the formation of Os-I bonds (**Figure 6.16**), providing a possible explanation to the regeneration of $[2-I]^+$. Finally, the presence of fluctuations in GSH, together with the fact that over 30 mM of Os-I bonds are hydrolysed (31.2 mM in total,

calculated from the amounts of $[2-I]^+$ and **2-SG** species indicated by LCF) by 15 mM of GSH also supports a possible catalytic nature of the reaction that has been observed in NMR experiments (Section 4.3.1 of Chapter 4).

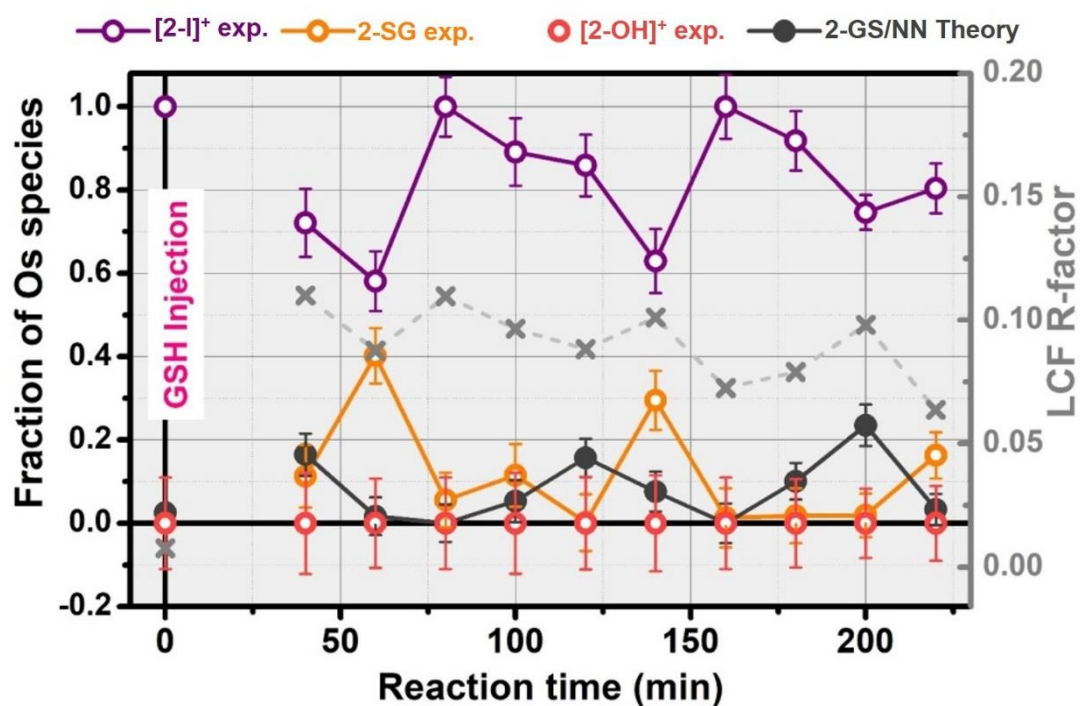


Figure 6.15. Results from test LCF analysis of the time-resolved $k^2\chi(k)$ curves during reaction between $[2-I]^+$ (30 mM) with GSH (15 mM) at pH 5, Os : GSH = 2:1 including in the fitting model also the $[2-OH]^+$ model compound together with $[2-I]^+$, **2-SG**, and the theoretical intermediate **2-GS/NN**. The LCF R-factors (grey x) were also presented (right ordinated axis). The fraction of $[2-OH]^+$ was optimized at (0.0 ± 0.1) over the whole investigated reaction time range, demonstrating that the $[2-OH]^+$ species was not detectable under the XAS experimental conditions.

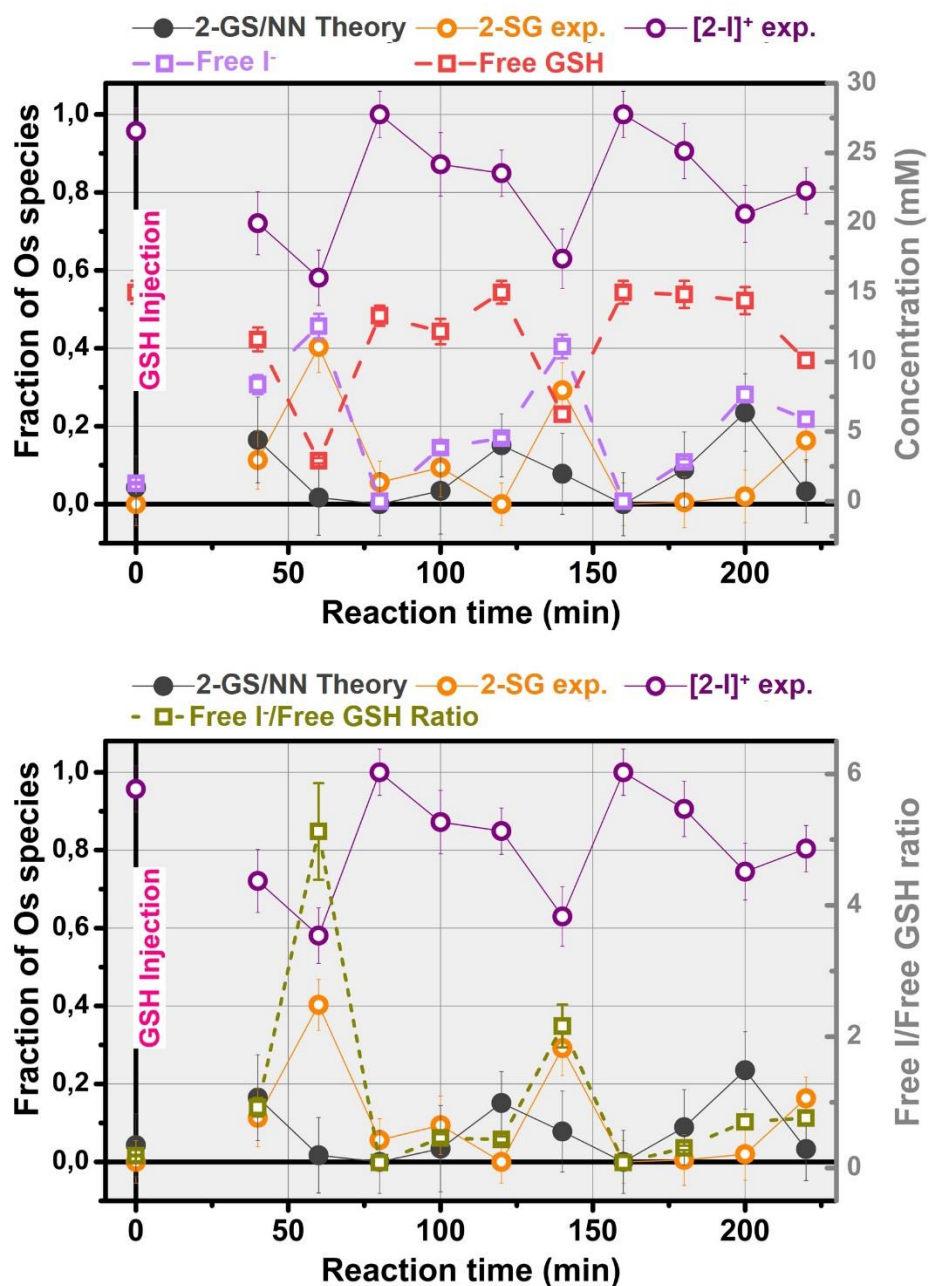


Figure 6.16. Top panel: Comparison between the quantities of free I⁻ ions and free GSH in the reaction environment with results of LCF analysis of the time-resolved $k^2\chi(k)$ spectra collected during reaction between [2-I]⁺ (30 mM) with GSH (15 mM) at pH 5, Os:GSH = 2:1, using a three-component model (reactant [2-I]⁺ and product 2-SG, and theoretical intermediate 2-GS/NN). Bottom panel: Comparison between the ratio of free I⁻ ions/free GSH in the reaction environment with results of LCF analysis of the time-resolved $k^2\chi(k)$ spectra collected during reaction between [2-I]⁺ (30 mM) with GSH (15 mM) at pH 5, Os : GSH = 2:1, using a three-component model (reactant [2-I]⁺ and product 2-SG, and theoretical intermediate 2-GS/NN).

6.4. Discussion

Osmium-based anticancer candidate complex **[2-I]⁺** has been reported to have a high potency.^{1,2} Surprisingly, **[2-I]⁺** is highly inert under physiological conditions, but the intracellular tripeptide GSH can catalyse the hydrolysis of **[2-I]⁺** to form the hydroxido adduct **[2-OH]⁺** through attacking the -N=N- azo bond based on the combined theoretical-experimental studies performed in **Chapter 4**. In the proposed mechanism of action, a sulfenylhydrazide intermediate **2-GS/NN** is perceived to represent a key intermediate in the catalytic hydrolysis of **[2-I]⁺** by GSH. As yet, this intermediate **2-GS/NN** has not been detected. Detection of intermediates in the chemical reactions is always challenging. The attack of thiols on -N=N- has been widely observed for organic diazenes and diazenes coordinated to Ru(II) or Ir(III).⁴⁻⁸ However, the thiolated-hydrazine intermediate has never been detected, only the hydrazine reduction products were detected for some systems.^{4,7}

Contributing to the overall aim of exploring the mechanism of action of **[2-I]⁺** in this thesis, efforts were made in this **Chapter 6** to detect the intermediate **2-GS/NN** in the reaction of **[2-I]⁺** with GSH using XAS technology. Initially, the reference XAS spectra were acquired for the complexes **[2-I]⁺**, **[2-Cl]⁺**, **[2-OH]⁺**, **2-SG**, which might be observed in the reaction of **[2-I]⁺** with GSH. This was performed in order to: 1)

determine if XAS methods could be used to discriminate between the different adducts; 2) validate the structural models of the different species involved in the reaction generated by DFT calculations; and 3) generate a valid simulation of the XAS spectra of the intermediate **2-GS/NN** that could be used to study the reaction between **[2-I]⁺** and GSH. The results showed that EXAFS was sensitive enough to distinguish between these osmium adducts. Important differences were observed for **[2-I]⁺** in EXAFS spectra compared to other species (**[2-Cl]⁺**, **[2-OH]⁺**, **2-SG**) although it was not readily possible to distinguish between **[2-Cl]⁺** and **2-SG** because of the small difference in atomic number between S and Cl.

Based on these reference EXAFS spectra, as well as the reported X-ray crystal structure of **[2-I]⁺**,³ the structural models of for **[2-I]⁺**, **2-SG** and intermediate **2-GS/NN** and their EXAFS spectra were validated. It is exciting to find that from computational **2-GS/NN** exhibits a distinct EXFAS spectrum, the absence of scattering contribution from close high-Z atomic neighbours (in this case, S is ~ 4.5 Å from Os), compared with **[2-I]⁺** and **2-SG**, which make it possible to attempt detect the presence of **2-GS/NN** when the reaction between **[2-I]⁺** and GSH was followed *in situ* EXAFS.

However, the initial attempts to detect the signal for **2-GS/NN** from the reaction of **[2-I]⁺** with GSH are disappointing. In the experiment with a

Os:GSH ratio of 1:2 at pH 7, the reaction was predominantly completed after 40 min, which was faster than HPLC experiments studied in **Chapter 4** as expected due to the different concentrations of recants (30 mM **[2-I]⁺** for XAS experiments and 75 μ M **[2-I]⁺** for HPLC experiment). LCF analysis indicated that the EXAFS spectra for reaction was mainly contributed by **2-SG** and **[2-Cl]⁺** with no contribution assignable to **2-GS/NN**. On the contrary, in the experiment with as Os:GSH mol ratio of 1:2 at pH 3, the EXAFS spectra for the reaction were almost identical to **[2-I]⁺** standards, and remained unchanged over the whole duration of the study. The pH influence on the XAS experiment followed the same trends as the HPLC experiments, which demonstrated that acidic conditions inhibit the reaction of **[2-I]⁺** with GSH. Intrinsically, this also suggested that it might be possible to capture some dynamics related to the hydrolysis of **[2-I]⁺** in presence of GSH by carefully tuning the reaction conditions (i.e. pH, Os:GSH molar ratio) to reach an appropriate reaction rate.

Thus further attempts to probe intermediate **2-GS/NN** were made using the higher Os:GSH mol ratio of 2:1 and pH 5 for the *in situ* XAS experiment. Interestingly, the EXAFS spectra showed an oscillatory behaviour within the reaction and certain time points showed dampened contributions from the Os-I bond but without an increase in characteristic

Os-S features, suggesting the presence of additional unknown Os species. LCF analysis to the spectra was carried out employing three different models: two components (**[2-I]⁺** and **2-SG**), three components (**[2-I]⁺**, **2-SG** and **2-GS/NN**) and four components (**[2-I]⁺**, **2-SG**, **2-GS/NN** and **[2-OH]⁺**). The three-component model (**[2-I]⁺**, **2-SG** and **2-GS/NN**) gave the best fitting quality and maxima in the relative abundance of **2-GS/NN** from 16 to 24% total Os, and systematically precluded increases in the concentration of **2-SG** (**Figure 6.13**). This supported the presence of **2-GS/NN** species in the reaction mechanism, as predicted by the DFT calculations (**Section 4.3.7** of **Chapter 4**). Moreover, the oscillating behaviour of EXAFS spectra for the reaction indicated that ~30 mM Os-I was cyclically hydrolysed by 15 mM GSH, which supported the catalytic nature of the activation of **[2-I]⁺** by GSH, a result confirmed by NMR experiments (**Section 4.3.1** of **Chapter 4**). As the pathway probed by DFT calculations in **Chapter 4** (**Section 4.3.7**), this catalytic nature of GSH promoting Os-I is due to release of GSH from the **2-GS/NN** after the hydrolysis completing.

6.5. Conclusions

Contributing to the overall aim of this thesis of exploring the chemical mechanism of action of $[2-I]^+$, some experimental evidence is provided in this **Chapter 6** to support the presence of the sulfenylhydrazide intermediate **2-GS/NN** proposed from the DFT-predicted pathway for the reaction of $[2-I]^+$ with GSH. Based on the reference EXAFS spectra for the complexes $[2-I]^+$, $[2-Cl]^+$, $[2-OH]^+$, and **2-SG** observed in the reaction of $[2-I]^+$ with GSH, the structure models and characteristic computational EXAFS spectra for the intermediate are validated. *In situ* XAS experiments at different pH values and reactant ratios were carried out and analysed by LCF. The results suggest there is maximum of ~20% abundance of sulfenylhydrazide intermediate **2-GS/NN** in the reaction $[2-I]^+$ with GSH. This experimental evidence confirms a pathway in which GSH promotes the hydrolysis of $[2-I]^+$ through redox mediation by -N=N- azo group in the complexes. Moreover, the behaviour of acid inhibition and the catalytic nature of the reaction of $[2-I]^+$ with GSH observed during *in situ* experiments in this **Chapter 6** are line with the findings in **Chapter 4** and **Chapter 5**, which indeed again provided evidence for the mechanism of action of $[2-I]^+$ presented in this thesis.

6.6. References

- (1) Fu, Y.; Habtemariam, A.; Pizarro, A. M.; van Rijt, S. H.; Healey, D. J.; Cooper, P. A.; Shnyder, S. D.; Clarkson, G. J.; Sadler, P. J. *J. Med. Chem.* **2010**, *53*, 8192.
- (2) Hearn, J. M.; Romero-Canelón, I.; Munro, A. F.; Fu, Y.; Pizarro, A. M.; Garnett, M. J.; McDermott, U.; Carragher, N. O.; Sadler, P. *J. Proc. Natl. Acad. Sci. U.S.A.* **2015**, *112*, E3800.
- (3) Needham, R. J.; Sanchez-Cano, C.; Zhang, X.; Romero-Canelón, I.; Habtemariam, A.; Cooper, M. S.; Meszaros, L.; Clarkson, G. J.; Blower, P. J.; Sadler, P. J. *Angew. Chem. Int. Ed.* **2017**, *56*, 1017.
- (4) Kosower, E. M.; Miyadera, T. *J. Med. Chem.* **1972**, *15*, 307.
- (5) Kosower, E. M.; Kanety-Londner, H. *J. Am. Chem. Soc.* **1976**, *98*, 3001.
- (6) Dougan, S. J.; Habtemariam, A.; McHale, S. E.; Parsons, S.; Sadler, P. J. *Proc. Natl. Acad. Sci. U.S.A.* **2008**, *105*, 11628.
- (7) Li, G.; Chen, Y.; Wu, J.; Ji, L.; Chao, H. *Chem. Commun.* **2013**, *49*, 2040.
- (8) Zhou, Q.-X.; Zheng, Y.; Wang, T.-J.; Chen, Y.-J.; Li, K.; Zhang, Y.-Y.; Li, C.; Hou, Y.-J.; Wang, X.-S. *Chem. Commun.* **2015**, *51*, 10684.

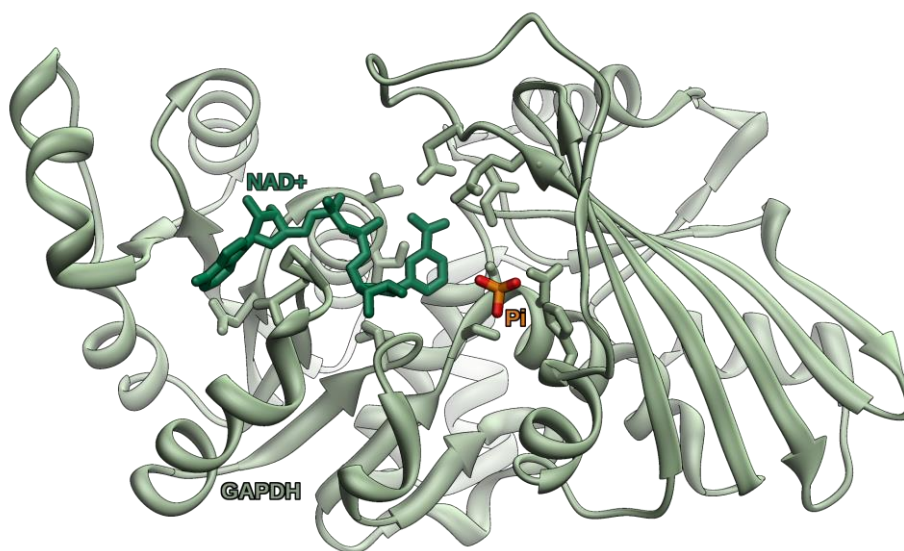
- (9) Sayers, D. E.; Stern, E. A.; Lytle, F. W. *Phys. Rev. Lett.* **1971**, 27, 1204.
- (10) Eisenberger, P.; Kincaid, B. M. *Science* **1978**, 200, 1441.
- (11) Mathon, O.; Beteva, A.; Borrel, J.; Bugnazet, D.; Gatla, S.; Hino, R.; Kantor, I.; Mairs, T.; Munoz, M.; Pasternak, S. *J. Synchrotron Radiat.* **2015**, 22, 1548.
- (12) Koningsberger, D. C. In *X-ray absorption: principles, applications, techniques of EXAFS, SEXAFS, and XANES*; Prins, R., Ed.; John Wiley and Sons: New York, 1988.
- (13) Henderson, G. S.; De Groot, F. M. F.; Moulton, B. J. A. *Rev. Mineral. Geochem.* **2014**, 78, 75.
- (14) Yano, J.; Yachandra, V. K. *Photosynth. Res.* **2009**, 102, 241.
- (15) Eisenberger, P.; Brown, G. S. *Solid State Commun.* **1979**, 29, 481.
- (16) Penner-Hahn, J. E. *Coord. Chem. Rev.* **1999**, 190, 1101.
- (17) Cinco, R. M.; Robblee, J. H.; Rompel, A.; Fernandez, C.; Yachandra, V. K.; Sauer, K.; Klein, M. P. *J. Phys. Chem. B* **1998**, 102, 8248.
- (18) Cinco, R. M.; McFarlane Holman, K. L.; Robblee, J. H.; Yano, J.; Pizarro, S. A.; Bellacchio, E.; Sauer, K.; Yachandra, V. K. *Biochemistry* **2002**, 41, 12928.

- (19) Cinco, R. M.; Rompel, A.; Visser, H.; Aromí, G.; Christou, G.; Sauer, K.; Klein, M. P.; Yachandra, V. K. *Inorg. Chem.* **1999**, 38, 5988.
- (20) Pushkar, Y.; Yano, J.; Glatzel, P.; Messinger, J.; Lewis, A.; Sauer, K.; Bergmann, U.; Yachandra, V. *J. Biol. Chem.* **2007**, 282, 7198.
- (21) Gransbury, G. K.; Kappen, P.; Glover, C. J.; Hughes, J. N.; Levina, A.; Lay, P. A.; Musgrave, I. F.; Harris, H. H. *Metallomics* **2016**, 8, 762.
- (22) Hall, M. D.; Foran, G. J.; Zhang, M.; Beale, P. J.; Hambley, T. W. *J. Am. Chem. Soc.* **2003**, 125, 7524.
- (23) Sooriyaarachchi, M.; Gailer, J.; Dolgova, N. V.; Pickering, I. J.; George, G. N. *J. Inorg. Biochem.* **2016**, 162, 96.
- (24) Leung, B. O.; Jalilehvand, F.; Szilagyi, R. K. *J. Phys. Chem. B* **2008**, 112, 4770.
- (25) Abbehausen, C.; de Paiva, R. E. F.; Bjornsson, R.; Gomes, S. Q.; Du, Z.; Corbi, P. P.; Lima, F. A.; Farrell, N. *Inorg. Chem.* **2017**, 57, 218.
- (26) Lebedev, D.; Pineda-Galvan, Y.; Tokimaru, Y.; Fedorov, A.; Kaeffer, N.; Copéret, C.; Pushkar, Y. *J. Am. Chem. Soc.* **2017**, 140, 451.
- (27) Sinfelt, J. H.; Via, G. H.; Lytle, F. W.; Greigor, R. B. *J. Chem. Phys.* **1981**, 75, 5527.

- (28) Zhang, X.; Canton, S. E.; Smolentsev, G.; Wallentin, C.-J.; Liu, Y.; Kong, Q.; Attenkofer, K.; Stickrath, A. B.; Mara, M. W.; Chen, L. *X. J. Am. Chem. Soc.* **2014**, *136*, 8804.
- (29) Brewer, S. A.; Brisdon, A. K.; Holloway, J. H.; Hope, E. G.; Levason, W.; Ogden, J. S.; Saad, A. K. *J. Fluor. Chem.* **1993**, *60*, 13.
- (30) Sanchez-Cano, C.; Gianolio, D.; Romero-Canelón, I.; Tucoulou, R.; Sadler, P. J. *Chem. Commun.* **2019**, 7065.
- (31) Sanchez-Cano, C.; Romer-Canelón, I.; Yang, Y.; Hands-Portman, I. J.; Bohic, S.; Cloetens, P.; Sadler, P. J. *Chem. Eur. J.* **2017**, *23*, 2512.
- (32) Ravel, B.; Newville, M. *J. Synchrotron Radiat.* **2005**, *12*, 537.
- (33) Salassa, L.; Borfecchia, E.; Ruiu, T.; Garino, C.; Gianolio, D.; Gobetto, R.; Sadler, P. J.; Cammarata, M.; Wulff, M.; Lamberti, C. *Inorg. Chem.* **2010**, *49*, 11240.
- (34) Borfecchia, E.; Maurelli, S.; Gianolio, D.; Groppo, E.; Chiesa, M.; Bonino, F.; Lamberti, C. *J. Phys. Chem. C* **2012**, *116*, 19839.
- (35) Borfecchia, E.; Lomachenko, K. A.; Giordanino, F.; Falsig, H.; Beato, P.; Soldatov, A. V.; Bordiga, S.; Lamberti, C. *Chem. Sci.* **2015**, *6*, 548.

Chapter 7

Conclusions and Future Work



7.1. Introduction

The aim of this thesis was to explore the molecular mechanism of action of $[\text{Os}(\eta^6\text{-p-cym})(4\text{-(2-pyridylazo)-}N,N\text{-dimethylaniline})\text{I}]^+$ **[2-I]**⁺ that serves as a promising anticancer drug candidate. In this **Chapter 7**, the main conclusions from each previous chapter (**Chapters 3 – 6**) will be summarized. Based on these findings, further studies related to **[2-I]**⁺ will be suggested, including interactions between **[2-I]**⁺ and enzymes involved in glycolysis, as well as separation and evaluation of chiral isomers of **[2-I]**⁺ and its analogues, the effect on the concentrations of intracellular reduced cytochrome *c*, and vibrational spectroscopic studies of **[2-I]**⁺ interactions with GSH.

7.2. Conclusions from Chapters 3 - 6

Exploring the molecular level mechanism of action of anticancer drugs is always challenging but an important process in their medical application, and eventually this will promote the development of the next generation of anticancer drugs. The half-sandwich osmium complex $[\text{Os}(\eta^6\text{-p-cym})(4\text{-(2-pyridylazo)-}N,N\text{-dimethylaniline})\text{I}]^+$ **[2-I]**⁺ and its analogues were first synthesised ~10 years ago.¹ Biological evaluations showed that **[2-I]**⁺ exhibits on average $49 \times$ higher potency than the current first line anticancer drug cisplatin towards 809 cancer lines,² and

promisingly, $[2-I]^+$ still maintains high potency to cisplatin-resistant cancer cells and is active *in vivo* in a mouse model.³ Since $[2-I]^+$ was first developed, many research studies about this anticancer drug candidate have been conducted. The results indicate that the cytotoxicity of $[2-I]^+$ to cancer cells mainly arises from two routes: increasing the superoxide level in cancer cells and shunting the energy generation focus of cancer cells from glycolysis to oxidative phosphorylation.² The intracellular tripeptide glutathione (γ -L-Glu-L-Cys-Gly, **GSH**) was found to play a crucial role in the potency of $[2-I]^+$ and tuning an appropriate concentration of intracellular GSH can maximize the potential cytotoxicity of $[2-I]^+$.^{4,5} The function of GSH towards $[2-I]^+$ might involve activating the hydrolysis of $[2-I]^+$ once uptaken by the cell.⁶ All these previous studies provided very important insight into the mechanism of action of $[2-I]^+$ but an improved understanding of the molecular behaviour of $[2-I]^+$, especially in reactions with GSH is still desired, which is an aim of this thesis.

In **Chapter 3**, complexes related to the reaction of $[2-I]^+$ with GSH (and other thiols) were synthesised and characterized including the lead complex $[2-I]^+$, the chlorido analogue $[2-Cl]^+$, the hydroxido analogue $[2-OH]^+$, glutathione adduct **2-SG** and the N-acetylcysteine adduct **2-NAC** (for structures see **Figure 7.4**). The chromatographic identification

(e.g. retention times, mass spectra) and electronic properties (e.g. extinction coefficients) of these complexes were determined. Moreover, by combining ICP-OES (inductively coupled plasma-optical emission spectrometry) and HPLC (high performance liquid chromatography) technologies, the proportional relationships between the concentration of these osmium complexes and HPLC peak areas were established. The work in **Chapter 3** provided the basis to identify, analyse and quantify the reactions of $[2-I]^+$ with GSH in the following chapters.

In **Chapter 4**, the hydrolysis of $[2-I]^+$ with GSH was systemically studied under various conditions. $[2-I]^+$ was found to be very stable under physiological conditions, but the presence of GSH dramatically increased the extent of hydrolysis to form the hydroxido analogue $[2-OH]^+$. With higher GSH : Os ratios, the thiolate adduct **2-SG** and sulfenate adduct **2-SOG** were observed. Besides GSH, other free thiols such as N-acetyl cysteine and dithiothreitol displayed the same function to promote the hydrolysis of $[2-I]^+$, which highlighted the importance of the thiol group in promoting this process. The pH influence of the hydrolysis of $[2-I]^+$ by GSH was also explored and the results showed that acidic conditions inhibited the reaction. This suggests that the deprotonated GS^- rather than GSH is a key species in the reaction with $[2-I]^+$. Moreover, the chlorido analogue $[2-Cl]^+$ and imino analogue $[2-imp\text{-}I]^+$ were compared with

the lead complex $[2-I]^+$. In the reaction with GSH, the azo group in complex $[2-Cl]^+$ exhibited a similar behaviour to the azo group in complex $[2-I]^+$ and GSH dramatically increased their hydrolysis. On the contrary, co-incubation with GSH did not increase the extent of hydrolysis of the imino complex $[2-imp-I]^+$. Comparison between azo complexes ($[2-I]^+$ and $[2-Cl]^+$) with the imino complex ($[2-imp-I]^+$) demonstrates the importance of the azo bond $-N=N-$. Based on these findings, pathways for the hydrolysis of $[2-I]^+$ in presence of GSH were proposed and probed by DFT (density functional theory) calculations. As a consequence, the pathway of deprotonated GS^- attacking the azo bond $-N=N-$ in the ligand of $[2-I]^+$ seems more likely to dominate its hydrolysis process.

In **Chapter 5**, free radical signals were detected in the reactions of osmium azo complexes (lead complex $[2-I]^+$, chlorido analogue $[2-Cl]^+$, hydroxido analogue $[2-OH]^+$) with GSH using EPR (electron paramagnetic resonance) spectroscopy. Under physiological conditions, $[2-OH]^+$ induced a mixture of free radicals: superoxide (O_2^-), hydroxyl radicals ($\bullet OH$) and hydrogen atoms ($\bullet H$) whilst $[2-I]^+$ and $[2-Cl]^+$ only induced the generation of hydroxyl radicals ($\bullet OH$). This may be related to the different reactivities of these three complexes. ($[2-OH]^+$ is more active than $[2-I]^+$ and $[2-Cl]^+$). More interestingly, under basic conditions

all these three osmium complexes can induce the mixture of free radicals, i.e. superoxide (O_2^-), hydroxyl radicals ($\bullet\text{OH}$), and hydrogen atoms ($\bullet\text{H}$). On the contrary, under acidic conditions, no free radical signals were observed for all of them. The influence of pH on free radical generation was in line with the influence of pH on the hydrolysis process, which indicated deprotonated GS^- rather than GSH was the active species which attacks the osmium complex. Moreover, no free radicals were detected when the reaction of the osmium azo complex with GSH was conducted under N_2 , which highlighted the importance of O_2 . The reaction of the imino analogue **[2-impy-Cl] $^+$** with GSH was also studied with EPR and no free radicals were generated. Comparison between the osmium azo complexes (**[2-I] $^+$** , **[2-Cl] $^+$** , **[2-OH] $^+$**) with imino complexes (**[2-impy-Cl] $^+$**) supported the azo bond $-\text{N}=\text{N}-$ as a key factor to induce free radicals. However, GSSG and H_2O_2 were detected from the reaction of osmium azo complexes with GSH. Based on all these findings, a mechanism involving attack of GS^- on the azo bond $-\text{N}=\text{N}-$ in the osmium complex and then donating electrons to O_2 to produce superoxide and oxidized GSSG was proposed. DFT calculations suggested a osmium-dioxygen complex as a possible intermediate in this free radical-producing process.

In **Chapter 6**, X-ray absorption spectroscopy was used in an attempt to detect the proposed thiolated-hydrazine **2-GS/NN** intermediate for the

reaction $[2-I]^+$ with GSH, because GSH reduction of the azo bond is the key to both the hydrolysis processes featured in **Chapter 4** and free radical generation in **Chapter 5**. The results showed there was a maximum of ~20% abundance of **2-GS/NN** in the reaction of $[2-I]^+$ with GSH and this confirmed a mechanism involving GSH reducing the azo bond to induce hydrolysis and free radical production.

7.3. Future Work

7.3.1. Interactions Between $[2-I]^+$ and Glycolytic Enzymes

In previous studies performed on $[2-I]^+$, cancer cells exposed to $[2-I]^+$ were found to undergo a metabolic shunt from glycolysis to oxidative phosphorylation.² In the studies of **Chapter 4**, the free thiols glutathione and N-acetyl-cysteine, which can be considered as models for cysteine containing enzymes, were found to bind to the osmium centre or reduce the azo bond in $[2-I]^+$. These studies suggested that interactions between $[2-I]^+$ and enzymes involved in glycolysis might be of interest for future research related to $[2-I]^+$.

Cancer cells tend to favour metabolism *via* glycolysis rather than the much more efficient oxidative phosphorylation pathway even under aerobic conditions (Warburg effect),⁷ which renders glycolysis a key

metabolic route to provide cancer cells with energy and nutrition. There are ten steps in glycolysis and nine enzymes are involved.

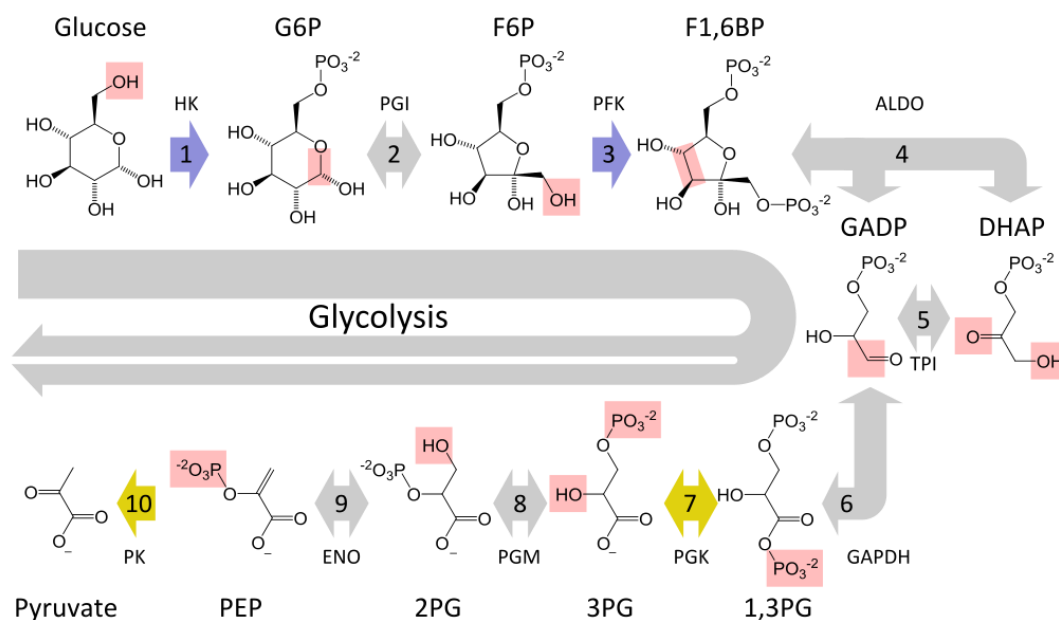


Figure 7.1. The glycolysis pathway in the cell (From Wikipedia)

In the glycolysis pathway, GAPDH (glyceraldehyde 3-phosphate dehydrogenase) is the enzyme that catalyzes the sixth step using GADP (glyceraldehyde 3-phosphate) as the substrate to produce 1,3PG (1,3-bisphosphoglycerate).⁸ Cancer cells frequently upregulate GAPDH to meet higher energy requirements than normal cells.⁹⁻¹¹ The catalysis mechanism of GAPDH involves a cysteine (Cys152) located at this enzyme's active pocket which firstly reduces the carbonyl group of the substrate GADP to form a thiohemiacetal intermediate, then NAD^+ accepts a hydride ion from thiohemiacetal intermediate to generate

NADH, whilst GAP is simultaneously oxidized to a thioester, and finally an inorganic phosphate attacks the thioester to release the product 1,3PG and free cysteine in the enzyme.^{12,13} It is clear that Cys152 is a key residue in the activity of GAPDH and could be a target site for **[2-I]⁺**. Preliminary molecular docking studies based on the reported crystal structure of **[2-I]⁺** and GAPDH (PDB code: 4WNC¹⁴) were performed using the Ligand Fit Dock protocol of Discovery Studio 3.5.¹⁵ The results from this study showed that a fragment of **[2-I]⁺** which has lost the arene function has the potential to enter into the active site of GAPDH.

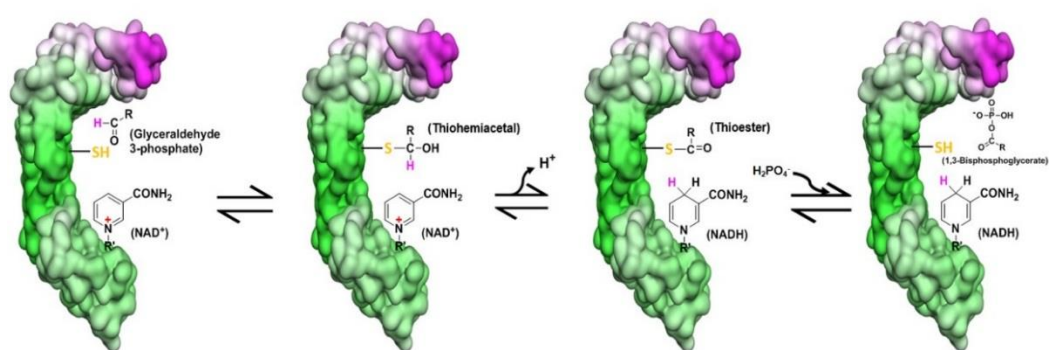


Figure 7.2. The catalysis mechanism of GAPDH.¹²

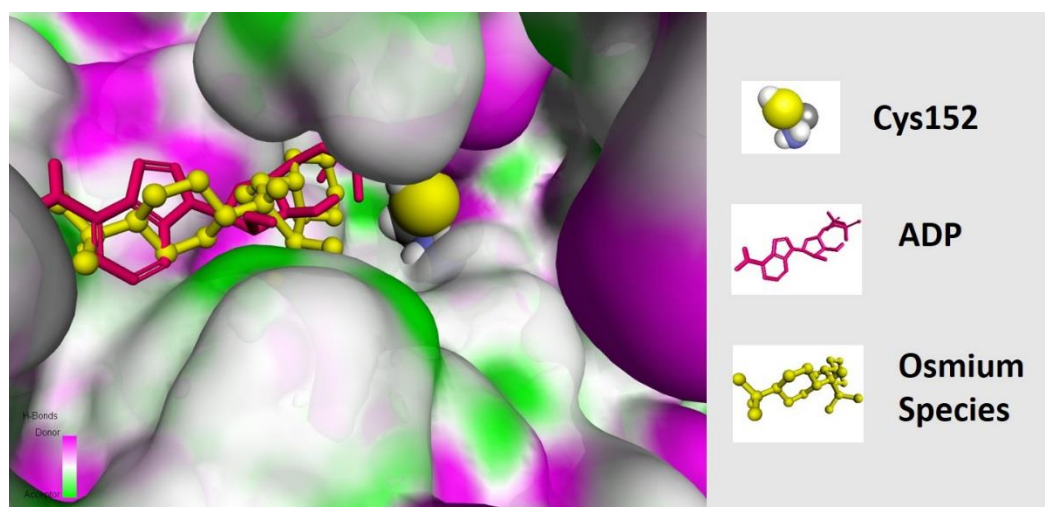


Figure 7.3. A 3D model of osmium species docked into the active site of GAPDH

7.3.2. Chiral Isomer Separation and Evaluation

In **Chapter 3**, several organo-osmium complexes were synthesised and characterized including lead complex **[2-I]⁺**, the chlorido analogue **[2-Cl]⁺**, the hydroxido analogue **[2-OH]⁺**, the N-acetyl-cysteine adduct **2-NAC** and the glutathione adduct **2-SG**. These complexes have one or more chiral centres and the chirality may influence their biological activities. Since the tragedy of severe birth defects caused by the S-isomer of thalidomide which was initially used as an antisedative drug, strict rules have been defined for the development of new stereoisomeric drugs.¹⁶⁻¹⁸ Several osmium-based anticancer complexes have been reported to exhibit stereoselectivity for their intracellular targets.^{19,20}

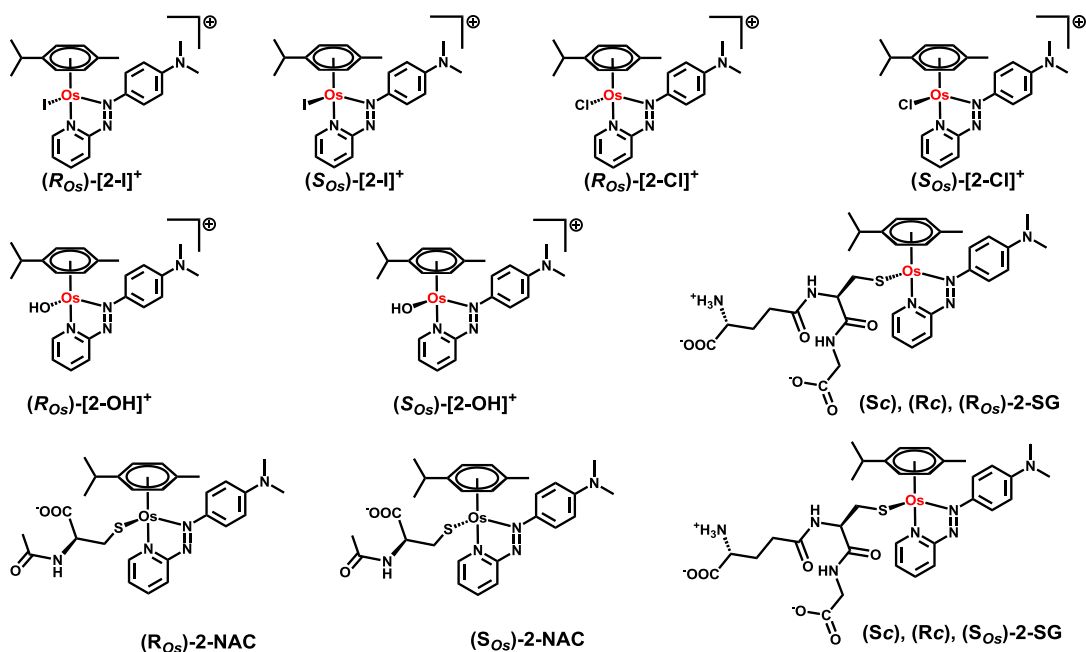


Figure 7.4. Isomers of osmium complexes related to **[2-I]⁺**.

7.3.3. Quantification of Intracellular Reduced Cytochrome *c*

In **Chapter 6**, it has been observed that osmium complexes ($[2-I]^+$, $[2-OH]^+$) react with GSH to produce superoxide which is able to reduce cytochrome *c*. It will be interesting to quantify intracellular reduced cytochrome *c* and a spectroscopic method has been reported.⁹ In the cell, cytochrome *c* mainly has two functions and both of these are closely related to its redox state.²¹ One is to be a key participant in the electron transport chain in mitochondria. Normally, oxidized cytochrome *c* accepts one electron from Complex III and transfer the electron to Complex IV.²¹ The other function of cytochrome *c* is to be released from mitochondria into cytoplasm to induce apoptosis.²¹⁻²⁴ However, only oxidized cytochrome *c* can activate caspase, which is required for apoptosis.^{25,26}

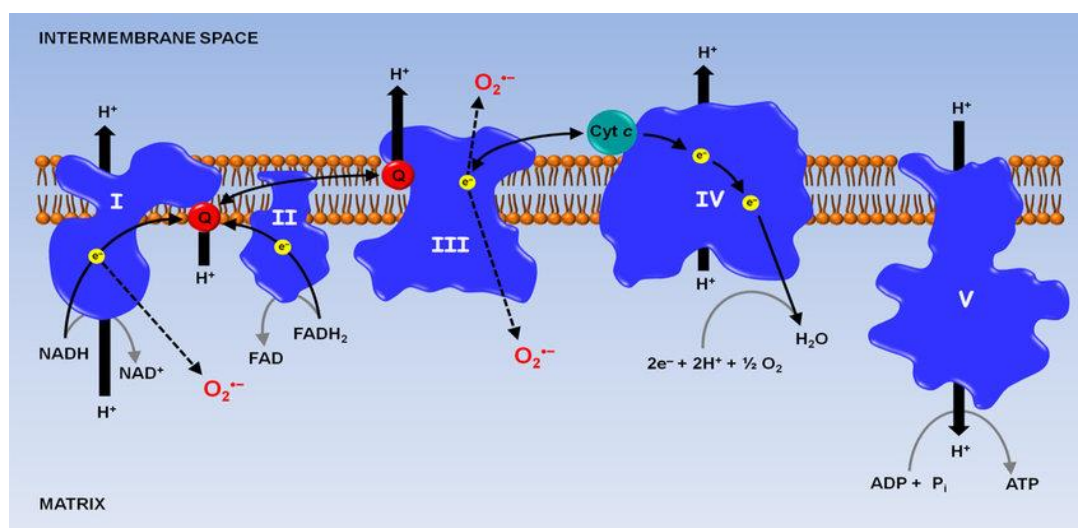


Figure 7.5. The role of cytochrome *c* in the electron transfer chain.²⁷

7.3.4. Vibrational Spectroscopy of the Reactions of $[2-I]^+$ with GSH

In **Chapter 4** and **Chapter 5**, the intermediate thiolated-hydrazine **2-GS/NN** and osmium-superoxido complex ($[2-O_2]^+$) were proposed to play key roles in the mechanism of the reaction of $[2-I]^+$ with GSH. Even through XAS signals assignable to **2-GS/NN** were captured in **Chapter 6**, more characterizations are required to identify these intermediates. Vibrational spectroscopy (infrared (IR) and Raman), is an energy-sensitive method and widely used for detecting intermediates.²⁸⁻³² Preliminary Raman studies of the reaction of $[2-I]^+$ with GSH were carried out and the intensity of a peak assignable to the azo bond (at 1236 cm^{-1} by DFT calculations) in $[2-I]^+$ was observed to change distinctly in the presence of GSH (**Figure 7.6**).

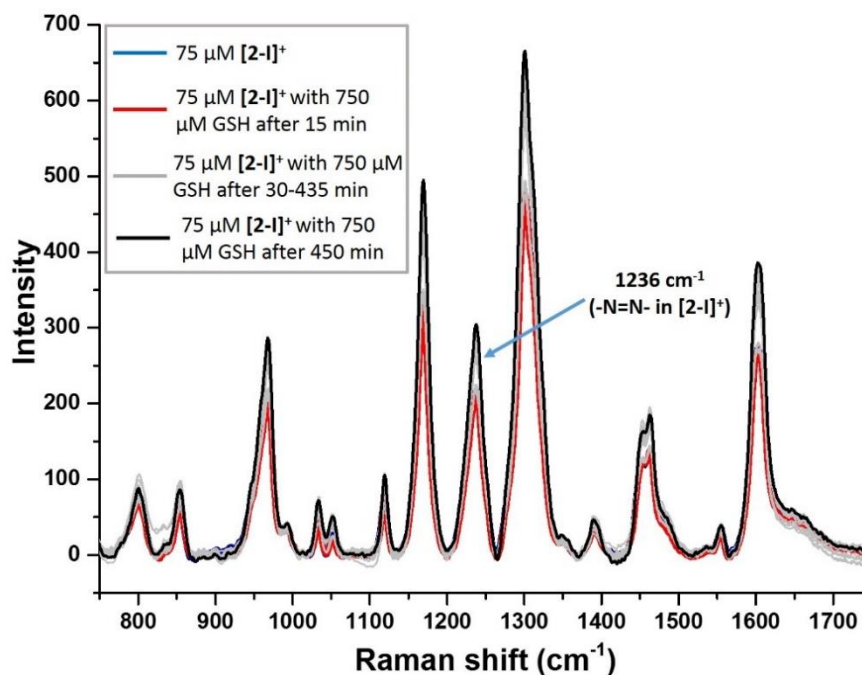


Figure 7.6. Raman spectra for $[2-I]^+$ (75 μM) in absence or presence of GSH (750 μM) at pH 7.4 during a 450 min incubation at 298 K upon irradiation at 633 nm.

7.4. References

- (1) Fu, Y.; Habtemariam, A.; Pizarro, A. M.; van Rijt, S. H.; Healey, D. J.; Cooper, P. A.; Shnyder, S. D.; Clarkson, G. J.; Sadler, P. J. *J. Med. Chem.* **2010**, *53*, 8192.
- (2) Hearn, J. M.; Romero-Canelón, I.; Munro, A. F.; Fu, Y.; Pizarro, A. M.; Garnett, M. J.; McDermott, U.; Carragher, N. O.; Sadler, P. *J. Proc. Natl. Acad. Sci. U.S.A.* **2015**, *112*, E3800.
- (3) Shnyder, S. D.; Fu, Y.; Habtemariam, A.; van Rijt, S. H.; Cooper, P. A.; Loadman, P. M.; Sadler, P. J. *MedChemComm* **2011**, *2*, 666.
- (4) Romero-Canelón, I.; Sadler, P. J. *Inorg. Chem.* **2013**, *52*, 12276.
- (5) Romero-Canelón, I.; Mos, M.; Sadler, P. J. *J. Med. Chem.* **2015**, *58*, 7874.
- (6) Needham, R. J.; Sanchez-Cano, C.; Zhang, X.; Romero-Canelón, I.; Habtemariam, A.; Cooper, M. S.; Meszaros, L.; Clarkson, G. J.; Blower, P. J.; Sadler, P. J. *Angew. Chem. Int. Ed.* **2017**, *56*, 1017.
- (7) Alfarouk, K. O.; Verduzco, D.; Rauch, C.; Muddathir, A. K.; Adil, H. H. B.; Elhassan, G. O.; Ibrahim, M. E.; Orozco, J. D. P.; Cardone, R. A.; Reshkin, S. J. *Oncoscience* **2014**, *1*, 777.
- (8) Tristan, C.; Shahani, N.; Sedlak, T. W.; Sawa, A. *Cell. Signal.* **2011**, *23*, 317.

- (9) Ramos, D.; Pellin-Carcelen, A.; Agusti, J.; Murgui, A.; Jorda, E.; Pellin, A.; Monteagudo, C. *Anticancer Res.* **2015**, *35*, 439.
- (10) Colell, A.; Green, D. R.; Ricci, J. E. *Cell Death Differ.* **2009**, *16*, 1573.
- (11) Revillion, F.; Pawlowski, V.; Hornez, L.; Peyrat, J. P. *Eur. J. Cancer* **2000**, *36*, 1038.
- (12) Seidler, N. W. *GAPDH: biological properties and diversity*; Springer Science & Business Media: Heidelberg, 2012.
- (13) Nicholls, C.; Li, H.; Liu, J. P. *Clin. Exp. Pharmacol. Physiol.* **2012**, *39*, 674.
- (14) White, M. R.; Khan, M. M.; Deredge, D.; Ross, C. R.; Quintyn, R.; Zucconi, B. E.; Wysocki, V. H.; Wintrode, P. L.; Wilson, G. M.; Garcin, E. D. *J. Biol. Chem.* **2015**, *290*, 1770.
- (15) Zhang, X.; Sangani, C. B.; Jia, L.-X.; Gong, P.-X.; Wang, F.; Wang, J.-F.; Zhu, H.-L. *RSC Adv.* **2014**, *4*, 54217.
- (16) Singhal, S.; Mehta, J.; Desikan, R.; Ayers, D.; Roberson, P.; Eddlemon, P.; Munshi, N.; Anaissie, E.; Wilson, C.; Dhodapkar, M. N. *Engl. J. Med.* **1999**, *341*, 1565.
- (17) D'Amato, R. J.; Loughnan, M. S.; Flynn, E.; Folkman, J. *Proc. Natl. Acad. Sci. U.S.A.* **1994**, *91*, 4082.
- (18) De Camp, W. H. *J. Pharm. Biomed. Anal.* **1993**, *11*, 1167.

- (19) Fu, Y.; Soni, R.; Romero, M. J.; Pizarro, A. M.; Salassa, L.; Clarkson, G. J.; Hearn, J. M.; Habtemariam, A.; Wills, M.; Sadler, P. J. *Chem. Eur. J.* **2013**, *19*, 15199.
- (20) Coverdale, J. P. C.; Romero-Canelon, I.; Sanchez-Cano, C.; Clarkson, G. J.; Habtemariam, A.; Wills, M.; Sadler, P. J. *Nat. Chem.* **2018**, *10*, 347.
- (21) Ow, Y.-L. P.; Green, D. R.; Hao, Z.; Mak, T. W. *Nat. Rev. Mol. Cell Biol.* **2008**, *9*, 532.
- (22) Ripple, M. O.; Abajian, M.; Springett, R. *Apoptosis* **2010**, *15*, 563.
- (23) Shi, Y. *Mol. Cell* **2002**, *9*, 459.
- (24) Boatright, K. M.; Salvesen, G. S. *Curr. Opin. Cell Biol.* **2003**, *15*, 725.
- (25) Hampton, B. M.; Zhivotovsky, B.; Slater, F. G. A.; Burgess, H. D.; Orrenius, S. *Biochem. J.* **1998**, *329*, 95.
- (26) Brown, G. C.; Borutaite, V. *Biochim. Biophys. Acta* **2008**, *1777*, 877.
- (27) Marzetti, E.; Bernabei, R.; Lorenzi, M.; Leeuwenburgh, C.; Calvani, R. In *Autophagy: Cancer, Other Pathologies, Inflammation, Immunity, Infection, and Aging*; Hayat, M. A., Ed.; Academic Press: Cambridge, 2014; Vol. 4, p 253.
- (28) Huang, Y.-F.; Kooyman, P. J.; Koper, M. T. M. *Nat. Commun.* **2016**, *7*, 12440.

- (29) Reijerse, E. J.; Pham, C. C.; Pelmeshnikov, V.; Gilbert-Wilson, R.; Adamska-Venkatesh, A.; Siebel, J. F.; Gee, L. B.; Yoda, Y.; Tamasaku, K.; Lubitz, W. *J. Am. Chem. Soc.* **2017**, *139*, 4306.
- (30) Zhang, S.; Shepherd, R. E. *Inorg. Chem.* **1988**, *27*, 4712.
- (31) Kieber-Emmons, M. T.; Annaraj, J.; Seo, M. S.; Van Heuvelen, K. M.; Tosha, T.; Kitagawa, T.; Brunold, T. C.; Nam, W.; Riordan, C. *J. Am. Chem. Soc.* **2006**, *128*, 14230.
- (32) Liu, L.-L.; Li, H.-X.; Wan, L.-M.; Ren, Z.-G.; Wang, H.-F.; Lang, J.-P. *Chem. Commun.* **2011**, *47*, 11146.

Appendix

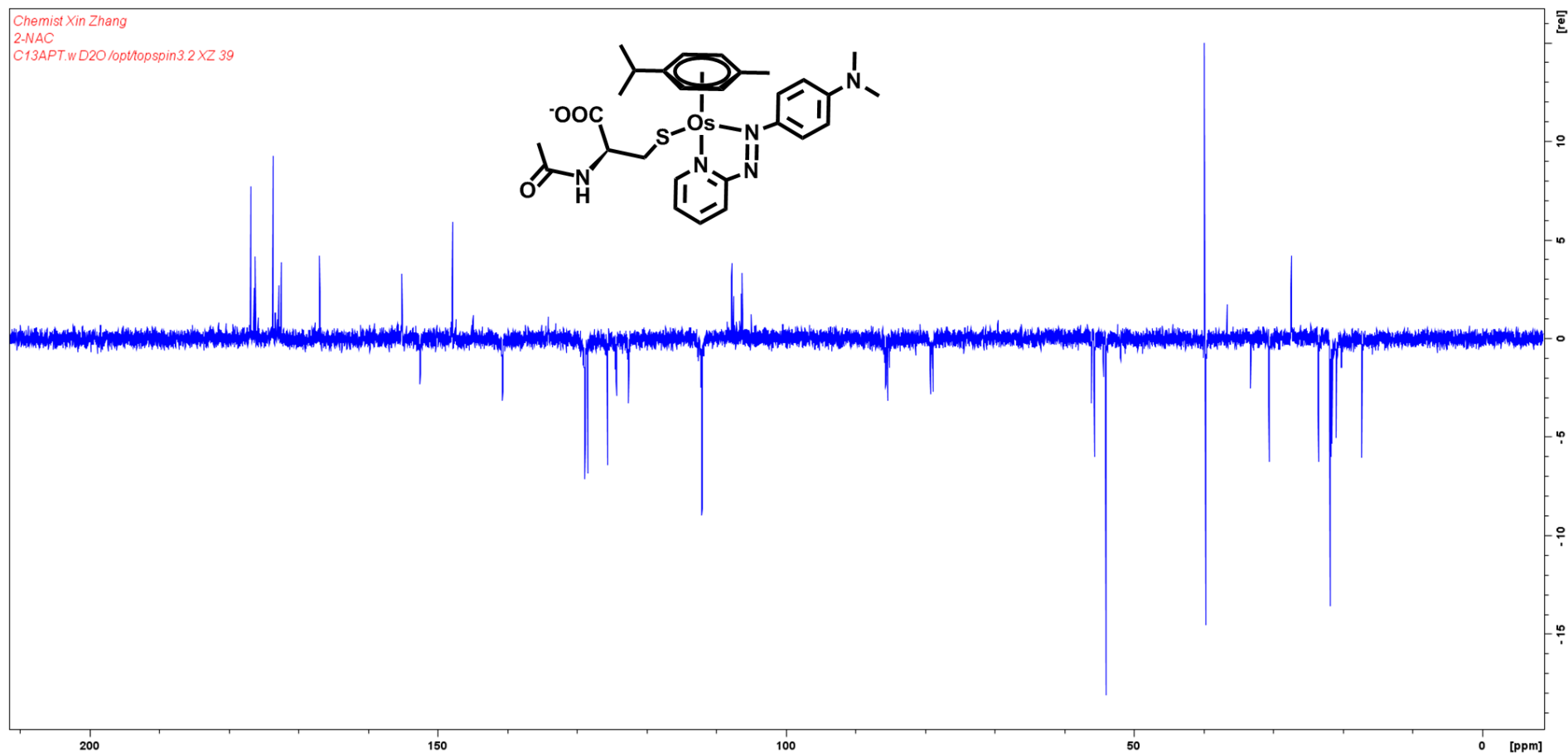


Figure A1. 600MHz ^{13}C NMR spectrum of 2-NAC in D_2O (20 mM).

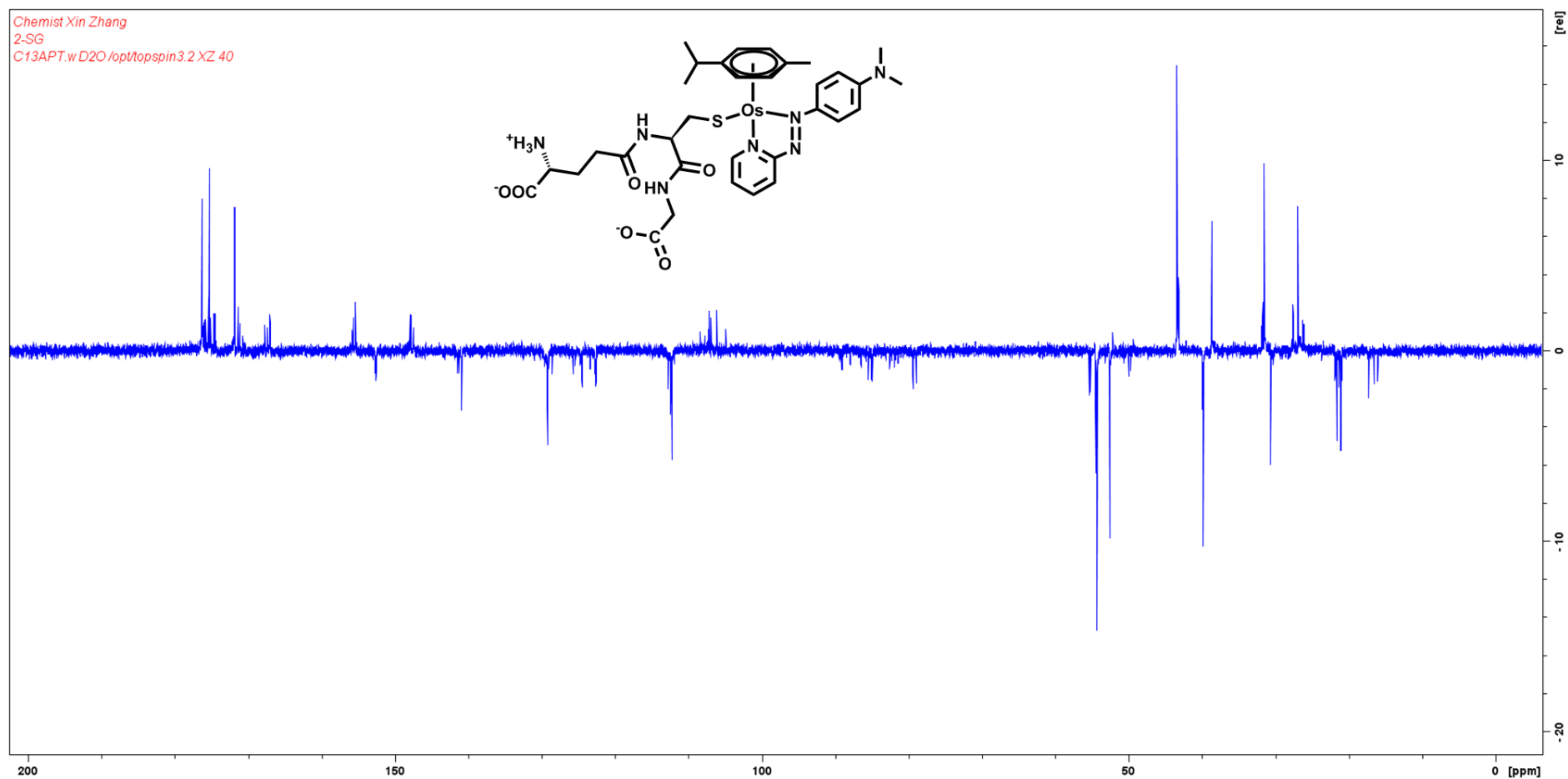


Figure A2. 600MHz ^{13}C NMR spectrum of **2-SG** in D_2O (20 mM).

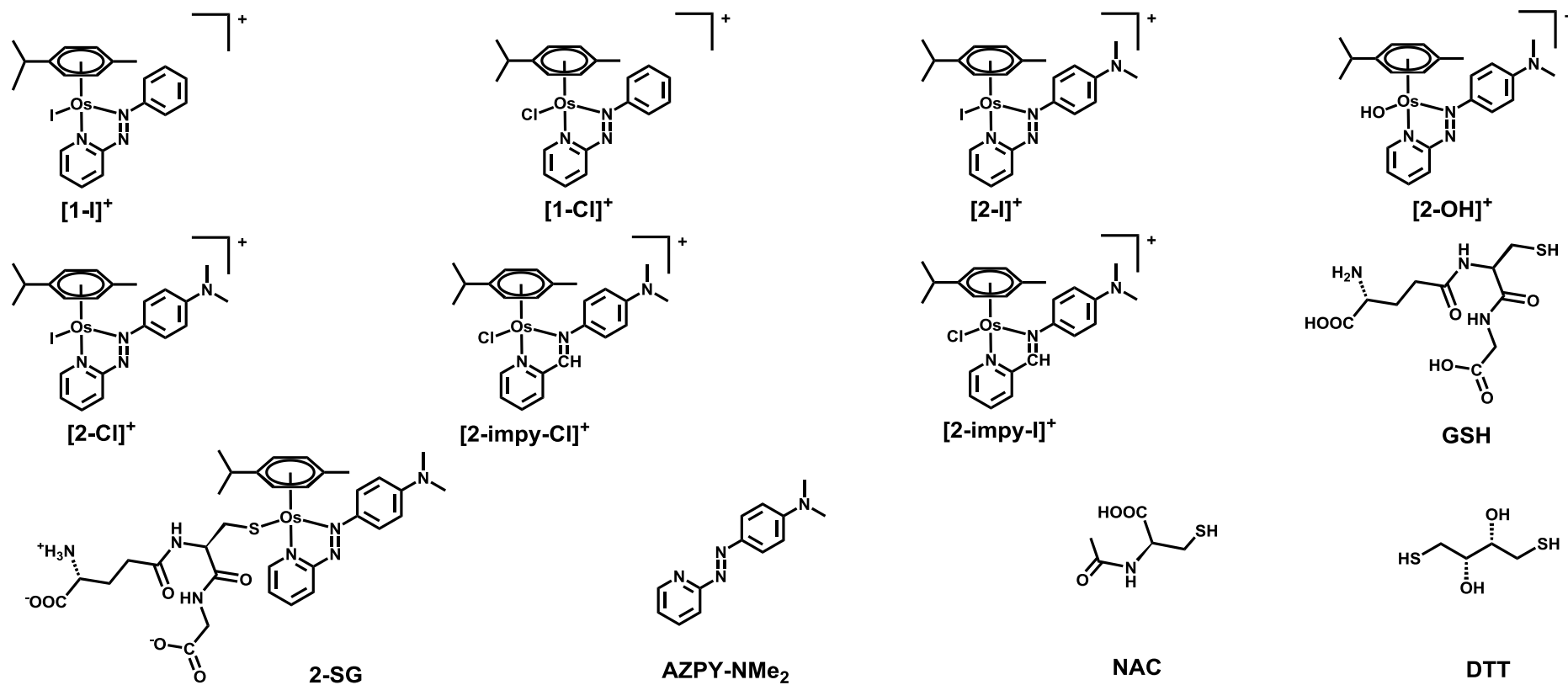


Figure A3. The molecular structures of compounds studied in this thesis.